An adjoint-based approach to the optimal control of separated flows

THÈSE N^O 6234 (2014)

PRÉSENTÉE LE 5 SEPTEMBRE 2014
À LA FACULTÉ DES SCIENCES ET TECHNIQUES DE L'INGÉNIEUR
LABORATOIRE DE MÉCANIQUE DES FLUIDES ET INSTABILITÉS
PROGRAMME DOCTORAL EN MÉCANIQUE

ÉCOLE POLYTECHNIQUE FÉDÉRALE DE LAUSANNE

POUR L'OBTENTION DU GRADE DE DOCTEUR ÈS SCIENCES

PAR

Edouard BOUJO

acceptée sur proposition du jury:

Prof. C. Ancey, président du jury
Prof. F. Gallaire, directeur de thèse
Dr C.-C. Caulfield, rapporteur
Prof. C. Cossu, rapporteur
Prof. T. Schneider, rapporteur

Acknowledgements

Acknowledgements

Abstract

Flow separation is relevant to many industrial applications, since it is detrimental to the aerodynamic performance of vehicles, induces vibrations in mechanical structures, but can also contribute to improve mixing in combustion devices.

In this thesis, the fundamental problem of separated flow control is addressed using adjoint-based methods applied to sensitivity analysis. Regions where steady control is the most effective to alter the flow are identified from so-called sensitivity maps. These maps are obtained by solving adjoint equations, at the same computational cost as that of solving the uncontrolled flow. The effect of any small-amplitude control being predicted from these maps, they provide useful information to find efficient control strategies, without the need to actually compute the controlled flow. Sensitivity information can also be used as a building block in iterative optimization algorithms aimed at designing optimal control configurations.

The problem is tackled from various angles by targeting several characteristic quantities of separated flows: amplification of external forcing (time-harmonic) or external noise (stochastic), geometric properties (position of separation and reattachment points, angle of the dividing streamline at the wall, area of backflow region and recirculation region), linear stability properties, and aerodynamic forces (drag, lift). The sensitivity of these quantities to control is systematically assessed. In particular, passive control by means of a small device introduced in the flow (e.g. a wire), and active control by means of blowing/suction at a solid wall are considered.

The amplification of external perturbations is typically large in globally stable but convectively unstable flows, because of non-normal effects, which might trigger bifurcation to unsteadiness and turbulence. It is observed that such amplification can be drastically reduced using appropriate control. In addition, in a backward-facing step flow the sensitivity of white noise amplification is found to be well captured when considering only the optimal perturbation at the most amplified frequency, thus simplifying control design.

In the steady flow past a wall-mounted bump, the position of the reattachment point is found to be very sensitive to control, with a sensitivity map largely similar to that of the backflow area and the recirculation area. In contrast, the separation point and the separatrix angles appear robust. In the flow past a typical bluff body, namely a circular cylinder, the sensitivity of the recirculation length is observed to be strongly correlated to that of the leading eigenmode's growth rate close to the linear instability threshold.

Finally, lift and drag sensitivities to steady actuation are presented for the steady flow past another bluff body, the square cylinder, at subcritical Reynolds number. It appears that lift

Résumé

La séparation des écoulements concerne de nombreuses applications industrielles car elle réduit les performances aérodynamiques, provoque des vibrations dans les structures mécaniques, mais peut aussi contribuer à améliorer le mélange dans les dispositifs de combustion. Dans cette thèse, le problème fondamental des écoulements séparés est abordé avec des méthodes adjointes appliquées à l'analyse de sensibilité. Les régions où un contrôle stationnaire est le plus efficace pour modifier l'écoulement sont identifiées à partir de cartes de sensibilités. Ces cartes sont obtenues en résolvant des équations adjointes, au même coût de calcul que pour résoudre l'écoulement non contrôlé. L'effet de n'importe quel contrôle de petite amplitude étant prédit par ces cartes, elles fournissent des informations utiles à l'élaboration de stratégies efficaces de contrôle, sans jamais avoir à calculer l'écoulement contrôlé. La sensibilité est également une information qui peut être utilisée dans des algorithmes itératifs d'optimisation visant à concevoir des configurations optimales de contrôle.

Ce problème est abordé sous plusieurs angles, en ciblant différentes quantités d'intérêt dans les écoulements séparés : amplification d'un forçage externe (harmonique en temps) ou d'un bruit externe (stochastique), propriétés géométriques (position des points de décollement et de recollement, angles de la séparatrice à la paroi, aire de la zone d'écoulement inverse et de la zone de recirculation), propriétés de stabilité linéaire, et forces aérodynamiques (traînée, portance). La sensibilité au contrôle de ces quantités est analysée de manière systématique. Sont considérés en particulier le contrôle passif au moyen de petits éléments introduits dans l'écoulement (par exemple cylindre) et le contrôle actif par soufflage/aspiration à la paroi.

L'amplification de perturbations externes est typiquement grande dans les écoulements globalement stables mais convectivement instables, en raison d'effets non-normaux qui peuvent provoquer la transition vers un régime instationnaire ou turbulent. Il est observé que cette amplification peut être réduite significativement en utilisant un contrôle approprié. De plus, la sensibilité de l'amplification de bruit blanc dans l'écoulement autour d'une marche descendante est bien capturée en ne considérant que la perturbation optimale à la fréquence la plus amplifiée, simplifiant ainsi la conception du contrôle.

Dans l'écoulement stationnaire au dessus d'une bosse sur une plaque plane, la position du point de recollement est très sensible au contrôle, avec une carte de sensibilité similaire à celle des aires des zones d'écoulement inverse et de recirculation. A l'inverse, les angles de la séparatrice à la paroi et le point de décollement sont robustes. Dans l'écoulement autour d'un corps non profilé typique, le cylindre circulaire, la sensibilité de la longueur de recirculation est fortement corrélée à celle du taux de croissance du mode propre dominant près du

seuil d'instabilité.

Enfin, les sensibilités de la traînée et de la portance à un contrôle stationnaire sont présentées pour l'écoulement autour d'un autre corps non profilé, le cylindre carré, à un nombre de Reynolds sous-critique. Il apparaît que portance et traînée peuvent être modifiées indépendamment avec un contrôle pariétal si sa position et son orientation sont bien choisies. Plus généralement, les sensibilités des forces de pression et forces visqueuses peuvent être calculées individuellement avec un problème adjoint modifié, et la sensibilité de n'importe quelle combinaison de la traînée et de la portance est facilement obtenue sans coût supplémentaire.

Comme cette thèse le suggère, une grande variété de propriétés des écoulements stationnaires peut être analysée en termes de sensibilité à un contrôle stationnaire, ouvrant des perspectives intéressantes pour le contrôle des écoulements séparés. Ce travail demande à être étendu aux écoulements et contrôles instationnaires, soit avec une méthode adjointe par allers-retours prenant en compte la dynamique complète de l'écoulement, soit avec une modélisation appropriée des caractéristiques moyennes.

Mots clefs : contrôle d'écoulements, instabilité hydrodynamique, méthodes adjointes, analyse de sensibilité, contrôle optimal, réponse harmonique, écoulements séparés

Contents

Contents

Introduction

Separated flows

Separation occurs when a fluid detaches from the body along which it is flowing. Typical situations where flows separate include bluff bodies, convex walls, and adverse pressure gradients. These situations can be encountered in a wide range of natural and industrial configurations: water flow past islands or bridges, air around past mountains, buildings or chimneys, blood flow in arteries with stenosis or aneurysm, flow around vehicles, in combustion engines, hydraulic and wind turbines, pumps, and so on.

In applications related to aerodynamics, separation causes a loss of performance: reduced lift and stability, increased drag and energy consumption. Separation might also induce oscillations, leading to undesirable noise at best, and to accelerated mechanical fatigue or even failure at worst. In contrast, separation is associated with a recirculation region, where the fluid travels upstream against the main flow, which often enhances mixing and is therefore desirable in combustion devices.

Separated flows are often remarkably unstable, as a consequence of the elongated shear layer, where the Kelvin-Helmholtz instability can feed on the intense vorticity layer. Despite negative velocities in the recirculation region, wall-bounded flows are however most often only convectively unstable and behave as "noise amplifiers" that selectively amplify external disturbances (Chomaz, 2005). An archetype of these wall-bounded separated flows is the backward facing step that will be analysed in chapter 3, and which is characterized by a geometrically constrained separation point. In contrast, in separated flows in the wake of bluff bodies, a pocket of absolute instability is often encountered in the lee of the obstacle which dictates a flow "oscillator" behaviour (Chomaz, 2005). An archetype of oscillator flow is the flow around a cylinder, investigated in section 4.3 and in chapter 5.

Control

Given the importance of flow separation, it is not a surprise that there is extensive research on its control (Seifert & Pack Melton, 2006). Back in 1904, Prandtl used a suction mechanism to modify the flow past a cylinder and demonstrate the role of the boundary layer in separation

(*a*)

(*b*)

(*c*)
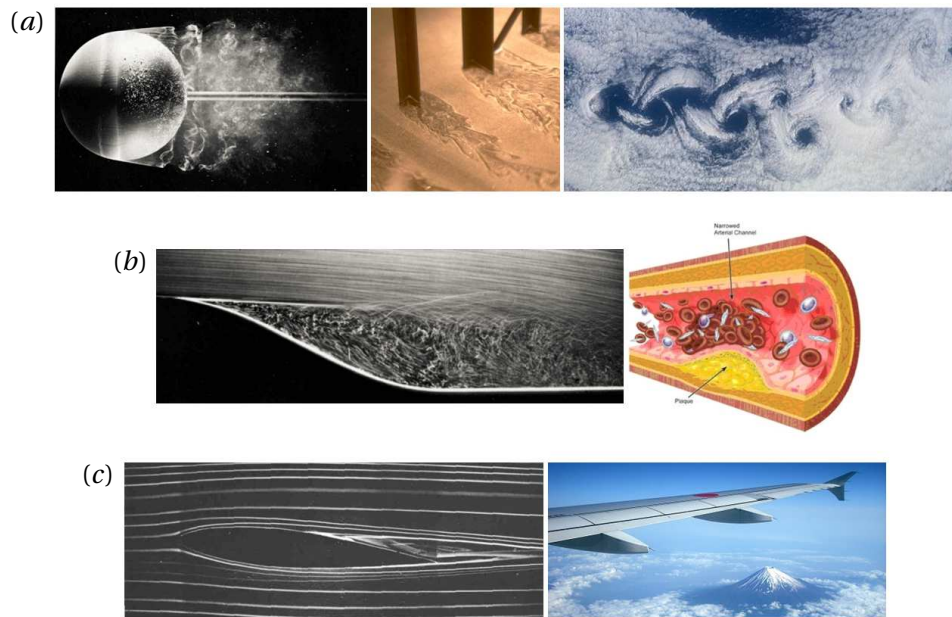
Figure 1 – Flow separation occurs in many situations: (*a*) around bluff bodies (sphere (Werlé, 1980), obstacles in a liquid stream, Kármán vortex street in clouds past a volcano), usually leading to oscillations; (*b*) past convex walls (rounded step (Werlé, 1974), arterial stenosis); (*c*) past streamlined objects in presence of an adverse pressure gradient (airfoil (Werlé, 1980), airplane).

(Schlichting, 1979). Driven by the development of aeronautics, many theoretical and experimental studies followed. A very large range of strategies do exist now, including in increasing order of complexity: (i) passive control, (ii) active open-loop control, with actuators requiring energy, (iii) active closed-loop control, where sensors provide measurements (Fiedler & Fernholz, 1990; Gad-el Hak, 1996; Choi, Jeon & Kim, 2008).

Based on the well-established modern linear control theory (Kim & Bewley, 2007), closed-loop control theory has the potential to bring performance and robustness. However, Its application to fluid flows still poses challenges, partly due to the large number of degrees of freedom involved. Closed-loop control therefore relies either on the use of black-box controllers (Henning & King, 2007; Beaudoin, Cadot, Aider & Wesfreid, 2006; Gautier & Aider, 2013) or on reduced order models, themselves built with identification methods (Tian, Song & Cattafesta, 2006; Becker, King, Petz & Nitsche, 2007; Juillet, Schmid & Huerre, 2013), extracted from projection on bases (Rowley, 2005; Barbagallo, Sipp & Schmid, 2009; Bagheri, Henningson, Hoepffner & Schmid, 2009; Ehrenstein, Passaggia & Gallaire, 2011), or motivated by physical insight (Roussopoulos & Monkewitz, 1996; Alam, Liu & Haller, 2006).

Open-loop control has been successfully applied to separation control: heating, pulsed synthetic jets, wall motion, as well as steady suction or blowing at the wall (McLachlan, 1989; Fiedler & Fernholz, 1990; Schumm, Berger & Monkewitz, 1994; Seifert, Darabi & Wygnanski, 1996; Garnier, Pamart, Dandois & Sagaut, 2012). Although theoretical analyses start to address the question (Sipp, 2012), the determination of the most effective forcing location and frequency is often left to extensive experimental or numerical parameter sweeps (Greenblatt & Wygnanski, 2000).

Passive control strategies rely either on geometry modification, from heuristic golf ball dimples to systematic shape optimisation (Mohammadi & Pironneau, 2001), or on devices such as cavities, plates, ribbons or vortex generators (Prasad & Williamson, 1997; Weickgenannt & Monkewitz, 2000; Pujals, Depardon & Cossu, 2010). Even rods or wires of small size, if inserted in well-chosen regions of the flow, can have a significant impact on flow instability, vortex shedding frequency, drag and lift forces, and the size of the recirculation region (Strykowski & Sreenivasan, 1990; Igarashi, 1997; Sakamoto, Tan & Haniu, 1991; Dalton, Xu & Owen, 2001; Parezanović & Cadot, 2012). In particular, Strykowski & Sreenivasan (1990) found that vortex shedding in the laminar wake of a circular cylinder could be completely suppressed using this kind of small control cylinder. Testing systematically all locations, they built detailed maps showing where control was successful (figure 2(a)). Parezanović & Cadot (2012) used the same method in the turbulent flow past a D-shaped cylinder, taking measurements at an impressive 5000 locations to make sensitivity maps of vortex shedding frequency, pressure drag and recirculation length.
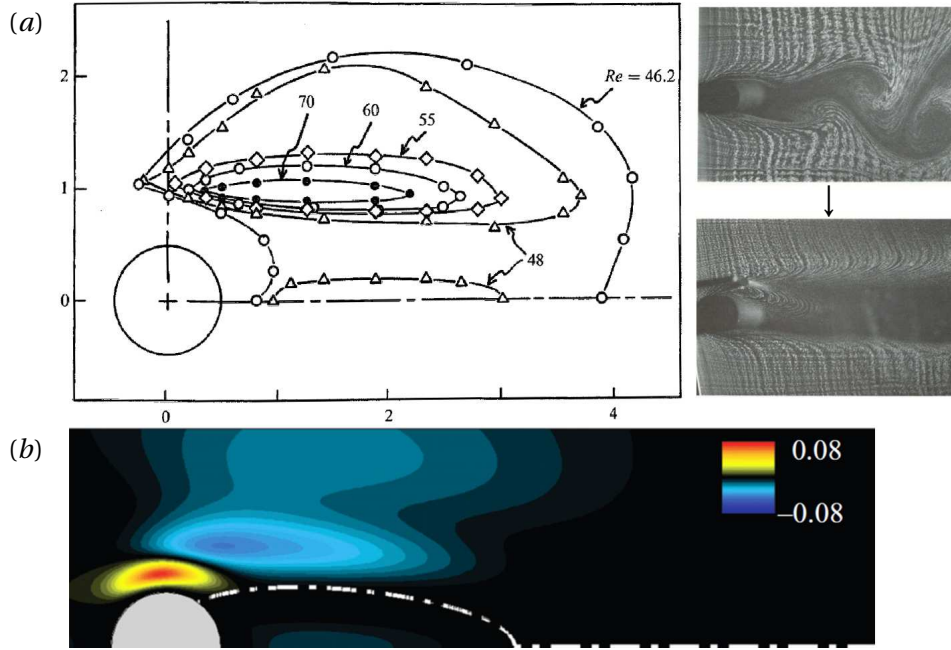
Figure 2 – Effect of a small control rod on vortex shedding in the wake of a circular cylinder. (*a*) Regions where vortex shedding is suppressed at different Reynolds numbers. From Strykowski & Sreenivasan (1990). (*b*) Variation of the leading eigenvalue's growth rate: red regions are destabilizing, blue regions are stabilizing. *Re* = 46.8 (Marquet *et al.*, 2008).

Adjoint-based methods

Although extensive parameter studies provide much useful information, they suffer from being highly time consuming. One way to tackle the problem of efficient control design is through sensitivity analysis, and more generally, adjoint-based methods. As detailed in chapter 1, the central idea is to compute how a flow property would be affected by *any* small-amplitude variation of a given control variable, in a *single* calculation, i.e. without ever computing the actually controlled flow. This tour de force, definitely puzzling when first encountered, is made possible by the derivation of a suitable adjoint problem. This kind of analysis was popularized in hydrodynamics by Hill (1992), who obtained a sensitivity map giving the effect of a small control wire on the most unstable eigenvalue of the linearized flow past a circular cylinder (responsible for vortex shedding when $Re \simeq 47$), and reproduced experimental results from Strykowski & Sreenivasan (1990). Still in the context of linear stability, Bottaro, Corbett & Luchini (2003) applied the same technique to a parallel flow to compute the sensitivity of eigenvalues (growth rate and frequency) to flow modification. They showed that minute changes in the base flow velocity profile could destabilize a plane channel flow. More recently, Marquet et al. (2008) revisited the circular cylinder flow (figure 2(b)), using linear analysis to assess the effect of an infinitely small control cylinder on the stability of the main cylinder flow. They first perform a global stability analysis of the uncontrolled flow and determine the growth rate and frequency of the vortex shedding eigenmode. Then, they compute

the eigenvalue variation induced by the control from the inner product between a sensitivity function (computed with the adjoint method, and representing the variational derivative of the eigenvalue with respect to a source of momentum in the flow field) and a localized body force mimicking the presence of the control cylinder. Finally, they determine regions of interest where the control cylinder would stabilize the vortex shedding eigenmode or modify its frequency. The approach is an attractive alternative to time-consuming "trial and error" methods since it allows to explore all possible positions of the control cylinder without ever calculating any controlled state. Meliga, Sipp & Chomaz (2010) extended the method to compressible flows and considered additional types of control such as heating and wall blowing or suction. Giannetti & Luchini (2007) also studied the sensitivity of eigenvalues to perturbations of the eigenvalue problem itself and to force-velocity coupling, and Giannetti, Camarri & Luchini (2010) generalized the approach to time-periodic base flows. Other examples include Fani, Camarri & Salvetti (2012) and Tchoufag, Magnaudet & Fabre (2013), who considered respectively the flow in more complex geometries and fluid-structure interaction.

The method was recently extended by Brandt, Sipp, Pralits & Marquet (2011) to compute the sensitivity of harmonic gain, i.e. the asymptotic amplification of harmonic forcing in stable flows. While global eigenvalues are important to characterize absolutely unstable flows (oscillators), harmonic gain is more relevant for convectively unstable flows (noise amplifiers) (Chomaz, 2005).

In another context, shape optimization is a famous example of optimal design based on sensitivity analysis (Mohammadi & Pironneau, 2001; Jameson, Martinelli & Pierce, 1998), where e.g. the sensitivity of aerodynamic forces to a small-amplitude displacement of the surface everywhere on the body is obtained in a single calculation, and used in an iterative way to minimize drag or optimize other objective functions. Sensitivity is also used in adaptive mesh refinement to minimize numerical errors (Hoffman, 2005).

Sensitivity analysis belongs to the larger group of adjoint-based methods, which are highly versatile, as showed by their many applications in fluid dynamics (Luchini & Bottaro, 2014). One typical use of these methods is to compute initial perturbations which undergo the largest amplification after some time T (Butler & Farrell, 1992; Corbett & Bottaro, 2000; Blackburn, Barkley & Sherwin, 2008). The concept of optimal perturbation and optimal transient growth is of importance since it might be linked with "by-pass transition" in flows which are predicted to be linearly stable at any Reynolds number but actually become unsteady or turbulent. Large transient growth as well as large harmonic gain are the consequence of the non-normality of the Navier–Stokes operator (Trefethen, Trefethen, Reddy & Driscoll, 1993; Chomaz, 2005). When small-amplitude perturbations are considered, optimal perturbations can be obtained by computing the norm of a matrix (i.e. solving an eigenvalue problem or a singular value problem), but if the full nonlinear dynamics are taken into account then adjoint equations are needed (Pringle & Kerswell, 2010; Cherubini, De Palma, Robinet & Bottaro, 2011; Rabin, Caulfield & Kerswell, 2012). Objective functions other than energy are also attracting attention: for example Monokrousos, Bottaro, Brandt, Di Vita & Henningson (2011)

consider viscous dissipation as a measure of turbulence, Foures, Caulfield & Schmid (2013) use an ∞-norm to spatially localize perturbations, and Foures, Caulfield & Schmid (2014) efficiently optimize the mixing of a passive scalar using variance as well as a "mix-norm" targeting large-scale structures.

Another major application of adjoint-based methods is the optimal control of unsteady, fully nonlinear flows, where linear control tools such as Riccati-based feedback (Kim & Bewley, 2007) might fail. This setting allows for unsteady and non-small control. Bewley, Moin & Temam (2001) achieved a spectacular relaminarization of a turbulent channel flow, and compared the performance of several objective functions. This method was also used in an attempt to control the separated flow past a wall-mounted bump (Passaggia & Ehrenstein, 2013). A similar approach is at the heart of estimation methods, for example in weather forecasting.

Present work

This thesis explores the potential of sensitivity analysis for the control of separated flows. Solving adjoint equations, sensitivity maps are computed to assess the effect of steady control in the flow or at the wall. Quantities which are not commonly targeted are considered here, for instance global indicators characterizing the flow geometry. The flow over a backward-facing step is used as a typical noise amplifier, and the flow past a cylinder as a typical oscillator. In addition, the flow above a wall-mounted bump, introduced a decade ago by Marquillie & Ehrenstein (2002), is also selected as a representative of more complex flows that are neither pure amplifiers (since they become globally unstable at large Reynolds number), nor pure oscillators (since the dynamics above threshold is far more complex than periodic vortex shedding); furthermore, geometrical properties of this flow are rich, with a separation point free to move along the bump surface depending on the Reynolds number.

The outline is the following. **Chapter 1** gives a brief overview of adjoint-based methods for constrained optimization and sensitivity, with examples of applications in hydrodynamics: optimal growth, optimal control, sensitivity of eigenvalues. **Chapter 2** deals with the amplification of harmonic forcing in the flow past a wall-mounted bump. Sensitivity analysis is used to design a simple open-loop wall suction control allowing to reduce amplification, as confirmed both numerically and experimentally. **Chapter 3** extends this study to the amplification of stochastic noise, with an application to the flow past a backward-facing step. **Chapter 4** tackles the problem of separation control from a different viewpoint, considering geometric quantities in separated flows: position of separation and reattachment points, angle of the separating streamline at the wall, and area of the backflow region and recirculation region. Illustrations are given in a wall-bounded flow and in the flow past a bluff body. An application of Interactive Boundary Layer theory is also presented, as an efficient means to compute separated flows. Finally, **chapter 5** is dedicated to the sensitivity analysis of aerodynamic forces and illustrated with the flow past a square cylinder.

Chapter 1

Adjoint-based methods for optimization and sensitivity

This chapter modestly aims at giving a brief overview of adjoint-based methods for constrained optimization and sensitivity analysis. Section 1.1 introduces governing equations used throughout this chapter and the whole thesis. Section 1.2 presents the concept of Lagrange multipliers and adjoint equations in a general setting. Sections 1.3 to 1.5 give classical examples in hydrodynamic stability: optimal growth, optimal control, and eigenvalue sensitivity. Most of the contents are based on existing literature (Schmid & Henningson, 2001; Gallaire, 2002; Cordier, 2009; Cossu, 2014).

1.1 Governing equations

This short section first gathers the main governing equations used throughout this thesis. Considering the two-dimensional flow of an incompressible fluid, its motion is governed by the Navier–Stokes equations for the state variable $\mathbf{Q}(\mathbf{x}, t) = (\mathbf{U}(\mathbf{x}, t), P(\mathbf{x}, t))$, where $\mathbf{U}$ denotes the velocity field of components U and V in the streamwise and cross-stream directions x and y, and P denotes the pressure field:

$$\nabla \cdot \mathbf{U} = 0, \quad \partial_t \mathbf{U} + \mathbf{U} \cdot \nabla \mathbf{U} + \nabla P - Re^{-1} \nabla^2 \mathbf{U} = \mathbf{0}. \tag{1.1}$$

Here $Re = U_\infty L / v$ is the Reynolds number based on some characteristic length L, a reference velocity U_∞ and the fluid kinematic viscosity v. Given appropriate boundary and initial conditions, these equations can be discretized in space and time and solved with a time-marching technique. If one looks for a steady base flow $\mathbf{Q}(\mathbf{x})$, the time derivative in equations (4.56) vanishes, $\partial_t \mathbf{U} = 0$, and the solution of the fixed-point problem

$$\nabla \cdot \mathbf{U} = 0, \quad \mathbf{U} \cdot \nabla \mathbf{U} + \nabla P - Re^{-1} \nabla^2 \mathbf{U} = \mathbf{0} \tag{1.2}$$

can be obtained with an iterative technique. When perturbations $\mathbf{q}'(\mathbf{x},t) = (\mathbf{u}'(\mathbf{x},t), p'(\mathbf{x},t))$ are superimposed on the flow, their evolution is governed by the perturbation equations:

$$\nabla \cdot \mathbf{u}' = 0, \quad \partial_t \mathbf{u}' + \mathbf{U} \cdot \nabla \mathbf{u}' + \mathbf{u}' \cdot \nabla \mathbf{U} + \mathbf{u}' \cdot \nabla \mathbf{u}' + \nabla p' - Re^{-1}\nabla^2 \mathbf{u}' = \mathbf{0}. \tag{1.3}$$

If these perturbations are of small amplitude compared to the base flow, one can neglect the nonlinear term $\nabla \mathbf{u}' \cdot \mathbf{u}'$ and obtain the linearised perturbation equations

$$\nabla \cdot \mathbf{u}' = 0, \quad \partial_t \mathbf{u}' + \mathbf{U} \cdot \nabla \mathbf{u}' + \mathbf{u}' \cdot \nabla \mathbf{U} + \nabla p' - Re^{-1}\nabla^2 \mathbf{u}' = \mathbf{0}. \tag{1.4}$$

Further, it is possible to analyse the linear stability of the base flow using the normal mode decomposition $\mathbf{q}'(\mathbf{x},t) = \mathbf{q}(\mathbf{x})e^{\sigma t} + c.c.$, where $c.c.$ stands for complex conjugate, and solving the resulting eigenvalue problem:

$$\nabla \cdot \mathbf{u} = 0, \quad \sigma \mathbf{u} + \mathbf{U} \cdot \nabla \mathbf{u} + \mathbf{u} \cdot \nabla \mathbf{U} + \nabla p - Re^{-1}\nabla^2 \mathbf{u} = \mathbf{0}. \tag{1.5}$$

Alternatively, one can investigate the linear harmonic response of the flow, i.e. the evolution of perturbations generated by a small-amplitude harmonic forcing $\mathbf{f}'(\mathbf{x},t) = \mathbf{f}(\mathbf{x})e^{i\omega t} + c.c.$:

$$\nabla \cdot \mathbf{u} = 0, \quad i\omega \mathbf{u} + \mathbf{U} \cdot \nabla \mathbf{u} + \mathbf{u} \cdot \nabla \mathbf{U} + \nabla p - Re^{-1}\nabla^2 \mathbf{u} = \mathbf{f}. \tag{1.6}$$

In shorthand notation, equations (1.1) to (1.6) become:

$$\mathbf{B}\partial_t \mathbf{Q} + \mathbf{N}(\mathbf{Q}) = \mathbf{0} \qquad \text{(unsteady Navier–Stokes equations)}, \tag{1.7}$$

$$\mathbf{N}(\mathbf{Q}) = \mathbf{0} \qquad \text{(steady Navier–Stokes equations)}, \tag{1.8}$$

$$\mathbf{B}\partial_t \mathbf{q}' + \mathbf{N}(\mathbf{Q} + \mathbf{q}') - \mathbf{N}(\mathbf{Q}) = \mathbf{0} \qquad \text{(nonlinear perturbation equations)}, \tag{1.9}$$

$$\mathbf{B}\partial_t \mathbf{q}' + \mathbf{N}_L(\mathbf{Q})\mathbf{q}' = \mathbf{0} \qquad \text{(linearized perturbation equations)}, \tag{1.10}$$

$$\sigma \mathbf{B}\mathbf{q} + \mathbf{N}_L(\mathbf{Q})\mathbf{q} = \mathbf{0} \qquad \text{(linearized eigenvalue problem)}, \tag{1.11}$$

$$i\omega \mathbf{B}\mathbf{q} + \mathbf{N}_L(\mathbf{Q})\mathbf{q} = (\mathbf{f},0)^T \qquad \text{(small-amplitude harmonic forcing)}, \tag{1.12}$$

where $\mathbf{B}$ is a "mass" operator such that $\mathbf{B}(\mathbf{U},P)^T = (\mathbf{U},0)^T$, $\mathbf{N}$ is the steady nonlinear Navier–Stokes operator, and $\mathbf{N}_L(\mathbf{Q}) = d\mathbf{N}/d\mathbf{Q}$ is the corresponding linear operator (linearised around the base flow $\mathbf{Q}$).

1.2 Optimization and sensitivity

In a given flow, what are the initial perturbations that experience the largest growth over some time interval? Can one reduce this growth using steady or unsteady control? If so, where should the steady control be located to have the maximal effect? What time-dependent law is the most efficient for unsteady control? How are flow properties such as eigenvalues or aerodynamic forces affected by a small amplitude control?

Lagrange multipliers are an elegant and powerful method to address these questions and many others. This method allows us to look for the optimum (maximum of minimum) of an objective function, given some constraints to be satisfied. The central idea is to transform a difficult constrained optimization problem into an easier unconstrained one.

1.2.1 Unconstrained optimization

Consider a simple example, with a finite number of discrete variables. The function $\mathcal{J}(q,c) = -(q-3)^2 - (c-2)^2 + 1$ is to be maximized. It has a global unconstrained maximum $\mathcal{J}(3,2) = 1$, shown as a triangle in figure 1.1. A hiker aiming for the summit of this hill could just walk towards it. But what if, in a more general case, this maximum cannot be found explicitly because $\mathcal{J}$ is too complex or not even known analytically? Our hiker is now surrounded by fog and cannot see the global landscape. One may resort to one of many numerical methods. Some are heuristic and based on a wide, global exploration of the parameter space: $\mathcal{J}$ is evaluated at several locations (x, y), based on which an approximate *response surface function* is built and successively refined as more evaluations are performed in regions where the maximum is expected and/or where the accuracy of the response surface function is deemed insufficient. Other heuristic methods like the *downhill simplex method* (or *amoeba method*) use local evaluations of $\mathcal{J}$ at a few locations to guess which neighbouring region should be explored next. A large class of deterministic methods is based on gradients (assuming continuous first derivatives): starting from a guess location (x, y) and using the local gradient information (indicating the direction of steepest slope), one moves iteratively toward a stationary point of $\mathcal{J}$. Such methods include for example the straightforward *steepest descent/ascent algorithm* and one of its classical improvements, the *conjugate gradient algorithm*. This would correspond to our hiker evaluating the slope in order to decide where to head for. If he turns into a diver, he might also want to find the deepest point below lake Geneva (figure 1.2). In the following, focus is on gradient-based methods. One way to compute the local gradient is with finite differences:

$$\nabla \mathcal{J} = \left(\frac{\mathrm{d}\mathcal{J}}{\mathrm{d}q}, \frac{\mathrm{d}\mathcal{J}}{\mathrm{d}c} \right)^T \simeq \left(\frac{\mathcal{J}(q+\epsilon q, c) - \mathcal{J}(q,c)}{\epsilon}, \frac{\mathcal{J}(q, c+\epsilon c) - \mathcal{J}(q,c)}{\epsilon} \right)^T. \tag{1.13}$$

1.2.2 Constrained optimization

What if now a constraint is enforced? Our hiker still looks for the highest point but he must follow a given path (black lines in figure 1.1). The unconstrained maximum cannot be reached any more. Instead, one looks for the largest value of $\mathcal{J}$ while staying on the constraint path $h(q,c) = 0$. In the previous simple example, if the constraint is $h(q,c) = c - q - 1 = 0$, one can substitute $c = q + 1$ into $\mathcal{J}(q, c(q)) = -(q-3)^2 - (q-1)^2 + 1$, set the derivative $\mathrm{d}\mathcal{J}/\mathrm{d}q = -2(2q-4)$ to zero and solve for q, obtaining finally $(q,c) = (2,3)$ and $\mathcal{J} = -1$.

However, more complex problems do not allow such an explicit substitution. For instance,
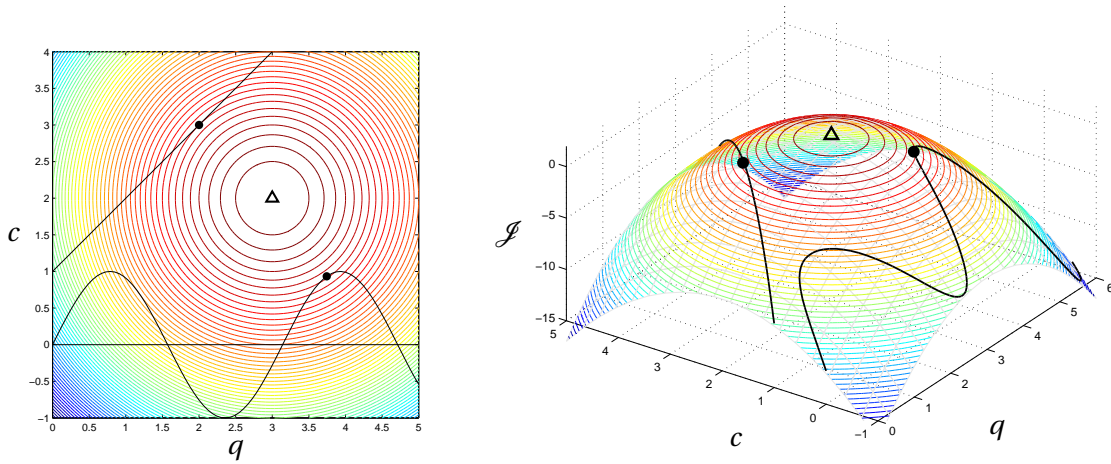
Figure 1.1 – The global maximum of $\mathcal{J}(q,c) = -(q-3)^2 - (c-2)^2 + 1$ is $\mathcal{J}(3,2) = 1$. If a given constraint $h(q,c) = 0$ has to be satisfied, then the constrained maximum is different: black lines show two examples, $h = c - q - 1$ and $h = c - \sin(2q)$.
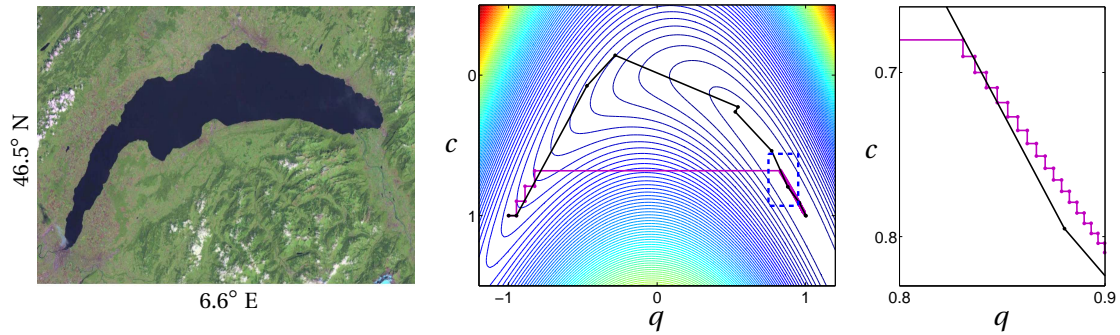
Figure 1.2 – Finding the deepest point below a lake, or minimizing Rosenbrock's banana function $\mathcal{J}(q,c) = (q-1)^2 + 10(q^2 - c)^2$. The steepest descent algorithm (purple) successively moves down along the steepest gradient (slope) until the minimum $\mathcal{J}(1,1) = 0$. The conjugate gradient algorithm (black) combines current and previous gradient information to speed up convergence in the long, narrow flat valley.

the constraint might be $h(q, c) = c - \sin(2q)$ or the Navier–Stokes equations. One way to circumvent this difficulty is to note that, at the constrained maximum, the constraint $h = 0$ is tangent to the contour level of the objective function $\mathcal{J}$ (if it were not, one could move along the constraint and increase $\mathcal{J}$, i.e the hiker could walk along the path and reach a higher place). This implies that the objective function and the constraint have parallel gradients:

$$\nabla \mathcal{J} = \lambda \nabla h. \tag{1.14}$$

Combining the objective function and the constraint into a new, single function

$$\mathcal{L}(q, c, \lambda) = \mathcal{J}(q, c) - \lambda h(q, c), \tag{1.15}$$

it can be observed that $\nabla \mathcal{L} = \mathbf{0}$ if (1.14) is satisfied. In other words, a stationary point of $\mathcal{L}$ is reached at the constrained maximum of $\mathcal{J}$. The function $\mathcal{L}$ is called *Lagrangian* (or *augmented objective function*) and λ is a *Lagrange multiplier* enforcing the constraint $h = 0$.

In the previous example, the Lagrangian is $\mathcal{L}(q, c, \lambda) = -(q-3)^2 - (c-2)^2 + 1 - \lambda(c - q - 1)$. Setting to zero its derivatives yields the system

$$\partial \mathcal{L} / \partial q = -2(q-3) + \lambda = 0, \tag{1.16}$$

$$\partial \mathcal{L} / \partial c = -2(c-2) - \lambda = 0, \tag{1.17}$$

$$\partial \mathcal{L} / \partial \lambda = c - q - 1 = 0, \tag{1.18}$$

resulting in $(q, c) = (2, 3)$, of course similar to the constrained maximum found previously.

What is the benefit of introducing $\mathcal{L}$? The original problem of finding a maximum of $\mathcal{J}(q, c)$ subject to the constraint $h(q, c) = 0$, which might be extremely difficult in general, is replaced by an easier and familiar unconstrained optimization problem for $\mathcal{L}(q, c, \lambda)$. This problem can be solved using gradient-based methods mentioned in 1.2.1. Strictly speaking, one does not look for extrema any more but for stationary points; if the problem is nonlinear (which is the case for $h(q, c) = c - \sin(2q)$), typical iterative resolution methods (e.g. Newton method) still require the computation of gradients.

Unfortunately, computing gradients with finite differences using (1.13) is impractical if the number of variables is large, and if a single evaluation of $\mathcal{J}$ or h is time-consuming. For instance, if the constraint involved in the problem is a differential equation, like the Navier–Stokes equations, a single evaluation of $h(q, c) = 0$ for a given control c requires a potentially costly simulation; if the control has several degrees of freedom, computing the gradient requires as many costly simulations. This is where another advantage of Lagrange multipliers appears, as detailed in the next section.

1.2.3 Adjoint methods

Let us jump at once to problems of interest in hydrodynamics stability and flow control. Consider for example that the state variable $\mathbf{q}$ denotes velocity and pressure fields, the control variable $\mathbf{c}$ is a volume force or a boundary condition, the constraint $\mathbf{h}(\mathbf{q}, \mathbf{c}) = \mathbf{0}$ to be satisfied by the flow and the control is the Navier–Stokes equations or one of the equations presented in 1.1, and the objective function $\mathscr{J}(\mathbf{q}, \mathbf{c})$ is any flow-dependent scalar quantity one wishes to maximize or minimize using the control variable. Assuming in a first step that the problem is time-independent and equations are discretized, so that variables are vector-valued quantities, the problem reads:

$$\max_{\mathbf{c}} \mathscr{J}(\mathbf{q}, \mathbf{c}), \quad \text{subject to } \mathbf{h}(\mathbf{q}, \mathbf{c}) = \mathbf{0}. \tag{1.19}$$

Introducing the Lagrange multiplier $\mathbf{q}^{\dagger}$ associated with $\mathbf{h} = \mathbf{0}$, the Lagrangian is

$$\mathscr{L}(\mathbf{q}, \mathbf{c}, \mathbf{q}^{\dagger}) = \mathscr{J}(\mathbf{q}, \mathbf{c}) - \mathbf{q}^{\dagger} \cdot \mathbf{h}(\mathbf{q}, \mathbf{c}), \tag{1.20}$$

whose stationarity yields the following relations:

$$\frac{\partial \mathscr{L}}{\partial \mathbf{q}} = \frac{\partial \mathscr{J}}{\partial \mathbf{q}} - \left(\frac{\partial \mathbf{h}}{\partial \mathbf{q}}\right)^{T} \mathbf{q}^{\dagger} = \mathbf{0}, \tag{1.21}$$

$$\frac{\partial \mathscr{L}}{\partial \mathbf{c}} = \frac{\partial \mathscr{J}}{\partial \mathbf{c}} - \left(\frac{\partial \mathbf{h}}{\partial \mathbf{c}}\right)^{T} \mathbf{q}^{\dagger} = \mathbf{0}, \tag{1.22}$$

$$\frac{\partial \mathscr{L}}{\partial \mathbf{q}^{\dagger}} = -\mathbf{h} = \mathbf{0}. \tag{1.23}$$

By construction, equation (1.23) is the constraint. In (1.21)-(1.22), transposition comes from the ith component of $\partial \mathscr{L}/\partial \mathbf{q}$ being $\partial \mathscr{J}/\partial q_i - \partial\left(c_k^{\dagger} h_k\right)/\partial q_i = \partial \mathscr{J}/\partial q_i - c_k^{\dagger}\partial h_k/\partial q_i$, and similarly for $\partial \mathscr{L}/\partial \mathbf{c}$. As mentioned earlier, this system of equations for $(\mathbf{q}, \mathbf{c}, \mathbf{q}^{\dagger})$ is in general nonlinear, and solving it with an iterative technique involves gradient calculations which are prohibitively time-consuming if performed with finite differences (1.13) for each degree of freedom.

However, inspection reveals that the gradient of the original objective function with respect to control can be obtained *via* the Lagrange multiplier:

$$\frac{\mathrm{d}\mathscr{J}}{\mathrm{d}\mathbf{c}} = \frac{\partial \mathscr{J}}{\partial \mathbf{c}} + \left(\frac{\mathrm{d}\mathbf{q}}{\mathrm{d}\mathbf{c}}\right)^{T} \frac{\partial \mathscr{J}}{\partial \mathbf{q}} \tag{1.24}$$

$$= \frac{\partial \mathscr{J}}{\partial \mathbf{c}} + \left(\frac{\mathrm{d}\mathbf{q}}{\mathrm{d}\mathbf{c}}\right)^{T} \left(\frac{\partial \mathbf{h}}{\partial \mathbf{q}}\right)^{T} \mathbf{q}^{\dagger}. \tag{1.25}$$

Partial derivatives $\partial \mathscr{J}/\partial \mathbf{c}$ and $\partial \mathbf{h}/\partial \mathbf{q}$ can usually be derived analytically, but one does not know how the flow field $\mathbf{q}$ depends on the control $\mathbf{c}$. This can be obtained indirectly by differ-

entiating the constraint (1.23),

$$\frac{\mathrm{d}\mathbf{h}}{\mathrm{d}\mathbf{c}} = \frac{\partial \mathbf{h}}{\partial \mathbf{c}} + \frac{\partial \mathbf{h}}{\partial \mathbf{q}}\frac{\mathrm{d}\mathbf{q}}{\mathrm{d}\mathbf{c}} = \mathbf{0},$$

(1.26)

and substituting into (1.25):

$$\frac{\mathrm{d}\mathscr{J}}{\mathrm{d}\mathbf{c}} = \frac{\partial \mathscr{J}}{\partial \mathbf{c}} - \left(\frac{\partial \mathbf{h}}{\partial \mathbf{c}}\right)^T \mathbf{q}^\dagger.$$

(1.27)

Here, both $\partial \mathscr{J}/\partial \mathbf{c}$ and $\partial \mathbf{h}/\partial \mathbf{c}$ are known analytically. Therefore, one can evaluate the gradient of the objective function with respect to control as follows: (i) solve the constraint $\mathbf{h}(\mathbf{q},\mathbf{c}) = \mathbf{0}$ to obtain the flow $\mathbf{q}$ for a given control $\mathbf{c}$; (ii) compute the Lagrange multiplier $\mathbf{q}^\dagger$ by solving equation (1.21); (iii) substitute into (1.27). This procedure requires only two simulations per gradient evaluation, irrespective of the number of degrees of freedom. In other words, the original constrained optimization problem (1.19) can be tackled very efficiently through the introduction of a Lagrange multiplier.

An alternative way to derive (1.27) is to notice that if the constraint is satisfied then $\mathscr{L} = \mathscr{J}$ and, additionally, if equation (1.21) is satisfied too then the total derivative

$$\frac{\mathrm{d}\mathscr{L}}{\mathrm{d}\mathbf{c}} = \frac{\partial \mathscr{L}}{\partial \mathbf{c}} + \left(\frac{\mathrm{d}\mathbf{q}}{\mathrm{d}\mathbf{c}}\right)^T \frac{\partial \mathscr{L}}{\partial \mathbf{q}} + \left(\frac{\mathrm{d}\mathbf{q}^\dagger}{\mathrm{d}\mathbf{c}}\right)^T \frac{\partial \mathscr{L}}{\partial \mathbf{q}^\dagger}$$

(1.28)

reduces to $\partial \mathscr{L}/\partial \mathbf{c}$ (since $\partial \mathscr{L}/\partial \mathbf{q} = \mathbf{0}$ and $\partial \mathscr{L}/\partial \mathbf{q}^\dagger = \mathbf{0}$); in this case,

$$\frac{\mathrm{d}\mathscr{J}}{\mathrm{d}\mathbf{c}} = \frac{\mathrm{d}\mathscr{L}}{\mathrm{d}\mathbf{c}} = \frac{\partial \mathscr{L}}{\partial \mathbf{c}} = \frac{\partial \mathscr{J}}{\partial \mathbf{c}} - \left(\frac{\partial \mathbf{h}}{\partial \mathbf{c}}\right)^T \mathbf{q}^\dagger.$$

(1.29)

The method of Lagrange multipliers can be generalized to differential equations, involving operators acting on continuous variables, rather than a set of discrete equations Lions (1971). The problem still reads

$$\max_{\mathbf{c}} \mathscr{J}(\mathbf{q},\mathbf{c}), \quad \text{subject to } \mathbf{h}(\mathbf{q},\mathbf{c}) = \mathbf{0},$$

(1.30)

where the Lagrangian is now defined with an inner product rather than a dot product:

$$\mathscr{L}(\mathbf{q},\mathbf{c},\mathbf{q}^\dagger) = \mathscr{J}(\mathbf{q},\mathbf{c}) - \left(\mathbf{q}^\dagger \,\middle|\, \mathbf{h}(\mathbf{q},\mathbf{c})\right).$$

(1.31)

The inner product is for example a space integral over the fluid domain or at boundaries if the problem depends on space, $\mathbf{q} = \mathbf{q}(\mathbf{x})$, $\mathbf{c} = \mathbf{c}(\mathbf{x})$. It might also involve time integration for unsteady problems $\mathbf{q} = \mathbf{q}(\mathbf{x}, t)$, $\mathbf{c} = \mathbf{c}(\mathbf{x}, t)$.

To express the stationarity of $\mathscr{L}$, one needs to use the Fréchet derivative, defined for an oper-

ator $\mathbf{A}$ as:

$$\left(\frac{\partial \mathbf{A}}{\partial \mathbf{s}} \,\middle|\, \delta \mathbf{s} \right) = \lim_{\epsilon \to 0} \frac{\mathbf{A}(\mathbf{s} + \epsilon \delta \mathbf{s}) - \mathbf{A}(\mathbf{s})}{\epsilon}. \tag{1.32}$$

The following system is obtained:

$$\left(\frac{\partial \mathscr{L}}{\partial \mathbf{q}} \,\middle|\, \delta \mathbf{q} \right) = \left(\frac{\partial \mathscr{J}}{\partial \mathbf{q}} \,\middle|\, \delta \mathbf{q} \right) - \left(\mathbf{q}^\dagger \,\middle|\, \frac{\partial \mathbf{h}}{\partial \mathbf{q}} \delta \mathbf{q} \right) = \mathbf{0} \quad \forall \delta \mathbf{q} \quad \Leftrightarrow \quad \frac{\partial \mathscr{J}}{\partial \mathbf{q}} - \left(\frac{\partial \mathbf{h}}{\partial \mathbf{q}} \right)^\dagger \mathbf{q}^\dagger = \mathbf{0}, \tag{1.33}$$

$$\left(\frac{\partial \mathscr{L}}{\partial \mathbf{c}} \,\middle|\, \delta \mathbf{c} \right) = \left(\frac{\partial \mathscr{J}}{\partial \mathbf{c}} \,\middle|\, \delta \mathbf{c} \right) - \left(\mathbf{q}^\dagger \,\middle|\, \frac{\partial \mathbf{h}}{\partial \mathbf{c}} \delta \mathbf{c} \right) = \mathbf{0} \quad \forall \delta \mathbf{c} \quad \Leftrightarrow \quad \frac{\partial \mathscr{J}}{\partial \mathbf{c}} - \left(\frac{\partial \mathbf{h}}{\partial \mathbf{c}} \right)^\dagger \mathbf{q}^\dagger = \mathbf{0}, \tag{1.34}$$

$$\left(\frac{\partial \mathscr{L}}{\partial \mathbf{q}^\dagger} \,\middle|\, \delta \mathbf{q}^\dagger \right) = -\left(\delta \mathbf{q}^\dagger \,\middle|\, \mathbf{h} \right) = \mathbf{0} \quad \forall \delta \mathbf{q}^\dagger \qquad \qquad \Leftrightarrow \quad \mathbf{h} = \mathbf{0}. \tag{1.35}$$

In these equations, the superscript $\dagger$ applied to an operator denotes the associated *adjoint operator*, defined as

$$(\mathbf{a} \,|\, \mathbf{A}\mathbf{b}) = (\mathbf{A}^\dagger \mathbf{a} \,|\, \mathbf{b}) \quad \forall \mathbf{a}, \mathbf{b}. \tag{1.36}$$

Note that the adjoint operator $\mathbf{A}^\dagger$ is inner product-dependent.

The system (1.33)-(1.35) is formally equivalent to (1.21)-(1.23). Steps similar to the derivation of (1.27) or (1.29) lead to the expression of the gradient

$$\frac{\mathrm{d}\mathscr{J}}{\mathrm{d}\mathbf{c}} = \frac{\partial \mathscr{J}}{\partial \mathbf{c}} - \left(\frac{\partial \mathbf{h}}{\partial \mathbf{c}} \right)^\dagger \mathbf{q}^\dagger, \tag{1.37}$$

where the Lagrange multiplier $\mathbf{q}^\dagger$ is solution of (1.33). This equation is called an *adjoint equation*, and $\mathbf{q}^\dagger$ is the *adjoint variable*. Computing adjoint operators $(\partial \mathbf{h}/\partial \mathbf{c})^\dagger$ and $(\partial \mathbf{h}/\partial \mathbf{q})^\dagger$ using (1.36) typically involves integration by parts, which creates boundary terms (largely speaking, i.e. for space and/or time) completing (1.33).

The following sections present three classical examples of applications of adjoint-based methods in hydrodynamics, where they have attracted a growing interest over the past decades due to their versatility: (i) optimal growth: computation of the initial condition which leads to the largest energy amplification over a given time interval; (ii) optimal control: computation of a time-dependent control aiming at minimizing energy (at a final time horizon or over an entire time interval); (iii) eigenvalue sensitivity: computation of sensitivity maps showing where flow modification and control have the largest effect on eigenvalues (i.e. on the growth rate and frequency of an instability, for instance).

1.3 Optimal growth

Consider a base flow $\mathbf{Q}(\mathbf{x})$ or $\mathbf{Q}(\mathbf{x}, t)$ solution of the steady or unsteady Navier–Stokes equations (4.56) or (4.57), and an initial perturbation $\mathbf{q}_0'(\mathbf{x}) = \mathbf{q}'(\mathbf{x}, 0)$ superimposed onto the base

flow at $t = 0$. What is the maximal amplification this perturbation can undergo from $t = 0$ to a given time $t = T$? Measuring amplification in terms of energy $E(t) = \big(\mathbf{q}'(\mathbf{x}, t) \,\big|\, \mathbf{q}'(\mathbf{x}, t)\big) = \int_\Omega \mathbf{q}'(\mathbf{x}, t)^2 \, d\Omega$, the objective function to be maximized is $\mathcal{J}(\mathbf{q}, \mathbf{c}) = E(T)/E(0)$. The state variable is the perturbation $\mathbf{q}'(\mathbf{x}, t)$ whose evolution is governed by the perturbation equations (1.3) or (1.4), while the control variable is $\mathbf{c} = \mathbf{q}'_0$. The question can be formulated as

$$\max_{\mathbf{q}'_0} \frac{\int_\Omega \mathbf{q}'(\mathbf{x}, T)^2 \, d\Omega}{\int_\Omega \mathbf{q}'(\mathbf{x}, 0)^2 \, d\Omega} = \max_{\mathbf{q}'_0} \frac{\big(\mathbf{q}' \,\big|\, \mathbf{q}'\big)}{\big(\mathbf{q}'_0 \,\big|\, \mathbf{q}'_0\big)} \quad \text{subject to (1.3) or (1.4).} \tag{1.38}$$

If the base flow is steady and the linearized evolution of small-amplitude perturbations is considered, this problem can actually be recast as an eigenvalue problem: writing (1.4) formally as $\partial_t \mathbf{q}' = \mathbf{A}\mathbf{q}'$, the solution at any time is given by $\mathbf{q}'(\mathbf{x}, t) = \exp(\mathbf{A}t)\mathbf{q}'_0(\mathbf{x})$ and (1.38) reads

$$\max_{\mathbf{q}'_0} \frac{\big(e^{\mathbf{A}t}\mathbf{q}'_0 \,\big|\, e^{\mathbf{A}t}\mathbf{q}'_0\big)}{\big(\mathbf{q}'_0 \,\big|\, \mathbf{q}'_0\big)} = \max_{\mathbf{q}'_0} \frac{\big((e^{\mathbf{A}t})^\dagger e^{\mathbf{A}t}\mathbf{q}'_0 \,\big|\, \mathbf{q}'_0\big)}{\big(\mathbf{q}'_0 \,\big|\, \mathbf{q}'_0\big)}. \tag{1.39}$$

The maximum of this Rayleigh quotient is the norm of the operator $\big(e^{\mathbf{A}t}\big)^\dagger e^{\mathbf{A}t}$ for the inner product used here, and can therefore be computed as its largest eigenvalue (or equivalently as the squared largest singular value of $e^{\mathbf{A}t}$) using classical algorithms. The optimal perturbation is the associated eigenvector (respectively the associated right singular vector).

If the base flow is unsteady or if the fully nonlinear pertubation dynamics are considered, the above procedure is no longer possible. Instead, the method presented in 1.2 can be used: a Lagrangian is introduced to enforce the constraints (governing equation and initial condition),

$$\mathcal{L}(\mathbf{q}, \mathbf{q}_0, \mathbf{q}^\dagger, \mathbf{q}_0^\dagger) = \frac{\big(\mathbf{q} \,\big|\, \mathbf{q}\big)}{\big(\mathbf{q}_0 \,\big|\, \mathbf{q}_0\big)} - \int_0^T \Big(\mathbf{q}^\dagger \,\Big|\, \partial_t \mathbf{q} - \mathbf{A}(\mathbf{q})\Big) \, dt - \Big(\mathbf{q}_0^\dagger \,\Big|\, \mathbf{q}(0) - \mathbf{q}_0\Big), \tag{1.40}$$

where for the sake of simplicity primes and space dependence are omitted and the perturbation equation is formally noted $\partial_t \mathbf{q} = \mathbf{A}(\mathbf{q})$. Stationarity conditions with respect to Lagrange multipliers give back the constraints, those with respect to the state and control variables yield:

$$\frac{\partial \mathcal{L}}{\partial \mathbf{q}} = \mathbf{0} \quad \Rightarrow \quad \partial_t \mathbf{q}^\dagger + \left(\frac{d\mathbf{A}}{d\mathbf{q}}\right)^\dagger \mathbf{q}^\dagger = \mathbf{0}, \quad \mathbf{q}^\dagger(T) = \frac{2\mathbf{q}(T)}{\big(\mathbf{q}_0 \,\big|\, \mathbf{q}_0\big)}, \tag{1.41}$$

$$\mathbf{q}_0^\dagger = \mathbf{q}^\dagger(0), \tag{1.42}$$

$$\frac{\partial \mathcal{L}}{\partial \mathbf{q}_0} = \mathbf{0} \quad \Rightarrow \quad \mathbf{q}_0^\dagger = 2\mathbf{q}_0 \frac{\big(\mathbf{q}(T) \,\big|\, \mathbf{q}(T)\big)}{\mathbf{q}_0 \mathbf{q}_0}. \tag{1.43}$$

The adjoint equation (1.41) for $\mathbf{q}^\dagger$ is to be integrated backward in time with terminal condi-

tion $\mathbf{q}^\dagger(T) = 2\mathbf{q}(T)/\left(\mathbf{q}_0 \,\middle|\, \mathbf{q}_0\right)$. Eliminating $\mathbf{q}_0^\dagger$ in (1.42)-(1.43) gives the condition

$$\mathbf{q}^\dagger(0) - 2\mathbf{q}_0 \frac{\left(\mathbf{q}(T) \,\middle|\, \mathbf{q}(T)\right)}{\left(\mathbf{q}_0 \,\middle|\, \mathbf{q}_0\right)} = \mathbf{0}, \tag{1.44}$$

or the gradient of the objective function with respect to the control variable (1.37):

$$\frac{\mathrm{d}\mathscr{J}}{\mathrm{d}\mathbf{q}_0} = \mathbf{q}^\dagger(0) - 2\mathbf{q}_0 \frac{\left(\mathbf{q}(T) \,\middle|\, \mathbf{q}(T)\right)}{\left(\mathbf{q}_0 \,\middle|\, \mathbf{q}_0\right)}. \tag{1.45}$$

This can be used in a gradient-based algorithm to converge iteratively towards a maximum of $\mathscr{J}$ as follows: given a current (non-optimal) value of the control, i.e. initial perturbation $\mathbf{q}_0 = \mathbf{q}(0)$, solve the perturbation equation forward in time, then solve the adjoint equation initialised with $\mathbf{q}^\dagger(T) = 2\mathbf{q}(T)/\left(\mathbf{q}_0 \,\middle|\, \mathbf{q}_0\right)$ backward in time, compute the gradient $\mathrm{d}\mathscr{J}/\mathrm{d}\mathbf{q}_0$ knowing $\mathbf{q}^\dagger(0)$, update the value of $\mathbf{q}_0$ based on the gradient information, and repeat. For instance, with the steepest ascent algorithm the update is in the direction of the gradient $\mathbf{q}_0^{k+1} = \mathbf{q}_0^k + \alpha^k \mathrm{d}\mathscr{J}/\mathrm{d}\mathbf{q}_0$. The step size can be either heuristic (fixed, proportional to the norm of the gradient, etc) or determined with a search along the gradient direction (*line search*), with a trade-off between computational time (each evaluation of $\mathscr{J}$ being a Navier–Stokes simulation) and detailed exploration of the phase space (potentially reducing the number of steps to reach convergence). As in Newton algorithms, it is also possible to use (1.44) (as if the gradient was zero) to set $\mathbf{q}_0^{k+1} = \mathbf{q}_0^{\dagger\,k}\left(\mathbf{q}_0^k \,\middle|\, \mathbf{q}_0^k\right)/2\left(\mathbf{q}(T)^k \,\middle|\, \mathbf{q}(T)^k\right)$ and iterate. This heuristic method amounts to the particular choice of step size $\alpha^k = \left(\mathbf{q}_0^k \,\middle|\, \mathbf{q}_0^k\right)/2\left(\mathbf{q}(T)^k \,\middle|\, \mathbf{q}(T)^k\right)$.

1.3.1 Application to the Ginzburg-Landau equation

In this section, optimal growth is illustrated with a simple toy model. The nonlinear one-dimensional Ginzburg-Landau (GL) equation describes well spatially developing flows such as jets and wakes. It governs the spatio-temporal evolution of the complex variable $q(x, t)$, which represents perturbation around the base flow close to the onset of instability:

$$\frac{\partial q}{\partial t} = -\kappa \frac{\partial q}{\partial x} + \mu q + \nu \frac{\partial^2 q}{\partial x^2} - \eta |q|^2 q + c, \quad q(x, 0) = q_0(x), \quad q(\pm\infty, t) = 0. \tag{1.46}$$

where the control $c(x, t)$ extends in the whole domain Ω. This governing equation $\partial_t q = \mathbf{A}(q) + c$ is indeed simpler than the Navier–Stokes equations but does include terms of advection, diffusion, instability, as well as a saturating nonlinear effect (Roussopoulos & Monkewitz, 1996; Lauga & Bewley, 2004). Coefficients $\kappa(x), \mu(x), \nu(x)$ and $\eta(x)$ allow us to tune the GL equation to the particular problem at hand. Here they are chosen so as to model the wake behind a circular cylinder, which becomes unstable for Reynolds numbers larger than the instability threshold $Re \leq Re_c = 47$ (where Re is built on the free-stream velocity and the cylinder diameter), resulting in vortex shedding behind the cylinder, as shown in Figure 1.3, and even to turbulence for even larger Re. Coefficients in (1.46) depend on Re, and although they are derived close to Re_c the resulting GL equation has been shown to provide useful results

for a wide range of Reynolds numbers.
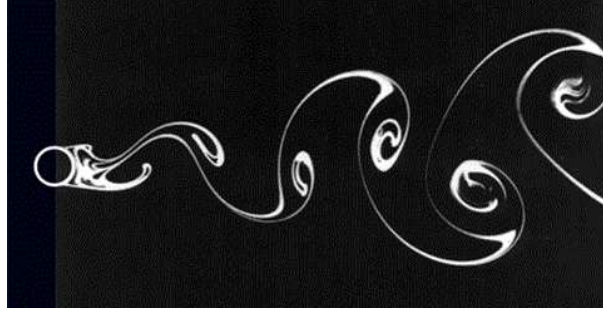
Figure 1.3 – Kármán vortex street behind a cylinder at $Re > Re_c = 47$ (from Van Dyke (1982), photograph by S. Taneda).

Figures 1.4(a)-(c) show the evolution of the state q and its energy $E(t) = \big(q(x,t) \big| q(x,t) \big)$ for the uncontrolled system in a stable case ($Re = 20$) and an unstable case ($Re = 100$), starting from a given initial perturbation $q_0(x)$ of energy $E_0 = 1$. For $Re < Re_c$ the amplitude of the state decreases everywhere with time, whereas for $Re > Re_c$ it increases in the region $0 \lesssim x \lesssim 5$ before reaching a limit cycle due to saturation from the nonlinear term $-\eta|q|^2 q$. In both cases perturbations are advected downstream, but when $Re > Re_c$ they are amplified in the unstable region before decaying downstream, leading to a global instability.

By construction, the linearized operator $d\mathbf{A}/dq = -\kappa\partial/\partial x + \mu + \nu\partial^2/\partial x^2$ becomes unstable at $Re = Re_c$, as illustrated in figure 1.4(d) showing its eigenspectrum, i.e. its eigenvalues $\sigma = \sigma_r + i\sigma_i$. At $Re = 20$ all eigenvalues have a negative real part and the system is stable, whereas at $Re = 100 > Re_c$ some eigenvalues have a positive real part and the system is unstable. As Re increases, more eigenmodes become unstable, the perturbations are amplified faster, and one can expect the system to become more difficult to control.

Optimal growth has been computed analytically by Cossu & Chomaz (1997) for the linear GL equation. Figure 1.5 shows their results as a function of maximization time T, for different values of the bifurcation parameter μ. The asymptotic behaviour is governed by linear stability properties: perturbations are amplified when the flow is globally unstable (curve e), saturate when the flow is just neutrally stable (curve d), and decay when the flow is stable (curves a, b, c). However, large transient growth ($\simeq 10^4$) is observed in some situations when the flow is locally unstable (curve c). This result was interpreted as an effect of *convective* (streamwise) non-normality, as opposed to *component*-type non-normality, responsible for the lift-up effect and Orr mechanism in parallel flows.

1.3.2 Application to hydrodynamics

Nowadays the computation of optimal growth is also tractable for flows in two and three dimensions. Ehrenstein & Gallaire (2008) evaluated linear transient growth in the flow past a
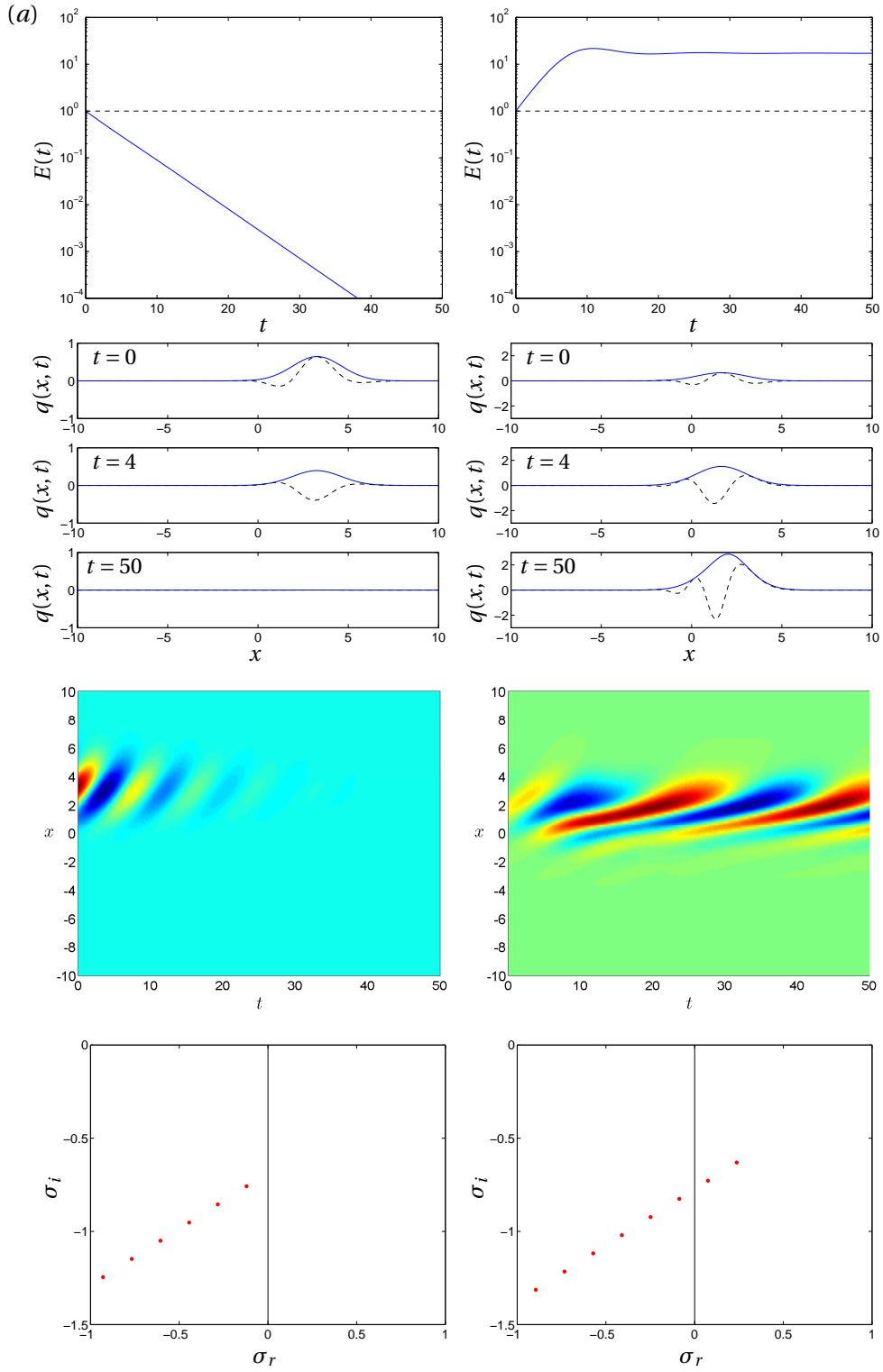
Figure 1.4 – Nonlinear GL equation in the stable (left, $Re = 20$) and unstable (right, $Re = 100$) regimes. (a) Energy of the perturbations. (b) Real part (- -) and amplitude (—) at $t = 0, 4, 50$. (c) Spatio-temporal evolution of the real part of the perturbations. (d) Growth rate σ_r and frequency σ_i of leading eigenvalues of the linearized operator **A**.
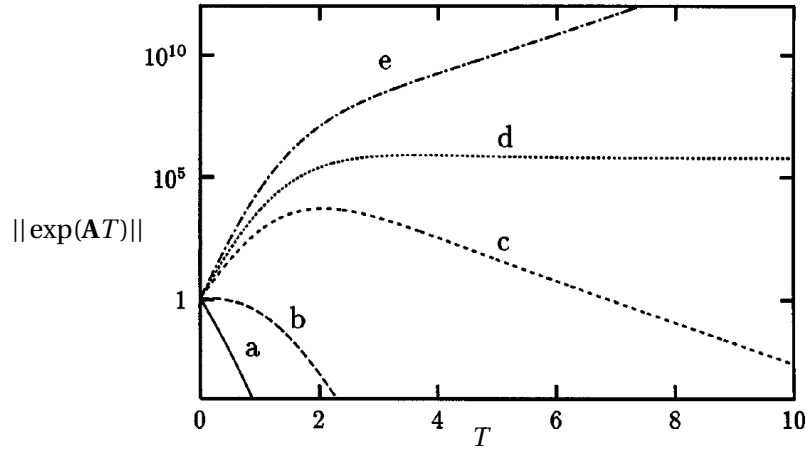
Figure 1.5 – Maximal transient growth versus time for the linear Ginzburg-Landau equation, when the flow is globally unstable (curve *e*), neutrally stable (curve *d*), or globally stable (curves *a*, *b*, *c*). From Cossu & Chomaz (1997).
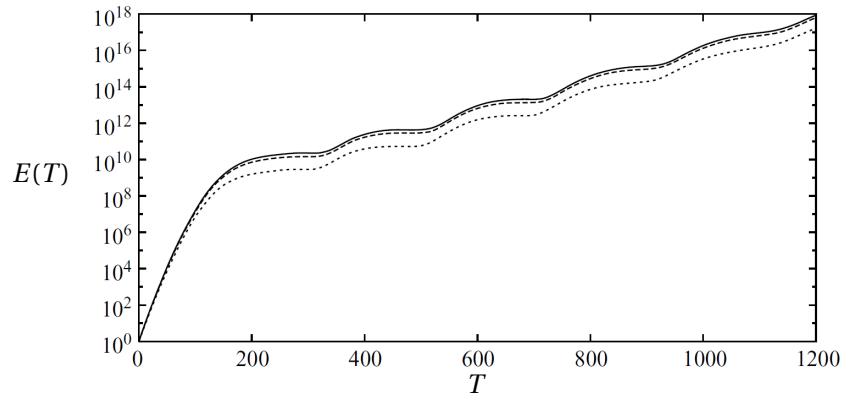
Figure 1.6 – Linear optimal transient growth in the flow past a wall-mounted bump. *Re* = 590. (Ehrenstein & Gallaire, 2008)

wall-mounted bump, whose geometry was originally designed to reproduce the pressure distribution on the upper surface of an airfoil at high angle of attack, and is now a typical wall-bounded noise amplifier flow. A very large growth is observed for short times (figure 1.6), again due to convective non-normality, and followed by slower amplification, itself modulated by oscillations interpreted as the beating of a set of weakly unstable modes.

Using adjoint-looping, Cherubini *et al.* (2011) computed the nonlinear optimal growth in a boundary layer (figure 1.7). Nonlinear optimal perturbations are similar to their linear counterpart for short times, but as *T* is increased the difference is marked: linear perturbations decay since the flow is stable (*Re* = 300) while nonlinear perturbations keep growing. Their spatial structures are significantly different too.

19
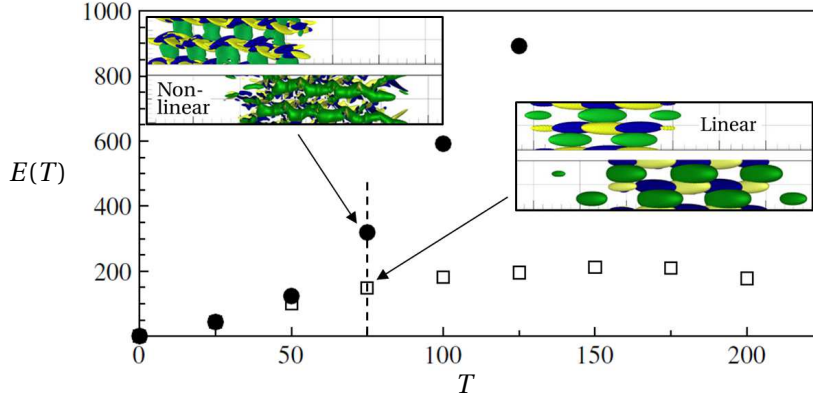
Figure 1.7 – Linear ($\square$) and nonlinear ($\bullet$) optimal transient growth versus optimization time T. Insets show, for $T = 75$, the initial perturbation at $t = 0$ (upper panel) and the corresponding response at $t = T$ (lower panel). $Re = 300$. From Cherubini *et al.* (2011).

1.4 Optimal control

Here the aim of the control is to drive perturbations to zero using the smallest amount of control as possible. The optimization problem can be cast for example as follows:

$$\min_{\mathbf{c}} \mathscr{J}(\mathbf{q}, \mathbf{c}) \quad \text{subject to } \partial_t \mathbf{q} = \mathbf{A}(\mathbf{q}) + \mathbf{c}, \tag{1.47}$$

where

$$\mathscr{J}(\mathbf{q}, \mathbf{c}) = \frac{l}{2T} \int_0^T (\mathbf{c} \,|\, \mathbf{c}) \, \mathrm{d}t + \frac{\omega_1}{2T} \int_0^T (\mathbf{q} \,|\, \mathbf{q}) \, \mathrm{d}t + \frac{\omega_2}{2} (\mathbf{q}(T) \,|\, \mathbf{q}(T)) + c.c. \tag{1.48}$$

Real-valued parameters l, ω_1 and ω_2 are relative weights, $(\mathbf{a} \,|\, \mathbf{b}) = \int_\Omega \bar{\mathbf{a}} \cdot \mathbf{b} \, \mathrm{d}\Omega$ denotes the one-dimensional Hermitian inner product, and *c.c.* stands for complex conjugate. The first term in $\mathscr{J}$ penalizes control (l being the "cost" of the control), while the second and third terms aim at reducing the energy of the perturbations, respectively over the whole time interval $[0, T]$ or at the final time $t = T$. Weights can be varied to modify the importance of suppressing perturbations relative to the perceived cost of the control. Since only relative amplitudes matter, ω_1 can actually be fixed to 1. The associated Lagrangian reads:

$$\mathscr{L}(\mathbf{q}, \mathbf{c}, \mathbf{q}^\dagger) = \mathscr{J}(\mathbf{q}, \mathbf{c}) - \int_0^T \left(\mathbf{q}^\dagger \,\middle|\, \partial_t \mathbf{q} - \mathbf{A}(\mathbf{q}) - \mathbf{c} \right) \mathrm{d}t, \tag{1.49}$$

and stationarity conditions give, in addition to the constraint:

$$\frac{\partial \mathscr{L}}{\partial \mathbf{q}} = 0 \quad \Rightarrow \quad \partial_t \mathbf{q}^\dagger + \left(\frac{\mathrm{d}\mathbf{A}}{\mathrm{d}\mathbf{q}} \right)^\dagger \mathbf{q}^\dagger = -\frac{\omega_1}{T} \mathbf{q}, \quad \mathbf{q}^\dagger(\mathbf{x}, T) = \omega_2 \, \mathbf{q}(\mathbf{x}, T), \tag{1.50}$$

$$\frac{\partial \mathscr{L}}{\partial \mathbf{c}} = 0 \quad \Rightarrow \quad \mathbf{q}^\dagger + \frac{l}{T} \mathbf{c} = 0. \tag{1.51}$$

The gradient of the objective function with respect to control is obtained from (1.51):

$$\frac{\mathrm{d}\mathscr{J}}{\mathrm{d}\mathbf{c}} = \mathbf{q}^\dagger + \frac{l}{T}\mathbf{c}. \tag{1.52}$$

For the nonlinear Ginzburg-Landau equation (1.46), for instance, the adjoint equation (1.50) reads

$$\frac{\partial q^\dagger}{\partial t} + \frac{\partial(\overline{\kappa}q^\dagger)}{\partial x} + \overline{\mu}q^\dagger + \frac{\partial^2(\overline{\nu}q^\dagger)}{\partial x^2} - \eta q^2\overline{q^\dagger} - 2\overline{\eta}|q|^2 q^\dagger = -\frac{\omega_1}{T}q, \tag{1.53}$$

$$q^\dagger(x,T) = \omega_2\, q(x,T), \quad q^\dagger(\pm\infty,t) = 0, \tag{1.54}$$

and as in 1.3, it has to be solved backward in time from a terminal condition $q^\dagger(x,T)$. Similar to 1.3 too is the fact that this terminal condition is linked to the terminal energy term in $\mathscr{J}$, while the gradient of $\mathscr{J}$ is linked to the control term. The new element in this problem is the distributed energy term in $\mathscr{J}$ which gives rise to a forcing term in the adjoint equation.

Note that if the system is linear, then the optimal control problem with terms penalizing the control and the distributed energy ($l \neq 0$, $\omega_1 \neq 0$, $\omega_2 = 0$ in (1.48)) reduces to a differential Riccati equation in general, and to an algebraic Riccati equation if $T \to \infty$ and if the system is time-invariant. Similar to classical proportional feedback, the control is taken "proportional" to the state in a multi-dimensional meaning, $\mathbf{c} = \mathbf{Kq}$, where the feedback gain $\mathbf{K}$ does not depend on $\mathbf{q}$ and can be computed "offline" (beforehands) if the dimension of the system is not too large (see Kim & Bewley (2007) for a review). Besides numerous successes in parallel flows, Gallaire, Chomaz & Huerre (2004) for instance applied the method to the control of the static instability associated to vortex breakdown in a straight pipe, exploiting the natural separation of variables in this flow to obtain a down-sized Riccati equation. In most spatially developing flows however, the dimensions of the linearized Navier-Stokes equations are so large that model reduction is necessary. Building a suitable model that both captures the uncontrolled flow behaviour and also allows to take into account the controlled dynamics remains a challenge (see Bagheri *et al.* (2009) or Barbagallo *et al.* (2009) for recent advances).

1.4.1 Application to the Ginzburg-Landau equation

Lauga & Bewley (2004) assessed the performance of a linear controller (designed from a Riccati equation) on the fully nonlinear GL equation, starting from the fully developed flow (limit-cycle mimicking vortex-shedding in the wake of a cylinder). Varying the cost l of the control, they managed to restabilize the system up to $Re \simeq 125$ with a single actuator at $x = 0$ (figure 1.8). It is remarkable that linear control performs so well so far from the instability threshold and from the linearisation point.

It was tempting to compute a fully nonlinear control for the same GL equation using adjoint-looping. An iterative method was used to solve the problem. At each step k:
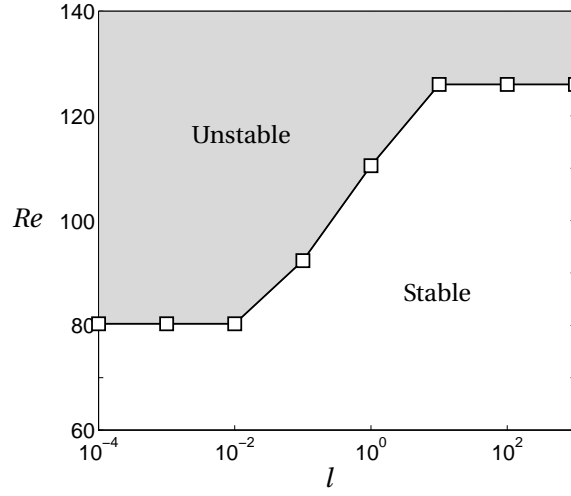
Figure 1.8 – Maximum Reynolds number for stability of the nonlinear Ginzburg-Landau equation with optimal linear control applied at $x = 0$, versus cost l of the control. From Lauga & Bewley (2004).

1. the state equation is solved forward in time for $q^k(x, t)$, with the current tentative control $c^k(x, t)$,

2. the adjoint equation is solved backward in time for $q^{\dagger k}(x, t)$ with the terminal condition $q^{\dagger k}(x, T) = \omega_2 \, q^k(x, T)$,

3. a convergence criterion is evaluated to decide whether to stop or not,

4. the sensitivity of the objective function $(\mathrm{d}\mathscr{J}/\mathrm{d}c)^k = q^{\dagger k} + l\, c^k/T$ is evaluated,

5. a new control c^{k+1} is calculated according to an update procedure.

Typically, the new control is calculated as $c^{k+1} = c^k + \alpha^k d^k$ where d is a descent direction and α the step size. The steepest descent algorithm uses the gradient itself as descent direction, $d_k = -(\mathrm{d}\mathscr{J}/\mathrm{d}c)^k$, but this method becomes very slow in some situations such as in narrow valleys where the gradient is large in one direction and small in another one, which might cause the algorithm to take many small steps (see figure 1.2). The conjugate gradient algorithm avoids this problem by successively eliminating previous descent directions, $d^k = -(\mathrm{d}\mathscr{J}/\mathrm{d}c)^k + \beta^k d^{k-1}$, where $\beta^k = \left(r^k \mid r^k - r^{k-1} \right) / \left(r^{k-1} \mid r^{k-1} \right)$ and $r^k = -(\mathrm{d}\mathscr{J}/\mathrm{d}c)^k$.

A number of methods exist to choose the step size α^k, from the simplest fixed step size method, $\alpha^k = \alpha$, to more or less refined methods performing a line search (approximate one-dimensional minimization) along the descent direction $\min_\alpha \mathscr{J}(c^k + \alpha d^k)$. Here the Brent method (Press, Teukolsky, Vetterling & Flannery, 1994) is used, which brackets a minimum with three points and successively moves closer to it, evaluating $\mathscr{J}$ at the expected minimum based on values at the bracketing points.

Convergence criteria can be based on the norm of the sensitivity $||(\mathrm{d}\,\mathscr{J}/\mathrm{d}c)^k|| < \epsilon$, on the variation of the control $||c^k - c^{k-1}|| < \epsilon$, or on the variation of the objective function $|\mathscr{J}^k - \mathscr{J}^{k-1}| = |\mathscr{J}(q^k, c^k) - \mathscr{J}(q^{k-1}, c^{k-1})| < \epsilon$. Here the retained criterion is based on the relative variation of the objective function at current and previous steps,

$$\frac{3}{2} \frac{|\mathscr{J}^k - \mathscr{J}^{k-1}| + |\mathscr{J}^{k-1} - \mathscr{J}^{k-2}|}{|\mathscr{J}^k| + |\mathscr{J}^{k-1}| + |\mathscr{J}^{k-2}|} < \epsilon, \tag{1.55}$$

with $\epsilon = 10^{-5}$, which prevents early stopping when the algorithm takes a step associated with a small variation of $\mathscr{J}$.

In the following some results are given for a particular choice of control $c(x, t) = \hat{c}(t)S(x)$, where only the time variation $\hat{c}(t)$ is optimized, while $S(x)$ is a fixed shape function, namely a Gaussian centred on $x = 0$ and of standard deviation (characteristic width) 0.3.

Numerical calculations are performed with a spatial discretization based on Hermite functions (Bagheri *et al.*, 2009). Time integration of the GL equation (1.46) and the adjoint equation (1.50) is done with the Crank-Nicolson method. The uncontrolled system is first simulated until the saturated limit cycle is well established, then control is turned on at $t = 0$ and optimization is performed on $[0, T]$ with the control guess value $c^0(x, t) = 0$.

Figure 1.9(*a*) shows the energy of the controlled system after optimization, for $Re = 70$, $l = 100$ and $\omega_2 = 0$. The system is fully stabilized, the energy being reduced by a factor 100 before $t \simeq 30$. Figure 1.9(*b*) shows the intensity $c(t)$ of the optimal control. It is smooth and goes to zero as perturbations are damped, meaning that no control is spent once the system is stabilized.
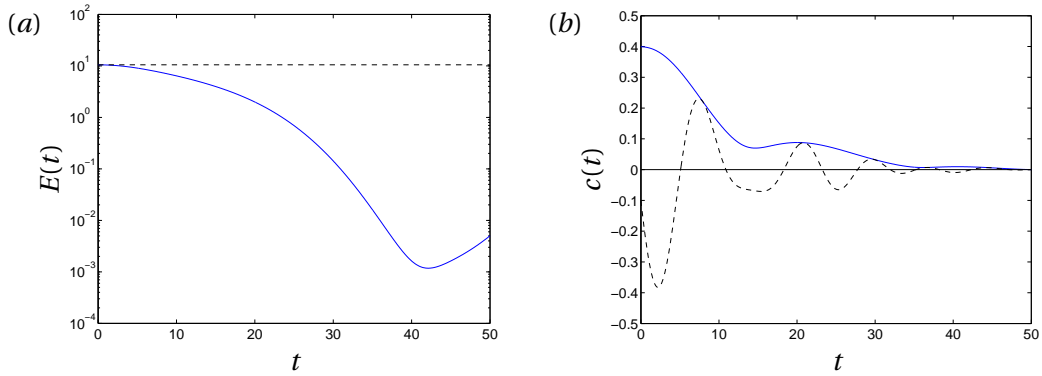
Figure 1.9 – (*a*) Energy of the controlled system after optimization. The dashed line indicates the initial energy value, i.e. the energy level of the limit cycle (here $E_0 \simeq 10.5$). (*b*) Intensity of the optimal control: real part $\Re(c(t))$ (- -) and amplitude $|c(t)|$ (—).

Figure 1.10(*a*) shows the effect of Re and horizon time T. The system is stabilized for $Re = 50$ and $Re = 70$ provided T is large enough. However, the energy is not reduced significantly for $Re \geq 90$ with this choice of l and ω_2. This might be due to a fundamental limitation, the system being impossible to control at high Reynolds number with the particular control con-

figuration chosen here (single actuator at $x = 0$), or this might be related to the descent algorithm getting trapped in a local minimum (recall that the problem is nonlinear). In the present case, one-dimensional "cuts" in the control space show that the objective function has indeed more and more local minima as Re increases.
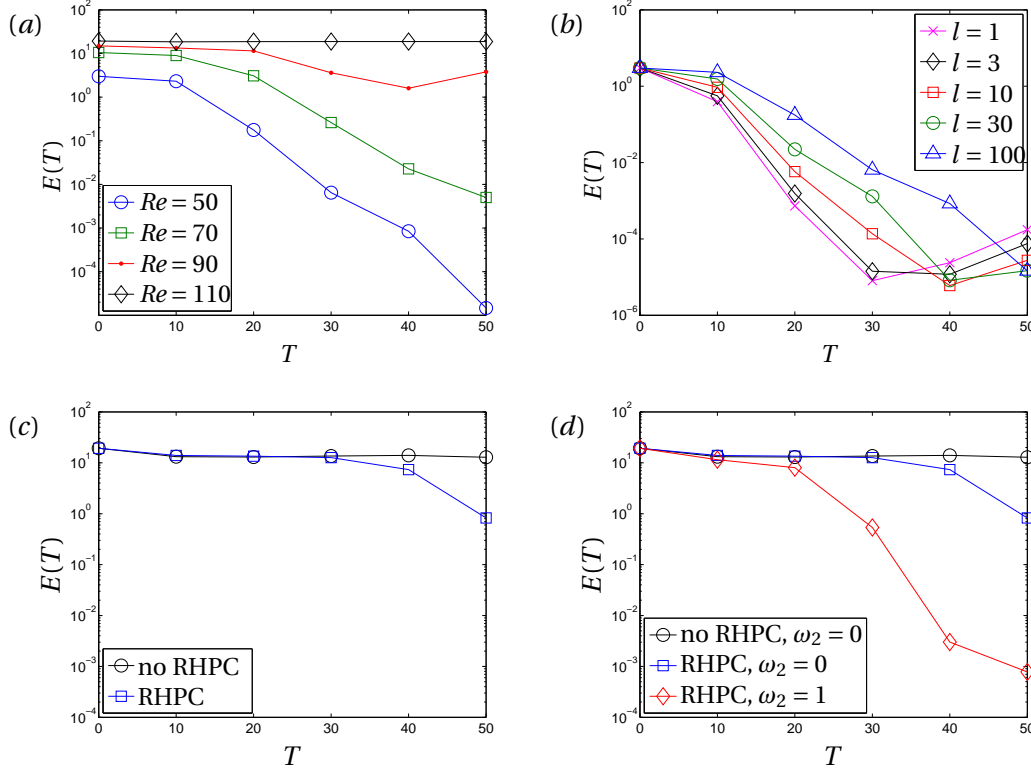
Figure 1.10 – Terminal energy after optimization for different horizon times. (a) Effect of Reynolds number for $l = 100$, $\omega_2 = 0$. (b) Effect of the cost of control for $Re = 50$, $\omega_2 = 0$. (c) Effect of receding horizon predictive control for $Re = 110$, $l = 10^{-3}$, $\omega_2 = 0$. (d) Effect of penalizing terminal energy with $\omega_2 \neq 0$ for $Re = 110$, $l = 10^{-3}$.

Figure1.10(b) illustrates the effect of l at $Re = 50$ and for $\omega_2 = 0$. Making the control cheaper by decreasing l allows to damp perturbations more quickly.

One way to circumvent the increasing difficulty to control the system is to use receding horizon predictive control (RHPC). The idea is to divide the time interval $[0, T]$ into shorter subintervals or "windows", possibly with some overlap, and to optimize independently over each of them. Considering smaller intervals reduces the number of control degrees of freedom and makes the objective function smoother. RHPC is only sub-optimal in the sense that it does not aim at minimizing the original objective function over $[0, T]$, but it might prove more efficient. Figure1.10(c) compares results from optimal control over $[0, T]$ and from RHPC over 4 time windows with 50% overlap, at $Re = 110$ and for $l = 10^{-3}$, $\omega_2 = 0$. RHPC is able to reduce the amplitude of perturbation for large time horizons, a first step to full stabilization.

So far, no penalization term for terminal energy was considered, $\omega_2 = 0$. Letting $\omega_2 = 1$ in

the same configuration ($Re = 110$, $l = 10^{-3}$) and with the same RHPC setting now results in a very efficient stabilization, as shown in figure1.10(d). However it comes at the price of a longer computational time, so this trade-off must be considered in the choice of the relative weights.

1.4.2 Application to hydrodynamics

Among the vast literature on adjoint flow control, let us point out two studies, one Riccati-based and the other adjoint-looping-based, that are particularly relevant to the boundary layer flow over a wall-mounted bump (also studied in this thesis from the point of view of open-loop control of harmonic response in chapter 2 and separation characteristics in chapter 4).

Ehrenstein *et al.* (2011) applied Riccati-based linear control to the nonlinear bump flow in the stable regime, with a volume actuator just downstream of the bump, and without full state information (six sensors in the recirculation region measuring wall shear stress), using a reduced order model of global eigenmodes to make the computation tractable. As shown in figure 1.11(a), with a suitable projection to build this reduced order model, the controller is able to damp optimal perturbations after the large initial growth (the latter is unaffected since perturbations are only felt with some delay, when they reach the first sensor downstream of the bump).

Next, Passaggia & Ehrenstein (2013) attempted to control the same flow in the unstable regime using adjoint-based nonlinear control, with wall actuation in the bump region and full state information. It proved more difficult: the vortex-shedding dynamics was attenuated but the flow remained unsteady (figure 1.11(b)). Typical issues involved in nonlinear optimization (local minima) and adjoint looping (computation time, memory requirements) appeared in this particular problem too.

1.5 Eigenvalue sensitivity

As mentioned in the introduction, there has been an increased interest in the sensitivity of eigenvalues over the past years, since it not only allows for a better understanding of instability mechanisms in "oscillator" flows, but also establishes a guideline (sensitivity maps) to optimal steady flow control design (Hill, 1992; Marquet *et al.*, 2008; Meliga *et al.*, 2010; Fani *et al.*, 2012). In addition, it also enables to lump steady flow control into amplitude equations that characterize the bifurcation close to the instability threshold (see Meliga & Gallaire (2011) for instance).
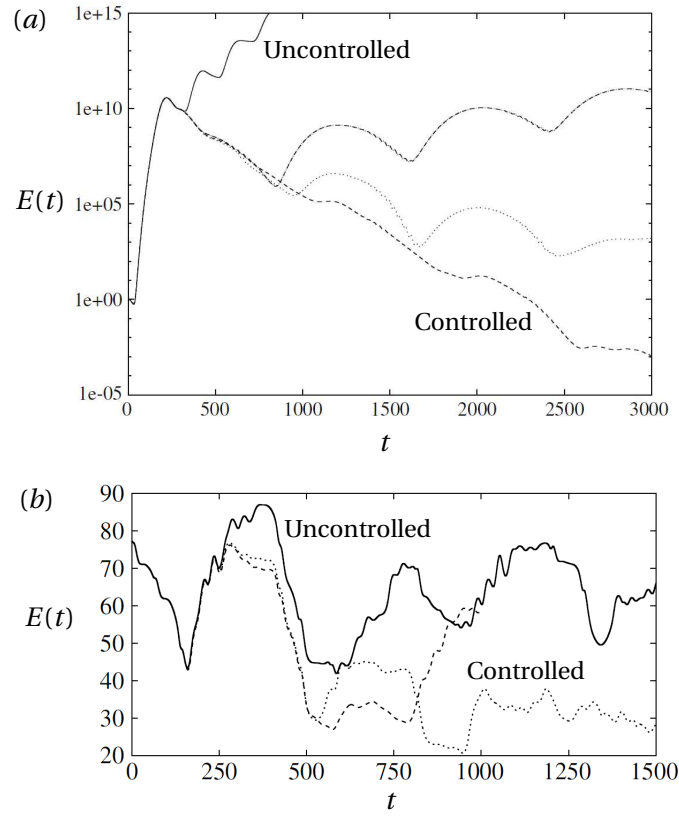
Figure 1.11 – Energy of the flow past a wall-mounted bump, showing the effect of control. (*a*) Linear control built on a reduced order model of gobal modes. Appropriate projection for the reduced order model yields an efficient attenuation of optimal perturbations in the stable regime $Re = 590$ (Ehrenstein *et al.*, 2011). (*b*) Adjoint-based nonlinear control manages to attenuate perturbations in the unstable regime $Re = 605$ (Passaggia & Ehrenstein, 2013).

1.5.1 Sensitivity to flow modification

Consider the eigenvalue problem (1.5) for flow perturbations $\sigma \mathbf{Bq} + \mathbf{N}_L(\mathbf{Q})\mathbf{q} = \mathbf{0}$ resulting from linearization of the Navier–Stokes equations. The objective function is the eigenvalue $\mathscr{J} = \sigma$ and the control variable the base flow $\mathbf{Q}$, i.e. the sensitivity to base flow modification is investigated. Note that here the objective function does not depend explicitly on any other variable but is rather an independent variable on its own. The Lagrangian reads

$$\mathscr{L}_f(\sigma, \mathbf{q}, \mathbf{Q}, \mathbf{q}^\dagger) = \sigma - \left(\mathbf{q}^\dagger \,\middle|\, \sigma \mathbf{Bq} + \mathbf{N}_L(\mathbf{Q})\mathbf{q} \right), \tag{1.56}$$

and its stationarity yields

$$\frac{\partial \mathscr{L}_f}{\partial \mathbf{q}} = \mathbf{0} \quad \Rightarrow \quad \overline{\sigma}\mathbf{B}^\dagger \mathbf{q}^\dagger + \mathbf{N}_L(\mathbf{Q})^\dagger \mathbf{q}^\dagger = \mathbf{0}, \tag{1.57}$$

$$\frac{\partial \mathscr{L}_f}{\partial \sigma} = \mathbf{0} \quad \Rightarrow \quad \left(\mathbf{q}^\dagger \,\middle|\, \mathbf{Bq} \right) = 1, \tag{1.58}$$

$$\frac{\partial \mathscr{L}_f}{\partial \mathbf{Q}} = \mathbf{0} \quad \Rightarrow \quad \left(\frac{\partial}{\partial \mathbf{Q}} \left(\mathbf{N}_L(\mathbf{Q})\mathbf{q} \right) \right)^\dagger \mathbf{q}^\dagger = \mathbf{0}, \tag{1.59}$$

or:

$$\nabla \cdot \mathbf{u}^\dagger = 0, \quad -\overline{\sigma}\mathbf{u}^\dagger + \mathbf{U} \cdot \nabla \mathbf{u}^\dagger - \mathbf{u}^\dagger \cdot \nabla \mathbf{U}^T + Re^{-1}\nabla^2 \mathbf{u}^\dagger + \nabla p^\dagger = \mathbf{0}, \tag{1.60}$$

$$\left(\mathbf{q}^\dagger \,\middle|\, \mathbf{Bq} \right) = 1, \tag{1.61}$$

$$\frac{\mathrm{d}\sigma}{\mathrm{d}\mathbf{Q}} = -\mathbf{u}^\dagger \cdot \nabla \mathbf{u}^H + \overline{\mathbf{u}} \cdot \nabla \mathbf{u}^\dagger. \tag{1.62}$$

The result is an adjoint equation (adjoint eigenvalue problem) for $\mathbf{q}^\dagger$, together with a normalization condition (since the adjoint equation is linear and homogeneous, its solution is defined up to a multiplicative factor). Therefore, the sensitivity of a given eigenvalue is readily computed from (1.62), where only the associated direct eigenvector and adjoint eigenvector need to be solved.

1.5.2 Sensitivity to control

Now the sensitivity of the eigenvalue to control is investigated. The objective function is still $\mathscr{J} = \sigma$ and the eigenvalue problem is still a constraint for σ and $\mathbf{q}$, but the control variable is control, e.g. a force $\mathbf{C}$ or wall actuation $\mathbf{U}_c$, and the base flow is another state variable subject to its own constraint (the forced Navier-Stokes equations). The Lagrangian reads:

$$\mathscr{L}_c(\sigma, \mathbf{q}, \mathbf{Q}, \mathbf{C}, \mathbf{U}_c, \mathbf{q}^\dagger, \mathbf{Q}^\dagger, \mathbf{U}_c^\dagger) = \mathscr{L}_f(\sigma, \mathbf{q}, \mathbf{Q}, \mathbf{q}^\dagger) - \left(\mathbf{Q}^\dagger \,\middle|\, \mathbf{N}(\mathbf{Q}) - \mathbf{C} \right) - \left\langle \mathbf{U}_c^\dagger \,\middle|\, \mathbf{U} - \mathbf{U}_c \right\rangle, \tag{1.63}$$

where $\langle \mathbf{a} | \mathbf{b} \rangle = \int_{\Gamma_w} \overline{\mathbf{a}} \cdot \mathbf{b} \, \mathrm{d}\Gamma$ is the one-dimensional Hermitian inner product on walls. Clearly, derivatives with respect to σ and $\mathbf{q}$ yield the exact same normalization condition and adjoint eigenvalue problem as for the sensitivity to flow modification above, since $\mathscr{L}_c$ is made of $\mathscr{L}_f$
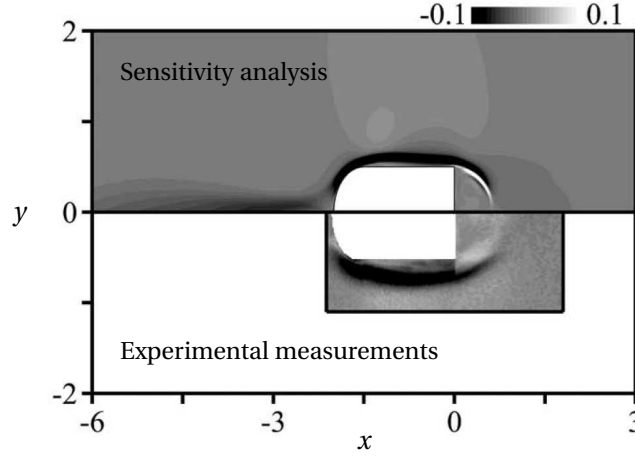
Figure 1.12 – Eigenfrequency variation caused by the introduction of a small control cylinder (diameter $d = 0.04$) in the flow past a D-shaped cylinder at $Re = 13000$. Upper half: adjoint-based sensitivity analysis (Meliga *et al.*, 2012); lower half: measurements (Parezanović & Cadot, 2012).

and two inner products where σ and $\mathbf{q}$ do not appear. Other derivatives yield:

$$\frac{\partial \mathscr{L}_c}{\partial \mathbf{Q}} = \mathbf{0} \quad \Rightarrow \quad \left(\frac{d\mathbf{N}(\mathbf{Q})}{d\mathbf{Q}}\right)^\dagger \mathbf{Q}^\dagger = \frac{d\sigma}{d\mathbf{Q}}, \tag{1.64}$$

$$\mathbf{U}_c^\dagger = -P^\dagger \mathbf{n} - Re^{-1} \nabla \mathbf{U}^\dagger \mathbf{n}, \tag{1.65}$$

$$\frac{\partial \mathscr{L}_c}{\partial (\mathbf{C}, \mathbf{U}_c)} = \mathbf{0} \quad \Rightarrow \quad \frac{d\sigma}{d\mathbf{C}} = \mathbf{U}^\dagger, \quad \frac{d\sigma}{d\mathbf{U}_c} = \mathbf{U}_c^\dagger. \tag{1.66}$$

The adjoint equation (1.64) for $\mathbf{U}^\dagger$ is linear ($d\mathbf{N}(\mathbf{Q})/d\mathbf{Q} = \mathbf{N}_L(\mathbf{Q})$ is the linearized Navier–Stokes operator) and non-homogeneous, the forcing term being precisely the sensitivity to base flow modification derived in 1.5.1:

$$\nabla \cdot \mathbf{U}^\dagger = 0, \quad -\mathbf{U} \cdot \nabla \mathbf{U}^\dagger + \mathbf{U}^\dagger \cdot \nabla \mathbf{U}^T - Re^{-1} \nabla^2 \mathbf{U}^\dagger - \nabla P^\dagger = \frac{d\sigma}{d\mathbf{Q}}. \tag{1.67}$$

The other adjoint variable $\mathbf{U}_c^\dagger$ appears to be the adjoint stress at the wall (1.65), i.e. a by-product obtained at no additional cost once $\mathbf{Q}^\dagger$ is known. It comes from integration by part in space (using the divergence theorem).

Recently, Meliga, Pujals & Serre (2012) extended this method to turbulent flows, deriving adjoint equations for the full system governing both the flow and the turbulent variable of their unsteady Reynolds-averaged Navier–Stokes model. Considering the flow past a D-shaped cylinder at $Re = 13000$, they evaluated the sensitivity of the (mean flow) leading eigenvalue to the presence of a small control cylinder. Comparison with eigenfrequency sensitivity maps measured by Parezanović & Cadot (2012) was excellent (figure 1.12).

1.5.3 Lagrangian-free method

The sensitivity of an eigenvalue to base flow modification (1.62) can actually be obtained using an alternative method. First, consider a general eigenvalue problem $\mathbf{A}\mathbf{x} = \sigma\mathbf{x}$. A small variation $\boldsymbol{\delta}\mathbf{A}$ of the operator yields at first order:

$$(\mathbf{A}+\boldsymbol{\delta}\mathbf{A})(\mathbf{x}+\boldsymbol{\delta}\mathbf{x}) = (\sigma+\delta\sigma)(\mathbf{x}+\boldsymbol{\delta}\mathbf{x}) \quad \Rightarrow \quad \mathbf{A}\boldsymbol{\delta}\mathbf{x}+\boldsymbol{\delta}\mathbf{A}\mathbf{x} = \delta\sigma\mathbf{x}+\sigma\boldsymbol{\delta}\mathbf{x} \tag{1.68}$$

Keeping only fist-order terms, and taking the inner product with the adjoint eigenvector $\mathbf{y}$ associated with σ (such that $\mathbf{A}^\dagger\mathbf{y} = \overline{\sigma}\mathbf{y}$):

$$\left(\mathbf{y}\,\middle|\,\mathbf{A}\boldsymbol{\delta}\mathbf{x}\right) + \left(\mathbf{y}\,\middle|\,\boldsymbol{\delta}\mathbf{A}\mathbf{x}\right) = \left(\mathbf{y}\,\middle|\,\delta\sigma\mathbf{x}\right) + \left(\mathbf{y}\,\middle|\,\sigma\boldsymbol{\delta}\mathbf{x}\right) \tag{1.69}$$

$$\left(\mathbf{A}^\dagger\mathbf{y}\,\middle|\,\boldsymbol{\delta}\mathbf{x}\right) + \left(\mathbf{y}\,\middle|\,\boldsymbol{\delta}\mathbf{A}\mathbf{x}\right) = \left(\mathbf{y}\,\middle|\,\delta\sigma\mathbf{x}\right) + \left(\overline{\sigma}\mathbf{y}\,\middle|\,\boldsymbol{\delta}\mathbf{x}\right) \tag{1.70}$$

$$\left(\mathbf{y}\,\middle|\,\boldsymbol{\delta}\mathbf{A}\mathbf{x}\right) = \delta\sigma\left(\mathbf{y}\,\middle|\,\mathbf{x}\right) \tag{1.71}$$

$$\delta\sigma = \frac{\left(\mathbf{y}\,\middle|\,\boldsymbol{\delta}\mathbf{A}\mathbf{x}\right)}{\left(\mathbf{y}\,\middle|\,\mathbf{x}\right)}. \tag{1.72}$$

This is a classical result for the variation of an eigenvalue caused by general operator modification (Trefethen *et al.*, 1993; Chomaz, 2005; Giannetti & Luchini, 2007).

Second, applying this relation to the eigenvalue problem (1.5) for flow perturbations, and choosing the normalization $\left(\mathbf{q}^\dagger\,\middle|\,\mathbf{q}\right) = 1$, the eigenvalue variation resulting from a base flow modification $\boldsymbol{\delta}\mathbf{Q}$ is

$$\delta\sigma = \left(\mathbf{q}^\dagger\,\middle|\,-\boldsymbol{\delta}(\mathbf{N}_L(\mathbf{Q}))\mathbf{q}\right) = \left(\mathbf{q}^\dagger\,\middle|\,-\left(\frac{\partial}{\partial\mathbf{Q}}\left(\mathbf{N}_L(\mathbf{Q})\mathbf{q}\right)\right)\boldsymbol{\delta}\mathbf{Q}\right) = \left(-\left(\frac{\partial}{\partial\mathbf{Q}}\left(\mathbf{N}_L(\mathbf{Q})\mathbf{q}\right)\right)^\dagger\mathbf{q}^\dagger\,\middle|\,\boldsymbol{\delta}\mathbf{Q}\right). \tag{1.73}$$

Therefore, since $\delta\sigma = \left(\mathrm{d}\sigma/\mathrm{d}\mathbf{Q}\,\middle|\,\boldsymbol{\delta}\mathbf{Q}\right)$, (1.62) is recovered: $\mathrm{d}\sigma/\mathrm{d}\mathbf{Q} = -\mathbf{u}^\dagger\cdot\nabla\mathbf{u}^H + \overline{\mathbf{u}}\cdot\nabla\mathbf{u}^\dagger$.

1.6 In this thesis

In the following chapters, focus is on sensitivity analysis, similar to section 1.5, applied to several quantities relevant to separated flows:

1. eigenvalues $\mathscr{J} = \sigma$;

2. harmonic gain in stable flows, i.e. gain from a small-amplitude harmonic forcing $\mathbf{f}$ to the asymptotic response $\mathbf{u}$ (Brandt *et al.*, 2011) $\mathscr{J} = G^2 = (\mathbf{u}\,|\,\mathbf{u})\,/\,(\mathbf{f}\,|\,\mathbf{f})$;

3. geometric properties of separation:

   - location of stagnation points $\mathscr{J}(\mathbf{Q}) = \mathbf{x}_{s/r}(\mathbf{Q})$ (separation and reattachment points characterized by zero wall shear stress, $\tau_{s/r} = \partial_n U_t(\mathbf{x}_{s/r}) = 0$);

- angle between the separatrix and the wall at stagnation points $\mathscr{J}(\mathbf{Q}) = \alpha_{s/r}(\mathbf{Q}) = \tan^{-1}(-3\partial_{nt}U_t/\partial_{nn}U_t)_{\mathbf{x}_{s/r}}$;

- area of the backflow region where the flow goes upstream, $\mathscr{J}(\mathbf{Q}) = A_{back}(\mathbf{Q}) = \int_\Omega \mathbb{1}_{\Omega_{back}}(\mathbf{x})\,\mathrm{d}\Omega$;

- area of the recirculation region $\mathscr{J}(\mathbf{Q}) = A_{rec}(\mathbf{Q}) = \int_\Omega \mathbb{1}_{\Omega_{rec}}(\mathbf{x})\,\mathrm{d}\Omega$;

4. aerodynamic drag and lift coefficients: $\mathscr{J}(\mathbf{Q}) = C_{D/L}(\mathbf{Q}) = 2\mathbf{e}_x \cdot \oint_{\Gamma_w} P\mathbf{n} - Re^{-1}(\nabla\mathbf{U} + \nabla\mathbf{U}^T) \cdot \mathbf{n}\,\mathrm{d}\Gamma$.

These quantities can be grouped into two categories: 3 and 4 depend explicitly on the flow, while 1 and 2 depend implicitly on the flow. In all cases, sensitivity to control requires the solution of a linear non-homogeneous adjoint equation forced by the sensitivity to flow modification. Sensitivity to flow modification, however, differs depending on the category: for 3 and 4 it is known analytically from $\mathscr{J} = \mathscr{J}(\mathbf{Q})$; for 1 and 2 the objective function is rather a variable on its own $\mathscr{J} = j$ which appears in a constraint, and in this case (as in section 1.5) sensitivity to flow modification is obtained from a linear homogeneous adjoint equation and a normalization condition.

Chapter 2

Amplification of harmonic forcing

This chapter is dedicated to the computation of sensitivity maps of the optimal harmonic gain, using as a representative configuration the flow above a wall-mounted bump, a geometry introduced in the context of laminar flows by Marquillie & Ehrenstein (2002, 2003) and further studied by Gallaire, Marquillie & Ehrenstein (2007); Ehrenstein & Gallaire (2008); Ehrenstein *et al.* (2011); Passaggia, Leweke & Ehrenstein (2012); Passaggia & Ehrenstein (2013). Not only is this separated flow of interest for its topological properties, which will be analyzed in section 4.1 (for instance the separation point is free to move, in contrast with the celebrated backward-facing step, studied in chapter 3), but it also exhibits a very elongated and thin shear layer, of great interest for the resulting stability properties.

At Reynolds number below about 600 the flow behaves as an extremely intense noise amplifier, and becomes globally unstable for $Re \gtrsim 600$, immediately exhibiting several unstable modes suspected to interact to produce low-frequency fluctuations, referred to as flapping (Ehrenstein & Gallaire, 2008). This complex behaviour above threshold differentiates this flow from prototypical oscillator flows, like bluff body wakes such as those studied in section 4.3 and chapter 5.

Section 2.1 studies altogether (i) the sensitivity of the harmonic response below threshold, (ii) the sensitivity of unstable modes above threshold, and (iii) the effect of a linearly designed control. To investigate this latter effect, two types of unsteady nonlinear direct numerical simulations (DNS) are performed: DNS of the flow submitted to external harmonic forcing or random noise below threshold, and DNS of the intrinsic dynamics of the unforced flow above threshold.

From an experimental point of view, the conjunction of strong amplification below threshold and of the complex global stability behaviour above threshold makes the well-controlled realization of this flow particularly challenging. Two experimental campaigns, respectively in air and water, are reported in section 2.2.

2.1 Paper: *Open-loop control of noise amplification in a separated boundary layer flow*

Open-loop control of noise amplification
in a separated boundary layer flow

E. Boujo[1], U. Ehrenstein[2] and F. Gallaire[1]

[1]LFMI, École Polytechnique Fédérale de Lausanne, CH-1015 Lausanne, Switzerland
[2]Aix Marseille Université, CNRS, Centrale Marseille, IRPHÉ UMR 7342, F-13384, Marseille, France

Linear optimal gains are computed for the subcritical two-dimensional separated boundary-layer flow past a bump. Very large optimal gain values are found, making it possible for small-amplitude noise to be strongly amplified and to destabilize the flow. The optimal forcing is located close to the summit of the bump, while the optimal response is the largest in the shear layer. The largest amplification occurs at frequencies corresponding to eigenvalues which first become unstable at higher Reynolds number. Non-linear direct numerical simulations show that a low level of noise is indeed sufficient to trigger random flow unsteadiness, characterized here by large-scale vortex shedding.

Next, a variational technique is used to compute efficiently the sensitivity of optimal gains to steady control (through source of momentum in the flow, or blowing/suction at the wall). A systematic analysis at several frequencies identifies the bump summit as the most sensitive region for control with wall actuation. Based on these results, a simple open-loop control strategy is designed, with steady wall suction at the bump summit. Linear calculations on controlled base flows confirm that optimal gains can be drastically reduced at all frequencies. Non-linear direct numerical simulations also show that this control allows the flow to withstand a higher level of stochastic noise without becoming non-linearly unstable, thereby postponing bypass transition.

In the supercritical regime, sensitivity analysis of eigenvalues supports the choice of this control design. Full restabilization of the flow is obtained, as evidenced by direct numerical simulations and linear stability analysis.

1 Introduction

Flows can undergo bifurcation well below the critical Reynolds number Re_c predicted by linear stability analysis. Examples of such subcritical flows include both parallel flows (e.g. Couette and Hagen-Poiseuille, which are linearly stable for any Reynolds number, i.e. $Re_c = \infty$ (Schmid & Henningson, 2001)) and non-parallel flows (e.g. jets, backward-facing step). Classical linear stability theory, which focuses on the long-term fate of small perturbations, predicts that all linear eigenmodes are damped for $Re < Re_c$. However, it has become clear in the past decades that perturbations can be amplified by non-modal mechanisms, a phenomenon that modal linear stability analysis fails to capture (Trefethen *et al.*, 1993). If large

enough, amplification of these perturbations might destabilize the flow and trigger unsteadiness or spatial symmetry breaking, thus leading to subcritical bypass transition.

While eigenvalues are not relevant to characterize such flows, non-modal mechanisms are well described by two complementary ideas: transient growth of initial conditions, and asymptotic amplification of forcing. These mechanisms are a result of the non-normality of the linearized Navier-Stokes operator which governs the dynamics of perturbations. For example, non-normality leads to large transient growth in parallel flows through the two-dimensional Orr mechanism and, more importantly, the three-dimensional lift-up effect (Butler & Farrell, 1992); in non-parallel flows, large transient growth is observed because of convective non-normality (Chomaz, 2005). For such flows, transient growth is a well-established notion, and most attempts to control convectively unstable flows naturally focus on reducing the largest possible transient growth, or "optimal growth" (Corbett & Bottaro, 2001). A great variety of control types and strategies exist (see e.g. reviews by Fiedler & Fernholz (1990); Gad-el Hak (1996); Choi *et al.* (2008)). Several techniques have been used to reduce transient growth, both active and passive. Among active control, the design of closed-loop schemes has received a lot of attention. Based on modern control theory (review by Kim & Bewley (2007)), and applied to physics-based reduced-order models (Rowley, 2005; Ehrenstein *et al.*, 2011) or to models obtained from system identification (Tian *et al.*, 2006; Henning & King, 2007), it has proven robust enough to be implemented in experiments. Based on Lagrangian optimization, receding-horizon predictive control was able to successfully relaminarize a plane channel flow at a centerline Reynolds number of 1712 (Bewley *et al.*, 2001). Open-loop control has also been proposed as a successful strategy to mitigate instabilities experimentally, be it active or passive (e.g. Fransson, Brandt, Talamelli & Cossu (2004) and Pujals *et al.* (2010) to mention a few recent achievements).

As a complementary notion to transient growth, optimal response to harmonic forcing (or "optimal gain") has drawn increasing attention too in the past years. Åkervik, Ehrenstein, Gallaire & Henningson (2008) computed the optimal gain in a flat-plate boundary layer using a reduced-order model of global eigenmodes. Alizard, Cherubini & Robinet (2009) used the same method to obtain the optimal gain in a flat plate boundary layer with adverse-pressure-induced separation. The optimal gain can also be calculated directly from the linearized Navier–Stokes operator, as did Garnaud, Lesshafft, Schmid & Huerre (2013) for an incompressible axsymmetric jet, Sipp & Marquet (2013) for a flat plate, and Dergham, Sipp & Robinet (2013) for a rounded backward-facing step.

Recently, Brandt *et al.* (2011) introduced Lagrangian-based sensitivity analysis to quantify the sensitivity of the largest asymptotic amplification to steady control, and applied it to a flat plate boundary layer. Lagrangian-based sensitivity analysis is a variational formulation which allows us to compute gradients at low cost through the use of adjoint variables. In particular, it can be applied to flow control with the aim of modifying eigenvalues (see Luchini & Bottaro (2014) for a recent, general review of adjoint equations). Hill (1992) derived the corresponding variational formulation and computed the sensitivity of the most
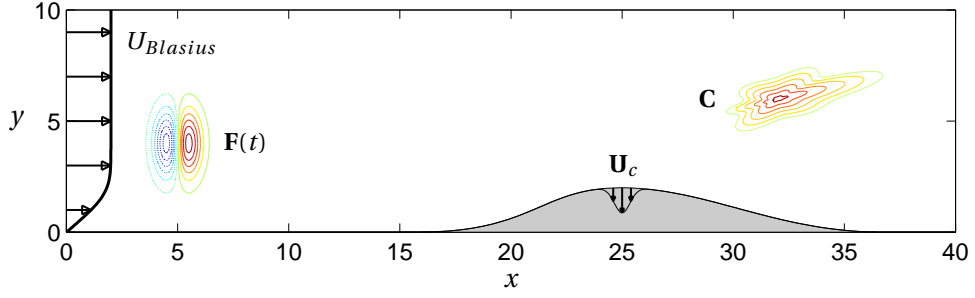
Figure 2.1 – Bump geometry $y = y_b(x)$, inlet velocity profile $(U, V) = (U_{Blasius}, 0)$, time-dependent forcing $\mathbf{F}(t)$, steady volume control $\mathbf{C}$ and steady wall control $\mathbf{U}_c$.

unstable eigenvalue to passive control in the incompressible flow past a circular cylinder. He reproduced most sensitive regions previously identified experimentally by Strykowski & Sreenivasan (1990), where a secondary, small control cylinder could suppress vortex shedding. Sensitivity analysis has then been used by several authors to compute the sensitivity of eigenvalues in absolutely unstable flows. Marquet *et al.* (2008) studied the effect of base flow modification and steady control in the bulk in the same flow as Hill (1992) and reproduced most sensitive regions. Meliga *et al.* (2010) managed to control the first oscillating eigenmode in the compressible flow past an axisymmetric body, considering its sensitivity to steady forcing in the bulk (with mass, momentum or energy sources) and at the wall (with blowing/suction or heating). Meliga *et al.* (2012) also computed the sensitivity of the shedding frequency (eigenfrequency of the leading global mode to the mean flow) in the fully turbulent wake past a bluff body and reproduced experimental data for the flow forced by a small control cylinder. The extension of sensitivity analysis to optimal gain by Brandt *et al.* (2011) now opens the way to the control of convectively unstable flows.

In this study, the flow past a wall-mounted bump is considered. This separated flow is characterized by a long recirculation region, high shear, strong backflow, and exhibits large transient growth (Ehrenstein & Gallaire, 2008; Ehrenstein *et al.*, 2011). Optimal gains are computed at different frequencies, and a sensitivity analysis is systematically performed in order to identify regions where they can be reduced with steady open-loop control. This paper is organized as follows. Section 2 describes the problem, including geometry and governing equations. The uncontrolled subcritical flow is studied in section 3 by computing linear optimal gains and characterizing noise amplification with DNS (direct numerical simulation). In section 4, a sensitivity analysis is performed in order to identify regions where optimal gains are most affected by steady control. Based on the results, we design one specific control configuration, with wall suction at the bump summit, and demonstrate its effectiveness in reducing not only linear optimal gains but also non-linear noise amplification. In section 5, we investigate flow stabilization in the supercritical regime: sensitivity analysis applied to global eigenvalues supports the choice of wall suction at the bump summit, which is further confirmed by results from DNS and linear stability analysis. Conclusions are drawn in section 6.

2 Problem description and governing equations

The flow past a 2D bump mounted on a flat plate is considered. The bump geometry $y = y_b(x)$ is shown in figure 2.1 and is the same as in Bernard, Foucaut, Dupont & Stanislas (2003); Marquillie & Ehrenstein (2003) and following studies (Ehrenstein & Gallaire, 2008; Ehrenstein *et al.*, 2011; Passaggia *et al.*, 2012). The incoming flow has a Blasius boundary layer profile, characterized by its displacement thickness δ^* at the reference position $x = 0$. The bump summit is located at $x = x_b = 25\delta^*$, and the bump height is $h = 2\delta^*$. All quantities in the problem are made dimensionless with inlet velocity U_∞ and inlet boundary layer displacement thickness δ^*. The Reynolds number is defined as $Re = U_\infty \delta^* / \nu$, with ν the fluid kinematic viscosity.

The fluid motion in the domain Ω is described by the velocity field $\mathbf{U} = (U, V)^T$ and pressure field P. The state vector $\mathbf{Q} = (\mathbf{U}, P)^T$ is a solution of the two-dimensional incompressible Navier–Stokes equations

$$\nabla \cdot \mathbf{U} = 0, \qquad \partial_t \mathbf{U} + \mathbf{U} \cdot \nabla \mathbf{U} + \nabla P - Re^{-1} \nabla^2 \mathbf{U} = \mathbf{F} + \mathbf{C} \quad \text{in } \Omega,$$
$$\mathbf{U} = \mathbf{U}_c \quad \text{on } \Gamma_c, \tag{2.1}$$
$$\mathbf{U} = \mathbf{0} \quad \text{on } \Gamma_w \setminus \Gamma_c.$$

In the most general case, $\mathbf{F}(t)$ is a time-dependent volume forcing, which will be specified as harmonic forcing or stochastic noise in sections 3-4. A steady control is applied through a volume force $\mathbf{C}$ in the flow, or through blowing/suction velocity $\mathbf{U}_c$ in some regions Γ_c of the wall. The no-slip condition applies on other parts of the wall $\Gamma_w \setminus \Gamma_c$.

Without forcing ($\mathbf{F} = \mathbf{0}$), the steady-state base flow $\mathbf{Q}_b = (\mathbf{U}_b, P_b)^T$ satisfies:

$$\nabla \cdot \mathbf{U}_b = 0, \qquad \mathbf{U}_b \cdot \nabla \mathbf{U}_b + \nabla P_b - Re^{-1} \nabla^2 \mathbf{U}_b = \mathbf{C} \quad \text{in } \Omega,$$
$$\mathbf{U}_b = \mathbf{U}_c \quad \text{on } \Gamma_c, \tag{2.2}$$
$$\mathbf{U}_b = \mathbf{0} \quad \text{on } \Gamma_w \setminus \Gamma_c.$$

To obtain the equation which governs the evolution of perturbations under small-amplitude forcing $\mathbf{F} = \mathbf{f}'$, the flow is written as the superposition of the steady-state base flow and small time-dependent perturbations, $\mathbf{Q} = \mathbf{Q}_b + \mathbf{q}'$. Linearizing equations (4.56) yields:

$$\nabla \cdot \mathbf{u}' = 0, \qquad \partial_t \mathbf{u}' + \mathbf{U}_b \cdot \nabla \mathbf{u}' + \mathbf{u}' \cdot \nabla \mathbf{U}_b + \nabla p' - Re^{-1} \nabla^2 \mathbf{u}' = \mathbf{f}' \quad \text{in } \Omega,$$
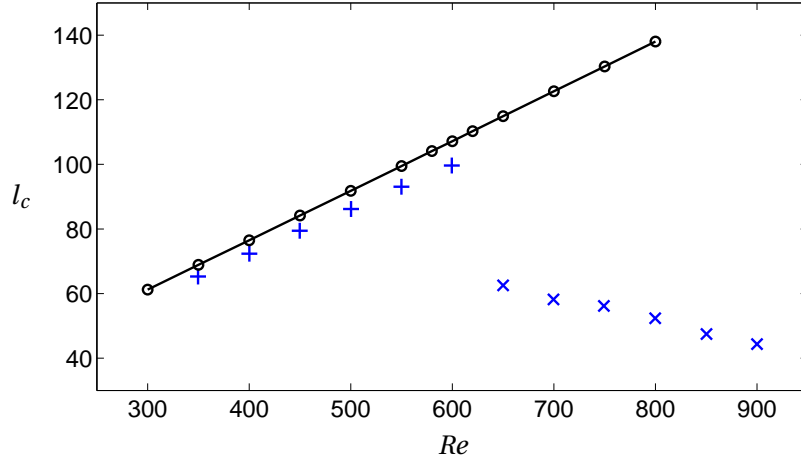$$\mathbf{u}' = \mathbf{0} \quad \text{on } \Gamma_w. \tag{2.3}$$

Figure 2.2 – Recirculation length as function of Reynolds number. Solid line: steady-state base flow calculated in the present study. Symbols: steady state computations (+) and time-averaged recirculation length of oscillatory flow field (×) obtained by Marquillie & Ehrenstein (2003).

3 Response to forcing: noise amplification

3.1 Base flow

The steady-state base flow $\mathbf{Q}_b$ is obtained with an iterative Newton method. A two-dimensional triangulation of the computational domain Ω ($0 \leq x \leq 400$, $y_b \leq y \leq 50$) is generated with the finite element software *FreeFem++* (http://www.freefem.org), and equations (2.2) are solved in their variational formulation, with the following boundary conditions: Blasius profile $\mathbf{U}_b = (U_{Blasius}, 0)^T$ at the inlet, no-slip condition $\mathbf{U}_b = \mathbf{0}$ on the wall, symmetry condition $\partial_y U_b = V_b = 0$ at the top border, and $-P_b\mathbf{n} + Re^{-1}\nabla\mathbf{U}_b\mathbf{n} = \mathbf{0}$ at the outlet, with $\mathbf{n}$ the outward unit normal vector. P2 and P1 Taylor-Hood elements are used for spatial discretization of velocity and pressure, respectively.

Figure 2.2 shows the recirculation length obtained for different Reynolds numbers. It can be seen that l_c increases linearly with Re, a behavior already observed experimentally and numerically in a variety of separated flows, both wall-bounded and past bluff bodies: backward-facing step (Sinha, Gupta & Oberai, 1981), bump (Passaggia *et al.*, 2012), cylinder (Zielinska, Goujon-Durand, Dušek & Wesfreid, 1997; Giannetti & Luchini, 2007), etc. The value of l_c at $Re = 500$ and 600 changed by 0.15% and 0.10% when refining the computational mesh so as to increase the number of elements by 50%. Results from DNS by Marquillie & Ehrenstein (2003) are also reported for reference, where values up to $Re \leq 600$ correspond to steady state computations and those for $Re > 600$ are obtained from time-averaged oscillatory flow fields. Slight differences stem from different choices of domain size and boundary conditions: in their direct numerical simulations, outlet and upper boundaries are located at $x = 200$ and $y = 80$, and the boundary conditions are respectively $(U, V) = (1, 0)$ and an outflow advection condition well suited for DNS. In the present study, the upper boundary is lower ($y = 50$)

37

and the outlet much farther ($x = 400$), and a stress-free boundary condition is prescribed at both boundaries since it is adapted to steady-state flows and appears as a natural condition when using finite elements. The present Newton method allows us to obtain base flows well beyond the critical Reynolds number and to confirm the linear dependency of l_c with Re.

3.2 Optimal gain

When harmonic forcing $\mathbf{F}(x, y, t) = \mathbf{f}(x, y)e^{i\omega t}$ is applied to a stable flow, the asymptotic response is harmonic at the same frequency ω, $\mathbf{q}'(x, y, t) = \mathbf{q}(x, y)e^{i\omega t}$. Then (2.3) becomes:

$$\nabla \cdot \mathbf{u} = 0, \qquad i\omega\mathbf{u} + \mathbf{U}_b \cdot \nabla\mathbf{u} + \mathbf{u} \cdot \nabla\mathbf{U}_b + \nabla p - Re^{-1}\nabla^2\mathbf{u} = \mathbf{f}. \tag{2.4}$$

In the following, the amplitude of perturbations $\mathbf{q}$ is measured in terms of their kinetic energy $E_p = \int_\Omega |\mathbf{u}|^2 \, d\Omega = ||\mathbf{u}||_2^2$ with $||.||_2$ the L^2 norm induced by the Hermitian inner product $(\mathbf{a}|\mathbf{b}) = \int_\Omega \mathbf{a}^* \cdot \mathbf{b} \, d\Omega$. The forcing amplitude is measured in a similar way with the L^2 norm $||\mathbf{f}||_2^2 = \int_\Omega |\mathbf{f}|^2 \, d\Omega$. For a given frequency ω and a given forcing $\mathbf{f}$, the asymptotic energy amplification is the gain $G(\omega) = ||\mathbf{u}||_2 / ||\mathbf{f}||_2$. In particular, it is of interest to determine the optimal forcing $\mathbf{f}_{opt}$ which leads to the largest energy amplification, i.e. the optimal gain:

$$G_{opt}(\omega) = \max_{\mathbf{f}} \frac{||\mathbf{u}||_2}{||\mathbf{f}||_2}. \tag{2.5}$$

In this study, optimal gains are computed using the same procedure as Garnaud *et al.* (2013) After spatial discretization, the linear dynamical system (2.4) is written as $(i\omega\mathbf{B} + \mathbf{L})\mathbf{q} = \mathbf{BPf}$, with $\mathbf{P}$ a prolongation operator from the velocity-only space to the velocity-pressure space. The optimal gain (2.5) is recast as

$$G_{opt}(\omega) = \max_{\mathbf{f}} \frac{||\mathbf{q}||_q}{||\mathbf{f}||_f}, \tag{2.6}$$

where the pseudonorm $||\mathbf{q}||_q^2 = \mathbf{q}^H\mathbf{Q}_q\mathbf{q}$ and the norm $||\mathbf{f}||_f^2 = \mathbf{f}^H\mathbf{Q}_f\mathbf{f}$ are discretized versions of the L^2 norm. Rearranging the expression of $G_{opt}^2(\omega) = \max_{\mathbf{f}} ||(i\omega\mathbf{B} + \mathbf{L})^{-1}\mathbf{BPf}||_q^2 / ||\mathbf{f}||_f^2$, the optimal gain can be expressed as the leading eigenvalue of the Hermitian eigenvalue problem

$$\mathbf{Q}_f^{-1}\mathbf{P}^H\mathbf{B}^H(i\omega\mathbf{B} + \mathbf{L})^{-H}\mathbf{Q}_q(i\omega\mathbf{B} + \mathbf{L})^{-1}\mathbf{BPf} = \lambda\mathbf{f}. \tag{2.7}$$

The operator $(i\omega\mathbf{B} + \mathbf{L})^{-1}$ is also called "resolvent" and the optimal gain $G_{opt}(\omega)$ the "resolvent norm". The largest eigenvalue $\max(\lambda) = G_{opt}^2(\omega)$ and the associated eigenvector $\mathbf{f}_{opt}$ are computed using an implicitly restarted Arnoldi method. Operators $\mathbf{Q}_f^{-1}$ and $(i\omega\mathbf{B} + \mathbf{L})^{-1}$ are obtained via LU decompositions. Operators $\mathbf{L}$ and $\mathbf{B}$ are obtained by spatially discretizing the linear system (2.4) with the same method, same mesh and same elements as for the base flow.

Previous studies using DNS (Marquillie & Ehrenstein, 2003) and linear global stability anal-
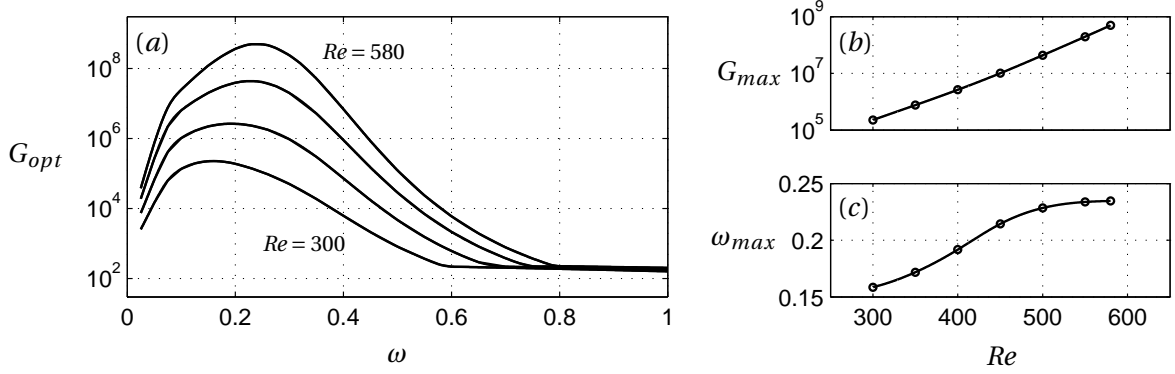
Figure 2.3 – (*a*) Optimal linear gain at $Re = 300$, 400, 500 and 580. (*b*) Variation of the maximal optimal gain with Reynolds number, and (*c*) frequency of this maximum.

ysis (Ehrenstein & Gallaire, 2008) reported a critical Reynolds number Re_c between 590 and 610. In this section, noise amplification is calculated for the subcritical bump flow at Reynolds numbers $Re \leq 580$.

Figure 2.3 shows the optimal gain $G_{opt}(\omega)$, its maximum value $G_{max} = \max_{\omega}(G_{opt}(\omega))$ and the corresponding frequency ω_{max}. The latter increases between 0.15 and 0.25, while the maximal optimal gain increases exponentially with Re and reaches values larger than 10^8 at $Re = 580$. This is in agreement with observations for other separated flows, for example pressure-induced recirculation bubbles (Alizard *et al.*, 2009). The large gain values found here suggest that an incoming noise of very low amplitude might be linearly amplified so much that it would eventually become of order one and possibly modify the base flow, or even completely destabilize the overall flow behavior.

Largest values of optimal gain are obtained for frequencies corresponding to the most unstable global eigenvalues (e.g. $0.15 \leq \omega \leq 0.30$ for the eigenvalues with largest growth rate near critical conditions in Ehrenstein & Gallaire (2008)). This is also true at lower values of *Re* even though these eigenvalues are strongly stable, a phenomenon known as "pseudoresonance" and a direct consequence of non-normality (Trefethen *et al.*, 1993). No peak is found at the low frequency corresponding to the flapping observed in DNS ($\omega \simeq 0.04$ in Marquillie & Ehrenstein (2003)).

Figure 2.4 shows the spatial structure of the optimal forcing and optimal response at $Re = 580$. The optimal forcing is located near the summit of the bump and at the beginning of the shear layer, with structures tilted against the base flow (which points to a contribution from the Orr mechanism to the total amplification (Åkervik *et al.*, 2008; Dergham *et al.*, 2013)). The forcing exhibits a layer-like structure in the *y* direction, and these layers become thinner as ω increases. The optimal response has a wave packet-like structure in the *x* direction, whose wavelength decreases with ω. At low frequency, $\omega \lesssim 0.1$, the response is located downstream of the reattachment point and is typical of the convective Tollmien-Schlichting instability (Ehrenstein & Gallaire, 2005; Åkervik *et al.*, 2008; Alizard & Robinet, 2007; Dergham *et al.*,
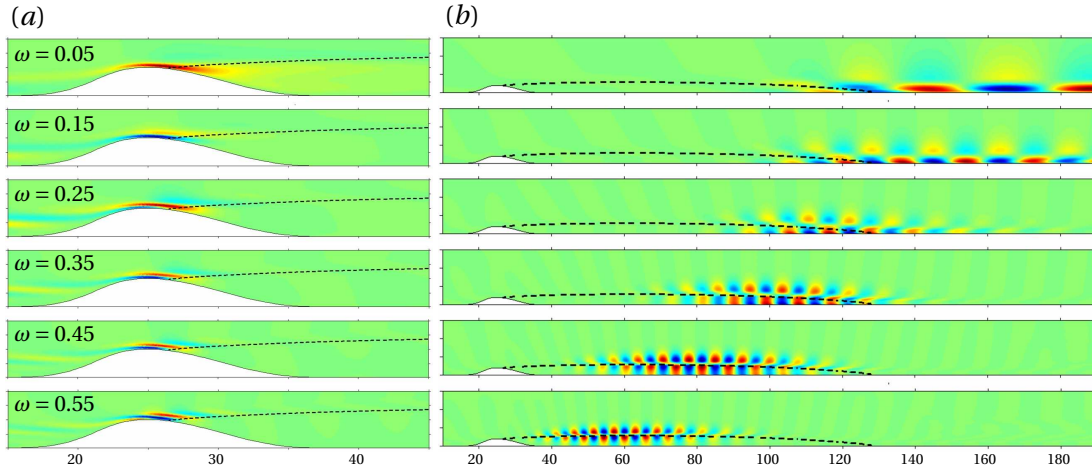
Figure 2.4 – (*a*) Optimal forcing and (*b*) optimal response at $Re = 580$ for different frequencies ω. The real part of the streamwise component is shown. The dashed line shows the base flow separating streamline.

2013). At intermediate frequencies, the response is located along the shear layer, and its structure is reminiscent of the most unstable global eigenmodes for the same flow (Ehrenstein & Gallaire, 2008), typical of Kelvin-Helmholtz instability in shear flows. This intermediate range includes frequencies of largest optimal gain G_{opt} (see figure 2.3). At higher frequency, $\omega \gtrsim 0.8$, the optimal forcing and response (not shown) are spread over a wide region and correspond to the combined effect of advection and diffusion (Dergham *et al.*, 2013).

3.3 Direct numerical simulations

In this section, the full non-linear Navier–Stokes system (4.56) is solved with direct numerical simulations, using the same procedure as Marquillie & Ehrenstein (2003). In the following, the subcritical flow at $Re = 580$ is forced with $\mathbf{F} = \mathbf{f}(x, y)\phi(t)$. This volume forcing will serve a twofold role: section 3.3.1 focuses on harmonic forcing, so as to investigate the fully non-linear asymptotic response, while section 3.3.2 deals with stochastic forcing, in order to mimic random noise. The spatial structure of the forcing is chosen as a divergence-free "double Gaussian" already used by Ehrenstein *et al.* (2011) and illustrated in figure 2.5:

$$
\begin{aligned}
f_x &= -(y - y_f) A \exp\left(-\frac{(x - x_f)^2}{2\sigma_x^2} - \frac{(y - y_f)^2}{2\sigma_y^2} \right), \\
f_y &= \frac{\sigma_y^2}{\sigma_x^2} (x - x_f) A \exp\left(-\frac{(x - x_f)^2}{2\sigma_x^2} - \frac{(y - y_f)^2}{2\sigma_y^2} \right).
\end{aligned}
\tag{2.8}
$$

with a variable amplitude A, a center located at $x_f = 5$, $y_f = 4$, and characteristic width and height $\sigma_x = 0.5$, $\sigma_y = 1.0$. The Gaussian-type forcing $\mathbf{f}$ is sufficiently far from the wall so that its L^2 norm is very close to the theoretical value $A\sqrt{\frac{\pi}{2}\sigma_x\sigma_y^3\left(1 + \sigma_y^2/\sigma_x^2\right)}$ one would obtain in
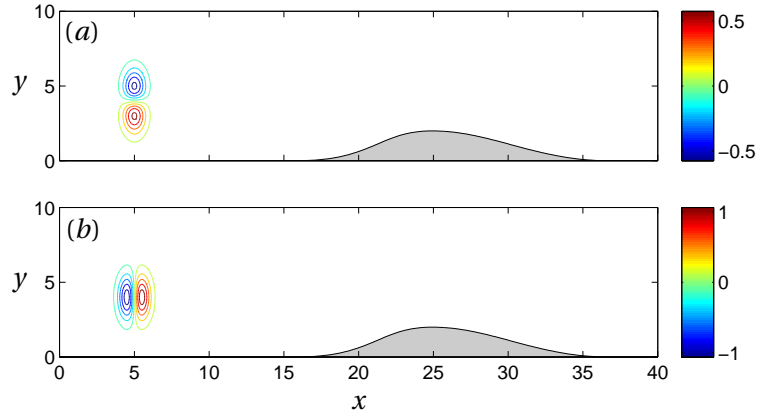
Figure 2.5 – Spatial structure of the divergence-free Gaussian forcing (2.8): (*a*) streamwise and (*b*) cross-stream components.

an unbounded domain, yielding $||\mathbf{f}|| \simeq 2A$. It should be stressed that $\mathbf{F}(t)$ aims at modelling an external forcing, and should not be confused with volume control $\mathbf{C}$ or wall control $\mathbf{U}_c$.

3.3.1 DNS with harmonic forcing

In this section the forcing is chosen as $\mathbf{F} = \mathbf{f}(x,y)\phi(t)$ with a harmonic time-dependency: $\phi(t) = e^{i\omega t}$. We introduce notations for different measures of harmonic amplification used in the following:

- *Linear optimal gain* ("resolvent norm") $G_{opt}(\omega)$, already defined by equation (2.5): largest energy amplification over all possible forcings $\mathbf{f}(x,y)$, it is solution of the eigenvalue problem (2.7);

- *Actual linear gain* $G_{lin}(\omega)$: energy amplification actually obtained for our particular choice of forcing (2.8) in a fully linearized setting, it is simply calculated by solving the linear system (2.4), i.e. $G_{lin}(\omega) = ||\mathbf{q}||_q/||\mathbf{f}||_f = ||(i\omega\mathbf{B} + \mathbf{L})^{-1}\mathbf{BPf}||_q/||\mathbf{f}||_f$;

- *Linear DNS gain* $G_{DNS}(\omega)$: energy amplification $||\mathbf{q}||/||\mathbf{f}||$ measured in non-linear DNS forced by our particular choice of forcing (2.8) in the linear regime, i.e. with forcing amplitudes small enough for non-linear effects to be negligible.

Figure 2.6(*a*) displays the evolution of the energy of the perturbations $E_p(t) = ||\mathbf{q}'(t)||^2 = ||\mathbf{Q}(t) - \mathbf{Q}_b||^2$ for different forcing amplitudes, at $\omega = 0.25$. For small values of A, the flow quickly reaches a steady-state regime, as E_p reaches an almost constant value, and the flow is harmonic as indicated by the regular velocity signal and the peaked power spectrum shown in figures 2.6(*c*, *d*). From the results in this small-amplitude forcing regime, it is possible to measure the amplification from forcing to response, or *linear DNS gain* $G_{DNS} = ||\mathbf{q}||/||\mathbf{f}|| = E_p^{1/2}/2A$. The variation of the mean asymptotic energy $\overline{E}_p$ (mean value of $E_p(t)$ after the transient regime) with A is shown in figure 2.6(*b*) in logarithmic scale. For small values of A, the
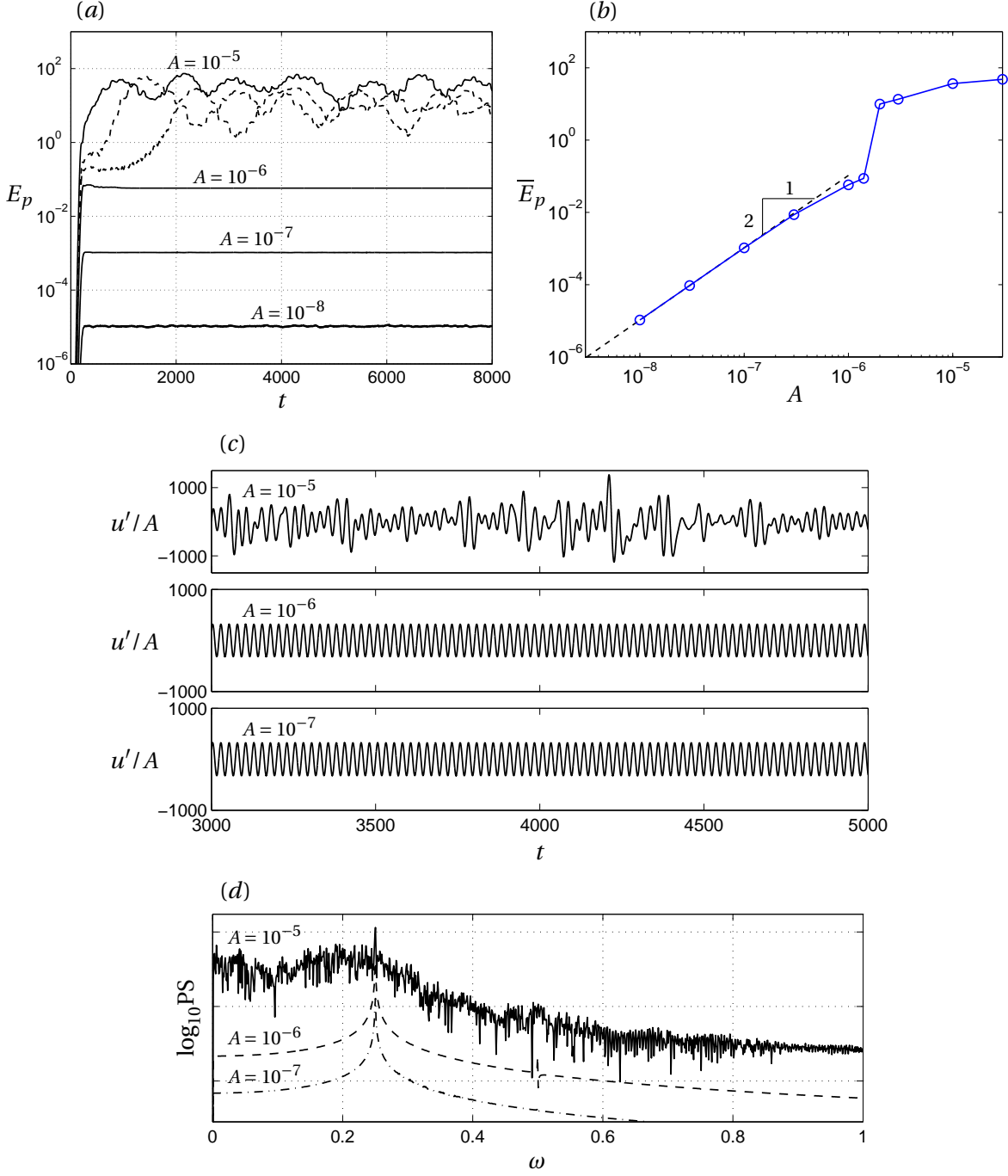
Figure 2.6 – Response to harmonic forcing at $Re = 580$, $\omega = 0.25$. (a) Time evolution of energy of the perturbations. Dashed lines correspond to $A = 2 \times 10^{-6}$ and 3×10^{-6}. (b) Mean asymptotic energy in the steady-state regime as function of the forcing amplitude A. The dashed line has a slope 2. (c) Time series of the streamwise perturbation velocity u' at $x = 80$, $y = 1$, for $A = 10^{-7}$, 10^{-6}, 10^{-5}. (d) Power spectrum of this velocity for forcing amplitudes $A = 10^{-7}$ (dash-dotted line), $A = 10^{-6}$ (dashed line), $A = 10^{-5}$ (solid line) (arbitrary unit, logarithmic scale).
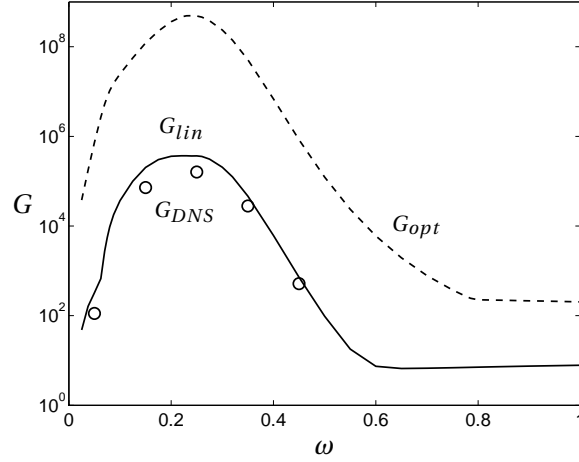
Figure 2.7 – Actual response to harmonic forcing $\mathbf{F} = \mathbf{f}(x, y)e^{i\omega t}$ with the particular choice (2.8) for the spatial structure $\mathbf{f}$. Solid line: actual linear gain G_{lin}; Symbols: linear DNS gain G_{DNS} obtained from DNS calculations with small-amplitude forcing. The dashed line indicates for reference the optimal gain G_{opt} (reported from figure 2.3).

slope of the curve is 2 as expected, and the *linear DNS gain* is $G_{DNS} \simeq 1.6 \times 10^5$. This value should be compared to the *actual linear gain* $G_{lin}(\omega)$. Values of G_{lin} and G_{DNS} are given in figure 2.7 and show good agreement.

For larger values of the forcing amplitude, non-linear effects become non-negligible and the energy amplification starts to depart from the linear gain. At some point, close to $A_c \simeq 2 \times 10^{-6}$ in the case illustrated here, transition to a different regime occurs. The flow is destabilized and becomes non-harmonic, as indicated by figures 2.6(c, d): although a sharp peak is still present at the forcing frequency, the field now also contains a whole range of low and mid frequencies. The perturbation energy jumps to a larger value. This phenomenon is a subcritical transition: small finite-amplitude perturbations are large enough to make the initially stable flow move away from a weakly non-linear oscillatory state to a disordered one. Increasing A further does not modify significantly the mean asymptotic energy, which saturates at $\overline{E}_p \simeq 100$.

3.3.2   DNS with stochastic forcing

In this section the forcing is chosen as $\mathbf{F} = \mathbf{f}(x, y)\phi(t)$ with a stochastic time-dependency: $\phi(t)$ is a random noise of normal distribution (zero mean, unit variance). After investigating the response to harmonic forcing and comparing with linear results in section 3.3.1, the aim is now to model a more realistic noise.

The time evolution of $E_p(t)$ and the variation of $\overline{E}_p$ with forcing amplitude are shown in figures 2.8(a, b). Qualitatively, they are very similar to their counterparts for harmonic forcing. In particular, $\overline{E}_p$ is proportional to A^2 for small amplitudes, increases more quickly after a

critical value $A_c \simeq 10^{-5}$, and then saturates. A_c is larger and the transition smoother than in the harmonic forcing case. This is consistent with the fact that a random white noise excites all frequencies, thus only part of the total forcing energy is available at amplified frequencies. This results in a larger forcing amplitude needed to obtain the same destabilizing effect. However, the level of noise that the system can withstand is still very low, which shows that the subcritical bump flow is a strong noise amplifier, easily destabilized by incoming noise (Chomaz, 2005).

Figure 2.8(c-f) shows streamwise velocity time series and power spectra computed from the streamwise velocity signals measured over $1500 \leq t \leq 8000$ at $y = 1$, from upstream ($x = 80$) to downstream ($x = 140$) of the reattachment point. Interestingly, power spectra shift towards lower frequencies as x increases, which is consistent with the fact that linear optimal response moves downstream when ω decreases (see figure 2.4). For the lower forcing amplitude $A = 10^{-7}$, power spectra in figure 2.8(e) are maximal in the range of frequencies $0.15 \lesssim \omega \lesssim 0.30$, close to the range where linear gain (thick curve) is large. The agreement between linear optimal gain and non-linear DNS power spectra is best at $x = 120$, where optimal responses are mostly located for this range of frequencies and in particular at $\omega_{max} = 0.23$ (figure 2.4). For the larger forcing amplitude $A = 10^{-5}$, power spectra in figure 2.8(f) are the same as those for $A = 10^{-7}$ inside the recirculation region. Downstream, however, they exhibit two distinct groups of frequencies: the same as for $A = 10^{-7}$, and another one at lower frequencies, related by a factor $1/2$. Inspection of velocity fields in this case, shown in figure 2.9, reveals a secondary subharmonic instability reminiscent of vortex pairing: structures downstream have a wavelength twice as large as the primary wavelength observed upstream, $\lambda_2 = 2\lambda_1$. For larger forcing amplitudes, the flow is more complex because of even stronger non-linear effects, and wavelengths are slightly increased. Note that perturbations in the linear regime (figure 2.9(a)) are very similar to the linear optimal response at $\omega = 0.25$ (figure 2.4(b)), close to the most amplified frequency.

4   Sensitivity analysis

4.1   Sensitivity of optimal gain

In order to design an efficient open-loop control strategy aiming at reducing the optimal gain, it is important first to understand the effect of a given control on $G_{opt}(\omega)$. Following Brandt *et al.* (2011), a variational technique formulated in a Lagrangian framework is used to evaluate the linear sensitivity of the optimal gain with respect to control. Considering the small variation of $G_{opt}^2(\omega)$ resulting from a small source of momentum $\boldsymbol{\delta C}$ in the domain Ω and small-amplitude wall blowing/suction $\boldsymbol{\delta U}_c$ on the control wall Γ_c, the sensitivities to these two types of control can be defined as $\delta G_{opt}^2 = (\nabla_{\mathbf{C}} G_{opt}^2 | \boldsymbol{\delta C}) + \langle \nabla_{\mathbf{U}_c} G_{opt}^2 | \boldsymbol{\delta U}_c \rangle$, where the second term is a one-dimensional inner product on the control boundary $\langle \mathbf{a} | \mathbf{b} \rangle = \int_{\Gamma_c} \mathbf{a}^* \cdot \mathbf{b} \, d\Gamma$. Through the use of a Lagrangian that includes the definition of the optimal gain (2.6), one
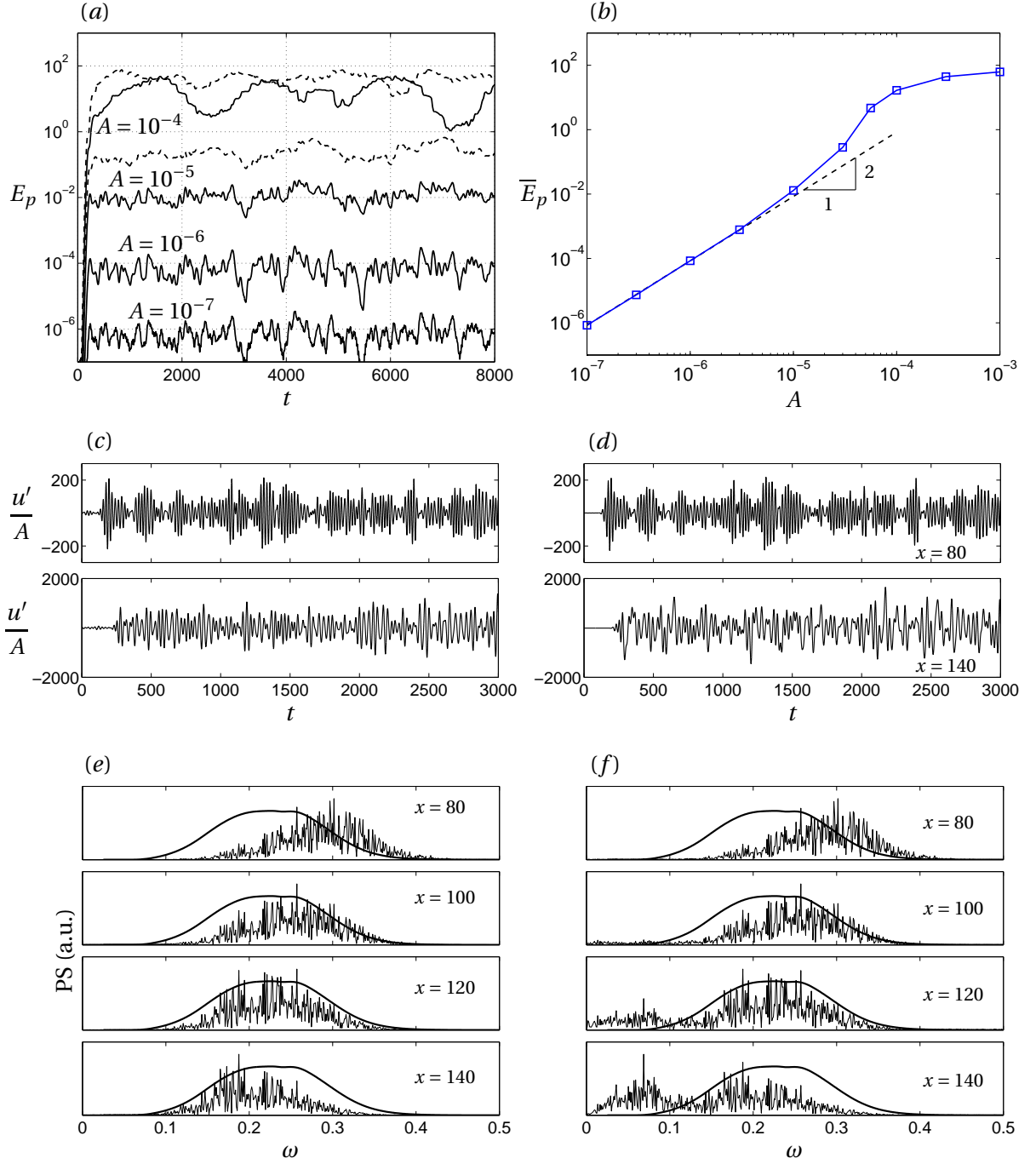
Figure 2.8 – Response to stochastic forcing at $Re = 580$. (a) Time evolution of the perturbation energy E_p. Dashed lines correspond to $A = 3 \times 10^{-5}$ and 3×10^{-4}. (b) Mean asymptotic energy in the steady-state regime as function of the forcing amplitude A. (c, d) Time series of the streamwise perturbation velocity u' measured at $y = 1$ and $x = 80$ and 140 for (c) $A = 10^{-7}$ and (d) $A = 10^{-5}$. (e, f) Power spectrum of the streamwise velocity measured at $y = 1$ and $x = 80, 100, 120, 140$, for (e) $A = 10^{-7}$ and (f) $A = 10^{-5}$. For reference, the thick line shows the (uncontrolled) linear gain $G_{lin}(\omega)$ from figure 2.7 (arbitrary unit, linear scale).
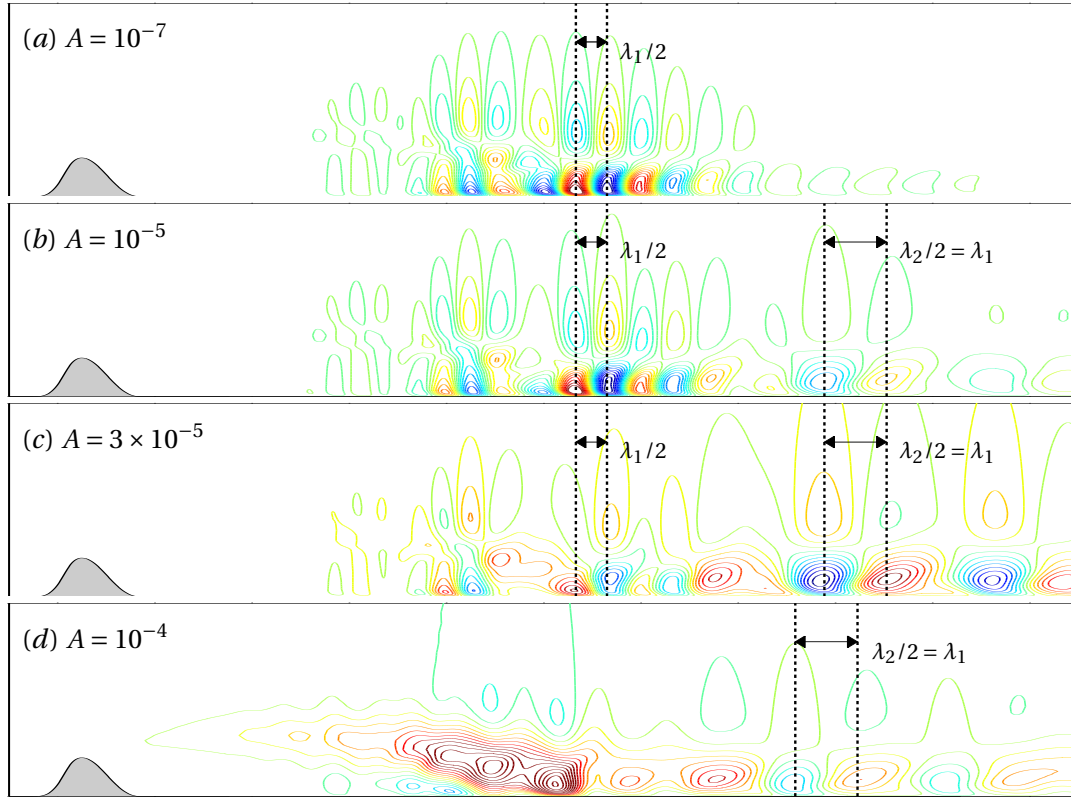
Figure 2.9 – Subharmonic instability occurs as a manifestation of non-linear effects when forcing amplitude is large enough. Amplitude of the stochastic forcing: (*a*) $A = 10^{-7}$, (*b*) $A = 10^{-5}$, (*c*) $A = 3 \times 10^{-5}$, (*d*) $A = 10^{-4}$. Contours of streamwise perturbation velocity, $t = 2000$, $Re = 580$. The axes are not to scale.

finds the expressions

$$\nabla_{\mathbf{C}} G^2_{opt} = \mathbf{U}^\dagger, \qquad \nabla_{\mathbf{U}_c} G^2_{opt} = P^\dagger \mathbf{n} + Re^{-1} \nabla \mathbf{U}^\dagger \mathbf{n}, \tag{2.9}$$

where the adjoint base flow $\mathbf{Q}^\dagger = (\mathbf{U}^\dagger, P^\dagger)^T$ is the solution of the linear, non-homogeneous system of equations

$$\nabla \cdot \mathbf{U}^\dagger = 0, \quad -\mathbf{U}_b \cdot \nabla \mathbf{U}^\dagger + \mathbf{U}^\dagger \cdot \nabla \mathbf{U}_b^T - \nabla P^\dagger - Re^{-1} \nabla^2 \mathbf{U}^\dagger = \nabla_{\mathbf{U}} G^2_{opt} \quad \text{in } \Omega,$$
$$\mathbf{U}^\dagger = \mathbf{0} \quad \text{on } \Gamma_w, \tag{2.10}$$

and $\nabla_{\mathbf{U}} G^2_{opt} = 2 G^2_{opt} \text{Re}(-\mathbf{f}_{opt} \cdot \nabla \mathbf{u}_{opt}^H + \mathbf{u}_{opt}^* \cdot \nabla \mathbf{f}_{opt})$ is the sensitivity to base flow modification, when the forcing is normalized as $\|\mathbf{f}_{opt}\| = 1$. Note that the expression for $\nabla_{\mathbf{U}} G^2_{opt}$ assumes arbitrary base flow variation. As mentioned by Brandt *et al.* (2011), it is possible to restrict this sensitivity field to divergence-free base flow modifications by solving a subsequent Poisson equation.

For each frequency ω of interest, the optimal forcing and response are computed according to the method described in section 3.2, and the sensitivity to base flow modification $\nabla_{\mathbf{U}} G^2_{opt}$ is calculated. Then, the sensitivities to control are obtained as follows: first, the variational formulation of (4.10) is discretized and solved using *FreeFem++* (with the same mesh and elements as for base flow calculation); second, sensitivities (2.9) are evaluated. The boundary conditions used to compute the adjoint base flow are $\mathbf{U}^\dagger = \mathbf{0}$ at the inlet and on the wall, $\partial_y U^\dagger = V^\dagger = 0$ at the top border, and $P^\dagger \mathbf{n} + Re^{-1} \nabla \mathbf{U}^\dagger \mathbf{n} + \mathbf{U}^\dagger (\mathbf{U}_b \cdot \mathbf{n}) = \mathbf{0}$ at the outlet.

Figure 2.10 displays the streamwise component of the sensitivity of G^2_{opt} to base flow modification, denoted as $\nabla_U G^2_{opt} = \nabla_{\mathbf{U}} G^2_{opt} \cdot \mathbf{e}_x$, at $Re = 580$. It shows where a modification of the base flow $\boldsymbol{\delta}\mathbf{U} = (\delta U, 0)^T$ has the largest effect on the optimal gain at each frequency, and if G_{opt} would increase or decrease, according to $\delta G^2_{opt} = (\nabla_{\mathbf{U}} G^2_{opt} | \boldsymbol{\delta}\mathbf{U})$. Two elongated regions of large sensitivity are located in the shear layer and move upstream with ω: a region of negative sensitivity along the separatrix, and a region of positive sensitivity just above. The interior of the recirculation region is sensitive too at intermediate (i.e. most amplified) frequencies, with structures reminiscent of the optimal response (figure 2.4(*b*)).

Figure 2.11(*a*) shows the streamwise component of the sensitivity of G^2_{opt} to volume control, denoted as $\nabla_{C_x} G^2_{opt} = \nabla_{\mathbf{C}} G^2_{opt} \cdot \mathbf{e}_x$, at $Re = 580$. The optimal gain is the most sensitive to control in the shear layer. However, several observations make difficult the design of an efficient and robust open-loop control based on steady volume control. First, the location of largest sensitivity (in absolute value) depends on ω: it is close to the reattachment point at lower frequencies, and moves upstream as frequency increases. Thus, control applied at the location of maximal sensitivity at one frequency will not be optimal at other frequencies. Second, the sign of the sensitivity depends on space: thin regions of opposite sign are located close to
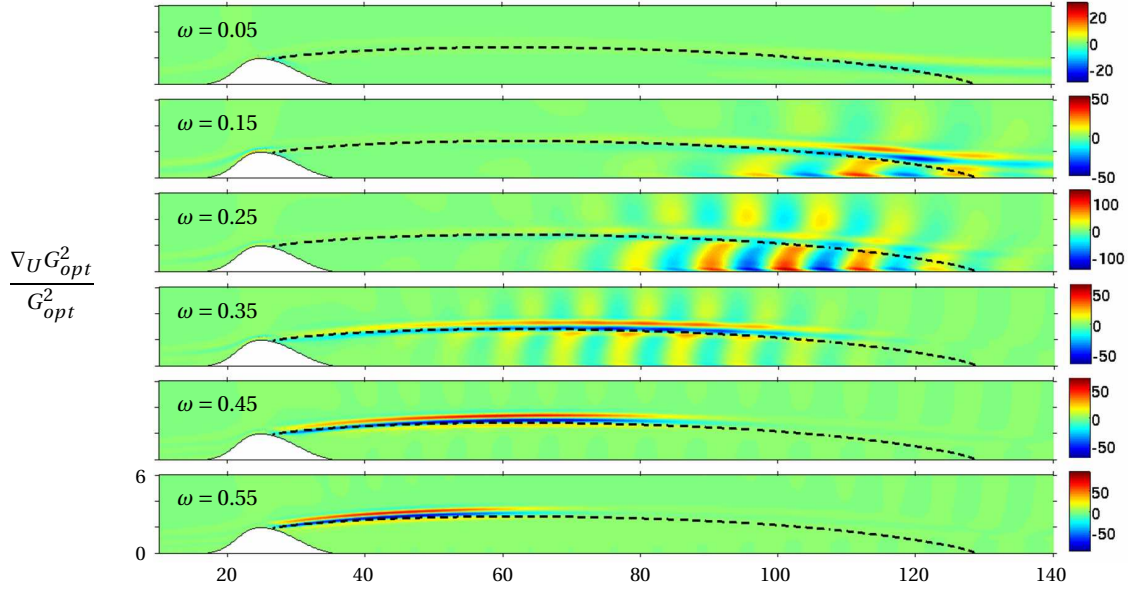
Figure 2.10 – Normalized sensitivity of optimal gain to base flow modification in the streamwise direction, $\nabla_U G_{opt}^2 / G_{opt}^2$, at $Re = 580$ and frequencies $\omega = 0.05, 0.15, \ldots 0.55$. The vertical dashed line is the base flow separatrix. The axes are not to scale.

each other (e.g. vertically in the shear layer and, for intermediate ω, horizontally in the recirculation region). Slightly misplacing a force intended to reduce the optimal gain might actually increase it. Third, in some locations the sign of the sensitivity is varying with frequency. Therefore, without choosing its location carefully, a control might reduce the optimal gain at some frequencies and increase it at others. Despite these limitations, one can focus on most amplified frequencies and find a location where volume control reduces the optimal gain at these frequencies. At $(x, y) = (75, 3.5)$ for instance (black circles in figure 2.11(a)), the sensitivity $\nabla_{C_x} G_{opt}^2$ is positive for $0.15 \leq \omega \leq 0.45$, and small for frequencies outside this range. A force at this location and oriented along $-\mathbf{e}_x$ should therefore have an overall reducing effect on noise amplification. We will come back to this control configuration later on.

We now look at the sensitivity of optimal gain to wall control. Figure 2.11(b) shows the normalized sensitivity to wall control $\nabla_{\mathbf{U}_c} G_{opt}^2 / G_{opt}^2$. Arrows show the orientation of positive sensitivity, i.e. wall control in the same direction and orientation as the arrows would increase the optimal gain. The sensitivity is essentially normal to the wall, indicating that normal actuation has a much stronger effect than tangential actuation (more specifically: one to two orders of magnitude). The sensitivity appears to be maximal at the summit of the bump for all frequencies. The maximum point-wise L^2 norm along the wall (inset in figure 2.11(b)) follows with ω the same trend as G_{opt}, meaning that wall control authority is larger at frequencies which are more amplified. In addition, one can observe that $\nabla_{\mathbf{U}_c} G_{opt}^2$ changes sign with ω at some locations (e.g. upstream of the bump, and in the downstream half of the recirculation region); however, at the bump summit it is oriented towards the fluid domain for all frequencies, and therefore wall suction at this location would reduce G_{opt} for all frequencies.
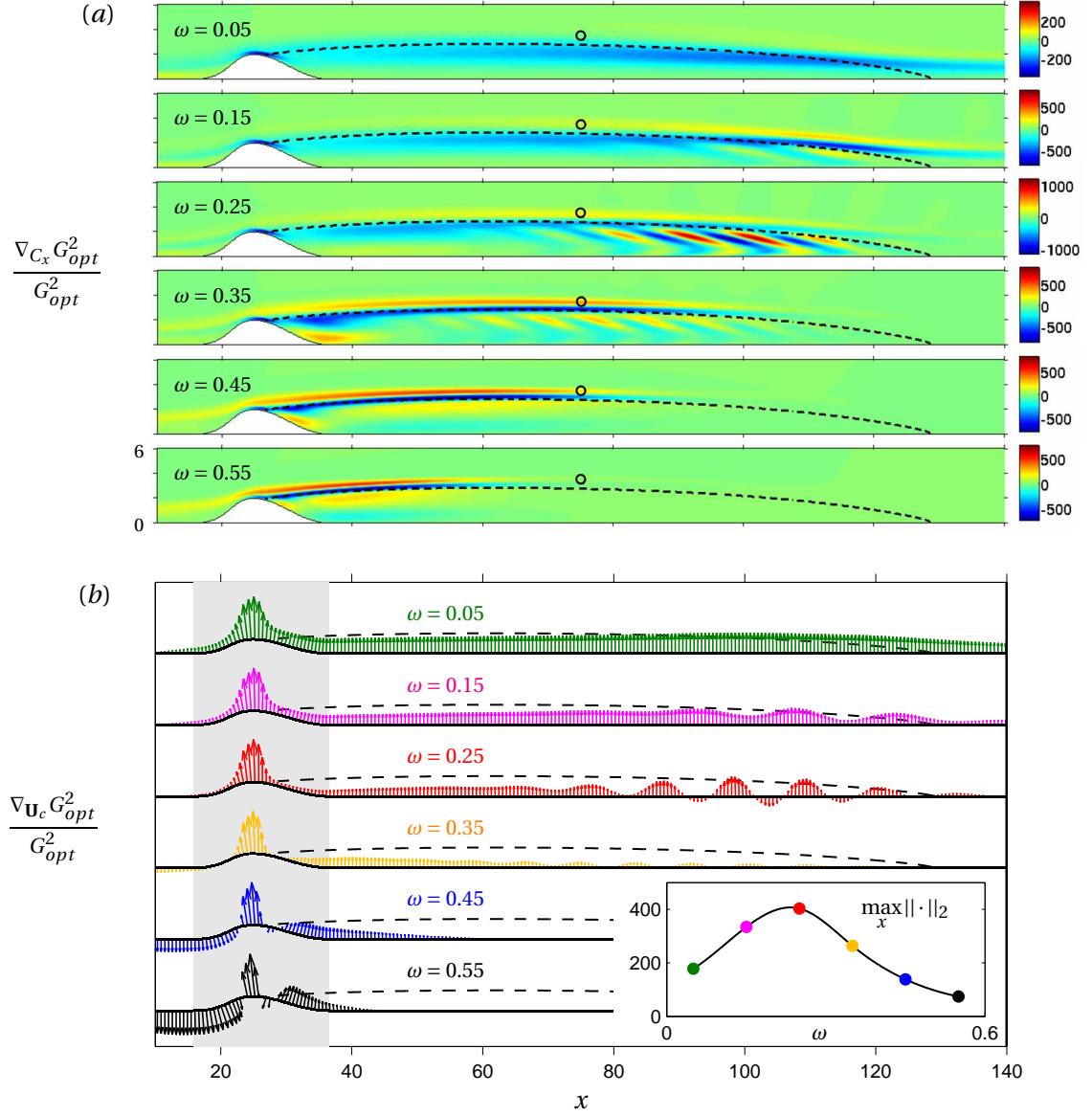
Figure 2.11 – Sensitivity of optimal gain to control at $Re = 580$ and frequencies $\omega = 0.05, 0.15, \ldots 0.55$. (*a*) Normalized streamwise component of the sensitivity to volume control, $\nabla_{C_x} G^2_{opt}/G^2_{opt}$. Black circles indicate the location of volume control $(x, y) = (75, 3.5)$ discussed in the text and in figure 2.12. The axes are not to scale. (*b*) Normalized sensitivity to wall control, $\nabla_{\mathbf{U}_c} G^2_{opt}/G^2_{opt}$, rescaled for each frequency by the largest point-wise L^2 norm on the wall $\max_x ||\nabla_{\mathbf{U}_c} G^2_{opt}/G^2_{opt}||_2$. This maximal value is shown by symbols in the inset (where the solid line is an indicative fit through the data). The grey region shows the streamwise extension of the bump. The dashed line is the base flow separatrix.

Figure 2.12 – Variation of the optimal gain at $Re = 580$ when applying at $(x, y) = (75, 3.5)$ a steady volume control of amplitude C_x in the streamwise direction. (a) Prediction from sensitivity analysis (SA, red solid line) and non-linear controlled base flows (NL, blue symbols) at $\omega = 0.25$. The main plot is in logarithmic scale, the inset in linear scale (the sensitivity is a straight line). (b) $G_{opt}(\omega)$ for $C_x = 0$ (thick solid line), $C_x = -0.01$ (thin solid line) and $C_x = -0.02$ (dashed line).

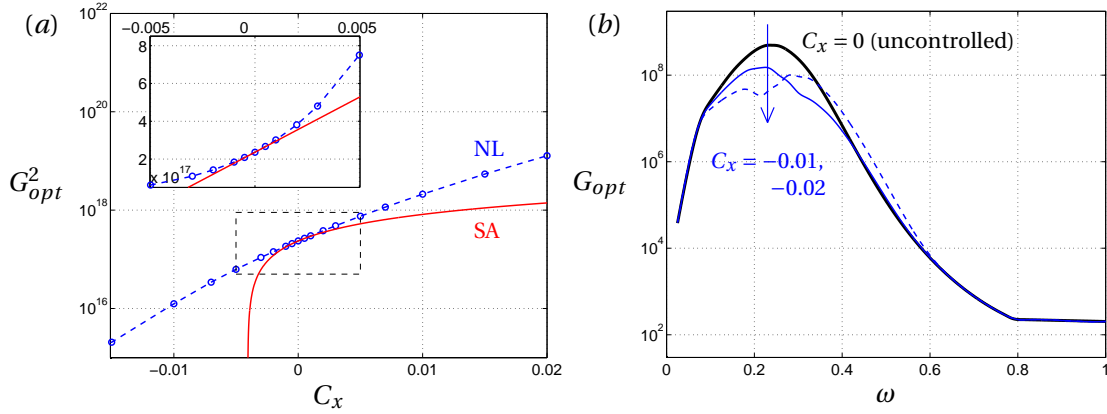The above considerations on the sensitivity to volume control and wall control suggest designing the following open-loop control: no actuation in the domain, $\mathbf{C} = \mathbf{0}$, and vertical wall suction $\mathbf{U}_c = (0, U_c)^T$ at the bump summit $x = x_b$. In the following, the Gaussian profile $U_c(x) = W \exp(-(x - x_b)^2/\sigma_c^2)/(\sigma_c\sqrt{\pi})$, with 2D flow rate W, will be applied at the wall $(x, y_b(x))$.

In order to validate the sensitivity calculations, comparisons were made for several volume and wall control configurations. We present results for two particular configurations in figures 2.12 and 2.13. First, figure 2.12(a) shows the variation of the optimal gain at $\omega = 0.25$ when a steady volume force in the streamwise direction $\mathbf{C} = (C_x, 0)^T$ is applied in the flow at $(x, y) = (75, 3.5)$. Predictions from linear sensitivity analysis (with $\delta G_{opt}^2 = (\nabla_{\mathbf{C}} G_{opt}^2 | \boldsymbol{\delta}\mathbf{C})$) are compared to calculations of G_{opt} on non-linear controlled base flows. The agreement is excellent for the slope, with the sensitivity prediction (solid line) tangent to the curve for actual base flows (dashed line) at zero-amplitude control. However, strong non-linear effects are at hand, with the difference between the two curves quickly growing with $|C_x|$. Figure 2.12(b) shows the actual optimal gain for different control amplitudes. At $C_x = -0.01$, the optimal gain is reduced for frequencies $0.1 < \omega < 0.4$. At $C_x = -0.02$ (dashed line), further reduction is obtained for $0.1 < \omega < 0.25$ but not for higher frequencies as strong non-linear effects come into play; compared to the uncontrolled case, an increase of G_{opt} is observed for $\omega \geq 0.35$. Note that the effect of a small control cylinder placed in the flow as in the experiment of Strykowski & Sreenivasan (1990) can be modelled by a volume force of opposite direction and same amplitude as the drag force felt by the control cylinder (Hill, 1992; Marquet *et al.*, 2008; Meliga *et al.*, 2010). Here, at $(x, y) = (75, 3.5)$, the flow is in the streamwise direction (1% of cross-stream velocity), and given the velocity magnitude, a volume control of $C_x = -0.01$ would correspond to a control cylinder diameter $d = 0.007$.
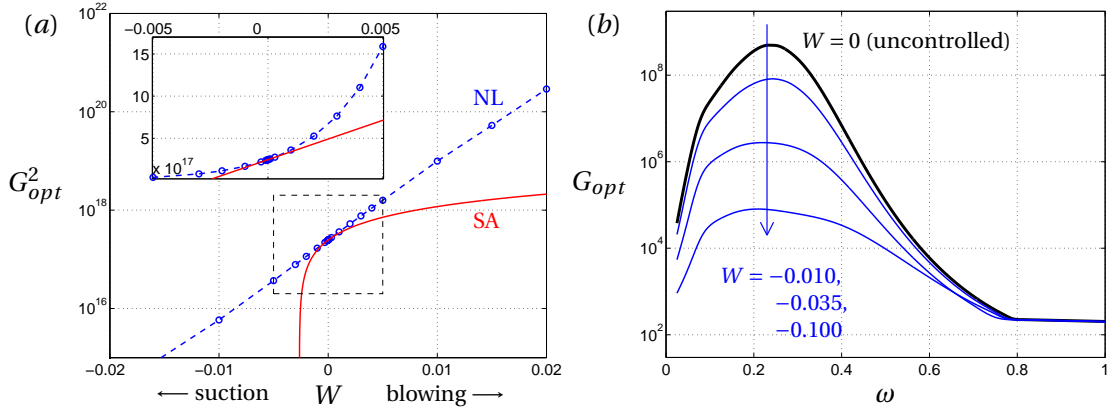
Figure 2.13 – Variation of the optimal gain at $Re = 580$ when applying vertical wall blowing/-suction at the bump summit. (a) Prediction from sensitivity analysis (SA, red solid line) and non-linear controlled base flows (NL, blue symbols). The main plot is in logarithmic scale and shows that G_{opt}^2 varies exponentially with flow rate. In linear scale (inset), the sensitivity is a straight line. (b) Reduction of $G_{opt}(\omega)$ with flow rates $W = -0.010$, -0.035, -0.100.

Figure 2.13(a) shows the variation of the optimal gain at $\omega = 0.25$ when vertical wall actuation (blowing/suction) is applied at the bump summit. Predictions from linear sensitivity analysis (with $\delta G_{opt}^2 = \langle \nabla_{\mathbf{U}_c} G_{opt}^2 | \boldsymbol{\delta}\mathbf{U}_c \rangle$) are compared to calculations of G_{opt} on non-linear controlled base flows (with wall blowing/suction actually modelled as a boundary condition). It appears that G_{opt} varies exponentially with W (straight line in logarithmic scale). Again, the agreement is very good, and non-linear effects strong. Therefore, sensitivity analysis proves useful in identifying sensitive regions to design efficient control configurations, but the final quantitative control performance can only be assessed with non-linear simulations or experiments. Figure 2.13(b) shows the actual optimal gain for different suction flow rates, and confirms the efficiency of this control strategy: reasonably small control flow rates achieve a dramatic reduction of G_{opt} for all frequencies, thereby potentially increasing the level of noise the flow can withstand without being destabilized.

4.2 Reduction of non-linear noise amplification

The behavior of the controlled flow is assessed by DNS at $Re = 580$. The same series of simulations as in section 3.3 is performed, now with the steady open-loop control designed in section 4.1, with flow rate $W = -0.035$. Figure 2.14 compares the actual harmonic gain in the uncontrolled and controlled flows, with the forcing structure given by (2.8). It shows that the control achieves a significant reduction of about 200 to 300 for the most dangerous frequencies, which are now only amplified by a factor 10^3 instead of 10^5.

Results for harmonic and stochastic forcing are summarized in figure 2.15, which represents the standard deviation of $E_p(t)$ after the transient regime and gives an indication of how much the energy of the perturbations fluctuates. Typically, amplitudes larger by a factor 100 are needed to reach the same level of energy fluctuations. This is consistent with gain
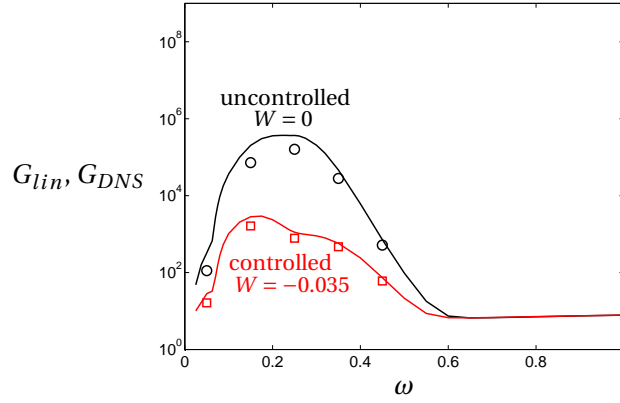
Figure 2.14 – Effect of wall suction on harmonic response. Upper line and symbols (reported from figure 2.7) show the actual gain in the uncontrolled case; lower line and symbols are for wall suction at the bump summit with flow rate $W = -0.035$. Solid lines: linear results G_{lin}; symbols: G_{DNS} from DNS calculations with small-amplitude harmonic forcing.
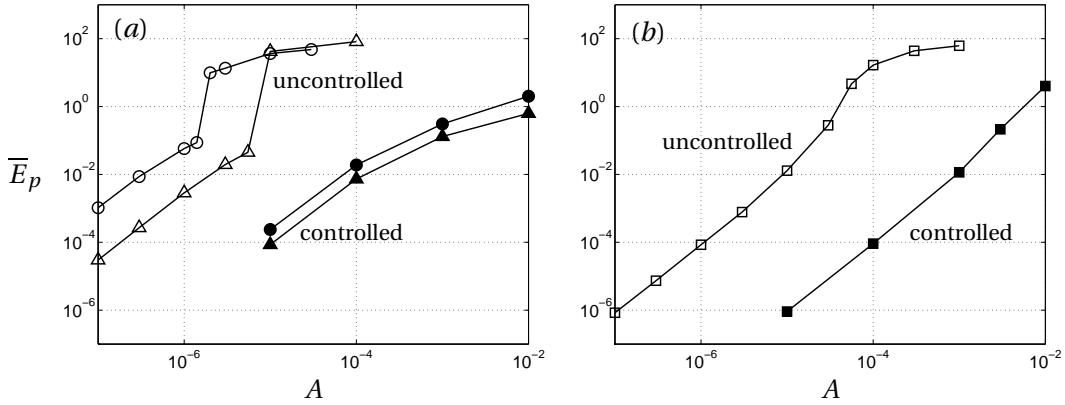
Figure 2.15 – Mean asymptotic energy of the perturbations vs. forcing amplitude, at $Re = 580$. Open symbols: without control; Filled symbols: with vertical wall suction at the bump summit (flow rate $W = -0.035$). (a) Harmonic forcing at $\omega = 0.25$ (circles) and $\omega = 0.35$ (triangles); (b) stochastic forcing.
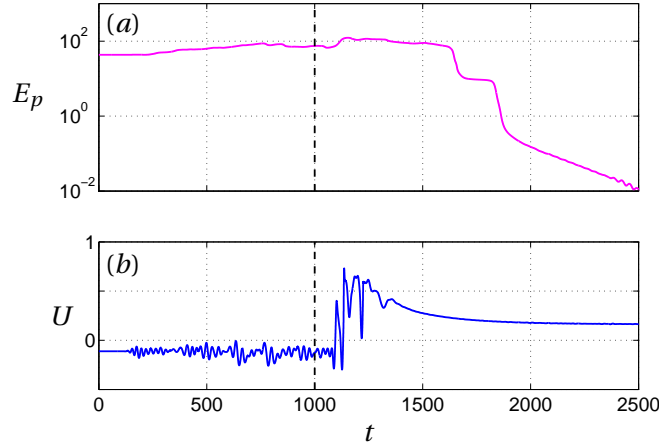
Figure 2.16 – Flow restabilization at $Re = 580$ in direct numerical simulations with steady vertical wall suction at the bump summit (flow rate $W = -0.035$). (*a*) Energy of the perturbations (calculated with the final steady-state as reference base flow). (*b*) Streamwise velocity of the total flow at $(x, y) = (80, 1)$. The subcritical flow, stationary for $t < 0$, is perturbed from $t = 0$ with stochastic forcing of amplitude $A = 3 \times 10^{-4}$, and control is turned on at $t = 1000$.

reductions of about 200 to 300 observed for the optimal gain in figure 2.13(*b*) and, as mentioned above, for the actual gain in figure 2.14. The conclusion is the same for harmonic and stochastic forcing: control reduces noise amplification dramatically. The controlled flow can withstand much higher levels of noise than the uncontrolled one before being destabilized.

As an illustration, figure 2.16 shows the result of a DNS where the flow is forced with stochastic noise of amplitude $A = 3 \times 10^{-4}$, large enough to destabilize the flow. Control with flow rate $W = -0.035$ is turned on at $t = 1000$. The flow is restabilized and becomes stationary. This new steady-state (different from the steady-state at the same Reynolds number without forcing nor control) is used as the reference base flow for the calculation of E_p, which quickly drops to zero after control is turned on. The streamwise velocity signal measured at $(x, y) = (80, 1)$ changes from negative to positive, showing that there is no backflow any more at this location and indicating that wall suction shortens the recirculation region.

5 Flow stabilization

We turn our attention to the supercritical regime. Unlike in the subcritical regime, it is not possible to assess the performance of any control in terms of its effect on optimal gain since the flow is unstable and the notion of asymptotic harmonic response is irrelevant. The natural tool to be used is global linear stability analysis. With a global mode decomposition for perturbations $\mathbf{q}'(x, y, t) = \mathbf{q}(x, y)e^{\sigma t}$, the linearized Navier–Stokes equations (2.3) without forcing yield the eigenvalue problem

$$\nabla \cdot \mathbf{u} = 0, \quad \sigma\mathbf{u} + \mathbf{U}_b \cdot \nabla\mathbf{u} + \mathbf{u} \cdot \nabla\mathbf{U}_b + \nabla p - Re^{-1}\nabla^2\mathbf{u} = \mathbf{0}, \tag{2.11}$$
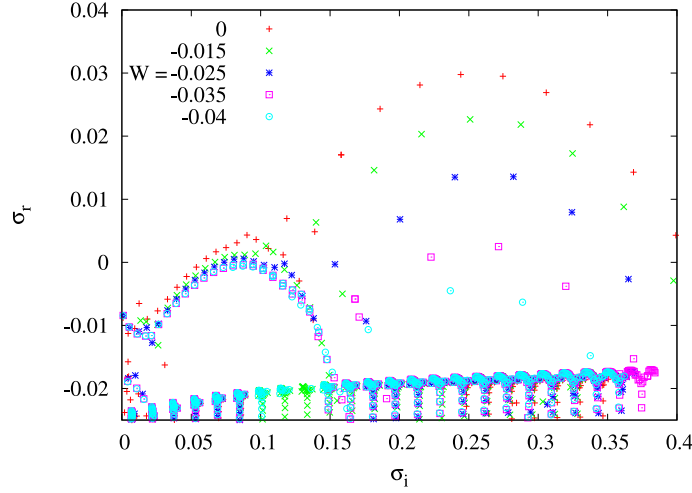
Figure 2.17 – Global linear eigenspectrum at $Re = 620$ of the uncontrolled flow and of the flow controlled with vertical wall suction at the bump summit with flow rate $W = -0.015$, -0.025, -0.035, -0.040.

where complex eigenvalues $\sigma = \sigma_r + i\sigma_i$ of positive (resp. negative) real part correspond to unstable (resp. stable) eigenmodes **q**. The aim of the control is now to reduce the growth rate σ_r of unstable modes.

The eigenvalue problem (2.11) is discretized as $(\sigma\mathbf{B} + \mathbf{L})\mathbf{q} = \mathbf{0}$, where $\mathbf{L} = \mathbf{L}(\mathbf{U})$ is the Jacobian matrix, and solved at $Re = 620$ with the method described in Ehrenstein & Gallaire (2008). Linearization is first performed around the uncontrolled base flow, then around a series of base flows controlled by vertical wall suction at the bump summit with increasing flow rates. In the uncontrolled case, the flow is globally unstable: we recover the eigenspectrum of Ehrenstein & Gallaire (2008) shown in figure 2.17 and characterized by two distinct branches of eigenvalues. The most unstable branch corresponds to a family of global modes of similar spatial structure localized around the reattachment point and associated with a Kelvin-Helmholtz instability of the shear layer. The other branch corresponds to weakly unstable convective modes, typical of Tollmien-Schlichting instability in boundary layers. As the control amplitude is increased, both branches become less unstable, until all modes are fully restabilized for $W \simeq -0.040$. Eigenvalues which are stable in the uncontrolled case are not destabilized by the control. Therefore the control strategy designed in section 4.1 has a direct and selective effect on unstable eigenvalues, efficiently moving them to the stable half-plane without destabilizing other eigenvalues. This trend could be expected because the main effect of normal wall suction is to shorten the recirculation region and reduce the strength of the shear layer, thus mitigating shear instabilities. Since noise amplification in the subcritical regime and unstable global eigenmodes in the supercritical regime are different manifestations of the same type of mechanisms (Orr, Tollmien-Schlichting, and more importantly Kelvin-Helmholtz as already mentioned in section 3.2), it seems reasonable that a well-chosen control can have a stabilizing effect on both.
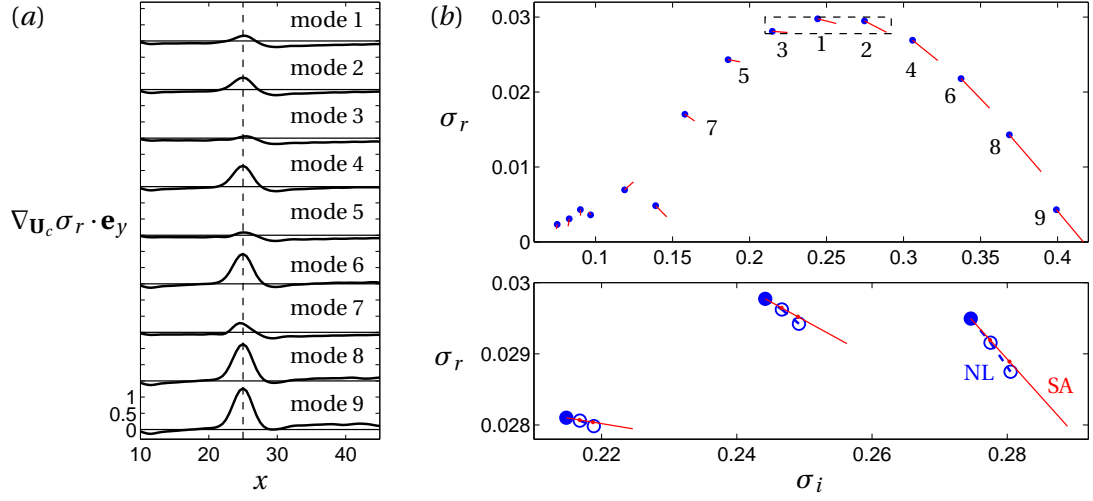
Figure 2.18 – Sensitivity analysis of the most unstable eigenvalues at $Re = 620$. (a) Sensitivity of the growth rate of modes 1 to 9 (Kelvin-Helmholtz branch) to vertical wall control. The dashed line shows the bump summit location. (b) Effect of vertical wall control at the bump summit, as predicted by sensitivity analysis. Red solid lines indicate a flow rate $W = -0.005$. The lower panel is a close-up view of eigenvalues 1 to 3, comparing sensitivity analysis (SA, red solid lines) and linear stability analysis results for non-linear base flows controlled with $W = -0.001$ and -0.002 (NL, blue circles).

More insight can be gained using a systematic sensitivity analysis to investigate the effect of steady wall control on most unstable eigenvalues. Similar to section 4.1 for the optimal gain, the variation of a given eigenvalue σ resulting from a small wall actuation $\boldsymbol{\delta U}_c$ is written as $\delta\sigma = \langle \nabla_{\mathbf{U}_c}\sigma | \boldsymbol{\delta U}_c \rangle$. Here a discrete method is employed to compute the sensitivity $\nabla_{\mathbf{U}_c}\sigma$. The above eigenvalue shift is equivalent to $\delta\sigma = (\nabla_{\mathbf{U}}\sigma | \boldsymbol{\delta U})$, where the base flow modification $\boldsymbol{\delta U}$ caused by wall actuation is solution of the linear system $\mathbf{L}\boldsymbol{\delta U} = \boldsymbol{\delta U}_c$, solved for each wall location, while the sensitivity $\nabla_{\mathbf{U}}\sigma$ is computed once only as $(\nabla_{\mathbf{U}}\mathbf{L}\mathbf{q})^H \mathbf{q}\dagger$, with $\mathbf{q}\dagger$ the adjoint mode associated with the global mode $\mathbf{q}$.

Figure 2.18(a) shows results for the most unstable eigenmodes of the Kelvin-Helmholtz branch. At the bump summit ($x = 25$) the sensitivity of their growth rate to vertical actuation along $\mathbf{e}_y$ is positive, therefore vertical wall suction has a stabilizing effect on all these modes. Any other control configuration would be less effective. For instance, vertical wall blowing at $x = 30$ would be slightly more effective in stabilizing modes 3 and 5, but would require more control amplitude, and might also destabilize mode 9. Figure 2.18(b) shows that convective eigenmodes ($\sigma_i \leq 0.15$) are weakly sensitive. Global eigenvalues calculated from non-linear base flows controlled at the bump summit with small-amplitude vertical suction ($W = -0.001$ and -0.002) closely follow prediction from sensitivity analysis, as illustrated in the close-up view.

Finally, direct numerical simulations were performed at several supercritical Reynolds numbers. Since the flow is naturally unstable, no forcing was added, and self-sustained oscillations characterized by low-frequency, large-scale vortex shedding developed (Marquillie &
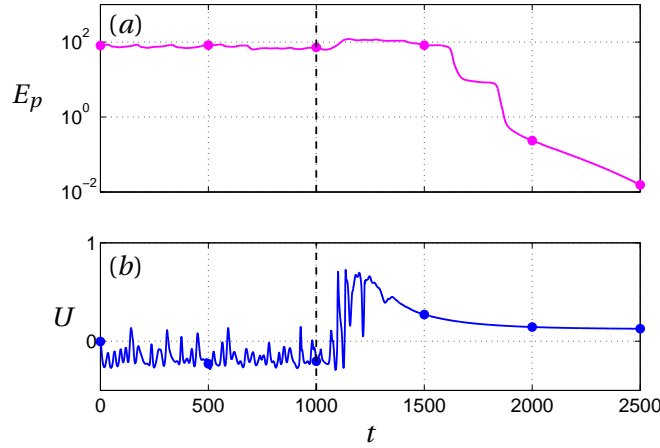
Figure 2.19 – Flow restabilization at $Re = 620$ in direct numerical simulations with steady vertical wall suction at the bump summit (flow rate $W = -0.035$). Same notations as figure 2.16. The supercritical flow is naturally unsteady, no perturbation is added, and control is turned on at $t = 1000$. Dots correspond to the times of snapshots in figure 2.20.

Ehrenstein, 2003). Steady vertical wall suction at the summit was turned on at $t = 1000$. Figure 2.19 illustrates how the flow was fully restabilized at $Re = 620$ with control amplitude of $W = -0.035$. (The eigenspectra of figure 2.17 suggest that the flow is still unstable with this flow rate. This is due to the different domain size and numerical methods used in the linear stability analysis and in the DNS.) As in the subcritical case, the streamwise velocity measured at $(x, y) = (80, 1)$ is largely fluctuating in the uncontrolled regime, but quickly reaches a steady value once control is turned on. It changes from negative without control to positive with control, because wall suction shortens the recirculation region. The energy of the perturbations (with the final steady-state taken as reference base flow) quickly decreases to zero as the flow is stabilized and perturbations are advected downstream. Snapshots of the vorticity field in figure 2.20 clearly depicts how large-scale perturbations are advected while the control efficiently prevents the formation of new structures and finally drives the flow to a perfectly steady state.

Other direct numerical simulations at $Re = 620$, which is only slightly supercritical, yielded stable flows with a control amplitude as low as $W = -0.010$, while with $W = -0.035$ the flow could be restabilized for $Re \geq 700$. We did not attempt to determine accurate threshold values of restabilizing control amplitudes $W_c(Re)$.

6   Conclusions

The maximal possible linear amplification of harmonic forcing was computed at several frequencies in the globally stable 2D separated boundary layer past a wall-mounted bump. Very large values of the linear optimal gain confirmed the strong non-normal character of this flow, which had already been evidenced by large transient growth in previous studies (Ehrenstein
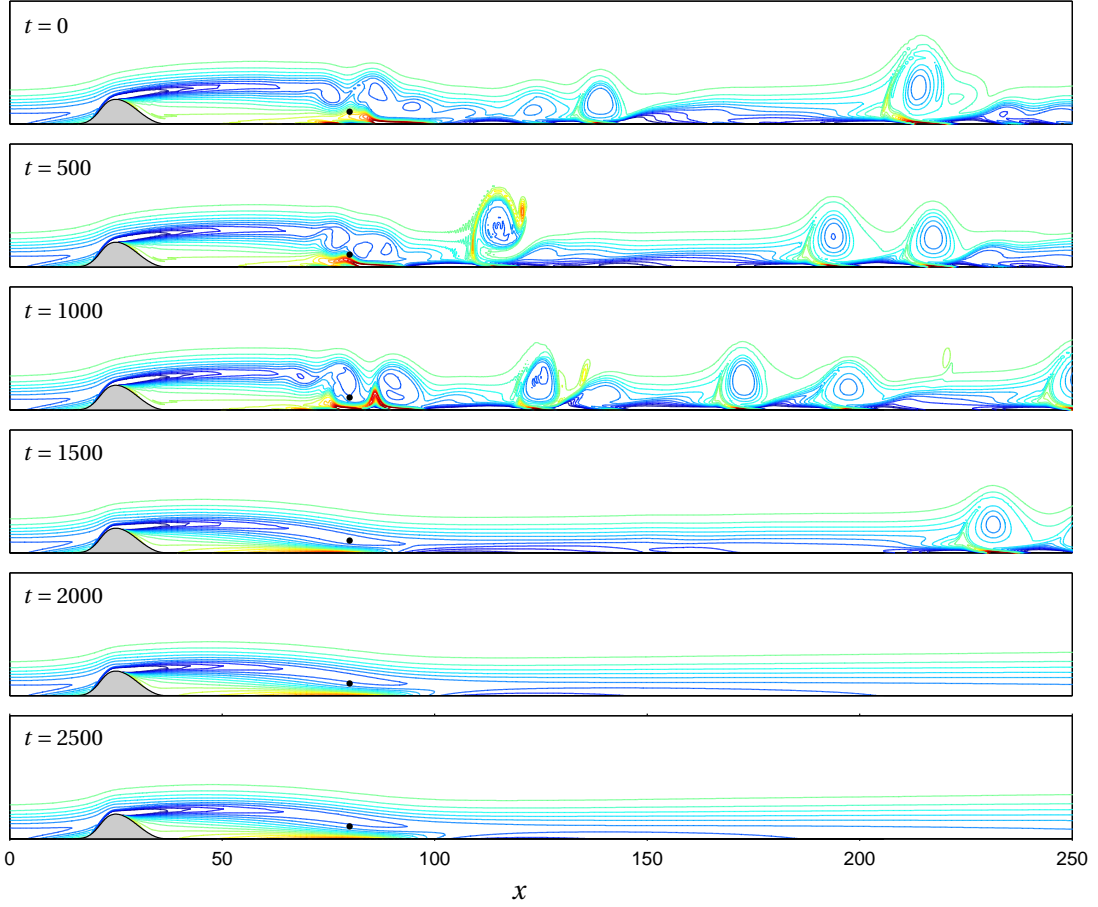
Figure 2.20 – Flow restabilization in the supercritical regime, $Re = 620$, in DNS with steady vertical wall suction at the bump summit (flow rate $W = -0.035$): contours of vorticity of the total flow at $t = 0, 500, 1000... 2500$. The black dot shows the location of the point $(x, y) = (80, 1)$ where the velocity signal of figure 2.19 is recorded. The axes are not to scale.

& Gallaire, 2008; Ehrenstein *et al.*, 2011). DNS confirmed that a small-amplitude noise, harmonic or stochastic in time, could lead to a subcritical bifurcation by destabilizing the flow and triggering random unsteadiness.

Using sensitivity analysis, regions where steady control has a desirable reducing effect on optimal gains were identified. A simple open-loop control inspired by this analysis successfully reduced linear asymptotic response to harmonic forcing at all frequencies. DNS revealed that this control efficiently dampened noise amplification in the non-linear regime too, which demonstrates that linear analysis captures the essential mechanisms involved in non-modal growth, and is able to delay bypass transition in such separated open flows.

The success of the present sensitivity-based control method is encouraging. While being based on physical grounds, it keeps the final design both simple and efficient. The control strategy, optimally designed in the subcritical regime, is able not only to dampen noise amplification and delay bypass transition in the subcritical regime, but also to restabilize the

unstable flow in the supercritical regime.

We plan to pursue this study further. First, an ongoing experiment will tell whether this control strategy is robust to 3D effects, and to noise with realistic time and space distributions. Second, it would be useful to circumvent the need to repeat sensitivity analysis at each frequency of interest; this will require finding a suitable surrogate for optimal gain.

Acknowledgements

2.2 Experimental study

In section 2.1, the optimal location for wall actuation was determined based on a linear sensitivity analysis targeting the harmonic gain response below instability threshold ($Re \simeq 600$). This design was also found efficient above threshold, using a linear eigenvalue sensitivity analysis. Nonlinear direct numerical simulations demonstrated the effectiveness of the chosen control scheme in restabilizing the flow.

This section aims at confirming these results experimentally, by demonstrating the stabilizing action of a well-chosen actuation region, namely the summit of the bump. Two experimental campaigns, respectively in air and water, are reported. The first campaign took place in 2010 at LFMI (EPFL). Wind-tunnel measurements of the length of the recirculation region evidenced transition to unsteadiness at low Reynolds number, possibly induced by large noise amplification, and in agreement with previous numerical and experimental studies (Marquillie & Ehrenstein, 2003; Passaggia *et al.*, 2012). The second campaign was made possible in 2013 by a collaboration with IRPHÉ (Aix-Marseille Université, Centrale Marseille, CNRS). Measurements in a water channel confirmed the effectiveness of the simple open-loop control proposed in 2.1 based on sensitivity analysis. To this end, suction was applied through a porous medium. It should be mentioned that such experiments are extremely challenging, not only because of the three-dimensional nature of any real flow, but also because of the strong amplification potential below threshold, together with a complex global stability behaviour above threshold.

2.2.1 Recirculation length transition

The experimental facility used in the first campaign is a vertical closed-circuit, low-speed wind-tunnel with low turbulent intensity $\simeq 0.3$ %. It has also been used to study, among others, streaks instability in a laminar boundary layer (Rüedi, 2002). The closed test-section is 120 mm high, 760 mm wide and 3290 mm long (figure 2.21). Its roof has an adjustable slope, which allows to control the longitudinal pressure gradient and the boundary layer development. A rounded-leading-edge aluminium flat plate of thickness 6 mm, width 700 mm and length 2770 mm is mounted in the test section to produce a laminar boundary layer, together with a bump of height $h = 6$ mm, its summit being fixed at $x_b = 675$ mm from the leading edge. It is invariant in the spanwise direction, and its profile $y_b(x)$ is the same as in Bernard *et al.* (2003) and following numerical studies (Marquillie & Ehrenstein, 2002, 2003; Ehrenstein & Gallaire, 2005, 2008). The surfaces of the plate and the bump are made black by anodizing so as to reduce laser reflections. A Pitot tube (MKS 698A + MKS 270) mounted on a side wall upstream of the bump measures the dynamic pressure $\Delta P = \rho U_\infty^2 / 2$, from which are deduced the free-stream velocity U_∞ and the Reynolds number $Re_{h/2} = U_\infty h / 2\nu$ based on the bump (half) height. Lengths have been chosen so as to yield $Re_{\delta^*} = Re_{h/2} = 600$ when $U_\infty = 3$ m/s, whereas in 2.1 and previous studies, $Re_{\delta^*} = U_\infty \delta^* / \nu$ is the Reynolds number based on the boundary layer displacement thickness at the upstream location $x = x_b - 25\delta^*$.
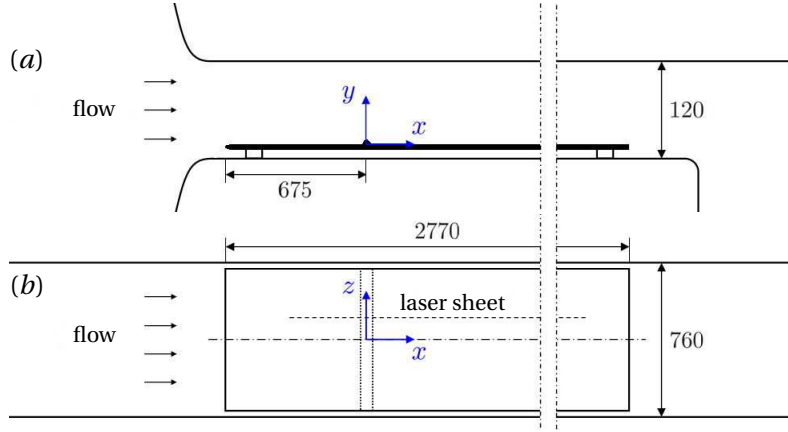
Figure 2.21 – Experimental set-up: (*a*) side view and (*b*) top view (units: mm). For clarity, vertical dimensions (along *y*) are stretched by a factor 4.
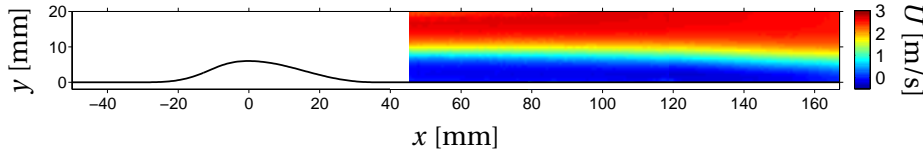
Figure 2.22 – Mean velocity fields obtained by PIV at $Re_{h/2} = 450$ (from two fields of view $46 \leq x \leq 118$ and $79 \leq x \leq 167$), averaging $N = 100$ instantaneous fields. Streamwise velocity $U \in [-0.5, 3.0]$ m/s.

Particle image velocimetry was used to measure the mean length of the recirculation region downstream of the bump. Many other methods exist to determine wall shear stress τ (Naughton & Sheplak, 2002) such as surface fence, wall pulsed wire, oil film interferometry (Fernholz, Janke, Schober, Wagner & Warnack, 1996) or more recent MEMS (Löfdahl & Gad-el Hak, 1999). Stagnation points where $\tau = 0$ can also be deduced by direct visualization, but in the present case surface oil flow visualization (Lu, 2010) and tuft visualization were difficult because of the low speed. An already available PIV system (Vonlanthen & Monkewitz, 2013) was a practical, easy-to-calibrate and non-intrusive alternative technique. The flow is seeded with diethyl hexyl sebacate (DEHS) particles of mean diameter 1.6 μm. A pulsed Nd-YAG laser of wavelength 532 nm (Quantel Brilliant Twins B) and a set of lenses produce a thin sheet illuminating the flow in a vertical $x - y$ plane in the centre of the test section. Pairs of images are acquired with a 4008 × 2672 px camera (TSI PowerView Plus CCD with Nikkor 105 mm f/1.8 lens) and post-processed with an in-house code (Ursenbacher, 2000) to obtain two-dimensional velocity fields. Figure 2.22 shows the mean flow at $Re_{h/2} = 450$, averaged from 100 instantaneous fields. Then, points of zero streamwise velocity U are interpolated with a law $y(x) = ae^{bx} + ce^{dx}$, whose extrapolation to $y = 0$ gives the location of the stagnation point. Figure 2.23 shows an example of such processing at $Re_{h/2} = 450$.
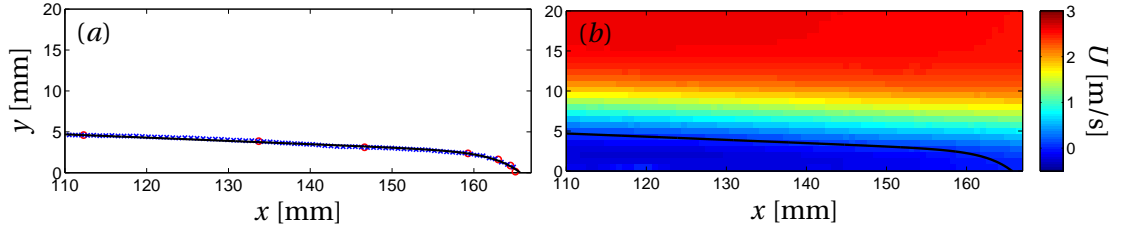
Figure 2.23 – Illustration at $Re_{h/2} = 450$ of the method to compute the recirculation length from the mean flow: (a) points where $U = 0$ in each pixel column (×) and each pixel row (○), and interpolation curve $y(x) = ae^{bx} + ce^{dx}$ from which the reattachment point is determined. (b) same curve reported onto the mean field of figure 2.22.
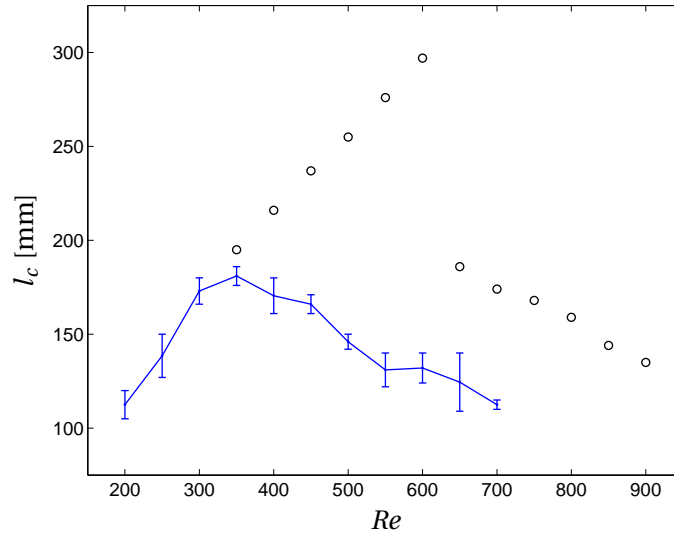
Figure 2.24 – Recirculation length: numerical results versus Re_{δ^*} (○) from Marquillie & Ehrenstein (2003), and experimental measurements versus $Re_{h/2}$ (—).

Figure 2.24 shows the recirculation length l_c as a function of Reynolds number. PIV measurements and numerical results from Marquillie & Ehrenstein (2003) both grow with increasing Reynolds number before they reach a maximum, and then decrease with increasing Re. At lower Reynolds number the flow is steady and the recirculation length is increasing, while after transition the mean recirculation length of the unsteady flow is decreasing, as typically occurs in many separated flows (Sinha *et al.*, 1981; Zielinska *et al.*, 1997). In the present experiment, transition occurs at $Re_{h/2} \simeq 350$, in good agreement with Passaggia *et al.* (2012), and is not as sharp as in numerical simulations. It is worth mentioning that the set-up and Reynolds number in this experiment and in previous studies differ: numerical results are reported for Re_{δ^*} with a constant ratio h/δ^*, while the present measurements are for $Re_{h/2}$ with fixed bump height and location. In order to keep h/δ^* constant as the free-stream velocity increases and the boundary layer displacement thickness decreases, it would be necessary to change the bump size or location as in Passaggia *et al.* (2012).
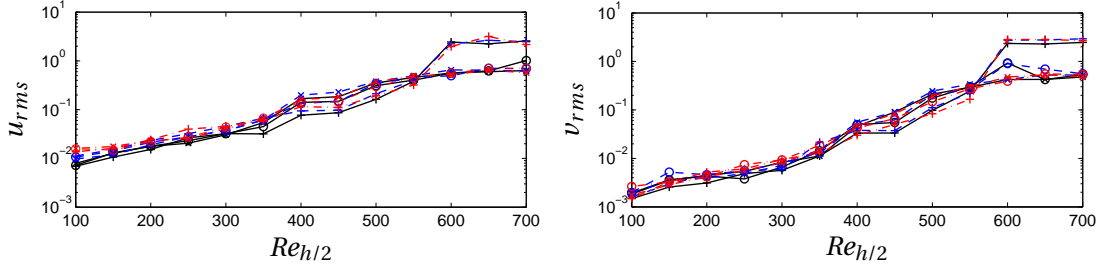
Figure 2.25 – Standard deviation of streamwise and cross-stream velocity fluctuations (from $N = 100$ measurements) versus Reynolds number $Re_{h/2}$, at several points inside and outside the recirculation region: $x = 115$ (+), 135 (○), 155 (×) mm, and $y = 4$ (solid lines), 6 (dashed lines), 8 (dash-dotted lines) mm.

Figure 2.25 shows the standard deviation of velocity fluctuations u_{rms} and v_{rms} at nine points of coordinates $x = 115, 135, 155$ mm, $y = 4, 6, 8$ mm. Their smooth increase with Reynolds number suggests that transition in this flow might be due to noise amplification rather than to an intrinsic instability. However, care is needed since results might be affected by the different set-up (fixed bump position) and by three-dimensional effects observed in particular at the lateral walls.

2.2.2 Open-loop control using wall suction

The second measurement campaign was conducted in a free-surface water channel at IRPHÉ. The set-up and methods are largely similar to those described in Passaggia *et al.* (2012). The test section is 500 mm high, 380 mm wide and 1500 mm long (figure 2.26). An aluminium bump of height $h = 5$ mm was located at the fixed location 500 mm from the sharp leading edge of a 20 mm thick Plexiglas flat plate. A suction mechanism was added to the original set-up (figure 2.27): a slit of width 3 mm and length $L = 243$ mm is opened through the whole height of the bump down to a cavity inside the flat plate (20 mm wide and 11 mm deep), and tubes connects 6 holes in the cavity floor to a gear pump (ISMATEC BVP-Z). The slit in the bump and the cavity in the flat plate are filled with porous material (Porex polyethylene of average pore size 40-100 μm) in order to make the flow homogeneous (in the spanwise direction and inside the slit and the cavity) and to ensure that the flow sees a smooth surface when passing over the slit. The pump adjustable rotation speed has been calibrated against flow rate W. New PIV measurements were performed and processed with the software DPIV-Soft (Meunier & Leweke, 2003) to check the free-stream velocity calibration and to measure the boundary layer thickness $\delta(x) = \gamma\sqrt{\nu x/U_\infty}$, with γ a proportionality factor. With fixed bump height h and location x_b, operating conditions in the plane $(Re_{\delta^*}, h/\delta^*)$ are located along a straight line parametrized by the free-stream velocity, as shown in figure 2.28 and in agreement with the theoretical relation

$$\frac{h}{\delta^*} = \left(\frac{Re_{\delta^*}}{\gamma^2} + 25\right)\frac{h}{x_b}, \tag{2.12}$$
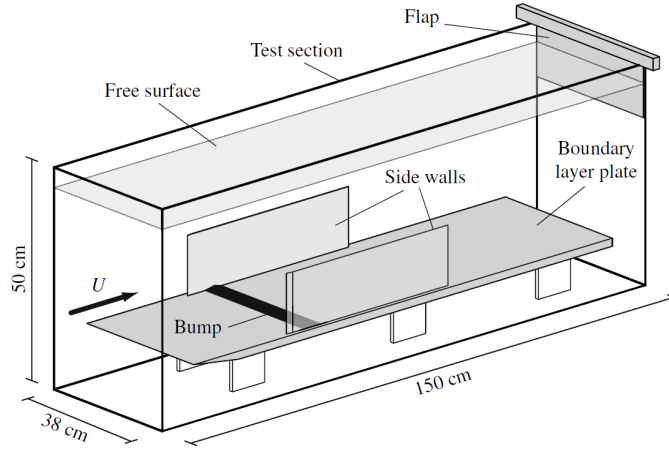
Figure 2.26 – Experimental set-up (from Passaggia *et al.* (2012)).
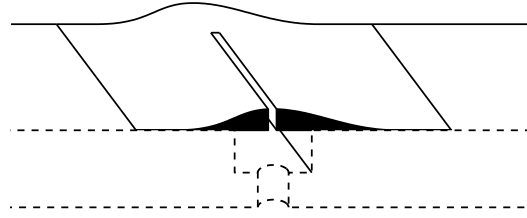
Figure 2.27 – Close-up view (vertical cut) of the bump and its slit above the flat plate, the cavity (filled with porous medium), and one of the holes connected to the pump.

obtained by combining the Reynolds number $Re_{\delta^*} = U_\infty \delta^* / \nu$, the reference displacement thickness $\delta^* = \gamma \sqrt{\nu x^* / U_\infty}$, and the reference location $x^* = x_b - 25\delta^*$ where δ^* is measured. These operating conditions allow us to cover all regimes identified in Passaggia *et al.* (2012): quasi-steady flow at very low Re_{δ^*}, but above all weak transverse instability for $Re_{\delta^*} \lesssim 500$ and low-frequency flapping for larger Re_{δ^*}.

A series of visualizations were performed at different free-stream velocities with and without suction. Fluorescein dye was injected in the recirculation region, and side views of the center plane illuminated with an Argon laser sheet were recorded at 30 fps. Figure 2.29 shows typical images of the uncontrolled flow ($W = 0$). In addition to low-frequency flapping, high-frequency oscillations are also observed at large Re_{δ^*} values (lower snapshots). They appear very regular and might be related to a Kelvin-Helmholtz instability of the shear layer. Note that the separation point moves slightly upstream (consistent with chapter 4). As an alternative view, vertical cuts at fixed x locations are shown in figure 2.30 as $y - t$ spatio-temporal diagrams. They illustrate spatial amplification, with a larger displacement of the shear layer downstream, as well as high-frequency oscillations at large Re_{δ^*}.

More quantitative data was extracted by processing images with two different methods, measuring at different x locations: (i) the height of the separatrix y_{sep} (easily identified since fluorescein is often concentrated in the shear layer and absent outside the recirculation re-
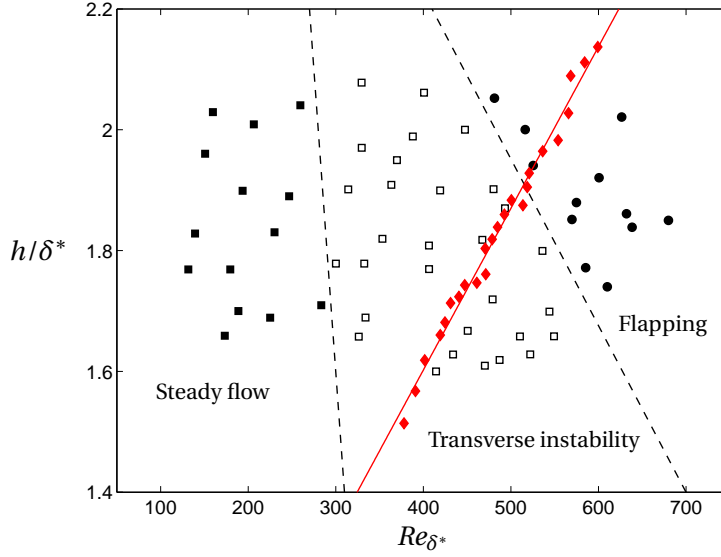
Figure 2.28 – Operating conditions (red solid line and diamonds) in the plane $(Re_{\delta^*}, h/\delta^*)$ with the present set-up (fixed bump position $x_b = 500$ mm from the flat plate leading edge, fixed bump height $h = 5$ mm). Stability diagram (black dashed lines and other symbols) reproduced from Passaggia *et al.* (2012).

gion), and (ii) the total intensity I integrated vertically. Figure 2.31 shows the power spectrum density obtained from the temporal signal $y_{sep}(t)/\delta^*$ measured at $x = x^* + 40\delta^*$. A high-frequency peak is visible at $f h/U_\infty \simeq 0.14$ for $Re_{\delta^*} \geq 500$. Its amplitude increases with Re_{δ^*}, similar to the low-frequency peak at $f \delta^*/U_\infty \lesssim 0.01$ identified in Passaggia *et al.* (2012) (note the different scaling, pointing to different mechanisms).

Figures 2.32 and 2.33 show how the flow at $Re_{\delta^*} = 448$ is modified when control is turned on. The total flow rate varies between $W = 0$ and 1.17 L/min, which corresponds to an equivalent non-dimensional flow rate per unit spanwise length varying between $W/LU_\infty\delta^* = 0$ and 0.21 (of the same order $\simeq 0.1$ as in 2.1). Unsurprisingly, the shear layer is deflected downwards and the separation point moves downstream, resulting in a much smaller recirculation region. The shear layer appears to fluctuate much more at weak suction (second row from top) than other cases.

The spatio-temporal evolution of the controlled flow at $Re_{\delta^*} = 448$ is shown in figure 2.34. Compared to the uncontrolled case (top row), fluctuations visible downstream globally have a smaller amplitude with larger flow rates $W/LU_\infty\delta^* = 0.14$ and 0.21 (two bottom rows). However, the high-frequency instability observed only for $Re_{\delta^*} \lesssim 500$ in the uncontrolled case now appears to be triggered at low suction flow rate (second row). As an explanation, cavity oscillations can be ruled out since: (i) the porous media is carefully flush-mounted in the slit, (ii) typical frequencies for such cavity oscillations are more than one order of magnitude larger (given the dimensions and velocities in the present flow) than those observed here, and (iii) the same oscillations appeared at low W in complementary experiments with suction
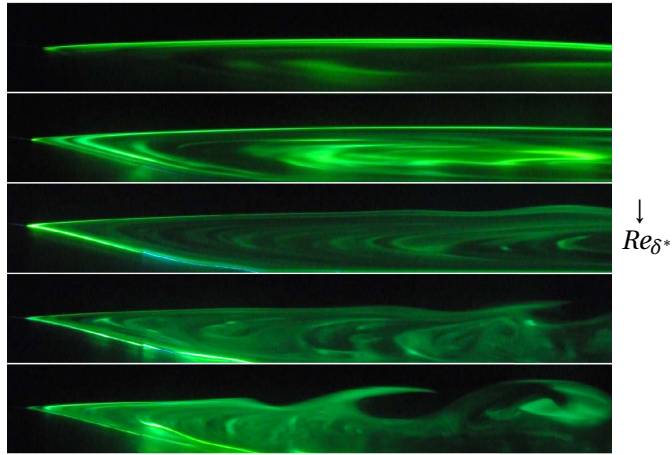
Figure 2.29 – Dye visualization snapshots of the uncontrolled flow at $Re_{\delta^*} = 383, 509, 538, 593, 619$ (top to bottom).
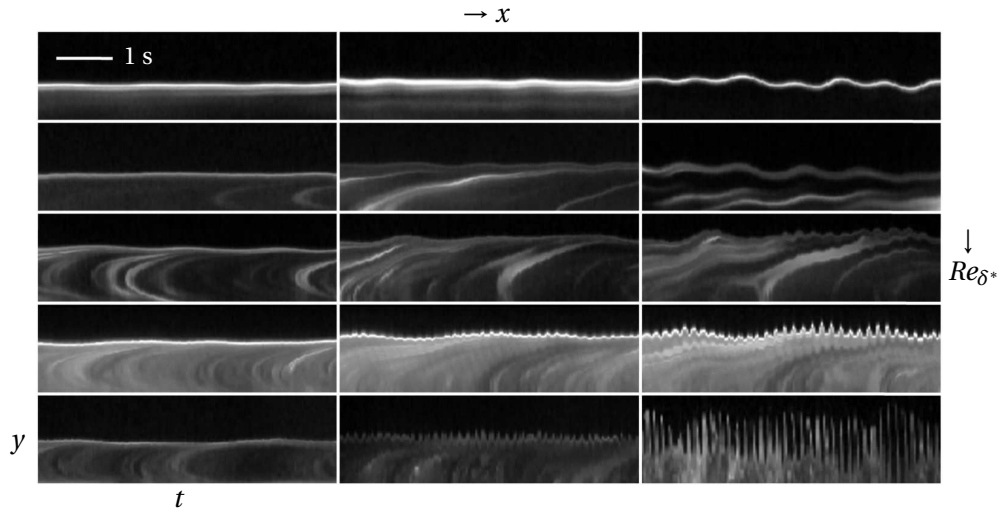
Figure 2.30 – Spatio-temporal $y - t$ diagrams of the uncontrolled flow at $x = x^* + 30\delta^*$, $x^* + 35\delta^*$, $x^* + 40\delta^*$ (left to right), and $Re_{\delta^*} = 383, 448, 509, 566, 619$ (top to bottom).
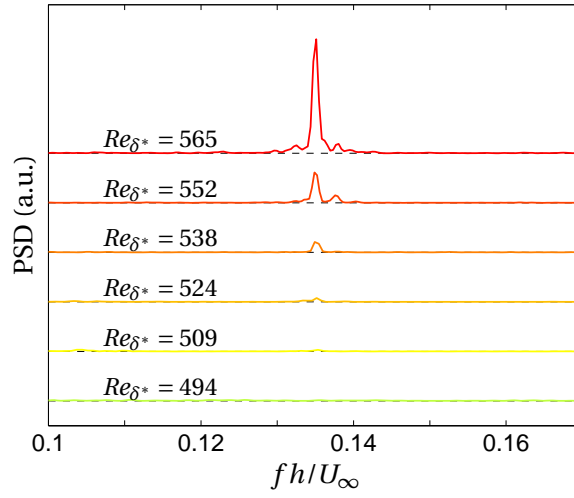
Figure 2.31 – Power density spectra of the shear layer height for the uncontrolled flow at $x = x^* + 40\delta^*$.
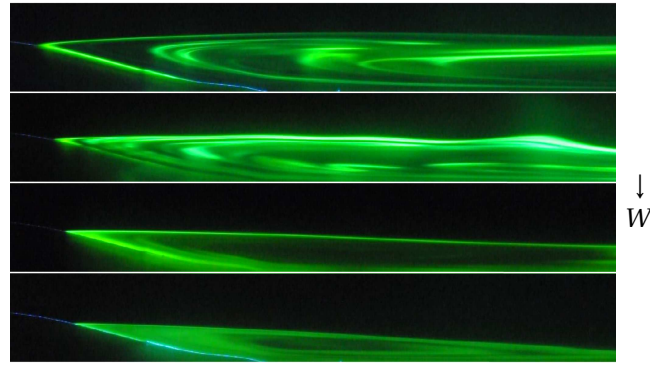
Figure 2.32 – Snapshots showing the effect of wall control on the flow at $Re_{\delta^*} = 448$: suction flow rate $W = 0$, 0.39, 0.78, 1.17 L/min, i.e. $W/LU_\infty\delta^* = 0$, 0.07, 0.14, 0.21 (top to bottom).
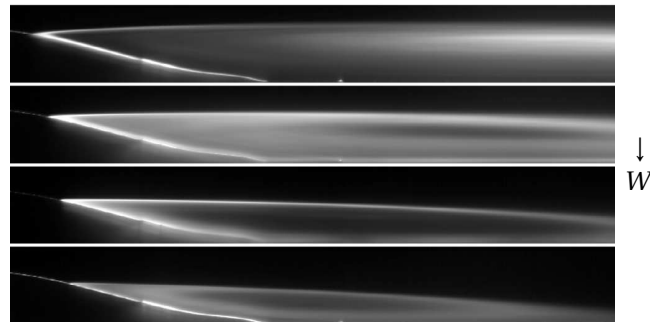
Figure 2.33 – Effect of wall control on the mean flow at $Re_{\delta^*} = 448$: suction flow rate $W = 0$, 0.39, 0.78, 1.17 L/min, i.e. $W/LU_\infty\delta^* = 0$, 0.07, 0.14, 0.21 (top to bottom).
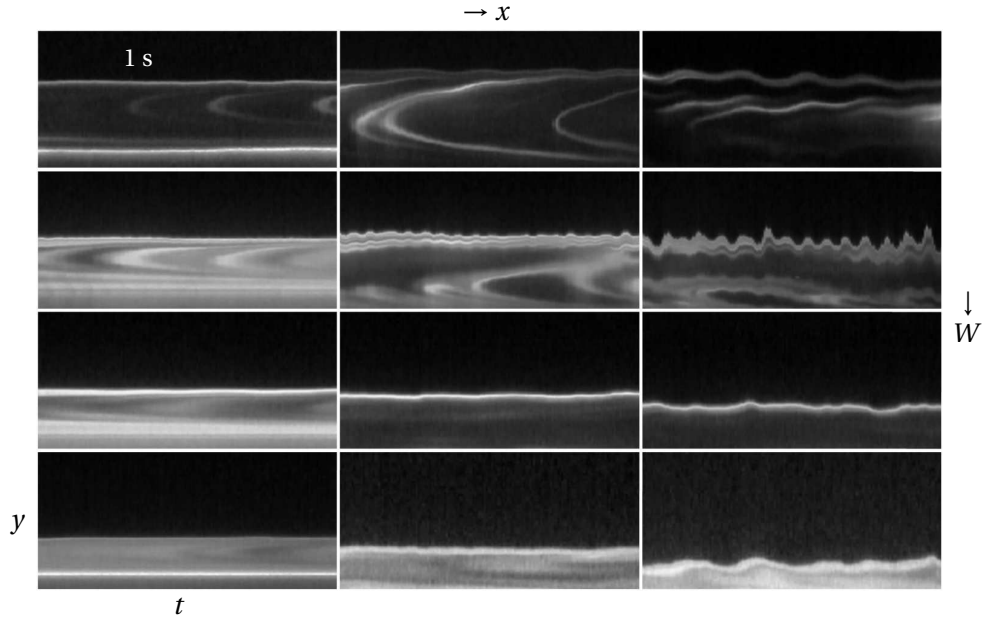
Figure 2.34 – Spatio-temporal $y - t$ diagrams of the controlled flow: suction flow rate $W/LU_\infty\delta^* = 0$, 0.07, 0.14, 0.21 (top to bottom) at $x = x^* + 30\delta^*$, $x^* + 35\delta^*$, $x^* + 40\delta^*$ (left to right).

installed *downstream* of the separation. These oscillations might rather be related to a thinning of the shear layer caused by wall suction, resulting in a more unstable Kelvin-Helmholtz mechanism. This destabilizing effect (increased shear) is therefore competing with the primary stabilizing effect of suction (shorter recirculation length). Further investigation would yield additional insight into this phenomenon.

Figure 2.35 shows the normalized standard deviation of the separatrix height $\tilde{\sigma}(y_{sep})$ and of the intensity integrated vertically $\tilde{\sigma}(I)$, at $Re_{\delta^*} = 448$. In the uncontrolled case (thick line), perturbations are clearly amplified as they travel downstream. With weak wall suction (dashed line), the Kelvin-Helmholtz instability is triggered, and shear layer oscillations are amplified by up to 4 at $x = x^* + 45\delta^*$. Far downstream, the breakdown of the recirculation region provokes strong disorder in the flow, and the shear layer is not well-defined any more. Intensity fluctuations, however, can be measured even in this case. They confirm that perturbations are quickly amplified, earlier ($x \simeq x^* + 40\delta^*$ to $x^* + 45\delta^*$) than in the uncontrolled case, where vortex shedding is visible only from $x \simeq x^* + 50\delta^*$. When wall suction is increased (thin solid lines), shear layer fluctuations come back to their uncontrolled level, and intensity fluctuations downstream are reduced.

In conclusion, these observations are consistent with the numerical simulation results of section 2.1. The shear layer length is reduced by suction, limiting the overall amplification.
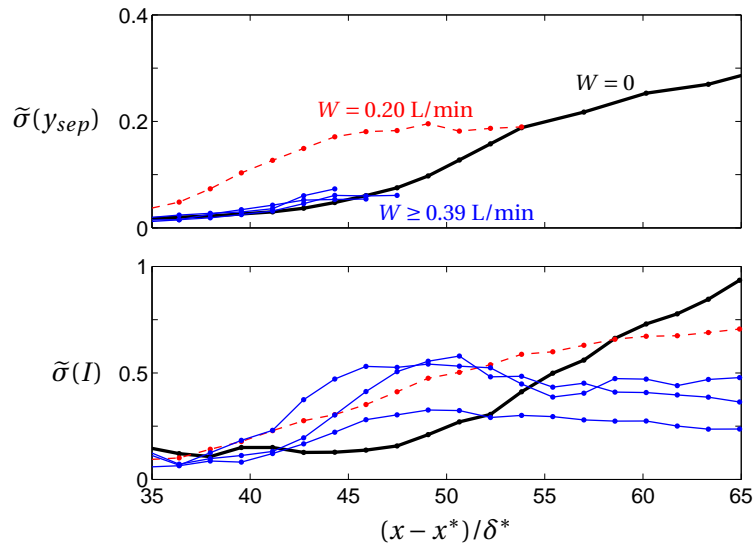
Figure 2.35 – Normalized standard deviations of shear layer height and dye intensity for wall suction flow rates $W = 0$ L/min (black thick line), 0.20 (red dashed line), and 0.39, 0.59, 0.98 L/min (blue thin lines).

Chapter 3

Amplification of stochastic forcing

The amplification of harmonic perturbations and the sensitivity of the optimal harmonic gain were studied in chapter 2, in the flow past a wall-mounted bump. The harmonic viewpoint is relevant in a linear framework since arbitrary time signals can be decomposed as Fourier components. Although harmonic amplification was found to be successfully reduced by wall suction at the bump summit, the design of this control configuration was not straightforward because all frequencies had to be taken into account simultaneously. In this regard, one might ask if it is possible to consider instead the response to stochastic perturbations, and thus deal with a single quantity of interest.

In this chapter, the amplification of white noise is investigated, taking advantage of a convenient expression of the *stochastic gain* (statistically stationary variance of the response) in terms of individual *harmonic gains* at each frequency. Then, the sensitivity of the stochastic gain is simply computed as a weighted sum of the sensitivities of optimal and sub-optimal harmonic gains. In the flow past a backward-facing step, it is found that the sensitivity of the stochastic gain is well captured by that of the optimal harmonic gain at the optimal frequency, both for volume control and for wall control, which greatly simplifies control design. Although further studies are needed to confirm or invalidate the generality of this result for convectively unstable open flows, we hypothesize that it might hold (i) if amplification is large in a particular range of frequencies and (ii) if the optimal harmonic gain is well separated from sub-optimal gains in this range.

Paper: *Sensitivity and open-loop control of stochastic response in a noise amplifier flow: the backward-facing step*

Sensitivity and open-loop control of stochastic response in a noise amplifier flow: the backward-facing step

E. Boujo and F. Gallaire

LFMI, École Polytechnique Fédérale de Lausanne, CH-1015 Lausanne, Switzerland

A variational technique is proposed to evaluate the sensitivity of noise amplification in globally stable open flows. Existing sensitivity methods are extended in two ways, with the aim of dealing with a realistic representation of incoming noise: (i) perturbations are time-stochastic rather than time-harmonic, (ii) perturbations are localized at the inlet rather than distributed in space.

The sensitivity of the stochastic response with respect to flow modification and to steady control is computed in the canonical flow over a backward-facing step. The stochastic response can be reduced by passive control by inserting a small cylinder in regions of large positive streamwise velocity downstream of the step. Active control by means of wall blowing and suction is effective too, in particular on the step vertical wall and on upstream horizontal walls. Boundary control upstream of the step is found to shorten the lower or upper recirculation regions when applied on the lower or upper wall, respectively, in accordance with sensitivity analysis of the recirculation length.

One key observation for both volume control and boundary control is that sensitivity maps of stochastic noise are largely similar to sensitivity maps of the optimal harmonic perturbation at the most amplified frequency. This suggests that the design of steady control in strong noise amplifier flows can be simplified and conducted by focusing on the most dangerous perturbation at the most dangerous frequency.

1 Introduction

In his famous pipe flow experiment, Reynolds (1883) observed transition to turbulence and showed that the critical value of a governing non-dimensional parameter, to be later coined *Reynolds number*, was strongly dependent on the level of external noise. However, linear stability theory predicts the Hagen-Poiseuille flow to be asymptotically stable for any value of Re (Schmid & Henningson, 2001). It is now well understood that linear stability theory successfully captures bifurcations and instability mechanisms for some flows (e.g. Rayleigh–Bénard convection, Taylor–Couette flow between rotating cylinders, or flow past a cylinder), but fails for other flows: the Navier–Stokes equations which govern fluid motion constitute a non-normal system, able to amplify perturbations through non-modal mechanisms (Trefethen *et al.*, 1993); then, if amplification is large enough it may drive the system away from lin-

early stable solutions. Non-normal stable systems can exhibit large *transient growth* $G(t) = ||\mathbf{u}(\mathbf{x}, t)||/||\mathbf{u}(\mathbf{x}, 0)||$, i.e. temporary amplification of initial conditions $\mathbf{u}(\mathbf{x}, 0)$, as well as large *harmonic gain* $G(\omega) = ||\mathbf{u}(\mathbf{x})||/||\mathbf{f}(\mathbf{x})||$, i.e. asymptotic amplification of the response $\mathbf{u}(\mathbf{x})\cos(\omega t)$ to external harmonic forcing $\mathbf{f}(\mathbf{x})\cos(\omega t)$. Classical linear algebra techniques allow one to find the largest amplification possible together with *optimal perturbations*, i.e. those specific structures associated with maximal transient growth or harmonic gain. Extensive literature exists about the calculation of transient growth (Butler & Farrell, 1992; Corbett & Bottaro, 2000; Blackburn *et al.*, 2008) and harmonic gain (Åkervik *et al.*, 2008; Alizard *et al.*, 2009; Garnaud *et al.*, 2013; Sipp & Marquet, 2013; Dergham *et al.*, 2013).

A question of fundamental importance is whether these non-modal amplification mechanisms are robust or not: if they are significantly altered by small flow modifications, one can design control strategies with a wide variety of applications such as mixing enhancement, aerodynamic performance improvement, or noise and vibration reduction. To investigate this point, adjoint methods are particularly well suited, as they provide maps of sensitivity showing regions where a given quantity of interest is the most affected by small-amplitude flow modification or steady control. Since the actual modified flow is not needed, sensitivity analysis allows for a fast and systematic control design, without resorting to time-consuming parameter studies. In the context of linearly unstable flows, Hill (1992) used such a variational technique to derive the gradient of the leading eigenvalue with respect to flow modification and to steady control, and successfully reproduced maps of vortex shedding suppression obtained experimentally by Strykowski & Sreenivasan (1990). Similar methods were later applied to eigenvalues in several parallel and non-parallel configurations (Bottaro *et al.*, 2003; Marquet *et al.*, 2008; Meliga *et al.*, 2010). For unstable flows, Brandt *et al.* (2011) followed a similar technique to give an expression for the sensitivity of the optimal harmonic gain $G(\omega)$ with respect to flow modification and to steady control in the volume or at the wall. They applied their formula to parallel and non-parallel flat-plate boundary layers and discussed the sensitivity of $G(\omega)$ for Tollmien–Schlichting and lift-up instability mechanisms. Boujo, Ehrenstein & Gallaire (2013) used this method to identify sensitive regions in the separated flow past a wall-mounted bump. Choosing an appropriate location, they designed a simple open-loop wall actuation able to delay noise-induced subcritical transition. They observed, however, that sensitivity to volume control was dependent on frequency, indicating that a given control could reduce $G(\omega)$ at some frequencies but increase it at others. In this case, the effect of control on the overall response of the stochastically driven flow is unclear, and control design is uneasy.

In this paper, we extend sensitivity methods for linearly stable flows in two ways. First, we compute the sensitivity of amplification when the flow is subject to *stochastic forcing* rather than harmonic forcing. This step takes advantage of the relation between stochastic and harmonic amplification (Farrell & Ioannou, 1996). It allows us to consider the overall response of the flow to external noise, and to combine sensitivities at individual frequencies into a single sensitivity. Second, we derive an expression for the sensitivity of amplification when the flow is forced *at the inlet* rather than in the whole domain, with the aim of dealing with a
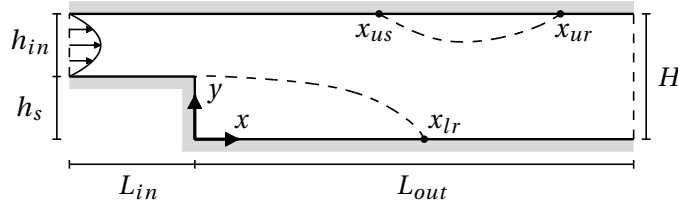
Figure 3.1 – Sketch of the geometry.

realistic model of incoming perturbations in convectively unstable open flows. The method is illustrated with the two-dimensional incompressible flow past a backward-facing step, a canonical noise-amplifier flow.

This paper is organized as follows. Section 2 recalls how to characterize the response to harmonic and stochastic forcing located in the volume or at the inlet, and presents the sensitivities of these responses. Section 3 details the numerical method and its validation. Then, the harmonic response of the backward-facing step flow for a specific set of Reynolds number Re and step expansion ratio Γ is presented in section 4, and a connection with local stability analysis is established. Results about sensitivity are given in section 5: section 5.1 is dedicated to the sensitivities of harmonic and stochastic responses and reveals the predominant role of the optimal harmonic response at the optimal frequency; in section 5.2 the sensitivity analysis is validated against nonlinear calculations for illustrative examples of control; section 5.3 looks at the link with the sensitivity of recirculation lengths; section 5.4 investigates a possible method to take advantage of pressure differences in order to use passive wall control; finally section 5.5 investigates other Re-Γ configurations. Conclusions are drawn in section 6.

2 Problem formulation

2.1 Flow configuration

We consider the flow over a backward-facing step, shown schematically in figure 3.1. Geometrical parameters are the inlet height h_{in}, the step height h_s, and the outlet height $H = h_s + h_{in}$, any set of these three values uniquely defining the step to outlet expansion ratio $\Gamma = h_s/H$ or, equivalently, the outlet to inlet expansion ratio $e = H/h_{in} = 1/(1-\Gamma)$. Throughout this paper we will consider the classical geometry $\Gamma = 0.5$ ($e = 2$), and a smaller step characterised by $\Gamma = 0.3$ ($e \simeq 1.43$). The vertical wall and outlet lower wall define the $x = 0$ and $y = 0$ axes respectively. The incoming flow is assumed to have a fully developed parabolic Poiseuille profile of maximum (centerline) velocity U_∞ at the inlet Γ_{in} located at $x = -L_{in}$, while the outlet is at $x = L_{out}$. The reference length is chosen as $L = H/2$ and the reference velocity as U_∞. The Reynolds number is consequently defined as $Re = LU_\infty/\nu$, where ν is the fluid kinematic viscosity.

The steady-state base flow ($\mathbf{U}_b, P_b$) is solution of the stationary, incompressible Navier–Stokes

equations in the domain Ω, with no-slip boundary conditions at the walls Γ_w:

$$\nabla \cdot \mathbf{U}_b = 0,$$
$$\mathbf{U}_b \cdot \nabla \mathbf{U}_b + \nabla P_b - Re^{-1}\nabla^2 \mathbf{U}_b = \mathbf{0}, \tag{3.1}$$
$$\mathbf{U}_b = \mathbf{0} \quad \text{on } \Gamma_w.$$

2.2 Response to forcing

In the following, we consider the response of a stable steady-state base flow to forcing. The focus of this paper is on *stochastic inlet* forcing, but we mention *harmonic* and/or *volume* forcing to help understanding and highlight differences. More details can be found for example in Farrell & Ioannou (1996) and Schmid & Henningson (2001). We first recall how the response to a small-amplitude harmonic forcing $\mathbf{f}'(\mathbf{x}, t) = \mathbf{f}(\mathbf{x})\,e^{i\omega t}$ is characterised. Since the flow is linearly stable, the asymptotic response is also harmonic at the same frequency. The forcing therefore introduces perturbations $(\mathbf{u}', p')(\mathbf{x}, t) = (\mathbf{u}, p)(\mathbf{x})\,e^{i\omega t}$ to the base flow whose dynamics are governed by the linearised equations

$$\nabla \cdot \mathbf{u}_{vol} = 0,$$
$$i\omega\mathbf{u}_{vol} + \mathbf{U}_b \cdot \nabla \mathbf{u}_{vol} + \mathbf{u}_{vol} \cdot \nabla \mathbf{U}_b + \nabla p_{vol} - Re^{-1}\nabla^2 \mathbf{u}_{vol} = \mathbf{f}_{vol}, \tag{3.2}$$
$$\mathbf{u}_{vol} = \mathbf{0} \quad \text{on } \Gamma_{in} \cup \Gamma_w,$$

for volume forcing in Ω, and by

$$\nabla \cdot \mathbf{u}_{in} = 0,$$
$$i\omega\mathbf{u}_{in} + \mathbf{U}_b \cdot \nabla \mathbf{u}_{in} + \mathbf{u}_{in} \cdot \nabla \mathbf{U}_b + \nabla p_{in} - Re^{-1}\nabla^2 \mathbf{u}_{in} = \mathbf{0},$$
$$\mathbf{u}_{in} = \mathbf{f}_{in} \quad \text{on } \Gamma_{in}, \tag{3.3}$$
$$\mathbf{u}_{in} = \mathbf{0} \quad \text{on } \Gamma_w$$

for inlet forcing on Γ_{in} (Garnaud *et al.*, 2013). We write formally (3.2) as $\mathbf{u}_{vol} = \mathscr{R}_{vol}(\omega)\mathbf{f}_{vol}$ and (3.3) as $\mathbf{u}_{in} = \mathscr{R}_{in}(\omega)\mathbf{f}_{in}$, where in both cases $\mathscr{R}(\omega)$ is the resolvent operator. For a given forcing, one simply needs to invert a linear system to obtain the response. We introduce the usual Hermitian scalar product $(\mathbf{a}|\mathbf{b}) = \int_\Omega \overline{\mathbf{a}} \cdot \mathbf{b}\,d\Omega = \int_\Omega \mathbf{a}^H \mathbf{b}\,d\Omega$ or $(\mathbf{a}|\mathbf{b}) = \int_{\partial\Omega} \overline{\mathbf{a}} \cdot \mathbf{b}\,d\Gamma = \int_{\partial\Omega} \mathbf{a}^H \mathbf{b}\,d\Gamma$ for complex fields defined respectively in the domain or on (part or all of) the boundary, where $\overline{\cdot}$ and $\cdot^H$ stand for conjugate and conjugate transpose. The norm induced by this scalar product is used to measure amplification in the flow, or harmonic gain $G(\omega) = ||\mathbf{u}||/||\mathbf{f}||$. A natural quantity to look for is the largest value the gain may take, or optimal gain, together with the associated "most dangerous" forcing, or optimal forcing. This worst-case scenario is classically investigated by introducing the adjoint operator of the resolvent, and recasting the harmonic gain as a Rayleigh quotient

$$G^2(\omega) = \frac{||\mathbf{u}||^2}{||\mathbf{f}||^2} = \frac{(\mathscr{R}\mathbf{f}|\mathscr{R}\mathbf{f})}{(\mathbf{f}|\mathbf{f})} = \frac{(\mathscr{R}^\dagger \mathscr{R}\mathbf{f}|\mathbf{f})}{(\mathbf{f}|\mathbf{f})}. \tag{3.4}$$

The largest value of G is by definition the induced norm of the resolvent $||\mathcal{R}||$, which can be calculated as the largest singular value of $\mathcal{R}$. Alternatively, solving the symmetric eigenvalue problem $\mathcal{R}^{\dagger}\mathcal{R}\mathbf{f}_k = G_k^2\mathbf{f}_k$ yields a set of real positive eigenvalues $G_1^2 \geq G_2^2 \geq G_3^2 \ldots$ and a set of orthogonal eigenvectors $\mathbf{f}_k$, from which one deduces the optimal gain:

$$G_1(\omega) = \max_{\mathbf{f}} \frac{||\mathbf{u}||}{||\mathbf{f}||} = \frac{||\mathbf{u}_1||}{||\mathbf{f}_1||}. \tag{3.5}$$

The response of the flow to the optimal forcing is the optimal response $\mathbf{u}_1 = \mathcal{R}\mathbf{f}_1$. One can similarly define sub-optimal gains, forcings and responses as $G_k = ||\mathbf{u}_k||/||\mathbf{f}_k||$, $\mathbf{u}_k = \mathcal{R}\mathbf{f}_k$ (Garnaud *et al.*, 2013; Dergham *et al.*, 2013).

We now turn our attention to stochastic forcing. We assume that the flow is continuously forced by componentwise uncorrelated, white noise of unit variance, expressed as $\mathbf{f}'(\mathbf{x},t) = \int_{-\infty}^{\infty}\mathbf{f}(\mathbf{x},\omega)\,e^{i\omega t}\,d\omega$ and such that $\mathcal{E}\left(f_j(\mathbf{x},\omega_1)f_k(\mathbf{x},\omega_2)\right) = \delta_{jk}\delta(\omega_1 - \omega_2)/2\pi$ where $\mathcal{E}(\cdot)$ denotes the mean or expected value of a random variable. Unless one has specific knowledge about temporal and spatial characteristics of incoming perturbations, this assumption has the advantage of being both reasonable and simple. The stochastic response is then characterised by the stationary ensemble variance (Farrell & Ioannou, 1996; Zhou, Doyle & Glover, 1996)

$$E = \mathcal{E}\left(||\mathbf{u}||_2^2\right) = \frac{1}{2\pi}\int_{-\infty}^{\infty}\mathrm{Tr}\left(\mathcal{R}(\omega)^{\dagger}\mathcal{R}(\omega)\right)d\omega, \tag{3.6}$$

which can be expressed in terms of eigenvalues of $\mathcal{R}^{\dagger}\mathcal{R}$:

$$E = \frac{1}{2\pi}\int_{-\infty}^{\infty}\sum_k G_k^2(\omega)\,d\omega = \frac{1}{\pi}\int_0^{\infty}\sum_k G_k^2(\omega)\,d\omega = \sum_k I_k. \tag{3.7}$$

For convenience we call E the *stochastic gain*, in contrast with the *harmonic gain $G(\omega)$*.

2.3 Sensitivity of harmonic and stochastic gain

In this section we give the expressions of sensitivities (gradients) of harmonic and stochastic gains with respect to flow modification and to steady control. They are gradients, which allow us to identify regions of the domain Ω and the wall Γ_w where gains are most sensitive, and to predict the effect of small-amplitude flow modification and control on the asymptotic amplification of harmonic and stochastic perturbations.

Starting with harmonic gain, we look for the two-dimensional sensitivity field $\nabla_{\mathbf{U}}G_1^2$ defined in Ω such that a modification $\boldsymbol{\delta U}$ of the base flow induces a variation of the (squared) optimal gain $\delta G_1^2 = (\nabla_{\mathbf{U}}G_1^2 | \boldsymbol{\delta U})$. Using a Lagrangian-based variational technique, Brandt *et al.* (2011) derived an expression for the sensitivity of the optimal harmonic gain for the case of volume forcing. This expression is straightforwardly generalised to any sub-optimal gain $G_{vol,k}$, $k > 1$, replacing the optimal forcing $\mathbf{f}_{vol,1}$ and optimal response $\mathbf{u}_{vol,1}$ by the kth sub-optimal

forcing and response:

$$\nabla_{\mathbf{U}} G_{vol,k}^2 = 2 G_{vol,k}^2 \, \mathrm{Re}\{-\nabla \mathbf{u}_{vol,k}^H \cdot \mathbf{f}_{vol,k} + \nabla \mathbf{f}_{vol,k} \cdot \overline{\mathbf{u}_{vol,k}}\}. \tag{3.8}$$

Using the same technique, we derived an expression for the case of inlet forcing:

$$\nabla_{\mathbf{U}} G_{in,k}^2 = 2 \, \mathrm{Re}\{-\mathbf{u}_{in,k}^\dagger \cdot \nabla \mathbf{u}_{in,k}^H + \overline{\mathbf{u}_{in,k}} \cdot \nabla \mathbf{u}_{in,k}^\dagger\} \tag{3.9}$$

where the adjoint perturbation $(\mathbf{u}_{in,k}^\dagger, p_{in,k}^\dagger)$ is a solution of the linear system $\mathbf{u}_{in,k}^\dagger = \mathscr{R}_{vol}^\dagger \mathbf{u}_{in,k}$:

$$\nabla \cdot \mathbf{u}_{in,k}^\dagger = 0,$$
$$-i\omega \mathbf{u}_{in,k}^\dagger + \mathbf{U}_b \cdot \nabla \mathbf{u}_{in,k}^\dagger - \mathbf{u}_{in,k}^\dagger \cdot \nabla \mathbf{U}_b^T + \nabla p_{in,k}^\dagger + Re^{-1} \nabla^2 \mathbf{u}_{in,k}^\dagger = \mathbf{u}_{in,k}, \tag{3.10}$$
$$\mathbf{u}_{in,k}^\dagger = \mathbf{0} \quad \text{on } \Gamma_{in} \cup \Gamma_w.$$

In the case of sensitivity to *volume* forcing (3.8), no adjoint variable needs to be computed (Brandt *et al.*, 2011). This comes from the fact that the operator $\mathscr{R}_{vol}^\dagger \mathscr{R}_{vol}$ involved in the *volume* forcing problem and associated gain sensitivity is self-adjoint (see figure 3.2(*a*)). In other words, even though an adjoint perturbation has to be included in the Lagrangian *a priori*, calculations show that it can be replaced by $G_{vol}^2 \mathbf{f}_{vol}$: indeed, equation (3.3) is $\mathbf{u}_{vol} = \mathscr{R}_{vol} \mathbf{f}_{vol}$ and implies $\mathscr{R}_{vol}^\dagger \mathbf{u}_{vol} = \mathscr{R}_{vol}^\dagger \mathscr{R}_{vol} \mathbf{f}_{vol} = G_{vol}^2 \mathbf{f}_{vol}$; at the same time, detailed calculations lead to the adjoint perturbation equation $\mathbf{u}_{vol}^\dagger = \mathscr{R}_{vol}^\dagger \mathbf{u}_{vol}$, and therefore $\mathbf{u}_{vol}^\dagger = G_{vol,k}^2 \mathbf{f}_{vol}$. The situation is quite different for *inlet* forcing. The operator $\mathscr{R}_{in}^\dagger \mathscr{R}_{in}$ involved in the *inlet* forcing problem is self-adjoint too (fig. 3.2(*b*)), but the operator $\mathscr{R}_{vol}^\dagger \mathscr{R}_{in}$ needed to obtain the associated sensitivity is not (fig. 3.2(*c*)). Consequently, the adjoint perturbation $(\mathbf{u}_{in}^\dagger, p_{in}^\dagger)$ which appears in the expression of sensitivity to *inlet* forcing (3.9) has to be computed on its own. Interestingly, note that although we are dealing with *inlet* forcing, the adjoint perturbation is a solution of an equation forced in the *volume* by the response $\mathbf{u}_{in}$.

Next, we turn to the sensitivity of harmonic gain to steady volume control $\mathbf{C}$ in Ω and steady wall control $\mathbf{U}_c$ on Γ_w. The former sensitivity is a two-dimensional field such that a small-amplitude volume control produces the variation $\delta G_k^2 = (\nabla_{\mathbf{C}} G_k^2 | \boldsymbol{\delta} \mathbf{C})$, while the latter is a one-dimensional field defined on Γ_w such that $\delta G_k^2 = (\nabla_{\mathbf{U}_c} G_k^2 | \boldsymbol{\delta} \mathbf{U}_c)$. Again, one can generalise the expression of Brandt *et al.* (2011) for optimal gain to any sub-optimal gain:

$$\nabla_{\mathbf{C}} G_k^2 = \mathbf{U}_k^\dagger, \tag{3.11}$$
$$\nabla_{\mathbf{U}_c} G_k^2 = P_k^\dagger \mathbf{n} + Re^{-1} \nabla \mathbf{U}_k^\dagger \mathbf{n}, \tag{3.12}$$

where $\mathbf{n}$ is the outward unit normal vector, and the adjoint base flow $(\mathbf{U}_k^\dagger, P_k^\dagger)$ is solution of the following linear system forced by the sensitivity to base-flow modification $\nabla_{\mathbf{U}} G_k^2$ defined

(*a*) Volume forcing: gain and sensitivity
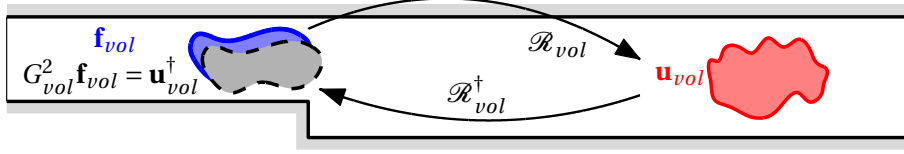
(*b*) Inlet forcing: gain
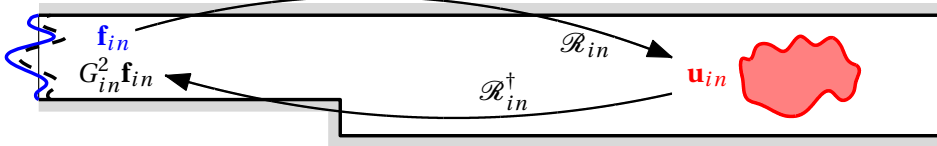
(*c*) Inlet forcing: sensitivity
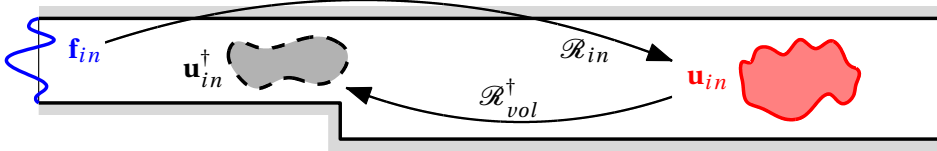
Figure 3.2 – Quantities and operators involved in the computation of the harmonic gain and of its sensitivity. (*a*) In the case of volume forcing, the gain is given by $G_{vol}^2 \mathbf{f}_{vol} = \mathcal{R}_{vol}^\dagger \mathcal{R}_{vol} \mathbf{f}_{vol} = \mathcal{R}_{vol}^\dagger \mathbf{u}_{vol}$, the operator $\mathcal{R}_{vol}^\dagger \mathcal{R}_{vol}$ is self-adjoint, and the adjoint perturbation $\mathbf{u}_{vol}^\dagger = G_{vol}^2 \mathbf{f}_{vol}$ does not need to be computed to evaluate the gain sensitivity (3.8). (*b*) In the case of inlet forcing, the gain is given by $G_{in}^2 \mathbf{f}_{in} = \mathcal{R}_{in}^\dagger \mathcal{R}_{in} \mathbf{f}_{in} = \mathcal{R}_{in}^\dagger \mathbf{u}_{in}$, where the operator $\mathcal{R}_{in}^\dagger \mathcal{R}_{in}$ is self-adjoint. (*c*) However, the adjoint perturbation $\mathbf{u}_{in}^\dagger = \mathcal{R}_{vol}^\dagger \mathbf{u}_{in}$ needed to evaluate the gain sensitivity (3.9) must be computed explicitly because the operator $\mathcal{R}_{vol}^\dagger \mathcal{R}_{in}$ is not self-adjoint.

in (3.8)-(3.9):

$$\nabla \cdot \mathbf{U}_k^\dagger = 0, \quad -\mathbf{U}_b \cdot \nabla \mathbf{U}_k^\dagger + \mathbf{U}_k^\dagger \cdot \nabla \mathbf{U}_b^T - \nabla P_k^\dagger - Re^{-1} \nabla^2 \mathbf{U}_k^\dagger = \nabla_{\mathbf{U}} G_k^2, \tag{3.13}$$

$$\mathbf{U}_k^\dagger = \mathbf{0} \quad \text{on } \Gamma_{in} \cup \Gamma_w. \tag{3.14}$$

This time, the same method holds for both inlet and volume forcing, so we omitted subscripts *in* and *vol* in (3.12)-(3.14).

Finally, by linearity of the stochastic gain (3.7), its sensitivity can be expressed in terms of the sensitivity of harmonic gains

$$\nabla_* E = \frac{1}{\pi} \int_0^\infty \sum_k \nabla_* G_k^2(\omega) \, d\omega = \sum_k \nabla_* I_k \tag{3.15}$$

where the subscript $*$ stands for either $\mathbf{U}$, $\mathbf{C}$ or $\mathbf{U}_c$ for the sensitivity to base-flow modification, volume control or wall control respectively. Again, expression (3.15) is valid for both inlet and volume forcing.

3   Numerical method and validation

All calculations are performed using methods described in Boujo *et al.* (2013). The finite element software *FreeFem*++ is used to generate a two-dimensional triangulation of the domain Ω and, based on P2 and P1 Taylor-Hood elements for velocity and presure respectively, to build all the discrete operators involved in calculations of base flow, eigenvalue and sensitivity, from their corresponding continuous expression in variational form. Steady-state base flows are obtained with an iterative Newton method, while eigenvalue calculations are conducted with an implicitly restarted Arnoldi method. Careful validation and convergence study (described below) led us to set the outlet length to $L_{out} = 50$ for $\Gamma = 0.5$ and $L_{out} = 250$ for $\Gamma = 0.3$, the entrance length to $L_{in} = 5$ for both geometries, and a mesh density distribution yielding 216340 and 298484 elements (0.98 and 1.36 million degrees of freedom) for $\Gamma = 0.5$ and $\Gamma = 0.3$ respectively.

Our choice of outlet length L_{out} is such that the outlet velocity profile is well developed for all conditions: specifically, it ensures that the difference between the base flow and the fully developed parabolic Poiseuille profile $\Delta U(y) = U_b(L_{out}, y) - U_P(y)$ is less than 1% for $\Gamma = 0.5$ and 3% for $\Gamma = 0.3$, both in L^2 norm $||\Delta U||_2$ (relative to $||U_P||_2$) and L^∞ norm $||\Delta U||_\infty$ (relative to $U_P(y^*)$ at the height y^* of largest $|\Delta U|$). Validation included a three-dimensional stability analysis: using global modes $\mathbf{u}'(x, y, z, t) = \mathbf{u}(x, y) e^{i\beta z + \sigma t}$ we calculated the critical Reynolds number Re_c (i.e. the smallest Re for which one global mode becomes unstable, $\text{Re}\{\sigma\} \geq 0$) and corresponding spanwise wavenumber β_c. Results are given in table 3.1 and show an excellent agreement with those of Barkley, Gomes & Henderson (2002) and Lanzerstorfer & Kuhlmann (2012), with differences smaller than 0.5%. We also looked at the positions of reattachment and separation points (x_{lr}, x_{us}, x_{ur}) (characterised by zero wall shear stress, see fig. 3.1) for

Γ		0.5			0.3	
L_{in}	1	5	10	1	5	10
(*a*) BGH02	(748, 0.91)	-	-	-	-	-
(*b*) LK12	(748, 0.92)	(714, 0.88)	(714, 0.88)	-	-	(2948, 1.02)
(*c*) BG14	(750, 0.92)	(715, 0.88)	(715, 0.88)	(3206, 1.13)	(2966, 1.01)	(2964, 1.01)

Table 3.1 – Critical Reynolds number and spanwise wavenumber (Re_c, β_c) for different expansion ratios Γ and entrance lengths L_{in}: (*a*) Barkley *et al.* (2002), (*b*) Lanzerstorfer & Kuhlmann (2012), (*c*) present study.

L_{in}	1	5	10
(*a*) BGH02	(11.91, 9.5, 20.6)	-	-
(*b*) BG14	(11.93, 9.45, 20.60)	(11.82, 9.34, 20.59)	(11.82, 9.34, 20.59)

Table 3.2 – Locations (x_{lr}, x_{us}, x_{ur}) of lower reattachment point, upper separation point and upper reattachment point at $Re = 600$, for $\Gamma = 0.5$ and different entrance lengths L_{in}: (*a*) Barkley *et al.* (2002), (*b*) present study.

$\Gamma = 0.5$. At all Reynolds numbers up to $Re \leq 1000$, our values were indistinguishable with data extracted from figures in Barkley *et al.* (2002) and Blackburn *et al.* (2008). At $Re = 600$ we find the values given in table 3.2, in excellent agreement with those reported by Barkley *et al.* (2002). The secondary recirculation zone appears at the upper wall at $Re = 272$, $x_u = 8.2$, consistent with the values $Re \simeq 275$, $x_u \simeq 8.1$ of Blackburn *et al.* (2008). Tables 3.1 and 3.2 show that the choice $L_{in} = 5$ is justified since all values are well converged. Mesh independence was checked by increasing the number of elements by 20% with a global and uniform refinement, which led to less than 0.05% variation for critical conditions (Reynolds number and wavenumber) and the locations of stagnation points.

The stochastic response (3.7) and its sensitivities (3.15) are evaluated as follows. Integrals I_k and $\nabla_* I_k$ are calculated using a trapezoidal rule with $n_\omega = 41$ points regularly distributed over the range of frequencies $\omega \in [0; \omega_c]$. Halving or doubling n_ω modifies the value of E by less than 1%. The cut-off frequency is set to $\omega_c = 2$ and kept fixed throughout the study. This value is well above the main peak of $G_1(\omega)$ at $\omega_0 = 0.5$, so as to include the contribution of amplification mechanisms, while optimal and sub-optimal forcings and responses at higher frequencies correspond only to advection and diffusion; therefore the exact value of E does depend on ω_c but qualitative results are unaffected (see appendix 3). Sums over k are computed with the full set of optimal and sub-optimals. The effect of taking a limited number of sub-optimals is reported in appendix 3. Note that although evaluating E and $\nabla_* E$ is relatively costly, computations are largely parallelisable since different frequencies can be treated independently.
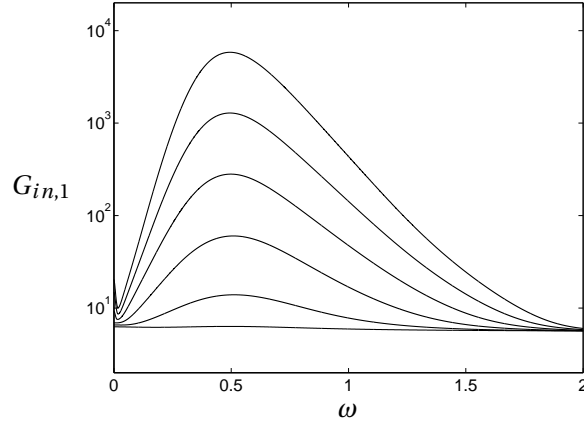
Figure 3.3 – Optimal harmonic gain for inlet forcing, $\Gamma = 0.5$, $Re = 100, 200\ldots, 600$.

4   Harmonic response

In this section we present results about the response of the flow to small-amplitude harmonic forcing. Although the focus of this paper is on *stochastic* forcing at the *inlet* of the domain as a realistic model of random perturbations advected by the flow, we mention here *harmonic* forcing since it is a building block of the stochastic problem, and forcing in the *volume* for comparison purposes. The configuration $\Gamma = 0.5$, $Re = 500$ is considered unless otherwise stated.

Figure 3.3 shows the optimal harmonic gain for inlet forcing, for $\Gamma = 0.5$. The maximal optimal gain increases from 6.33 at $Re = 100$ to 5.83×10^3 at $Re = 600$, the optimal frequency being close to $\omega_0 = 0.5$ for all Reynolds numbers. Focusing on $Re = 500$ from now on, we compare the optimal harmonic gain for inlet forcing and volume forcing in figure 3.4. We observe that the gain is larger in the case of volume forcing. This is a consequence (i) of the choice of the norm used to measure forcing amplitude (two-dimensional versus one-dimensional), and (ii) of the greater efficiency with which two-dimensional forcing structures (somewhat artificially allowed to occupy the whole domain) excite the flow, compared to one-dimensional forcing structures restricted to the inlet. The maximum gain is $\max G_{in,1} = 1.29 \times 10^3$ at $\omega_0 = 0.49$ for inlet forcing, and $\max G_{vol,1} = 7.46 \times 10^3$ at $\omega_0 = 0.48$ for volume forcing. The latter values are in excellent agreement with those reported by Marquet & Sipp (2010*b*): $\max G_{vol,1} = 7.5 \times 10^3$ at $\omega_0 = 0.47$. Sub-optimal branches in figure 3.4 have a much lower gain and mainly correspond to advection and diffusion. As pointed out by Marquet & Sipp (2010*b*), the flow response should therefore be dominated by the optimal response. Boujo *et al.* (2013) observed this behaviour in a direct numerical simulation of a different geometry, with a predominance of the optimal response at optimal frequency. As discussed later, the sensitivity of the stochastic gain is also dominated by the sensitivity of the optimal harmonic gain at the optimal frequency.

Their oscillations have a shorter wavelength as ω increases, consistent with most studies of

Figure 3.4 – Optimal harmonic gain for (*a*) inlet and (*b*) volume forcing. $\Gamma = 0.5$, $Re = 500$. Insets show the same data and a few sub-optimal gains in logarithmic scale.
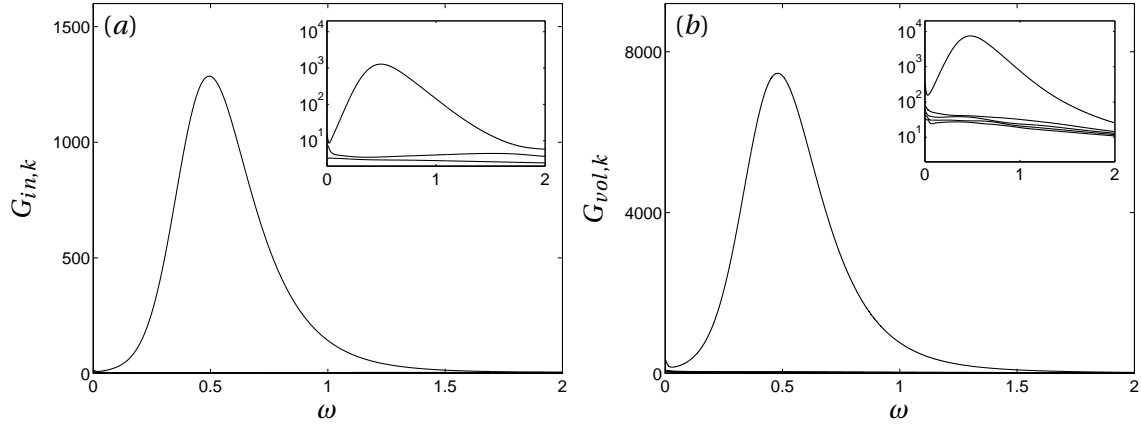
harmonic optimal gain in convective flows (Alizard *et al.*, 2009; Garnaud *et al.*, 2013; Dergham *et al.*, 2013; Boujo *et al.*, 2013). The volume optimal forcing is maximal close to the step corner for all frequencies. The optimal response is maximal downstream of the step corner: close to the upper reattachment point at $\omega = 0.1$, farther downstream as ω increases towards the optimal frequency $\omega_0 \simeq 0.5$, then farther upstream as frequency continues to increase. Interestingly, the optimal inlet forcing $\mathbf{f}_{in,1}(y)$ in figure 3.5(*b*) is very similar to the profile of optimal volume forcing in figure 3.5(*a*)) close to the inlet $\mathbf{f}_{vol,1}(x \to -L_{in}^{+}, y)$. Furthermore, these optimal inlet and volume forcings lead to very similar structures of optimal response (except for slight differences best seen at low frequency near the step corner and the lower recirculation region). Garnaud *et al.* (2013) observed the same phenomenon over a broad range of frequencies. At higher frequencies, where amplification is small, the optimal inlet forcing tends to a plug profile and the response is concentrated at the step corner (figure 3.6).

Interesting complementary information can be obtained from a local linear stability analysis, where the flow is assumed parallel. At each streamwise location, the Orr-Sommerfeld equation was first solved for the temporal problem, i.e. the eigenvalue problem of the complex frequency $\omega^{(T)}$ for a given real streamwise wavenumber k. We found at most one unstable eigenmode for all values of x and k. Next, the same Orr-Sommerfeld equation was solved for the spatial problem, i.e. the eigenvalue problem of the complex wavenumber $k^{(S)}$ for a given real frequency ω. Gaster's relation (Gaster, 1962) was used to estimate the spatial growth rate $-k_i^{(S)} = \omega_i^{(T)}/c_g$ from the temporal growth rate $\omega_i^{(T)}$ and the group velocity $c_g = \partial \omega_r^{(T)}/\partial k_r^{(T)}$, and to identify the correct eigenvalue close to the neutral curve where $k_i^{(S)} = \omega_i^{(T)} = 0$. Figure 3.7 shows the temporal and spatial growth rates at several locations. The flow is unstable between $x = 0$ and $x = 27$, which agrees well with the range where streamwise velocity profiles (fig. 3.7(*a*)) contain one or two inflection points. The temporal growth rate (fig. 3.7(*b*)) is decreasing monotonously with x since shear gradually weakens downstream, while the spatial growth rate (fig. 3.7(*c*)) is also globally decreasing with x but not monotonously at some frequencies, consistent with results from Kaiktsis, Em Karniadakis & Orszag (1996) for close
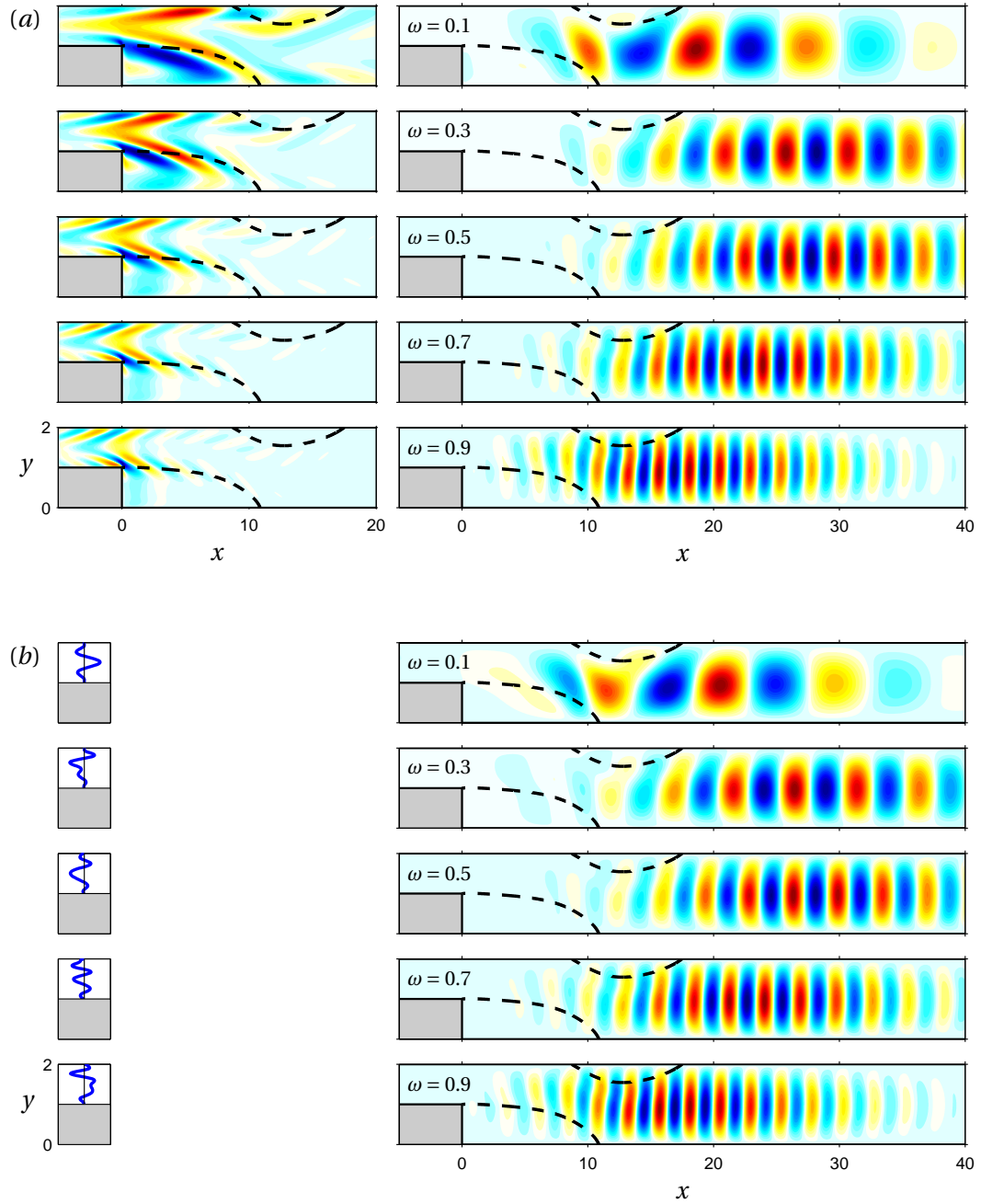
Figure 3.5 – Optimal harmonic forcing (left; real part of streamwise component $\mathbf{f}_1 \cdot \mathbf{e}_x$) and optimal harmonic response (right; real part of cross-stream component v_1): (*a*) volume forcing and corresponding response, (*b*) inlet forcing and corresponding response. $\Gamma = 0.5$, $Re = 500$.
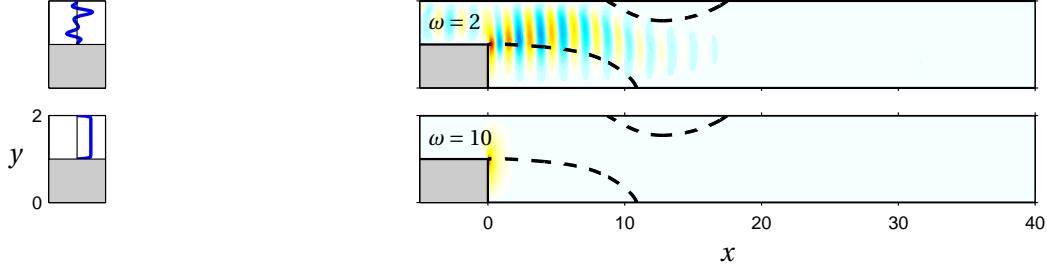
Figure 3.6 – Same as figure 3.5 at higher frequencies.

conditions ($\Gamma \simeq 0.49$, $Re \simeq 510$). This is best seen in figure 3.8(a), showing that $-k_i^{(S)}(x)$ has a local maximum around $9 \lesssim x \lesssim 11$, i.e. between upper separation and lower reattachment. The spatially unstable domain in the $x - \omega$ plane is summarized in figure 3.8(b). As frequency increases, the unstable region quickly widens, from $x \simeq 9\text{-}11$ at $\omega = 0$, to a long region extending downstream up to $x = 27$ at $\omega = 0.5$, before shrinking back towards the step corner $x = 0$, until the flow finally becomes stable everywhere for high frequencies $\omega \geq 2.2$. The downstream neutral curve is followed closely by the location x_{max} where the energy density of the global optimal harmonic response is maximal,

$$x_{max} = \arg\max_x \int ||\mathbf{u}_1(x, y)||_2^2 \, \mathrm{d}y, \tag{3.16}$$

consistent with the idea that perturbations grow spatially as long as $-k_i^{(S)} > 0$, and then decay. One can quantify more precisely how much perturbations are amplified as they propagate through the unstable region; to this aim, we computed the integral amplification factor

$$g(\omega) = \exp\left(\int -k_i^{(S)}(\omega, x) \, \mathrm{d}x \right) \tag{3.17}$$

over the unstable region, as reported in figure 3.8(c). The maximum amplification is obtained close to $\omega = 0.5$, in very good agreement with the global optimal harmonic gain. The shapes of $g(\omega)$ and $G_{in,1}(\omega)$ are comparable too, except at higher frequencies $\omega \gtrsim 2$; in this frequency range the local flow is stable, whereas in the global flow non-parallel effects and component-type non-normality (e.g. Orr mechanism) are at work. Overall, figures 3.8(b)-(c) indicate that the agreement between local and global stability analyses is remarkable. Note that Blackburn *et al.* (2008) obtained a maximum energy at $x = 27$ in a two-dimensional direct numerical simulation with small-amplitude perturbations (Gaussian white noise) at the inlet, consistent with Kaiktsis *et al.* (1996) and in very good agreement with our spatial and global analyses.
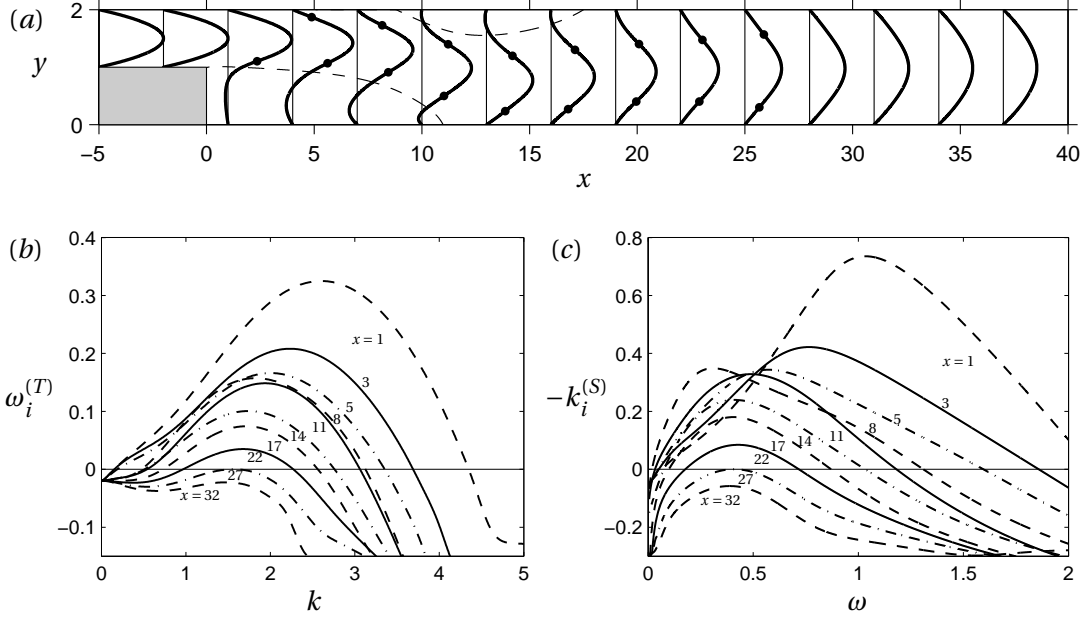
Figure 3.7 – (*a*) Profiles of streamwise velocity for $\Gamma = 0.5$, $Re = 500$, with inflexion points shown as dots. (*b*) Temporal and (*c*) spatial growth rates from local stability analysis.

5 Sensitivity and control of harmonic and stochastic gains

5.1 Sensitivity maps

In this section we present sensitivities of the optimal harmonic gain and of the stochastic gain, in the case of inlet forcing. Figure 3.9 shows sensitivities to base flow modification in the streamwise direction: regions of positive (resp. negative) sensitivity indicate where a small-amplitude increase of streamwise velocity would increase (resp. decrease) the gain. The optimal harmonic gain $G_{in,1}$ is most sensitive at the step corner, and in elongated regions parallel to the upper and lower shear layers (fig. 3.9(*a*)). However, the sign of the sensitivity changes with ω almost everywhere in the channel, meaning that a given modification of the base flow would increase $G_{in,1}$ at some frequencies and decrease it at others. This was also observed by Boujo *et al.* (2013) for the flow past a wall-mounted bump, and they empirically proposed to design their control based on frequencies close to the optimal one. This approach appears justified for the present flow geometry and conditions since the sensitivity of the stochastic gain E (fig. 3.9(*b*)) is essentially similar to that of $G_{in,1}$ at the optimal frequency $\omega_0 = 0.5$. Therefore, reducing the response to stochastic forcing is tantamount to reducing the optimal harmonic gain at optimal frequency, which brings substantial benefits in terms of simplicity and computational cost.

In the same way, figure 3.10 shows sensitivities to streamwise volume control: regions of positive (resp. negative) sensitivity indicate where a small-amplitude body force pointing in the $+x$ direction would increase (resp. decrease) the gain. Again, elongated regions of large
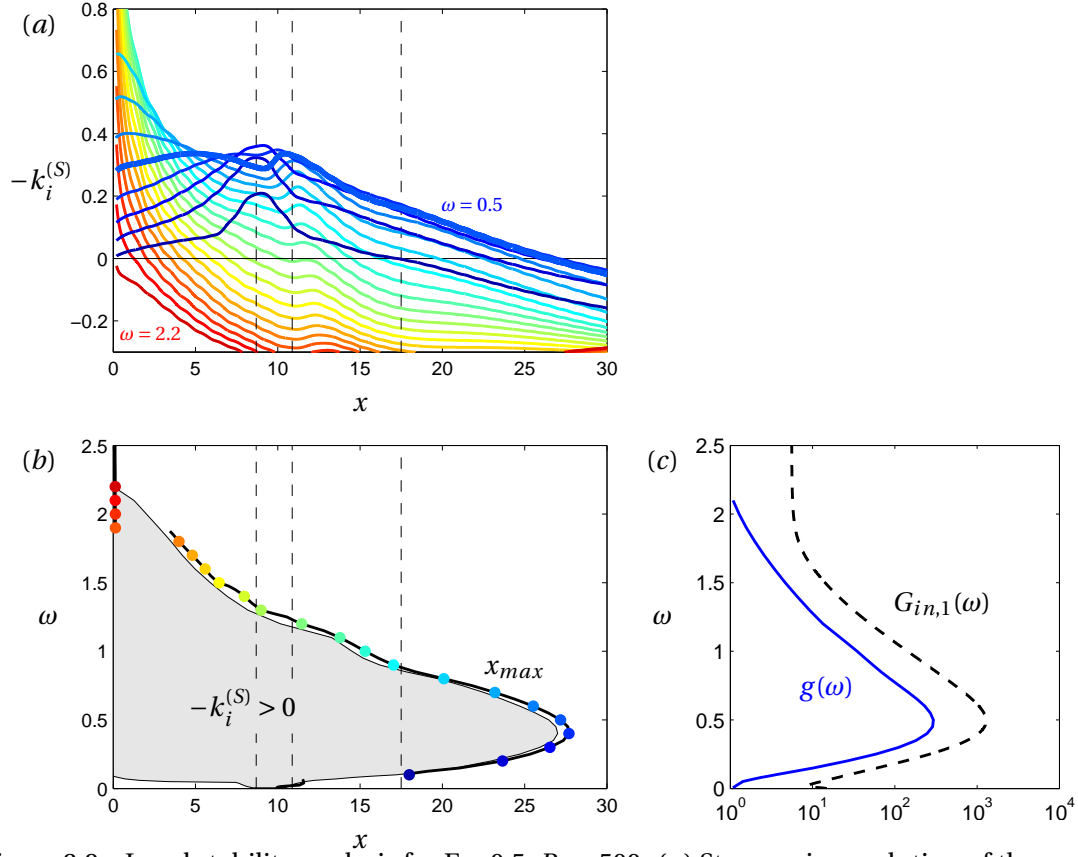
Figure 3.8 – Local stability analysis for $\Gamma = 0.5$, $Re = 500$. (a) Streamwise evolution of the spatial growth rate at different frequencies. (b) Region of instability (shaded area) and location of the maximum of the optimal response energy density (solid line and symbols). (c) Integral amplification factor (solid line) and optimal harmonic gain (dashed line, reproduced from fig. 3.4(a)). The thick line in (a) corresponds to the most amplified frequency $\omega = 0.5$.

(*a*) $\nabla_U G^2_{in,1}/G^2_{in,1}$

(*b*) $\nabla_U E/E$
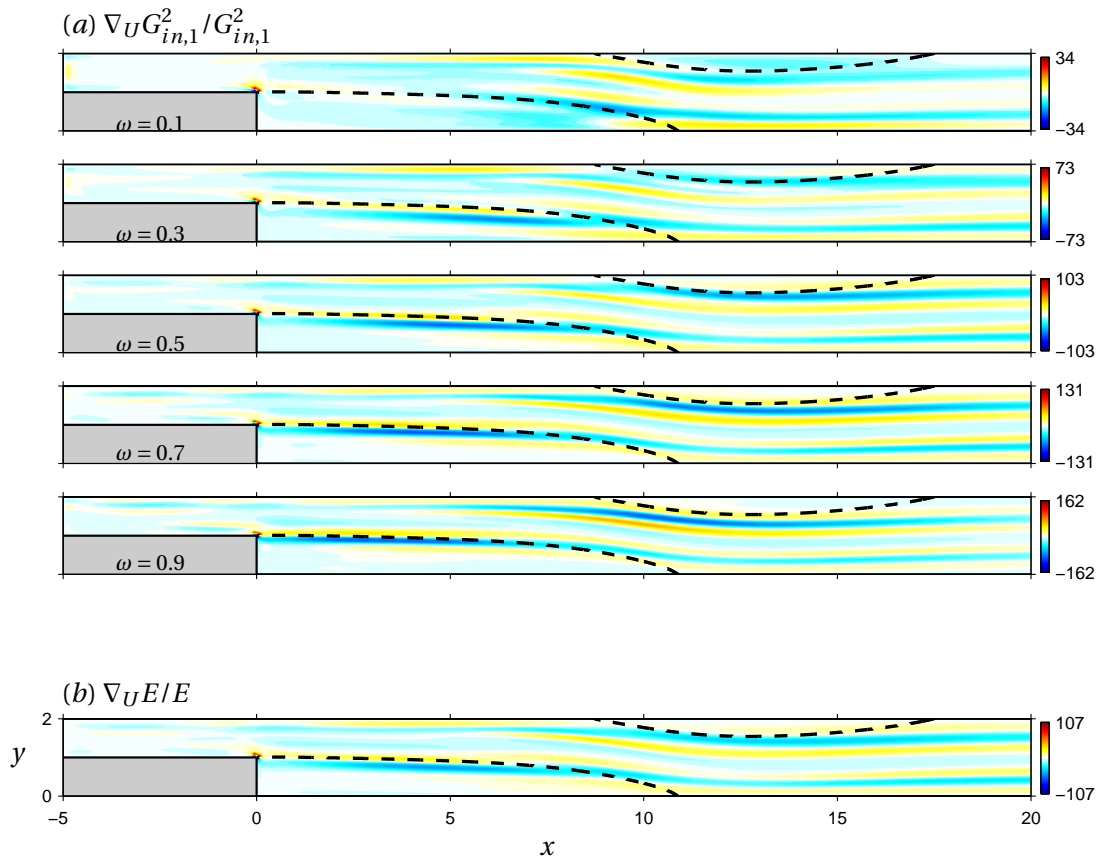
Figure 3.9 – Sensitivity of (*a*) optimal harmonic gain and (*b*) stochastic gain to base flow modification (streamwise component $\nabla_U = \mathbf{e}_x \cdot \nabla_\mathbf{U}$). $\Gamma = 0.5$, $Re = 500$.

(a) $\nabla_{C_x} G^2_{in,1}/G^2_{in,1}$

(b) $\nabla_{C_x} E/E$
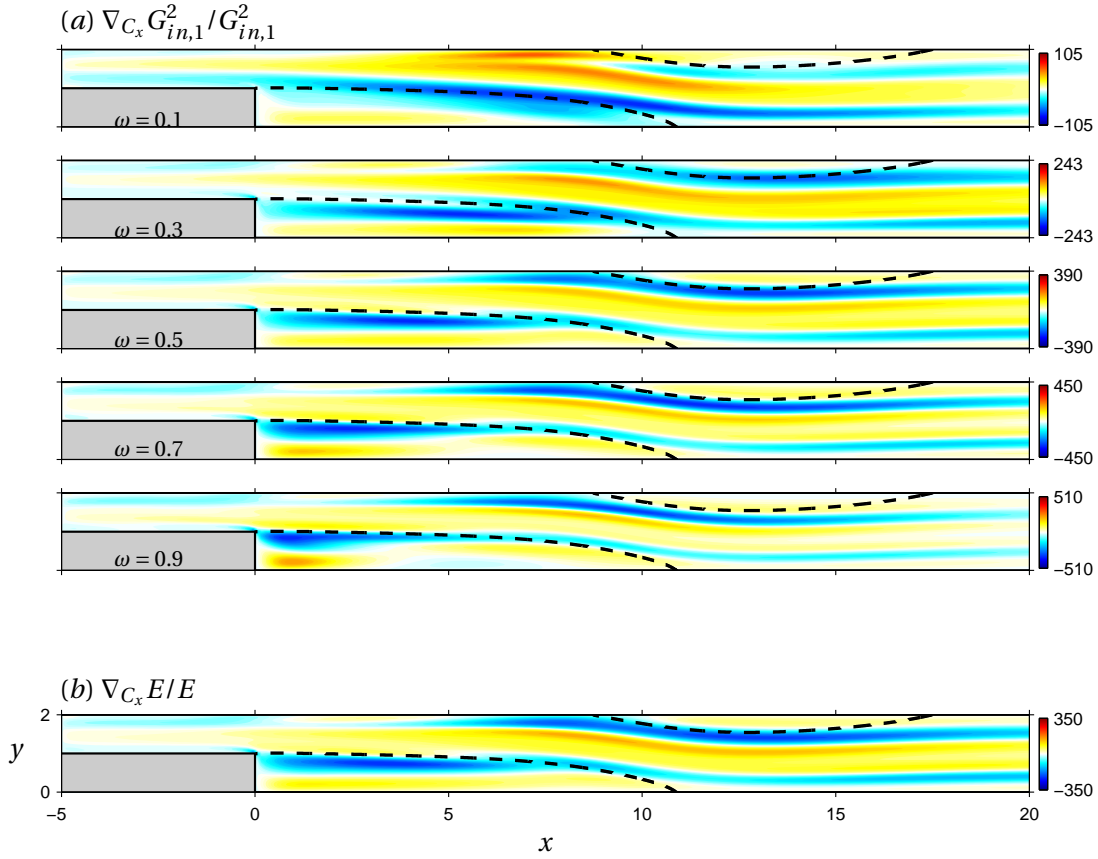
Figure 3.10 – Sensitivity of (a) optimal harmonic gain and (b) stochastic gain to volume control (streamwise component $\nabla_{C_x} = \mathbf{e}_x \cdot \nabla_{\mathbf{C}}$). $\Gamma = 0.5$, $Re = 500$.

sensitivity are found along the shear layers, but also in the lower recirculation zone, while the step corner is less prevalent. For the harmonic optimal gain (fig. 3.10(a)), variations with ω are still present, for instance near the upper wall upstream of the upper separation point. But in this case too, stochastic gain exhibits a sensitivity (fig. 3.10(b)) dominated by that of the harmonic optimal gain at optimal frequency.

It is common, both experimentally and numerically, to use a wire or small cylinder as a simple open-loop device aiming at controlling, for instance, aerodynamic forces or vortex shedding (Strykowski & Sreenivasan, 1990; Igarashi, 1997; Mittal & Raghuvanshi, 2001; Dalton *et al.*, 2001; Cadot, Thiria & Beaudoin, 2009; Parezanović & Cadot, 2009, 2012). Sensitivity analysis is well suited to estimate the effect of a small control cylinder of diameter d, using (i) the sensitivity to volume forcing already computed, and (ii) a simple model for the control force $\mathbf{C}$ exerted by the cylinder on the flow, namely a force opposite to the drag felt by the cylinder in a steady uniform flow at the local velocity $\mathbf{U}_b(x,y)$ (Hill, 1992; Marquet *et al.*, 2008; Meliga *et al.*, 2010; Pralits, Brandt & Giannetti, 2010; Fani *et al.*, 2012): $\delta\mathbf{C}(x,y) = -\frac{1}{2}dC_d(x,y)\|\mathbf{U}_b(x,y)\|\mathbf{U}_b(x,y)\delta(x-x_c, y-y_c)$, where δ is the two-dimensional Dirac delta function, and the drag coefficient C_d depends on the local Reynolds number $Re_d(x,y) = \|\mathbf{U}_b(x,y)\|d/\nu$. Here we choose $d = 0.05$, corresponding to Reynolds numbers $Re_d \leq 25$ ev-

(a) $\delta G^2_{in,1}/G^2_{in,1}$

(b) $\delta E/E$
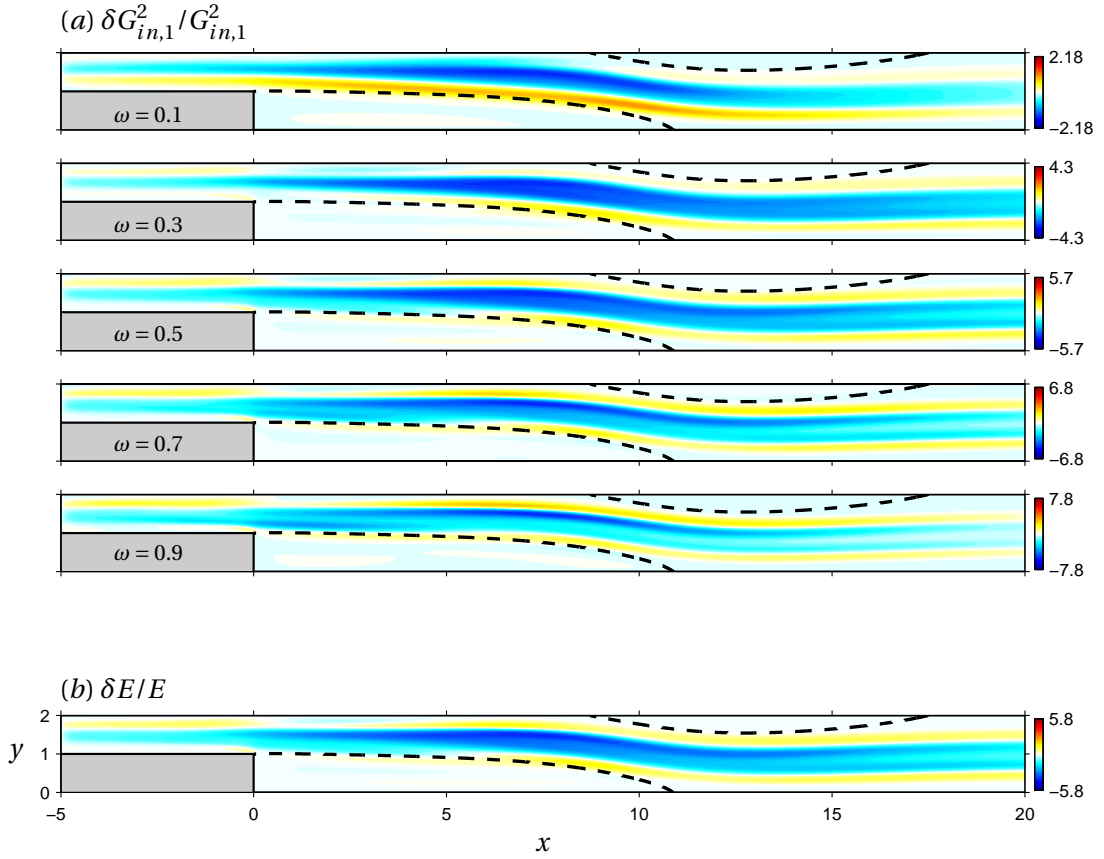
Figure 3.11 – Effect of a small control cylinder of diameter $d = 0.05$ on (a) optimal harmonic gain and (b) stochastic gain. $\Gamma = 0.5$, $Re = 500$.

erywhere in the flow. We therefore use the following composite expression for the drag coefficient:

$$0.5 \le Re_d \le 25: \quad C_d = a + bRe_d^c, a = 0.85, b = 10.6, c = -0.72,$$

$$Re_d \le 0.5: \quad C_d = \frac{8\pi}{Re_d S}\left(1 - \frac{Re_d^2}{32}\left(S - \frac{1}{2} + \frac{5}{16S}\right)\right), \tag{3.18}$$

where $S = \frac{1}{2} - \gamma - \log(Re_d/8)$ and γ is Euler's constant. The former expression is a fit of experimental data from Tritton (1959) and in-house numerical results, the latter is an extension of Oseen's formula $C_d = 8\pi/Re_d S$ for low Reynolds numbers (Oseen, 1910; Proudman & Pearson, 1957) derived by Tomotika & Aoi (1951). In practice, the exact value at low Reynolds number is of little importance: although the drag coefficient goes to infinity like $\sim 1/(Re_d \log Re_d)$ as $Re_d \to 0$ as an artificial consequence of the aerodynamic definition of C_d, the actual force exerted on the cylinder goes to zero like $\sim Re_d/\log Re_d$. The effect of a small control cylinder is shown in figure 3.11. The amplification of stochastic noise decreases when the control cylinder is inserted in a long region corresponding roughly to the region of large velocity, and conversely increases when the control cylinder is inserted in the outer vicinity of recirculation regions where shear is large. Recirculation regions themselves have no significant effect.

Finally, sensitivities to wall control are shown in figure 3.12. Arrows point in the direction of positive sensitivity: at each point along the wall, blowing or suction in the direction of the arrow at that point would increase the gain. More generally, an actuation direction whose scalar product with the sensitivity is positive would increase the gain, while an actuation direction orthogonal to the sensitivity would have no first-order effect. The sensitivity of the harmonic optimal gain (fig. 3.12(a)) is essentially normal to the wall and, again, changes sign with frequency, except notably at the inlet lower wall. The sensitivity of the stochastic gain (fig. 3.12(b)), once again mostly dominated by that of the harmonic optimal gain at optimal frequency, is maximum just upstream of the step corner. Given the sign of the sensitivity, wall suction at this location should reduce the amplification of random perturbations. The step corner is often chosen for wall control in this and related flows (Pastoor, King, Noack & Tadmor, 2005; Beaudoin *et al.*, 2006; Henning & King, 2007; Hervé, Sipp, Schmid & Samuelides, 2012). However, other locations have a sensitivity of comparable magnitude, such as the vertical wall (where blowing should reduce E) or the upper wall of the inlet channel (where suction should reduce E). They might offer interesting alternatives depending on technical feasibility constraints.

5.2 Validation

We illustrate the effect of steady wall control on the flow and use this opportunity to validate the sensitivity analysis. We consider several locations upstream and downstream of the step corner, both at the lower and upper walls, as represented in figure 3.13(a). For the sake of simplicity, and since we observed that sensitivity to wall-normal control was much larger than that of tangential control, we use blowing and suction in the normal direction only. We choose Gaussian actuation profiles $V_c(x) = (-\mathbf{n} \cdot \mathbf{e}_y) \, W \exp(-(x - x_c)^2/\sigma_c^2)/(\sigma_c\sqrt{\pi})$ for control on horizontal walls, and $U_c(y) = (-\mathbf{n} \cdot \mathbf{e}_x) \, W \exp(-(y - y_c)^2/\sigma_c^2)/(\sigma_c\sqrt{\pi})$ for control on the vertical wall; the characteristic width is $\sigma_c = 0.1$ and the flow rate W, positive for blowing and negative for suction since $\mathbf{n}$ points outward. We compare predictions from sensitivity analysis for harmonic and stochastic gains (obtained from sensitivity fields according to $\delta G_{in,k}^2 = (\nabla_{\mathbf{U}_c} G_{in,k}^2 | \boldsymbol{\delta} \mathbf{U}_c)$, $\delta E = (\nabla_{\mathbf{U}_c} E | \boldsymbol{\delta} \mathbf{U}_c)$, and results from full gain calculations for flows actually controlled with the Gaussian actuation profile applied as a boundary condition.

Figure 3.13(b) shows the effect of steady blowing and suction at the upper wall upstream of the step (configuration 4) on the harmonic optimal gain and the first two sub-optimal gains at the optimal frequency $\omega_0 = 0.5$. Predictions from sensitivity analysis (solid lines) are in good agreement with full calculations (symbols), as could be expected for small control amplitudes (less than 0.01, to be compared to the inlet flow rate $2U_\infty h_{in}/3 = 2/3$). The effect of wall suction on the optimal gain at other frequencies is shown in figure 3.13(c). For the stochastic gain, we observe in figure 3.13(d) a good agreement too, but also non-negligible non-linear effects for some configurations, especially configuration 5.

(a) $\nabla_{\mathbf{U}_c} G_{in,1}^2$

$\omega = 0.1$ $\max \| \cdot \|_2 = 3.2 \times 10^4$

$\omega = 0.3$ $\max \| \cdot \|_2 = 1.1 \times 10^7$

$\omega = 0.5$ $\max \| \cdot \|_2 = 1.3 \times 10^8$

$\omega = 0.7$ $\max \| \cdot \|_2 = 5.0 \times 10^7$

$\omega = 0.9$ $\max \| \cdot \|_2 = 6.8 \times 10^6$

(b) $\nabla_{\mathbf{U}_c} E$
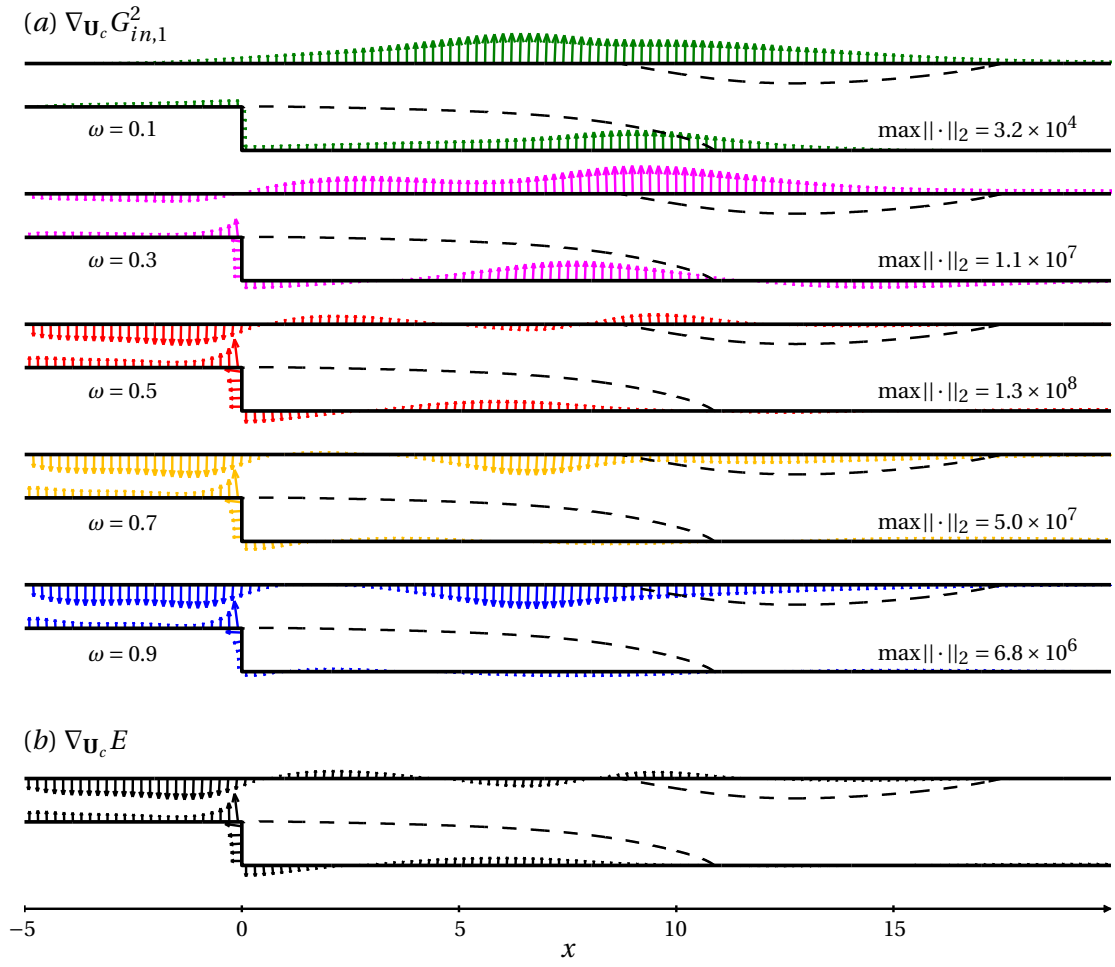
Figure 3.12 – Sensitivity of (a) optimal harmonic gain and (b) stochastic gain to wall control. $\Gamma = 0.5$, $Re = 500$.
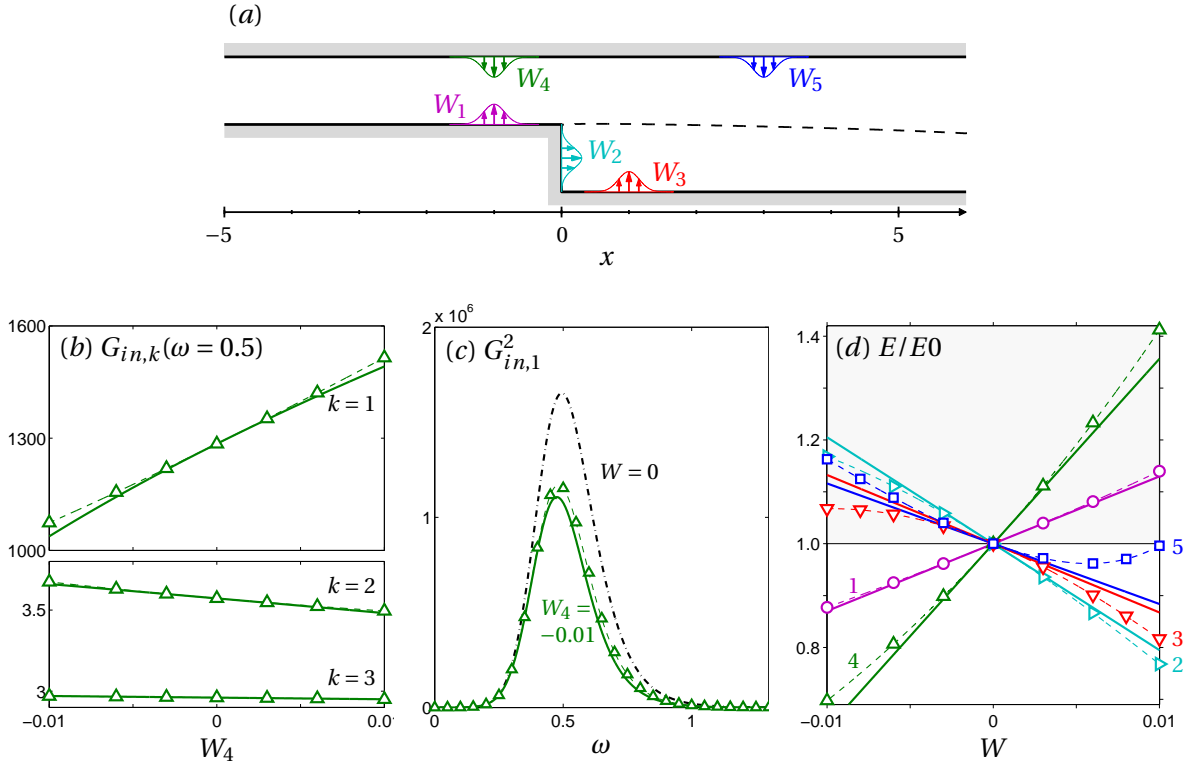
Figure 3.13 – Wall control with steady Gaussian blowing/suction for $\Gamma = 0.5$, $Re = 500$. (*a*) Control configurations 1 to 5. Blowing corresponds to positive flow rates ($W > 0$), suction to negative flow rates ($W < 0$). (*b*) Variation of harmonic gain at $\omega = 0.5$ with flow rate in configuration 4 ($x_c = -1$, $y_c = 2$). (*c*) Overall optimal harmonic gain reduction in control configuration 4 with suction flow rate $W_4 = -0.01$. (*d*) Variation of stochastic gain (normalized by its uncontrolled value) with flow rate. Solid lines show predictions from sensitivity analysis, symbols are actual results from controlled flows.
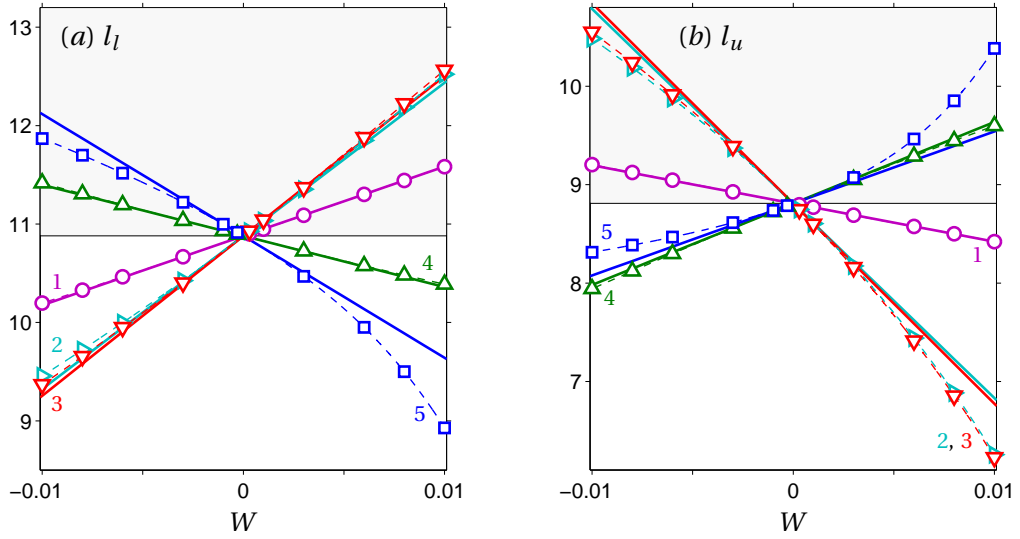
Figure 3.14 – Variation of lower (a) and upper (b) recirculation lengths with flow rate for the same wall control as in figure 3.13. Solid lines show predictions from sensitivity analysis, symbols are actual results from controlled flows.

5.3   Recirculation length

For reference, we show in figure 3.14 the effect of wall actuation on the length of the lower recirculation region, $l_l = x_{lr}$, and the length of the upper recirculation region, $l_u = x_{ur} - x_{us}$. We compare actual results from controlled flows and predictions from sensitivity analysis (Boujo & Gallaire, 2014) applied to the three stagnation points. Relatively small control amplitudes have a significant impact on both recirculation lengths. Inspection of individual contributions (not shown) reveals that the two upstream stagnation points x_{us} and x_{lr} are much more sensitive than x_{ur}. Variations conform to intuition: removing momentum at the lower wall ($W_1, W_2, W_3 < 0$) or injecting momentum at the upper wall ($W_4, W_5 > 0$) tends to deflect the flow downwards, which moves x_{us} and x_{lr} upstream, thereby shortening the lower recirculation region, $\delta l_l < 0$, and elongating the lower one, $\delta l_u > 0$. Comparing figures 3.13(d) and 3.14(a)-(b) for actuation upstream of the corner and on the vertical wall (configurations 1,2 and 4) reveals an interesting correspondence: the stochastic gain E is reduced with suction ($W_1, W_4 < 0$), which corresponds to a shorter lower recirculation region $\delta l_l < 0$ when using suction on the lower wall ($W_1 < 0$), and to a shorter upper recirculation region $\delta l_u < 0$ when using suction on the upper wall ($W_4 < 0$). This is actually true for *any* control location $x \lesssim 1$ on horizontal walls, as appears when inspecting the sensitivity fields of l_l and l_u (not shown here) and comparing with the sensitivity of E: actuation on the lower (resp. upper) wall reduces the stochastic gain when it shortens the recirculation region on the lower (resp. upper) wall.

91

5.4   Towards passive wall actuation

Wall control allows us to choose the actuation direction (blowing or suction) and orientation (angle) freely. This is an advantage over volume control where, typically, a small cylinder can only produce a force in the direction of the flow. The price to pay is a more complex actuation system and a potentially higher power requirement to drive this system, unless one takes advantage of pressure differences: connecting wall regions of relative higher and lower pressure with a small channel could induce natural suction and blowing at the inlet and at the outlet, respectively. This configuration would not require any mechanical device and would therefore constitute a means of passive control.

This could be implemented in the backward facing-step flow between the lower wall upstream of the corner (suction at higher pressure) and the vertical wall (blowing at lower pressure): figure 3.15(a) shows that pressure (solid line) along the horizontal wall is larger than on the vertical wall. At the same time, the sensitivity of E to wall normal actuation (dash-dotted line) is such that the stochastic response can precisely be reduced with blowing on the horizontal wall and suction on the vertical wall.

A crude but simple estimate of the expected reduction in E can be obtained by assuming that connecting points A and B of coordinates $\mathbf{x}_A = (x_A, h_s)$ and $\mathbf{x}_B = (0, y_B)$ with a straight channel results in a fully developed plane Poiseuille flow of mean velocity $U_m = Re\,h_c^2 \Delta P / 12 l_c$, where $\Delta P = P_A - P_B > 0$ is the pressure difference, and h_c and $l_c = \sqrt{x_A^2 + (h_s - y_B)^2}$ are the channel height and length. Assuming further that at both ends the induced flow is localized at points A and B, the velocity vector is

$$\boldsymbol{\delta}\mathbf{U}(\mathbf{x}_A) = \boldsymbol{\delta}\mathbf{U}(\mathbf{x}_B) = U_m \begin{pmatrix} \cos\theta \\ -\sin\theta \end{pmatrix} = \frac{U_m}{l_c} \begin{pmatrix} |x_A| \\ h_s - y_B \end{pmatrix}, \tag{3.19}$$

where $\theta > 0$ is the angle between the channel axis and the horizontal $\mathbf{e}_x$. Taking the inner product with the sensitivity yields the stochastic response reduction

$$\delta E = \frac{Re\,h_c^2 \Delta P}{12 l_c^2} \left(\nabla_{\mathbf{U}_c} E(\mathbf{x}_A) + \nabla_{\mathbf{U}_c} E(\mathbf{x}_B) \right) \cdot \begin{pmatrix} |x_A| \\ h_s - y_B \end{pmatrix}, \tag{3.20}$$

and a similar expression for harmonic gains $G_k^2(\omega)$. When choosing the locations of the channel inlet and outlet, a trade-off exists between pressure difference, channel length, channel angle, and sensitivity: for instance, choosing A far upstream increases both ΔP and l_c, which have opposite effects on the channel velocity; on the other hand, choosing A close to the step corner allows us to benefit from a larger sensitivity but increases the angle between the jet and the wall normal in B.

Figure 3.15(b) shows the optimal harmonic gain reduction for $x_A = -1$, $y_B = 0.75$ and $h_c = 0.15$, as estimated with (3.20) from geometry, pressure and sensitivity information only (solid line), and as obtained from the controlled flow with the channel included in the computa-
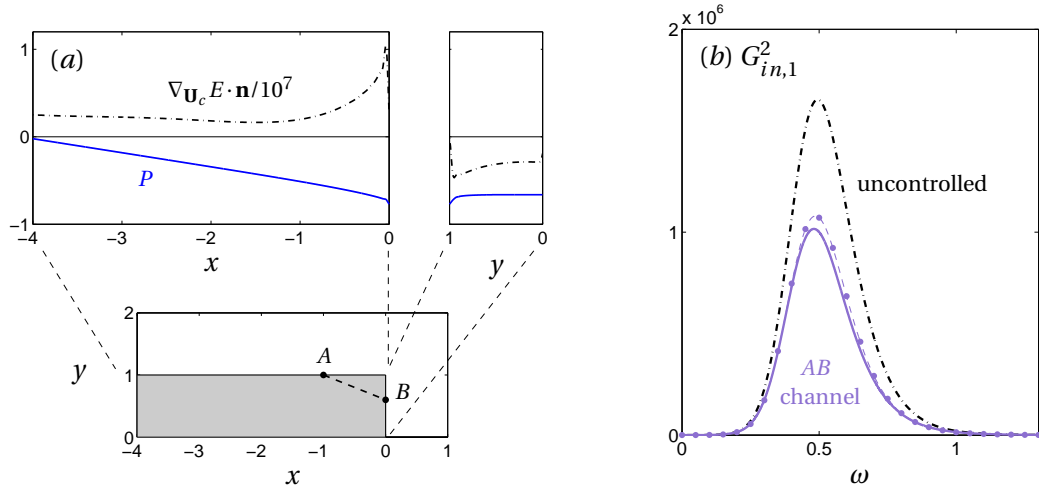
Figure 3.15 – (*a*) Passive control by means of a channel connecting regions of high and low pressure (solid line). The induced flow results in wall suction in *A* and wall blowing in *B*, and reduces the stochastic response *E* as predicted by the sensitivity to wall normal actuation (the dash-dotted line shows the normal component, much larger than the tangential component as observed in figure 3.12). (*b*) Reduction in optimal harmonic gain for $x_A = -1$, $y_B = 0.75$ and channel height $h_c = 0.15$. Dash-dotted line: uncontrolled flow, solid line: estimation from (3.20) (Poiseuille flow concentrated in *A* and *B*), symbols: actual optimal harmonic gain for the flow with channel.

tional mesh (symbols). In spite of strongly simplifying assumptions, the estimated reduction has the correct order of magnitude. Note that the channel velocity scales like h_c^2, thus only a limited benefit can be expected when using small channels.

5.5 Other flow configurations

After a detailed study of the configuration $\Gamma = 0.5$, $Re = 500$ in previous sections, we consider now two other configurations where the sensitivity of stochastic gain is more likely to differ from the sensitivity of the optimal harmonic gain at the optimal frequency. In the first configuration we keep the same geometry ($\Gamma = 0.5$) but decrease the Reynolds number to $Re = 200$; in the second one we use a smaller step with expansion ratio $\Gamma = 0.3$ at the stable Reynolds number $Re = 2800$ (recall that $Re_c > 2900$ for this expansion ratio, as mentioned in section 3). From the harmonic gains shown in figure 3.16 we can make the following remarks: (i) reducing the Reynolds number makes the peak of $G_{in,1}$ less marked, thus possibly increasing the relative importance of frequencies other than the optimal one, as well as the importance of sub-optimal forcings relative to the optimal one; (ii) a double peak appears when reducing the step height, which might result in contributions of equal importance from two well separated frequencies ($\omega_0 = 0.31$ and $\omega_0' = 0.55$ in the present case).

Figures 3.17 and 3.18 show sensitivities to wall control for these two flows. Although slight differences can be noticed, the stochastic gain still has a sensitivity largely dominated by the
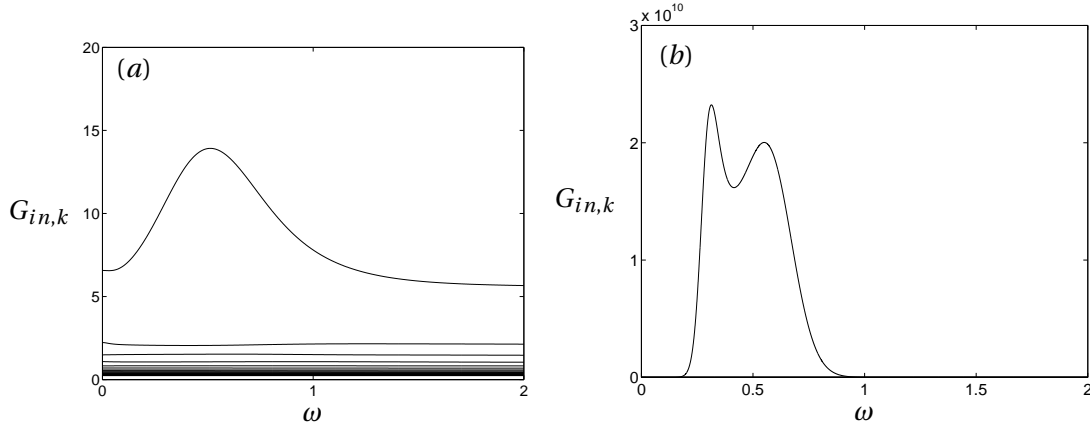
Figure 3.16 – Optimal harmonic gain and sub-optimal gains for inlet forcing. (a) $\Gamma = 0.5$, $Re = 200$, (b) $\Gamma = 0.3$, $Re = 2800$.

sensitivity of the harmonic optimal gain at optimal frequency ω_0. In particular, locations of maximal sensitivity of E appear to be captured robustly by the sensitivity of $G_{in,1}(\omega_0)$. There-fore, even though integrating over a range of frequencies (i.e. performing a weighted average) should have a smoothing effect, the net result is almost unaffected by frequencies far from the optimal one. Close inspection shows that all sensitivity fields (for base flow modification, volume control and wall control) change continuously with ω around the optimal frequency, and slowly enough for their integral to be eventually dominated by $\nabla_* G_{in,1}^2(\omega_0)$. For instance, the two distinct peaks in $G_{in,1}$ for $\Gamma = 0.3$, $Re = 2800$ (fig. 3.16(b)), are actually associated with very similar sensitivity fields. Regarding the insignificant contribution of sub-optimals $k \geq 2$, even for a separation factor with the optimal as small as ∼5-6 at ω_0 and ∼2-3 at other frequen-cies for $\Gamma = 0.5$, $Re = 200$ (fig. 3.16(a)), we conclude that the sub-optimals play a role only at even lower Reynolds numbers, where amplification mechanism are weak anyway. Therefore, sensitivity analysis and steady control design can be conducted with good confidence on the optimal harmonic gain at the optimal frequency alone, rather than on the full stochastic re-sponse, thereby dramatically reducing the computational cost of the process.

6   Conclusion

The response of the two-dimensional flow past a backward-facing step to time-harmonic and time-stochastic forcing localized at the inlet was analysed numerically. In the stable regime, very large amplification was observed, both for harmonic forcing (in a range of preferred fre-quencies) and for stochastic noise, typical of globally stable convectively unstable noise am-plifier flows. Very good agreement with a local spatial stability analysis was found, in terms of most amplified frequencies and of streamwise locations showing the largest response.

To study in a systematic way the effect of small-amplitude steady control in the domain or at the wall, a variational technique was used to derive analytical expressions for the sensitivity

(*a*) $\nabla_{\mathbf{U}_c} G^2_{in,1}$

$\omega = 0.1$
$\max \|\cdot\|_2 = 1.6 \times 10^2$

$\omega = 0.3$
$\max \|\cdot\|_2 = 2.1 \times 10^3$

$\omega = 0.5$
$\max \|\cdot\|_2 = 5.3 \times 10^3$

$\omega = 0.7$
$\max \|\cdot\|_2 = 4.4 \times 10^3$

$\omega = 0.9$
$\max \|\cdot\|_2 = 2.1 \times 10^3$

(*b*) $\nabla_{\mathbf{U}_c} E$

$\max \|\cdot\|_2 = 9.9 \times 10^2$

-5 0 5 10

x

Figure 3.17 – Sensitivity of (*a*) optimal harmonic gain and (*b*) stochastic gain to wall control. $\Gamma = 0.5$, $Re = 200$.

(a) $\nabla_{\mathbf{U}_c} G_{in,1}^2$

$\omega = 0.1$ $\max || \cdot ||_2 = 2.8 \times 10^{11}$

$\omega = 0.3$ $\max || \cdot ||_2 = 1.5 \times 10^{23}$

$\omega = 0.5$ $\max || \cdot ||_2 = 1.7 \times 10^{23}$

$\omega = 0.7$ $\max || \cdot ||_2 = 4.8 \times 10^{22}$

$\omega = 0.9$ $\max || \cdot ||_2 = 1.5 \times 10^{19}$

(b) $\nabla_{\mathbf{U}_c} E$

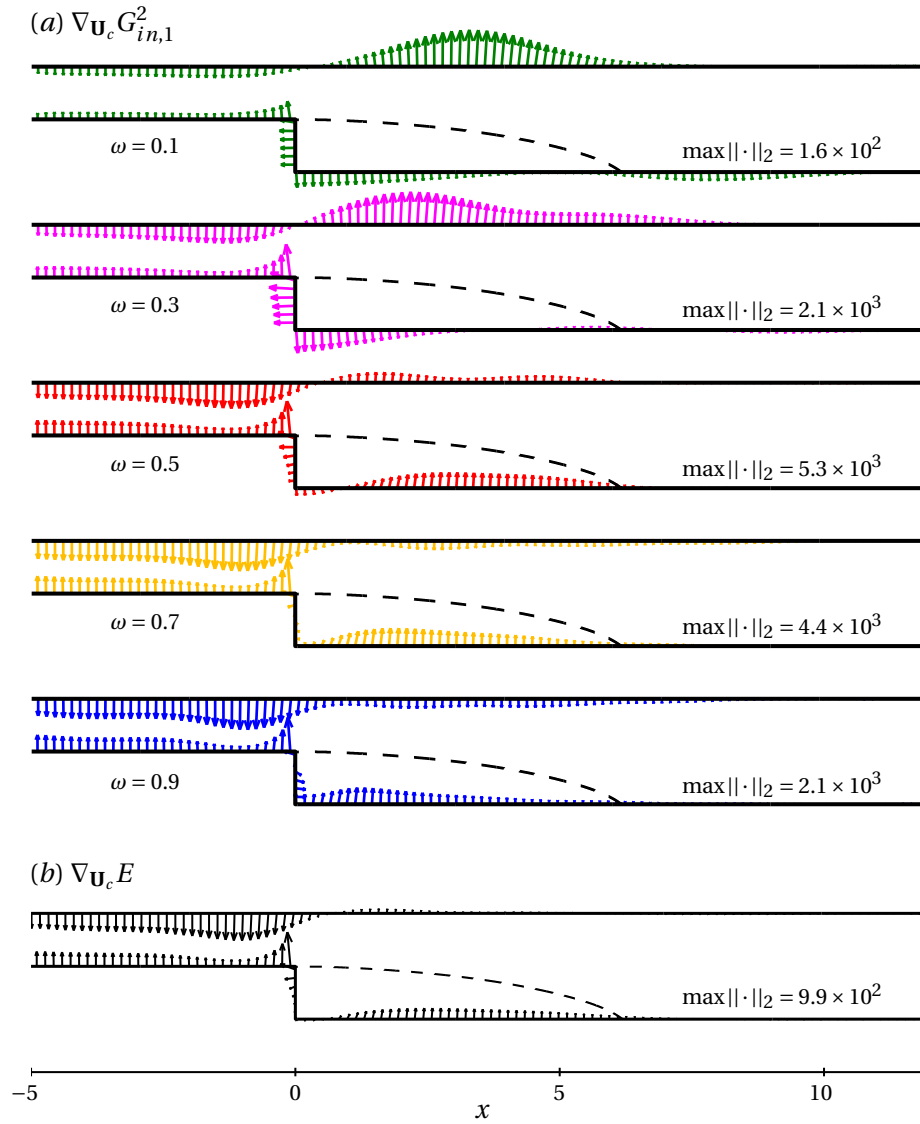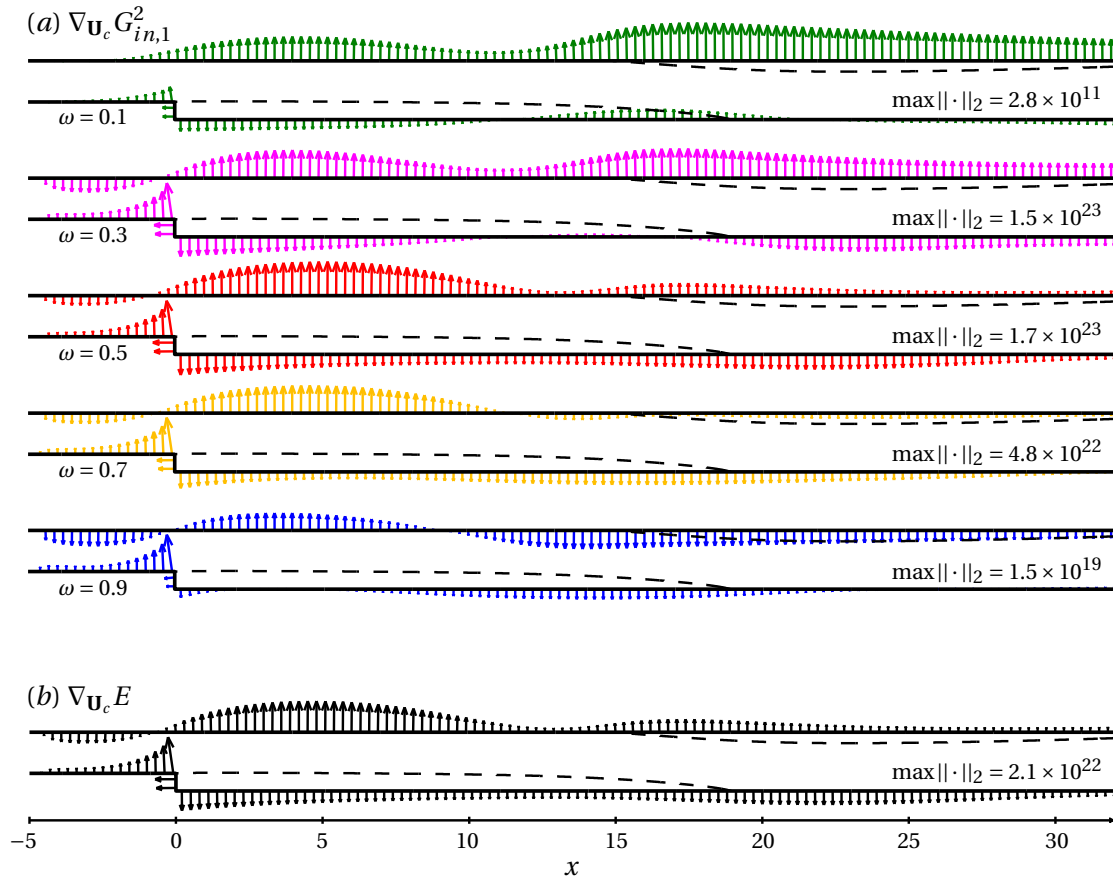$\max || \cdot ||_2 = 2.1 \times 10^{22}$

x

Figure 3.18 – Sensitivity of (a) optimal harmonic gain and (b) stochastic gain to wall control. $\Gamma = 0.3$, $Re = 2800$.

of harmonic and stochastic amplification. The sensitivity of the stochastic response is expressed as a simple combination of sensitivities of the harmonic response. Sensitivity maps resulting from this analysis allow us to identify most sensitive regions (where amplification can be controlled, i.e. increased or decreased, the most efficiently) without computing the actual controlled flows. For several Reynolds number and step heights, it was observed that the sensitivity of the stochastic response was dominated to a large extent by the sensitivity of the optimal harmonic response at the most amplified frequency. This suggests that the design of a passive control aiming at reducing the amplification of stochastic noise can be performed by targeting the optimal harmonic response at the optimal frequency only.

Possible extensions of this method include the analysis of unsteadiness (unsteady flow and/or control), and of three-dimensionality (three-dimensional flow and/or control).

Acknowledgements

Appendix A.   Influence of inlet length

Figures 3.19 and 3.20 show how the harmonic optimal gain, forcing and response depend on inlet length. In the case of volume forcing, the optimal gain $G_{vol,1}$ is not affected by the inlet length (fig. 3.19(a)), since the optimal forcing is well localized near the step corner and not much energy is introduced in the upstream inlet region. This is also illustrated for $\omega = 0.5$ in figure 3.20(a). In the case of inlet forcing, the optimal gain varies significantly when the inlet length is increased from $L_{in} = 1$ to $L_{in} \simeq 5$ (fig. 3.19(b)), consistent with the observation of Garnaud *et al.* (2013). Here $G_{in,1}$ decreases with L_{in} due to viscous effects which smooth out perturbations when they enter the flow farther away upstream of the step corner, i.e. upstream of the locally unstable region. Figure 3.20(b) shows that the optimal response keeps the same spatial structure although the inlet optimal forcing does vary with L_{in} due to a phase effect (as mentioned in section 3, the inlet optimal forcing is similar to the profile of the volume optimal forcing close to $x = L_{in}^+$, and here we fix the phase at $x = 0$, $y = 1.5$ for all cases).

Appendix B.   Influence of cut-off frequency

Figure 3.21 shows the effect of the cut-off frequency in the integral evaluation of the stochastic response. Increasing ω_c yields a slight increase in E because the optimal harmonic gain $G_{in,1}(\omega)$ saturates to a finite value at large frequencies $\omega \gtrsim 2$. However for large Reynolds numbers this saturated value is negligible compared to the peak value $\max_\omega G_{in,1}(\omega)$, and therefore E is unaffected by the exact value of the cut-off frequency, provided it is larger than
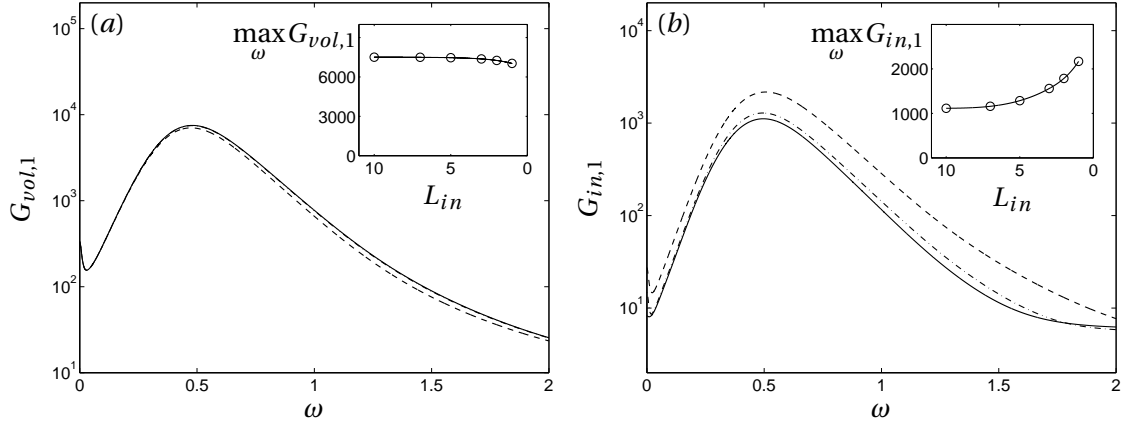
Figure 3.19 – Optimal harmonic gain for (*a*) volume and (*b*) inlet forcing for different inlet lengths: $L_{in} = 1$ (dashed line), $L_{in} = 5$ (dash-dotted line) and $L_{in} = 10$ (solid line). Insets show the convergence of the maximum gain value with increasing inlet length.
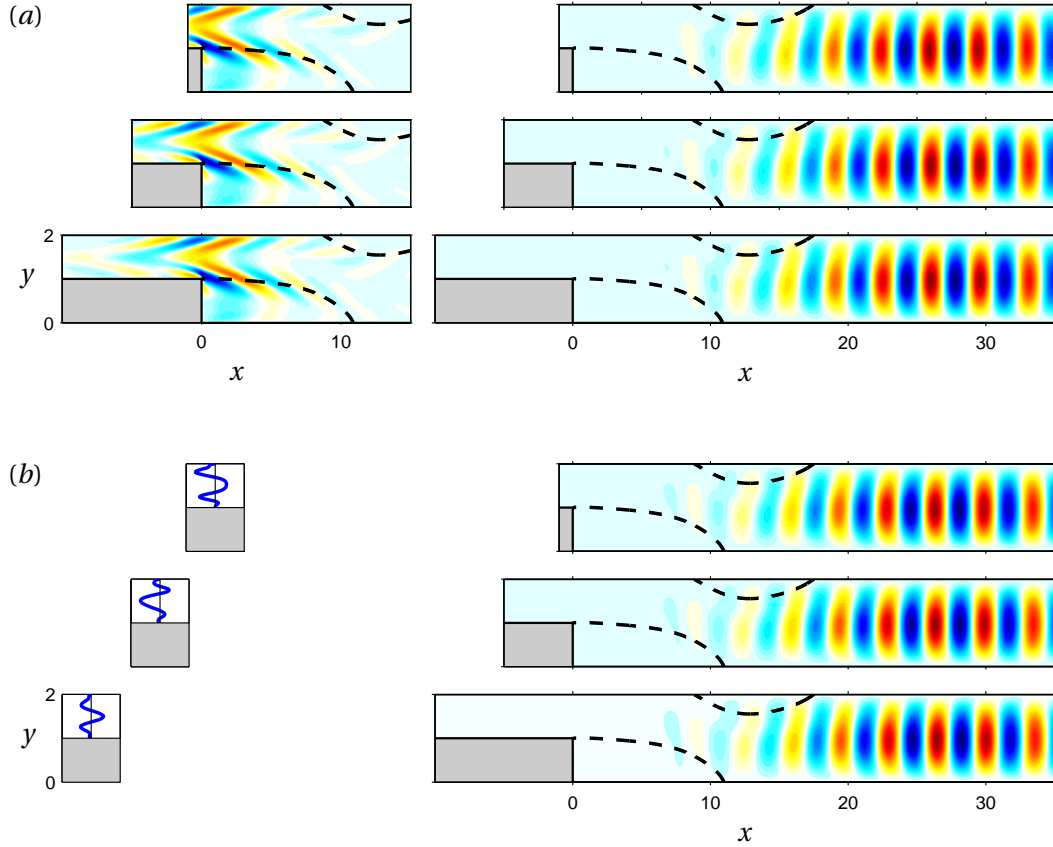
Figure 3.20 – Influence of inlet length ($L_{in} = 1$, 5 and 10 from top to bottom) on optimal harmonic forcing (left; real part of streamwise component $\mathbf{f}_1 \cdot \mathbf{e}_x$) and optimal harmonic response (right; real part of cross-stream component v_1): (*a*) volume forcing and corresponding response, (*b*) inlet forcing and corresponding response. $\Gamma = 0.5$, $Re = 500$, $\omega = 0.5$.
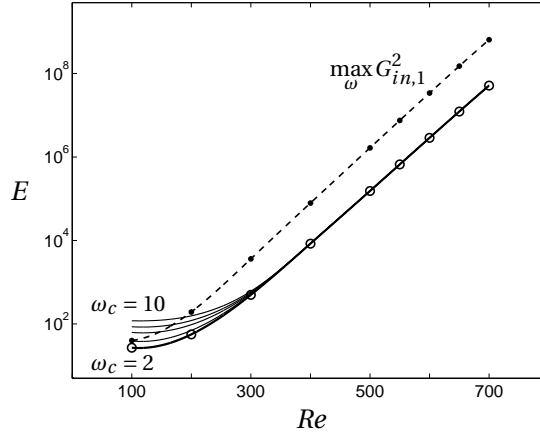
Figure 3.21 – Stochastic gain E vs Re (solid lines) for cut-off frequencies $\omega_c = 2$ (thick line) and $\omega_c = 3, 5, 7, 10$ (thin lines). The maximum harmonic optimal gain is also shown for reference (dashed line).
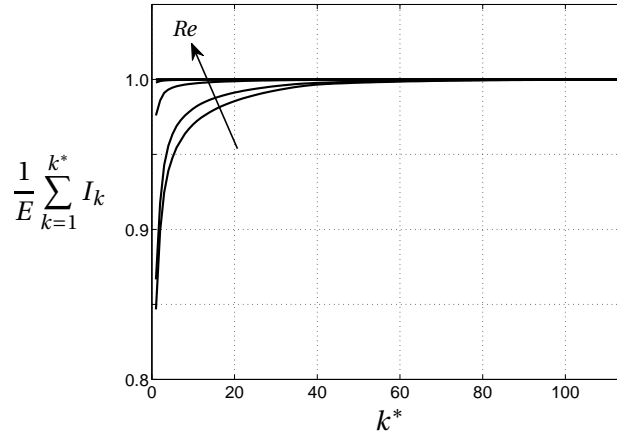
Figure 3.22 – Convergence of the partial sum $\sum_k I_k$ (3.7) towards the full stochastic gain E. Reynolds number Re=100, 200, …, 700.

the optimal frequency, $\omega_c \gtrsim \omega_0 = 0.5$.

Appendix C.   Influence of k and Re

As mentioned in section 5, the stochastic gain E and its sensitivities $\nabla_* E$ are mostly influenced by optimal harmonic quantities G_1^2 and $\nabla_* G_1^2$, especially at larger Reynolds numbers. Figure 3.22 quantifies this phenomenon. At $Re = 300$, the contribution from the optimal harmonic gain alone reaches more than 97% of E, while that of the first sub-optimal gain $k = 2$ amounts to a mere 1%. At a Reynolds number as low as $Re = 100$, $G_{in,1}$ contributes for 85%, $G_{in,2}$ for 5%, and 25 sub-optimals are enough to reach 99% of E.

Chapter 4

Control of flow separation: a geometric perspective

In this chapter, the geometric properties of separated flows are directly used as control objectives. This enables us to derive sensitivity maps of some of the main geometrical quantities in these flows, such as the recirculation length. The method is first demonstrated in section 4.1 on the flow above a wall-mounted bump, already analysed in chapter 2. Section 4.2 is a brief interlude on the approximate computation of separated flows using the Interactive Boundary Layer theory, which allows for an efficient computation of separation properties. Finally, section 4.3 deals with the sensitivity of the recirculation length in a typical oscillator flow, the flow around a circular cylinder, and demonstrates the ambiguity of geometric quantities as surrogate for stability properties above instability threshold.

4.1 Paper: *Manipulating flow separation: sensitivity of stagnation points, separatrix angles and recirculation area to steady actuation*

Manipulating flow separation: sensitivity of stagnation points, separatrix angles and recirculation area to steady actuation

E. Boujo and F. Gallaire

LFMI, École Polytechnique Fédérale de Lausanne, CH-1015 Lausanne, Switzerland

A variational technique is used to derive analytical expressions for the sensitivity of several geometric indicators of flow separation to steady actuation. Considering the boundary layer flow above a wall-mounted bump, the six following representative quantities are considered: the locations of the separation point and reattachment point connected by the separatrix, the separation angles prevailing at these stagnation points, the backflow area and the recirculation area. For each geometric quantity, linear sensitivity analysis allows us to identify regions which are the most sensitive to volume forcing and wall blowing/suction. Validations against full nonlinear Navier−Stokes calculations show excellent agreement for small-amplitude control for all considered indicators. With very resemblant sensitivity maps, the reattachment point, the backflow and recirculation areas are seen to be easily manipulated. In contrast, the upstream separation point and the separatrix angles are seen to remain extremely robust with respect to external steady actuation.

1   Introduction

Flow separation leads in many aerodynamic situations to performance loss, such as reduced lift, increased drag, enhanced fluctuations or noise production. In contrast, separation yields a recirculation region that is often desirable in combustion devices. It is thus not a surprise that there is extensive research on the control of flow separation (Seifert & Pack Melton, 2006). Attempts include, in decreasing order of complexity, closed-loop separation control, harmonic or steady active open-loop control and passive control devices.

Studies on closed loop control strategies remain few: while Alam *et al.* (2006) have provided an analytical approach to closed-loop separation control, based on a kinematic theory of unsteady separation (Haller, 2004), most experimental approaches rely either on low-order reduced models, extracted by physical means or using identification methods (Juillet *et al.*, 2013), or the design of black box controllers (Henning & King, 2007; Gautier & Aider, 2013).

Open-loop control has been successfully applied to separation control: harmonically pulsed synthetic jets (Seifert *et al.*, 1996; Garnier *et al.*, 2012), as well as steady suction or blowing at the wall (e.g. McLachlan (1989) and other references in Fiedler & Fernholz (1990), or Wilson, Schatzman, Arad, Seifert & Shtende (2013) as a combination of steady suction and pulsed blowing). The determination of the best placement and frequency of the actuators was of-

ten left to extensive parameter sweeps resorting to intensive experimental or computational campaigns.

Passive control strategies rely on the optimisation of the geometry or on the addition of appendices, like vortex generators (Pujals *et al.*, 2010). Their efficient and robust design requires ideally so-called sensitivity maps, which allow one to optimally act on the flow, again to the expense of intensive experimental or computational campaigns. A recent example is provided by Parezanović & Cadot (2012), who studied the influence of a thin control wire on the frequency, drag and recirculation length of the wake behind a D-shaped cylinder.

In all these control methods, an essential aspect is determining meaningful and unambiguous control variables. Among those the manipulation of the separation or reattachment locations (Wang, Haller, Banaszuk & Tadmor, 2003; Alam *et al.*, 2006), the recirculation length (Boujo & Gallaire, 2014) or the recirculation area (Gautier & Aider, 2013) appear as valuable and accessible geometric descriptors of the flow. The existence of a link between the geometric properties of separated flows and their stability properties and associated aerodynamic loads is indeed now well accepted.

It is known for instance that the destabilization of the wake of a bluff body as the critical Reynolds number is overcome takes place simultaneously with a decrease of the recirculation length caused by the mean flow distortion maintained by the progressive development of the instability (Zielinska *et al.*, 1997). Therefore, if one is willing to enhance mixing or reduce flow-induced structural vibrations, then it is natural to target the recirculation length. More recently, Parezanović & Cadot (2012) established a clear correlation between base pressure increase (and therefore drag reduction) and mean recirculation area increase in the wake of a D-shaped cylinder at $Re \sim 10^5$, suggesting the direct targeting of the separation properties as a promising control strategy. It is worth also noticing that, in some control attempts (Choi, Hinze & Kunisch, 1999; Passaggia & Ehrenstein, 2013), without being directly targeted, a modification of the recirculation length was observed as a by-product of the control scheme.

The present study is dedicated to the determination of analytical expressions for the sensitivity to steady actuation of the following six geometric indicators of flow separation: the locations of the two separation points which connect the separatrix, the separation angles prevailing at these separation points, the backflow area and the recirculation area. The flow configuration considered is the boundary layer flow above a wall-mounted bump, on which several open-loop (Boujo *et al.*, 2013) and closed-loop (Passaggia & Ehrenstein, 2013) control strategies have been tested numerically.

Section 2 introduces the quantities of interest. Section 3 presents the concepts of sensitivity analysis. Section 4 derives the expression of sensitivity to base flow modification for the quantities of interest. Section 5 gives results and validation.
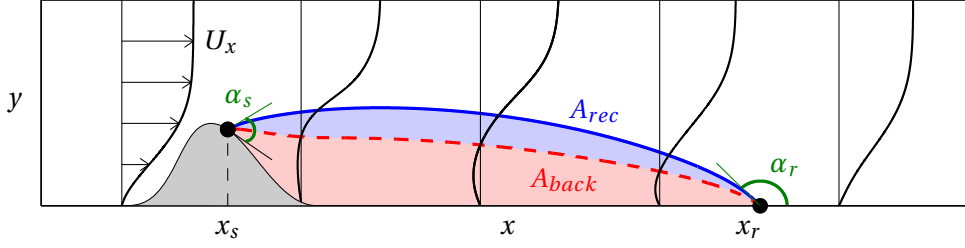
Figure 4.1 – Sketch of the bump flow. The flow separates at $\mathbf{x}_s$ and reattaches at $\mathbf{x}_r$ (black dots). The separatrix (blue solid line) encloses the recirculation region (blue shade) of area A_{rec} and makes angles α_s, α_r with the wall. Velocity profiles are shown with black lines. The curve where $U_x = 0$ (red dashed line) delimits the backflow area (red shade) of area A_{back}. The bump wall geometry is parametrized by $y_w(x)$ and the separatrix by $y_{sep}(x)$. The axes are not to scale.

2 Characteristic quantities in separated flows

The evolution of the recirculation length in separated flows with the increase in Reynolds number *Re* is well documented (Taneda, 1956; Acrivos, Leal, Snowden & Pan, 1968; Nishioka & Sato, 1978; Zielinska *et al.*, 1997; Barkley *et al.*, 2002; Marquillie & Ehrenstein, 2003; Giannetti & Luchini, 2007; Passaggia *et al.*, 2012). For instance, in the flow around a circular cylinder, the recirculation length is known to increase with *Re* in the steady laminar regime while it starts to decrease in mean value as *Re* is further increased in the unsteady laminar regime. In the present study, we turn our attention to several characteristic quantities which describe the separation, in complement to the recirculation length: the locations of the two separation points (x_s and x_r) which connect the separatrix, the separation angles (α_s and α_r) prevailing at these separation points, the backflow area A_{back} and the recirculation area A_{rec}.

As an archetypical flow configuration, we consider the flow of a boundary layer above a wall-mounted bump studied through DNS (Marquillie & Ehrenstein, 2003) and through global stability analysis (Ehrenstein & Gallaire, 2005).

Figure 4.1 is a schematic of typical flow separation. The recirculation region is delimited by the wall and the separating streamline. This particular streamline, or *separatrix*, makes angles α_s and α_r at the separation point $\mathbf{x}_s$ and reattachment point $\mathbf{x}_r$, respectively. The wall geometry is described by $y_w(x)$ and the separatrix by $y_{sep}(x)$, where x is the streamwise direction.

In this paper we focus on the following quantities:

1. The location of stagnation points, i.e. separation point $\mathbf{x}_s$ and reattachment point $\mathbf{x}_r$, characterized by zero wall shear stress

$$\tau_{s/r} = \partial_n U_t(\mathbf{x}_{s/r}) = 0; \qquad (4.1)$$

2. The angle between the separatrix and the wall at the separation and reattachment points, given by Lighthill's formula (Lighthill, 1963)

$$\tan(\alpha_{s/r}) = -3 \frac{\partial_{nt} U_t}{\partial_{nn} U_t}\bigg|_{\mathbf{x}_{s/r}};$$

(4.2)

3. The area of the backflow region $\Omega_{back} = \{(x, y) \,|\, U_x < 0\}$

$$A_{back} = \iint_\Omega \mathbb{1}_{\Omega_{back}}(\mathbf{x}) \, \mathrm{d}\Omega;$$

(4.3)

4. The area of the recirculation region enclosed between the separatrix and the wall $\Omega_{rec} = \{(x, y) \,|\, x_s \le x \le x_r, y_w(x) \le y \le y_{sep}(x)\}$,

$$A_{rec} = \iint_\Omega \mathbb{1}_{\Omega_{rec}}(\mathbf{x}) \, \mathrm{d}\Omega.$$

(4.4)

The steady-state flow $\mathbf{U}(\mathbf{x})$ is calculated by solving the Navier–Stokes equations with a finite element method and an iterative Newton procedure (see details and validation in Boujo *et al.* (2013) and Boujo & Gallaire (2014)) on a mesh highly refined near stagnation points. Stagnation points are found according to (4.1) with a bisection on the wall shear stress $\partial_n U_t$. Angles are calculated using Lighthill's formula (4.2), and are found to agree very well with geometric angles measured between the wall and the separatrix integrated from $\mathbf{U}(\mathbf{x})$ with a fourth-order Runge-Kutta method. Areas (4.3)-(4.4) are computed with a trapezoidal rule for the two-dimensional integration of the backflow region and recirculation region.

Figure 4.2 illustrates how the backflow and recirculation regions grow with Reynolds number in the bump flow. Figure 4.3 shows that the reattachment point moves downstream linearly with *Re*, which is typical of steady separated flows. The areas A_{back} and A_{rec} show the same trend but increase more than linearly since the backflow and recirculation regions become not only much longer but also slightly higher. The separation point moves a little upstream but stays downstream of the bump summit ($x_b = 25$). The reattachment angle is fairly constant, $180 - \alpha_r \simeq 13 - 15°$. The separation angle measured relative to the wall decreases from $\alpha_s = 19°$ to $13°$ between $Re = 100$ and 700, but measured relative to $\mathbf{e}_x$ it is small and almost constant, $\alpha_s + \theta_{wall} \simeq 6 - 8°$. These observations indicate that the main effect of *Re* is to elongate the recirculation region, while the flow remains mostly horizontal.

3 Sensitivity analysis

In this section, analytical expressions are given for the sensitivity of quantities of interest (4.1)-(4.4) to flow modifications, volume forcing and blowing/suction at the wall.

The sensitivity to flow modification of a quantity of interest, say ϕ, is a field defined through
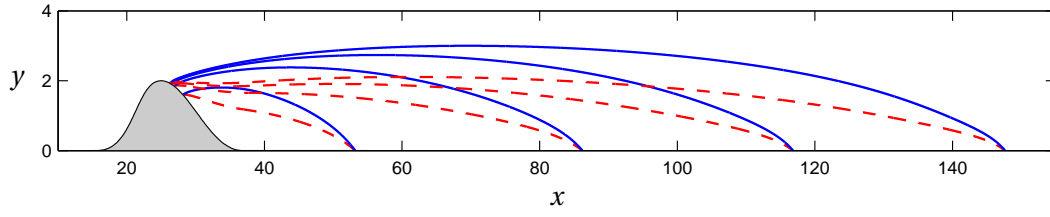
Figure 4.2 – Separatrix (blue solid line) and curve of zero streamwise velocity $U_x = 0$ (red dashed line), at $Re = 100, 300, 500$ and 700. The axes are not to scale.
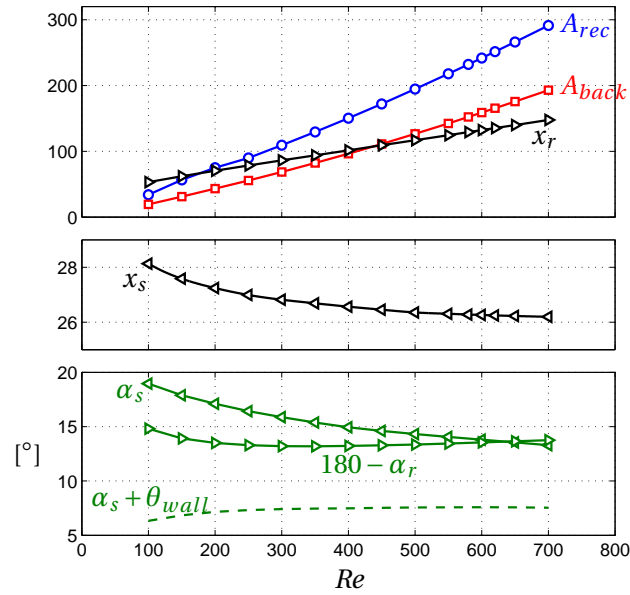
Figure 4.3 – Variation with Reynolds number of characteristic separation quantities: recirculation and backflow areas A_{rec} and A_{back}, separation and reattachment locations x_s and x_r, separation and reattachment angles α_s and α_r relative to the wall (the dashed line shows the "absolute" separation angle $\alpha_s + \theta_{wall}$, i.e. measured relative to $\mathbf{e}_x$).

the first-order variation $\delta\phi$ induced by a small flow modification $\boldsymbol{\delta U}$,

$$\delta\phi = \left(\nabla_{\mathbf{U}}\phi \,|\, \boldsymbol{\delta U}\right), \tag{4.5}$$

and it can be computed as:

$$\frac{\mathrm{d}\phi}{\mathrm{d}\mathbf{U}}\boldsymbol{\delta U} = \lim_{\epsilon\to 0}\frac{\phi(\mathbf{U}+\epsilon\boldsymbol{\delta U})-\phi(\mathbf{U})}{\epsilon}. \tag{4.6}$$

Here $(\mathbf{a}\,|\,\mathbf{b}) = \iint_{\Omega}\mathbf{a}\cdot\mathbf{b}\,\mathrm{d}\Omega$ denotes the two-dimensional inner product in Ω. In other words, the sensitivity $\nabla_{\mathbf{U}}\phi = \mathrm{d}\phi/\mathrm{d}\mathbf{U}$ is the gradient of ϕ with respect to flow modification. Anticipating on section 4, we summarize below the sensitivities to flow modification of stagnation points (4.20), separatrix angles (4.34), and areas (4.46)-(4.52):

$$\delta x_{s/r} = (\nabla_{\mathbf{U}}x_{s/r}\,|\,\boldsymbol{\delta U}) = -\frac{1}{\sqrt{1+y_w'^2}}\frac{\partial_n\delta U_t}{\partial_{nt}U_t}\bigg|_{\mathbf{x}_{s/r}},$$

$$\delta\alpha_{s/r} = (\nabla_{\mathbf{U}}\alpha_{s/r}\,|\,\boldsymbol{\delta U}) = -\frac{3}{A^2+9B^2}\left(A\partial_{nt}-B\partial_{nn}+\frac{A'B-B'A}{B\sqrt{1+y_w'^2}}\partial_n\right)\delta U_t\bigg|_{\mathbf{x}_{s/r}},$$

$$\delta A_{back} = (\nabla_{\mathbf{U}}A_{back}\,|\,\boldsymbol{\delta U}) = -\oint_{\Gamma_{back}}\frac{\delta U_x}{\partial_n U_x}\,\mathrm{d}\Gamma,$$

$$\delta A_{rec} = (\nabla_{\mathbf{U}}A_{rec}\,|\,\boldsymbol{\delta U}) = \int_{x_s}^{x_r}\frac{-1}{U_x(x,y_{sep}(x))}\left(\int_{y_w(x)}^{y_{sep}(x)}\delta U_x(\mathbf{x})\,\mathrm{d}y\right)\mathrm{d}x.$$

In practice, the base flow cannot be modified arbitrarily and one has to resort to an external control, e.g. passive obstacle, heating, magnetic field, geometry modification, wall motion, wall blowing or suction, etc. This control in turn alters the velocity field. Here we focus on steady control, either in the domain Ω by means of a body force (source of momentum) $\mathbf{C}$, or at the wall Γ_w by means of blowing/suction with velocity $\mathbf{U}_c$. However the method is general and easily handles other types of control.

Sensitivities to volume control and wall control can be defined through the variation $\delta\phi$ induced by small-amplitude control,

$$\delta\phi = (\nabla_{\mathbf{C}}\phi\,|\,\boldsymbol{\delta C}) + \langle\nabla_{\mathbf{U}_c}\phi\,|\,\boldsymbol{\delta U}_c\rangle, \tag{4.7}$$

where $\langle\mathbf{a}\,|\,\mathbf{b}\rangle = \int_{\Gamma_w}\mathbf{a}\cdot\mathbf{b}\,\mathrm{d}\Gamma$ denotes the one-dimensional inner product on Γ_w. Sensitivities $\nabla_{\mathbf{C}}\phi = \mathrm{d}\phi/\mathrm{d}\mathbf{C}$ and $\nabla_{\mathbf{U}_c}\phi = \mathrm{d}\phi/\mathrm{d}\mathbf{U}_c$ can be computed as:

$$\frac{\mathrm{d}\phi}{\mathrm{d}\mathbf{C}}\boldsymbol{\delta C} = \lim_{\epsilon\to 0}\frac{\phi(\mathbf{C}+\epsilon\boldsymbol{\delta C})-\phi(\mathbf{C})}{\epsilon}, \quad \frac{\mathrm{d}\phi}{\mathrm{d}\mathbf{U}_c}\boldsymbol{\delta U}_c = \lim_{\epsilon\to 0}\frac{\phi(\mathbf{U}_c+\epsilon\boldsymbol{\delta U}_c)-\phi(\mathbf{U}_c)}{\epsilon}. \tag{4.8}$$

Taking into account the definition of ϕ, and enforcing the Navier–Stokes equations to be sat-
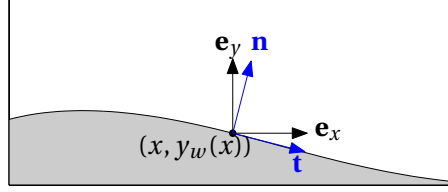
Figure 4.4 – Sketch of tangent and normal vectors to the wall at $(x, y) = (x, y_w(x))$.

isfied by the flow, a Lagrangian method yields the sensitivities

$$\nabla_{\mathbf{C}}\phi = \mathbf{U}^{\dagger}, \quad \nabla_{\mathbf{U}_c}\phi = -P^{\dagger}\mathbf{n} - Re^{-1}\nabla\mathbf{U}^{\dagger}\mathbf{n}, \tag{4.9}$$

where the adjoint flow $(\mathbf{U}^{\dagger}, P^{\dagger})^T$ is solution of the non-homogeneous linear equations

$$\nabla \cdot \mathbf{U}^{\dagger} = 0, \quad -\mathbf{U} \cdot \nabla\mathbf{U}^{\dagger} + \mathbf{U}^{\dagger} \cdot \nabla\mathbf{U}^{T} - \nabla P^{\dagger} - Re^{-1}\nabla^2\mathbf{U}^{\dagger} = \nabla_{\mathbf{U}}\phi, \tag{4.10}$$

with boundary condition $\mathbf{U}^{\dagger} = \mathbf{0}$ at the wall. The forcing term in (4.10) is the sensitivity of ϕ to flow modification (4.6), which must therefore be computed beforehand, using expressions derived in detail in section 4 for all quantities of interest (4.1)-(4.4). Using the same finite element method as for the determination of the base flow, sensitivities (4.9) are obtained by solving the adjoint equations (4.10) in weak form, particularly convenient to express the forcing term $\nabla_{\mathbf{U}}\phi$.

4 Derivation of sensitivities to flow modification

In this section, analytical expressions are derived for the sensitivity of quantities of interest (4.1)-(4.4) to flow modification.

We recall for later use that the wall Γ_w is parametrized by $(x, y) = (x, y_w(x))$, as shown in figure 4.4. Unit vectors tangent and normal to the wall are noted $\mathbf{t}$ and $\mathbf{n}$, and ∂_t, ∂_n stand for derivatives along $\mathbf{t}$ and $\mathbf{n}$.

4.1 Stagnation points

As expressed in (4.1), steady separation and reattachment points $\mathbf{x}_s = (x_s, y_w(x_s))$ and $\mathbf{x}_r = (x_r, y_w(x_r))$ are characterized by zero wall shear stress. Following Boujo & Gallaire (2014), stagnation points are redefined in terms of characteristic functions:

$$x_s = \int_0^{x^*} H(\tau(x)) \, \mathrm{d}x = \int_0^{x^*} G(x) \, \mathrm{d}x, \tag{4.11}$$

$$x_r = \int_{x^*}^{\infty} H(-\tau(x)) \, \mathrm{d}x + x^* = \int_{x^*}^{\infty} 1 - G(x) \, \mathrm{d}x + x^*, \tag{4.12}$$
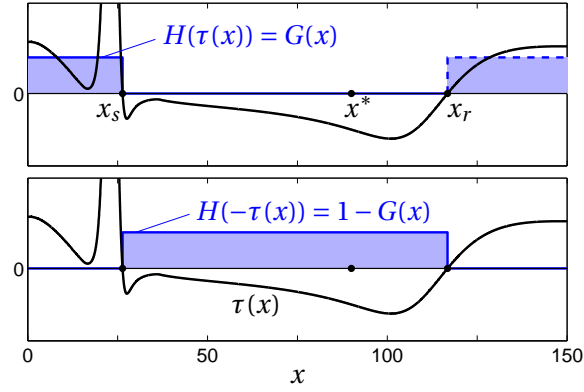
Figure 4.5 – Wall shear stress and associated Heaviside functions appearing in the expression of the stagnation points (4.11)-(4.12).

where $\tau(x) = \partial_n U_t|_{(x,y_w(x))}$ is the wall shear stress, H is the Heaviside step function defined as $H(\gamma < 0) = 0$, $H(\gamma > 0) = 1$, and x^* is any streamwise location inside the recirculation region. As illustrated in figure 4.5, the integrand in (4.11) is equal to 1 upstream of the separation point, therefore integrating over $0 \le x \le x^*$ does indeed yield the coordinate x_s. Similarly, the integrand in (4.12) is equal to 1 upstream of the reattachment point, and integrating in x yields the coordinate x_r.

We assume for the sake of clarity that reattachment occurs far enough downstream where the wall is horizontal and $\tau(x_r) = \partial_y U_x|_{(x_r,y_w(x_r))}$, which is verified in practice for all the Reynolds numbers considered. A flow modification $\delta\mathbf{U}$ makes the reattachment point move by the following amount:

$$\delta x_r = \lim_{\epsilon \to 0} \frac{x_r(\mathbf{U} + \epsilon\delta\mathbf{U}) - x_r(\mathbf{U})}{\epsilon} \tag{4.13}$$

$$= \lim_{\epsilon \to 0} \frac{1}{\epsilon} \int [H(-\tau(x) - \epsilon\delta\tau(x)) - H(-\tau(x))]\, \mathrm{d}x \tag{4.14}$$

$$= \int -\frac{\mathrm{d}H}{\mathrm{d}\gamma}\bigg|_{\gamma=-\tau(x)} \delta\tau(x)\, \mathrm{d}x \tag{4.15}$$

$$= \int -\left(\frac{\mathrm{d}\tau}{\mathrm{d}x}(x)\right)^{-1} \frac{\mathrm{d}G}{\mathrm{d}x}(x)\, \delta\tau(x)\, \mathrm{d}x \tag{4.16}$$

$$= \int -\left(\frac{\mathrm{d}\tau}{\mathrm{d}x}(x)\right)^{-1} \delta(x - x_r)\, \delta\tau(x)\, \mathrm{d}x \tag{4.17}$$

$$= -\frac{\delta\tau(x_r)}{\mathrm{d}_x\tau|_{(x_r,y_w(x_r))}} \tag{4.18}$$

where (4.16) comes from the chain rule differentiation $\dfrac{\mathrm{d}(1-G)}{\mathrm{d}x}(x) = -\dfrac{\mathrm{d}H}{\mathrm{d}\gamma}\bigg|_{\gamma=-\tau(x)} \dfrac{\mathrm{d}\tau}{\mathrm{d}x}(x)$, and (4.17) is the result of $\dfrac{\mathrm{d}G}{\mathrm{d}x}(x) = \delta(x - x_r)$ with $\delta(x)$ the Dirac delta function, since G increases
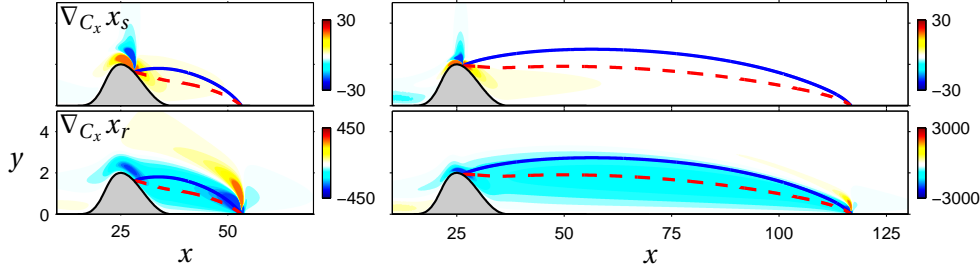
Figure 4.6 – Sensitivity of stagnation points x_s, x_r, with respect to streamwise volume control C_x. Left: $Re = 100$, right: $Re = 500$. The blue solid line is the separatrix, the red dashed line is the curve where $U_x = 0$.

from 0 to 1 at $x = x_r$. Finally:

$$\delta x_r = (\nabla_{\mathbf{U}} x_r \,|\, \boldsymbol{\delta U}) = - \left.\frac{\partial_y \delta U_x}{\partial_{xy} U_x}\right|_{\mathbf{x}_r}. \tag{4.19}$$

The variation of the separation point is obtained in a similar way, with only slight sign differences. First, the chain rule derivation of $G(x) = H(\tau(x))$ reads $\dfrac{\mathrm{d}G}{\mathrm{d}x}(x) = \left.\dfrac{\mathrm{d}H}{\mathrm{d}\gamma}\right|_{\gamma=\tau(x)} \dfrac{\mathrm{d}\tau}{\mathrm{d}x}(x)$. Second, the expression in terms of Dirac delta is $\dfrac{\mathrm{d}G}{\mathrm{d}x}(x) = -\delta(x - x_s)$ since G decreases from 1 to 0 at $x = x_s$. Taking into account the wall geometry, one obtains:

$$\delta x_s = (\nabla_{\mathbf{U}} x_s \,|\, \boldsymbol{\delta U}) = - \frac{1}{\sqrt{1 + y_w'^2}} \left.\frac{\partial_n \delta U_t}{\partial_{nt} U_t}\right|_{\mathbf{x}_s}. \tag{4.20}$$

Expression (4.20) is valid for the reattachment point too, where $y_w' = 0$, $\mathbf{t} \equiv \mathbf{e}_x$, and $\mathbf{n} \equiv \mathbf{e}_y$.

Figure 4.6 shows the sensitivity of stagnation points to volume control in the streamwise direction $C_x = \mathbf{C} \cdot \mathbf{e}_x$ obtained at $Re = 100$ and 500 using (4.19)-(4.20) and the method presented in section 3. Red (resp. blue) regions indicate where a localized, small-amplitude body force oriented along $\mathbf{e}_x$ would move stagnation points upstream, $\delta x_{s/r} > 0$ (resp. downstream, $\delta x_{s/r} < 0$). The separation point is mostly sensitive near $\mathbf{x}_s$. The reattachment point is sensitive near $\mathbf{x}_r$, but also at the bump summit, in the whole shear layer along the separatrix, and in the recirculation region.

110

4.2   Separation and reattachment angles

It is remarkable but not well known that the angle between the separatrix and the wall can be expressed analytically as a function of flow quantities at the stagnation point, as expressed in (4.2). We recall briefly Lighthill's original presentation (Lighthill, 1963). For the sake of simplicity we assume first that the wall is flat and horizontal, $y_w(x) = 0$. A Taylor expansion of the streamwise velocity near the wall, $y \ll 1$, reads

$$U_x(x, y) = U_x(x, 0) + \partial_y U_x(x, 0)\, y + \partial_{yy} U_x(x, 0) \frac{y^2}{2} + \mathcal{O}(y^3). \tag{4.21}$$

This expression is conveniently recast using (i) the no-slip condition $U_x(x, 0) = 0$, (ii) the vorticity $\omega(x, 0) = -\partial_y U_x(x, 0)$, and (iii) the streamwise momentum equation $\partial_{yy} U_x(x, 0) = Re\partial_x p(x, 0)$:

$$U_x(x, y) = -\omega(x, 0)\, y + \frac{Re}{2}\partial_x p(x, 0)\, y^2 + \mathcal{O}(y^3). \tag{4.22}$$

Equivalently, the stream function defined as $U_x = \partial_y \psi$ reads

$$\psi(x, y) = -\frac{1}{2}\omega(x, 0)\, y^2 + \frac{Re}{6}\partial_x p(x, 0)\, y^3 + \mathcal{O}(y^4). \tag{4.23}$$

The separatrix $\psi = 0$ is thus described by $y_{sep}(x) = 3\omega(x, 0)/Re\partial_x p(x, 0)$ and separates from or reattaches to the wall with the angle α such that

$$
\begin{aligned}
\tan(\alpha) &= \frac{\mathrm{d}y_{sep}}{\mathrm{d}x} = \frac{3}{Re}\left(\frac{\partial_x \omega}{\partial_x p} - \omega\frac{\partial_{xx} p}{(\partial_x p)^2}\right) \\
&= \frac{3}{Re}\frac{\partial_x \omega}{\partial_x p} = -3\frac{\partial_{xy} U_x}{\partial_{yy} U_x}
\end{aligned}
\tag{4.24}
$$

because $\omega(x_{s/r}, 0) = 0$. Equation (4.24) is valid for a curved or inclined wall too, hence recovering (4.2). A longer but similar derivation is possible following the steps of Haller (2004) for unsteady flows, and of course the same expression is also obtained if taking all quantities as steady in his final expression.

To derive the sensitivity of the angle, we introduce the function f defined on the wall

$$f(\mathbf{U}, x) = \tan^{-1}\left(-3\frac{\partial_{nt} U_t}{\partial_{nn} U_t}\bigg|_{(x, y_w(x))}\right), \tag{4.25}$$

where $\mathbf{U}$ and x are treated as independent variables. The separation and reattachment angles are equal to $\alpha_{s/r} = f(\mathbf{U}, x_{s/r})$. Their variation with flow modification is

$$\delta\alpha_{s/r} = (\nabla_{\mathbf{U}}\alpha_{s/r}\,|\,\delta\mathbf{U}) = \left(\frac{\partial f}{\partial \mathbf{U}} + \frac{\partial f}{\partial x}\bigg|_{x_{s/r}}\frac{\mathrm{d}x_{s/r}}{\mathrm{d}\mathbf{U}}\,\bigg|\,\delta\mathbf{U}\right), \tag{4.26}$$
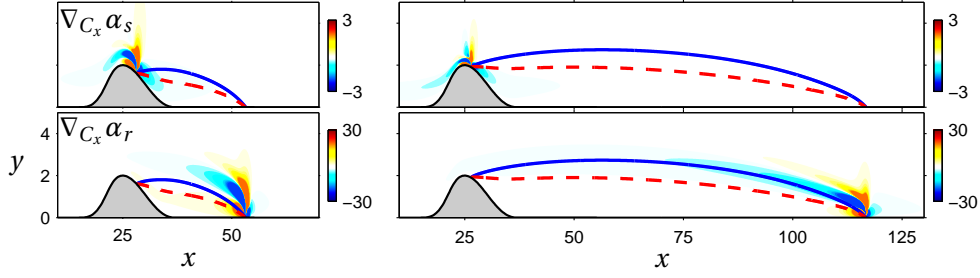
Figure 4.7 – Sensitivity of separation and reattachment angles α_s, α_r, with respect to streamwise volume control C_x. Left: $Re = 100$, right: $Re = 500$. The blue solid line is the separatrix, the red dashed line is the curve where $U_x = 0$.

where the first term of the sensitivity is the direct angle variation due to the change in tangential velocity U_t, while the second term is the indirect angle variation due to the displacement of the stagnation points $\mathbf{x}_{s/r}$. Before deriving in detail each of the terms of (4.26) we give their expression below:

$$\left(\frac{\partial f}{\partial \mathbf{U}} \,\middle|\, \boldsymbol{\delta}\mathbf{U} \right) = -3 \frac{A\partial_{nt}\delta U_t - B\partial_{nn}\delta U_t}{A^2 + 9B^2} \Bigg|_{\mathbf{x}_{s/r}}, \tag{4.27}$$

$$\frac{\partial f}{\partial x}\Bigg|_{\mathbf{x}_{s/r}} \delta x_{s/r} = -3 \frac{B'A - A'B}{A^2 + 9B^2} \delta x_{s/r}, \tag{4.28}$$

$$\delta x_{s/r} = \left(\frac{\mathrm{d}x_{s/r}}{\mathrm{d}\mathbf{U}} \,\middle|\, \boldsymbol{\delta}\mathbf{U} \right) = \left(\nabla_{\mathbf{U}} x_{s/r} \,\middle|\, \boldsymbol{\delta}\mathbf{U} \right), \tag{4.29}$$

where

$$A(x) = \partial_{nn} U_t(x, y_w(x)), \tag{4.30}$$

$$B(x) = \partial_{nt} U_t(x, y_w(x)), \tag{4.31}$$

$$A'(x) = 3 \frac{y_w''}{1 + y_w'^2} \partial_{nn} U_n + \sqrt{1 + y_w'^2} \partial_{nnt} U_t, \tag{4.32}$$

$$B'(x) = \frac{y_w''}{1 + y_w'^2} (\partial_{nn} U_t + 2\partial_{nt} U_n) - \sqrt{1 + y_w'^2} \partial_{nnt} U_n. \tag{4.33}$$

Combining equations (4.26)-(4.33) yields:

$$\delta\alpha_{s/r} = \left(\nabla_{\mathbf{U}} \alpha_{s/r} \,\middle|\, \boldsymbol{\delta}\mathbf{U} \right)$$

$$= -\frac{3}{A^2 + 9B^2} \left(A\partial_{nt} - B\partial_{nn} + \frac{A'B - B'A}{B\sqrt{1 + y_w'^2}} \partial_n \right) \delta U_t \Bigg|_{\mathbf{x}_{s/r}}. \tag{4.34}$$

Figure 4.7 shows the sensitivity of separatrix angles to streamwise volume control obtained at $Re = 100$ and 500 using (4.34). Like stagnation points, the separation angle is mostly sensitive

near $\mathbf{x}_s$, and the reattachment angle near $\mathbf{x}_r$. These sensitivity maps show complex structures, with regions of opposite signs close to each other. This indicates that a small displacement of the forcing location could result in changing the sign of the variation $\delta\alpha$.

We now turn to the derivation of the three terms in (4.26). The latter term (4.29) is precisely the variation of stagnation points (4.19)-(4.20). Next, the variation of f with flow modification (at fixed x) is:

$$\delta f = \left(\frac{\partial f}{\partial \mathbf{U}} \,\middle|\, \delta \mathbf{U} \right) = \lim_{\epsilon \to 0} \frac{f(\mathbf{U} + \epsilon \delta \mathbf{U}, x_{s/r}) - f(\mathbf{U}, x_{s/r})}{\epsilon}, \tag{4.35}$$

where, at first order:

$$\begin{aligned}
f(\mathbf{U} + \epsilon \delta \mathbf{U}, x_{s/r}) &= \tan^{-1}\left(-3 \frac{\partial_{nt}(U_t + \epsilon \delta U_t)}{\partial_{nn}(U_t + \epsilon \delta U_t)} \right) \\
&= \tan^{-1}\left(-3 \frac{\partial_{nt} U_t}{\partial_{nn} U_t} - 3\epsilon \frac{\partial_{nn} U_t \partial_{nt} \delta U_t - \partial_{nt} U_t \partial_{nn} \delta U_t}{(\partial_{nn} U_t)^2} \right) \\
&= \tan^{-1}\left(-3 \frac{\partial_{nt} U_t}{\partial_{nn} U_t} \right) - \frac{3\epsilon}{1 + \left(-3 \frac{\partial_{nt} U_t}{\partial_{nn} U_t} \right)^2} \frac{\partial_{nn} U_t \partial_{nt} \delta U_t - \partial_{nt} U_t \partial_{nn} \delta U_t}{(\partial_{nn} U_t)^2} \\
&= \tan^{-1}\left(-3 \frac{\partial_{nt} U_t}{\partial_{nn} U_t} \right) - 3\epsilon \frac{\partial_{nn} U_t \partial_{nt} \delta U_t - \partial_{nt} U_t \partial_{nn} \delta U_t}{(\partial_{nn} U_t)^2 + 9(\partial_{nt} U_t)^2},
\end{aligned} \tag{4.36}$$

which yields expression (4.27).

Finally, the variation of $f(\mathbf{U}, x) = \tan^{-1}(-3B(x)/A(x))$ with x (for fixed flow conditions) is derived in a similar way, with straightforward composition of derivatives of $\tan^{-1}$ and of a quotient:

$$\delta f = \frac{\partial f}{\partial x}\bigg|_{x_{s/r}} \delta x_{s/r} = -3 \frac{1}{1 + (3B/A)^2} \frac{AB' - BA'}{A^2} \tag{4.37}$$

$$= -3 \frac{B'A - A'B}{A^2 + 9B^2} \delta x_{s/r}, \tag{4.38}$$

which yields expression (4.28). However, some care is needed when computing the derivatives of A and B. Although the streamwise derivative of the *total* velocity field at the wall $\partial_x \mathbf{U}$ is related in a simple way to the tangential derivative $\partial_t \mathbf{U}$ by geometric considerations,

$$\mathrm{d}_x \mathbf{U}|_{(x, y_w(x))} = (\partial_x + y_w' \partial_y) \mathbf{U} = \sqrt{1 + y_w'^2} \, \partial_t \mathbf{U}, \tag{4.39}$$

this is true neither for *individual* velocity components nor for velocity *derivatives*. For example:

$$\mathrm{d}_x (\partial_n U_t)|_{(x, y_w(x))} \neq (\partial_x + y_w' \partial_y)(\partial_n U_t) = \sqrt{1 + y_w'^2} \, \partial_t (\partial_n U_t). \tag{4.40}$$

This is because the tangential velocity $U_t = \mathbf{U} \cdot \mathbf{t}$ depends on x not only through $\mathbf{U}$ but also

through the local tangent vector $\mathbf{t} = \mathbf{t}(x) = \mathbf{t}(x, y_w(x))$. Similarly, the normal derivative $\partial_n = \nabla \cdot \mathbf{n}$ depends on x because the normal vector $\mathbf{n} = \mathbf{n}(x) = \mathbf{n}(x, y_w(x))$ does. In (4.40), one must therefore take into account $d_x \mathbf{t}$ and $d_x \partial_n$. The calculation is straightforward but tedious when expressing all quantities in the basis $(\mathbf{e}_x, \mathbf{e}_y)$; instead, one can make a systematic use of the nabla operator:

$$
\begin{aligned}
d_x(\partial_n U_t) &= d_x \left((\nabla \cdot \mathbf{n})(\mathbf{U} \cdot \mathbf{t}) \right) \\
&= \nabla \cdot (d_x \mathbf{n})(\mathbf{U} \cdot \mathbf{t}) + (\nabla \cdot \mathbf{n})(d_x \mathbf{U} \cdot \mathbf{t}) + (\nabla \cdot \mathbf{n})(\mathbf{U} \cdot d_x \mathbf{t}) \\
&= \nabla \cdot \left(-\frac{y_w''}{1+y_w'^2} \mathbf{t} \right)(\mathbf{U} \cdot \mathbf{t}) + (\nabla \cdot \mathbf{n}) \left(\sqrt{1+y_w'^2} \, \partial_t \mathbf{U} \cdot \mathbf{t} \right) + (\nabla \cdot \mathbf{n}) \left(\mathbf{U} \cdot \frac{y_w''}{1+y_w'^2} \mathbf{n} \right) \\
&= -\frac{y_w''}{1+y_w'^2} \partial_t U_t + \sqrt{1+y_w'^2} \, \partial_{nt} U_t + \frac{y_w''}{1+y_w'^2} \partial_n U_n \\
&= \frac{y_w''}{1+y_w'^2} (\partial_n U_n - \partial_t U_t) + \sqrt{1+y_w'^2} \, \partial_{nt} U_t.
\end{aligned}
\tag{4.41}
$$

Compared to (4.40), two additional terms coming from the derivatives of ∂_n and $\mathbf{t}$ clearly appear. The calculation of A' and B' follows similar steps.

4.3 Backflow area

The backflow area (4.3) can be expressed as

$$
A_{back} = \iint_\Omega \mathbb{1}_{\Omega_{back}}(\mathbf{x}) \, d\Omega = \iint_\Omega H(-U_x(\mathbf{x})) \, d\Omega.
\tag{4.42}
$$

Its sensitivity is derived in the same vein as that of stagnation points (section 4.1):

$$
\begin{aligned}
\delta A_{back} &= \lim_{\epsilon \to 0} \frac{A_{back}(\mathbf{U} + \epsilon \boldsymbol{\delta U}) - A_{back}(\mathbf{U})}{\epsilon} \\
&= \lim_{\epsilon \to 0} \frac{1}{\epsilon} \iint_\Omega [H(-U_x(\mathbf{x}) - \epsilon \delta U_x(\mathbf{x})) - H(-U_x(\mathbf{x}))] \, d\Omega \\
&= \iint_\Omega -\left. \frac{dH}{du} \right|_{u=-U_x} \delta U_x(\mathbf{x}) \, d\Omega \\
&= \iint_\Omega (\partial_n U_x)^{-1} \left(\nabla \mathbb{1}_{\Omega_{back}}(\mathbf{x}) \cdot \mathbf{n} \right) \delta U_x(\mathbf{x}) \, d\Omega \\
&= \iint_\Omega -(\partial_n U_x)^{-1} \delta_{\Gamma_{back}}(\mathbf{x}) \, \delta U_x(\mathbf{x}) \, d\Omega \\
&= -\oint_{\Gamma_{back}} \frac{\delta U_x}{\partial_n U_x} \, d\Gamma,
\end{aligned}
\tag{4.43}
$$

where Γ_{back} is the boundary of the backflow region Ω_{back}, and $\partial_n U_x$ is the outward derivative normal to Γ_{back}. Here we used the chain-rule derivation $\nabla \mathbb{1}_{\Omega_{back}}(\mathbf{x}) \cdot \mathbf{n} = -\left. \frac{dH}{du} \right|_{u=-U_x} \partial_n U_x(\mathbf{x})$,
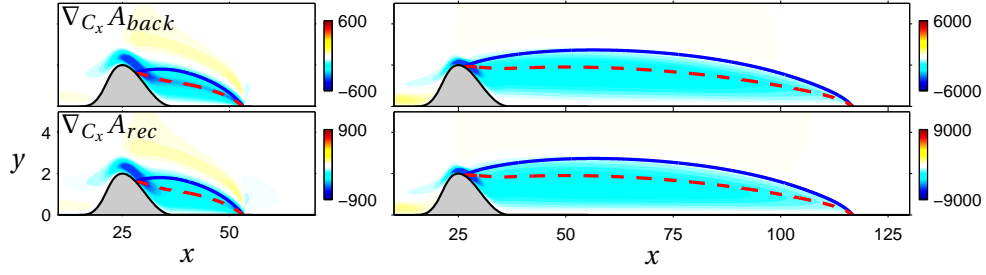
Figure 4.8 – Sensitivity of backflow and recirculation areas A_{back}, A_{rec}, with respect to streamwise volume control C_x. Left: $Re = 100$, right: $Re = 500$. The blue solid line is the separatrix, the red dashed line is the curve where $U_x = 0$.

and a higher-order generalization of the one-dimensional relation

$$\int \phi(x) \frac{\mathrm{d}H(x-x_0)}{\mathrm{d}x} \, \mathrm{d}x = \int \phi(x) \delta(x-x_0) \, \mathrm{d}x = \phi(x_0), \tag{4.44}$$

namely:

$$-\iint_\Omega \phi(\mathbf{x}) \nabla \mathbb{1}_{\Omega_{back}}(\mathbf{x}) \cdot \mathbf{n} \, \mathrm{d}\Omega = \iint_\Omega \phi(\mathbf{x}) \delta_{\Gamma_{back}}(\mathbf{x}) \, \mathrm{d}\Omega = \oint_{\Gamma_{back}} \phi(\mathbf{x}) \tag{4.45}$$

where $\delta_{\Gamma_{back}}$ is the two-dimensional delta function associated to $\mathbb{1}_{\Omega_{back}}$, and $\mathbf{n}$ the outward normal of Γ_{back}. Therefore

$$\delta A_{back} = (\nabla_{\mathbf{U}} A_{back} \,|\, \boldsymbol{\delta}\mathbf{U}) = - \oint_{\Gamma_{back}} \frac{\delta U_x}{\partial_n U_x} \, \mathrm{d}\Gamma. \tag{4.46}$$

The sensitivity of A_{back} to volume control obtained using (4.46) is shown in figure 4.8. Regions of large sensitivity extend from upstream of the bump summit all the way to the reattachment point, with opposite signs below and above the separatrix.

4.4 Recirculation area

We first rewrite the recirculation area (4.4) as

$$A_{rec} = \iint_\Omega \mathbb{1}_{\Omega_{rec}}(\mathbf{x}) \, \mathrm{d}\Omega = \int_{x_s}^{x_r} \int_{y_w(x)}^{y_{sep}(x)} \mathrm{d}y \, \mathrm{d}x. \tag{4.47}$$

Then we notice that it is possible to give an Eulerian characterization of the separatrix, namely that the flow rate through any vertical cross section of the recirculation region is zero:

$$\int_{x_s}^{x_r} \int_{y_w(x)}^{y_{sep}(x)} U_x(\mathbf{x}) \, \mathrm{d}y \, \mathrm{d}x = 0. \tag{4.48}$$

115

The sensitivity of the recirculation area with respect to flow modification is

$$\delta A_{rec} = \lim_{\epsilon \to 0} \frac{A_{rec}(\mathbf{U} + \epsilon \delta \mathbf{U}) - A_{rec}(\mathbf{U})}{\epsilon} \tag{4.49}$$

$$= \lim_{\epsilon \to 0} \frac{1}{\epsilon} \int_{x_s + \epsilon \delta x_s}^{x_r + \epsilon \delta x_r} \int_{y_w(x)}^{y_{sep}(x) + \epsilon \delta y_{sep}(x)} \mathrm{d}y \, \mathrm{d}x. \tag{4.50}$$

Next, we use (4.48) to obtain the first-order variation of the separatrix height:

$$\delta y_{sep}(x) = -\frac{1}{U_x(x, y_{sep}(x))} \int_{y_w(x)}^{y_{sep}(x)} \delta U_x(\mathbf{x}) \, \mathrm{d}y. \tag{4.51}$$

Substituting into (4.50), splitting integration intervals into $[y_w, y_{sep}] \cup [y_{sep}, y_{sep} + \epsilon \delta y_{sep}]$ and $[x_s + \epsilon \delta x_s, x_s] \cup [x_s, x_r] \cup [x_r, x_r + \epsilon \delta x_r]$, and keeping first-order terms finally leads to

$$\delta A_{rec} = (\nabla_{\mathbf{U}} A_{rec} \,|\, \delta \mathbf{U}) = \int_{x_s}^{x_r} \frac{-1}{U_x(x, y_{sep}(x))} \left(\int_{y_w(x)}^{y_{sep}(x)} \delta U_x(\mathbf{x}) \, \mathrm{d}y \right) \mathrm{d}x. \tag{4.52}$$

The sensitivity of A_{rec} to volume control obtained using (4.52) is shown in figure 4.8. As could have been expected, it is very similar to the sensitivity of the backflow area.

5 Results

5.1 Sensitivity maps

Figures 4.6, 4.7 and 4.8 already presented the sensitivity of all quantities of interest (4.1)-(4.4) to volume control. This sensitivity information can be used to compute the effect of a small control cylinder of diameter d inserted in the flow at (x_c, y_c). This effect is modelled as a steady volume force opposed to the hypothetical drag force the control cylinder would feel if it were invested by the uniform flow $\mathbf{x}_c = \mathbf{U}(x_c, y_c)$:

$$\delta \mathbf{C}(x, y) = -\frac{1}{2} d \, C_d(x, y) \, ||\mathbf{U}(x, y)|| \, \mathbf{U}(x, y) \, \delta(x - x_c, y - y_c) \tag{4.53}$$

where C_d is the cylinder drag coefficient. Its value depends on the local Reynolds number $Re_d(x, y) = ||\mathbf{U}_b(x, y)|| \, d/\nu$, which we compute from a fit of experimental and numerical data (Boujo *et al.*, 2013; Boujo & Gallaire, 2014). From (4.7) and (4.72), quantities of interest vary according to:

$$\delta \phi = (\nabla_{\mathbf{C}} \phi \,|\, \delta \mathbf{C}) = -\frac{1}{2} d \, C_d(\mathbf{x}_c) \, ||\mathbf{U}(\mathbf{x}_c)|| \, \nabla_{\mathbf{C}} \phi(\mathbf{x}_c) \cdot \mathbf{U}(\mathbf{x}_c). \tag{4.54}$$

Figure 4.9 shows the effect of a cylinder of diameter $d = 0.05$ at $Re = 500$. The separation point and separation angle are mostly affected if the cylinder is inserted close to $\mathbf{x}_s$, and hardly vary otherwise. The reattachment angle is sensitive close to $\mathbf{x}_r$, and is weakly increased if the control cylinder is located in the shear layer. Overall, these three quantities appear robust since
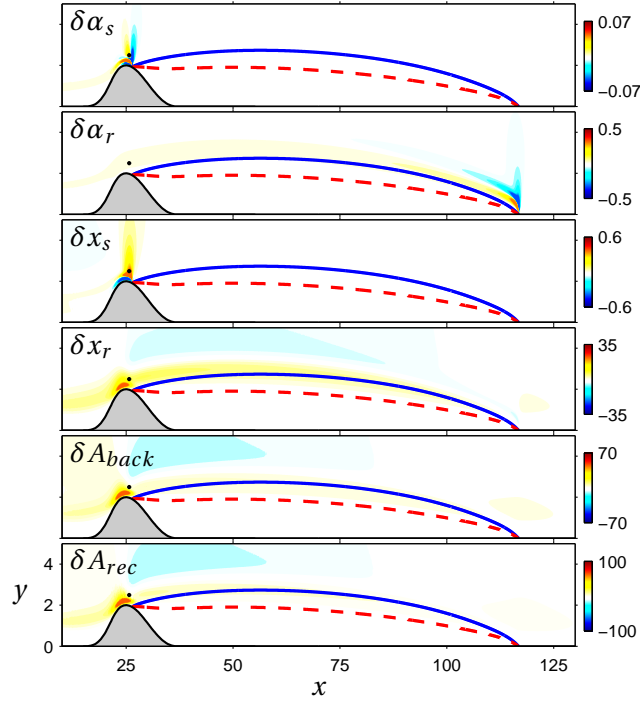
Figure 4.9 – Effect of a control cylinder of diameter $d = 0.05$ on separation and reattachment angles α_s, α_r, stagnation points x_s, x_r, backflow area A_{back} and recirculation area A_{rec}. $Re = 500$. The blue solid line is the separatrix, the red dashed line is the curve where $U_x = 0$. The black dot shows the position of the control cylinder $(x_c, y_c) = (25.7, 2.5)$ used for validation in section 4.1.

they cannot be modified easily (scales next to color bars confirm that their variations are of small amplitude). The reattachment point is much more sensitive and is predicted to move downstream if the control cylinder is inserted in the shear layer (particularly at the bump summit) or upstream, and should instead move slightly upstream for a cylinder farther away from the wall. Backflow and recirculation areas are affected in a fairly similar way, increasing when the control cylinder is located near the bump summit or upstream, and decreasing when the cylinder is farther above the bump or the early recirculation region.

Figure 4.10 shows sensitivity to wall control. Arrows point in the direction of positive sensitivity. All quantities are significantly more sensitive to normal actuation than to tangential actuation (axes are to scale, so that arrows show the actual orientation relative to the wall). Separation and reattachment angles are naturally most sensitive close to $\mathbf{x}_s$ and $\mathbf{x}_r$, respectively. More interestingly, α_s is also sensitive upstream of the bump and α_r at the bump summit and in the whole recirculation region. The separation point x_s is sensitive only at the bump summit. Finally, x_r, A_{back} and A_{rec} are efficiently controlled by wall actuation at the bump summit and to a lesser extent in the whole recirculation region; unsurprisingly, these three quantities have very similar sensitivities. Note that the sensitivities of α_s and x_s are very large at x_s, and the sensitivity of α_r is very large at x_r; for clarity, longest arrows at these
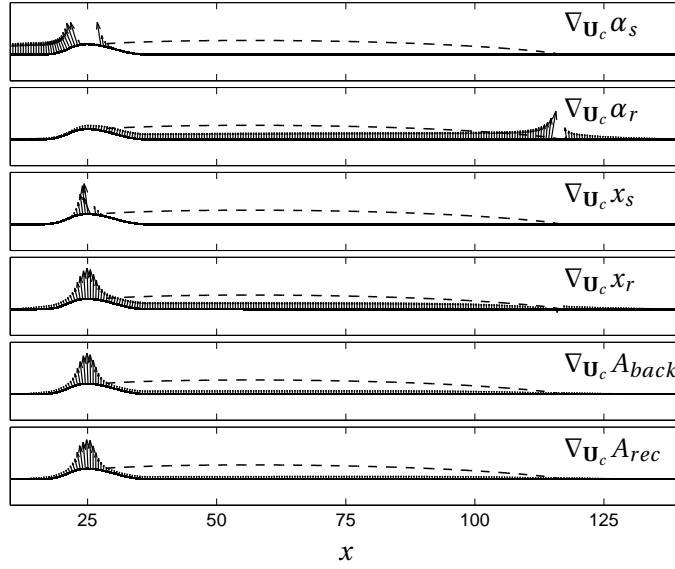
117

Figure 4.10 – Sensitivity of separation/reattachment angles α_s, α_r, locations x_s, x_r and backflow area A_{back} to wall control $\mathbf{U}_c$. Arrows point in the direction of positive sensitivity. The dashed line is the separatrix. $Re = 500$.

locations are not shown.

Figures 4.9-4.10 allow to identify regions where quantities of interest are affected the most by control and to which extent.

5.2 Validation and control

In this section, we illustrate how control configurations can be designed based on sensitivity information. We also validate the method by comparing sensitivity predictions against nonlinear results obtained from actually controlled flows at $Re = 500$.

Figure 4.11 shows how separatrix angles, stagnation locations, and backflow and recirculation areas vary when applying small-amplitude vertical wall suction ($U_c = 0, V_c < 0$) over $5 \leq x \leq 23$, with total flow rate W. All quantities decrease, although not by the same amount: the reattachment point moves significantly upstream, inducing a large reduction in backflow and recirculation areas. Separatrix angles decrease only slightly. The separation point is virtually fixed, reminiscent of the fact that it is fairly independent of Re in the uncontrolled case (figure 4.3). The agreement between sensitivity predictions (straight solid lines) and actual results (symbols) is excellent at small flow rate. However, nonlinear effects are non-negligible when $W \gtrsim 0.1 - 0.2$ and in all cases, make actual variations smaller than predicted by sensitivity analysis.

Figure 4.12 shows variations of quantities of interest when a small control cylinder of diameter $d = 0.05$ is inserted in the flow at $\mathbf{x}_c = (x_c, y_c) = (25.7, 2.5)$ (this location is shown in fig-
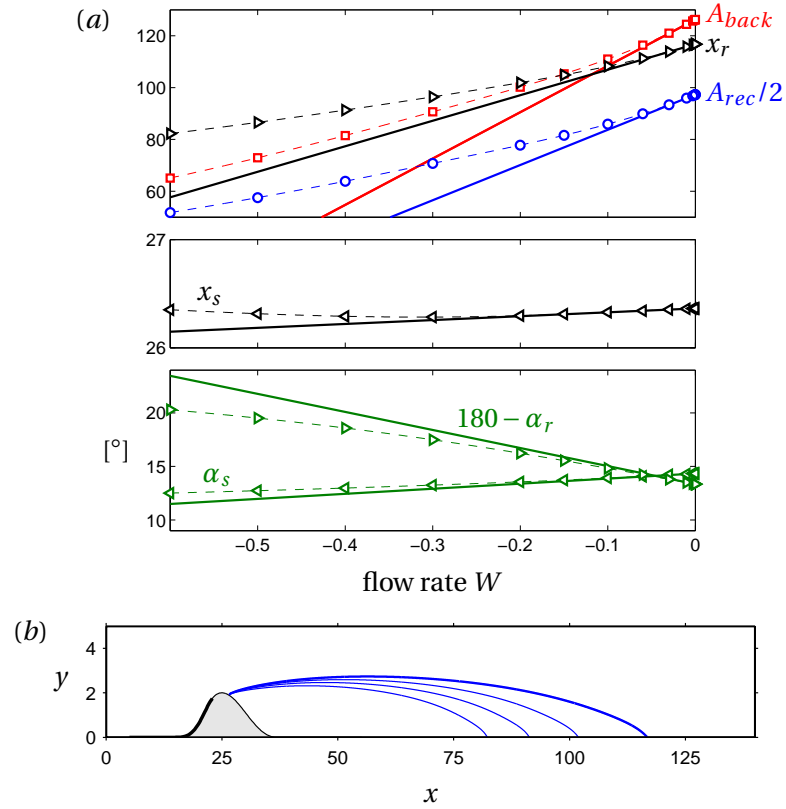
Figure 4.11 – Effect of wall suction applied over $5 \leq x \leq 23$ with total flow rate W, at $Re = 500$. (*a*) Variation of characteristic separation quantities (recirculation and backflow areas, stagnation locations, separation and reattachment angles). Thick solid lines show theoretical predictions from sensitivity analysis, while symbols show results from nonlinear calculations. (*b*) Separatrix for the uncontrolled flow ($W = 0$, thick line), and $W = 0.2$, 0.4 and 0.6 (thin lines).

ure 4.9 with a black dot). All quantities increase with the cylinder diameter, especially the reattachment point and recirculation and backflow areas, while the separatrix angles and separation point are less affected. Again, nonlinear effects are observed when $d \gtrsim 0.05$. Note that (4.73) is linear in $\boldsymbol{\delta C}$ but not in d (since the drag coefficient depends on d), therefore sensitivity predictions in figure 4.12 are not straight lines. We also report results obtained with the control cylinder included in the computational mesh (grey filled symbols) in order to assess the assumption of uniform flow underlying (4.72). Differences can be noticed when $d \gtrsim 0.05$, but sensitivity analysis does provide useful qualitative information regarding the influence of small passive control devices.

6 Conclusion

Considering the boundary layer flow above a wall-mounted bump as a prototype for separated flows, a variational technique was used to derive analytical expressions for the sensitiv-
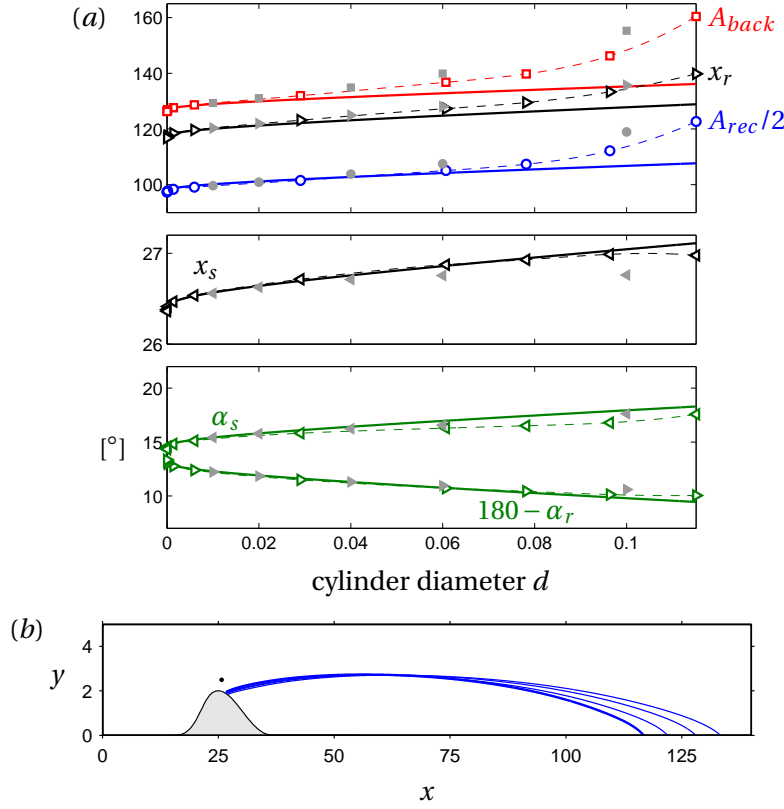
Figure 4.12 – Effect of a small control cylinder of diameter d inserted in the flow at $(x_c, y_c) = (25.7, 2.5)$, at $Re = 500$. (a) Variation of characteristic separation quantities (recirculation and backflow areas, stagnation locations, separation and reattachment angles). Thick solid lines show theoretical predictions from sensitivity analysis while open symbols show results from nonlinear calculations, both with the force model (4.72). Grey filled symbols show results from nonlinear calculations with the control cylinder included in the mesh. (b) Separatrix for the uncontrolled flow (thick line) and for $d = 0.02$, 0.04 and 0.06 (thin lines).

ity of several geometric indicators of flow separation to steady actuation: the locations of the two stagnation points (x_s and x_r), the angles of the separatrix (α_s and α_r) at these points, the backflow area A_{back} and the recirculation area A_{rec}. For each geometric quantity, analytical expressions for the linear sensitivity to base flow modification $\nabla_U *$ were obtained. This gradient information was further translated in sensitivity maps to localized volume forcing and wall blowing/suction through the introduction of the adjoint base flow, governed by linear adjoint equations forced by the previously determined gradient $\nabla_U *$. A suitable modelling of the addition of a small control cylinder as a localized force depending on the local velocity allowed to obtain sensitivity maps relevant to experimental studies.

Validations against full nonlinear Navier–Stokes calculations showed an excellent agreement for small-amplitude control for all considered indicators. With very resemblant sensitivity maps, the reattachment point, the backflow and recirculation areas were seen to be easily manipulated. In contrast, the upstream separation point and the separation and reattachment angles were found to remain extremely robust with respect to external steady actuation.

The present analysis, however, is limited to steady actuation and calls for a generalization to the sensitivity of mean recirculation properties to harmonic forcing, which is known to be a more realistic, reliable and efficient experimental control scheme. Additionally, the recent development of fast imaging techniques has now made these geometric descriptors accessible in real-time (Gautier & Aider, 2013), highlighting the need for the generalization of current open-loop control optimization tools to the dynamic closed-loop control of separation. The recent development of a solid theory for unsteady separation (Haller, 2004; Weldon, Peacock, Jacobs, Helu & Haller, 2008) provides a firm ground for this challenging objective.

4.2   Interactive Boundary Layer for flow separation

As shown in 4.1, topological properties such as stagnation point locations and backflow/re-circulation areas are important in separated flows, both because they are relevant to characterize these flows, and because they lend themselves to control applications. Although experimental techniques are available for real-time measurement of these properties, numerical simulations are still challenging and time consuming, especially at large Reynolds number. Traditional simplified methods like the ideal fluid / boundary layer decomposition allow to drastically reduce computation time, but cannot handle flow separation. More refined approximate methods do exist, however, which can successfully compute separated flows. These include Interactive Boundary Layer (IBL) theory and Triple Deck theory. This section presents the application of IBL to the separated flow past a wall-mounted bump introduced in chapter 2 and further studied in 4.1. Results show that IBL predicts well the location of stagnation points, the maximum wall shear stress and the strongest backflow for a wide range of Reynolds numbers and bump heights. The ability to quickly produce accurate results could be useful in control applications where computation time is of importance, or when parametric sweeps are needed.

It should be mentioned that this study is the result of a collaboration with P.-Y. Lagrée (Institut Jean le Rond d'Alembert, Université Pierre et Marie Curie, CNRS), who brought both the knowledge and the numerical tool. The central idea of IBL is to couple in a *strong* way the outer inviscid fluid and the inner viscous boundary layer (BL). The outer ideal fluid is a solution of the inviscid Euler equations (Navier–Stokes equations in the limit $1/Re = 0$) with slip boundary conditions at the wall ($U_n = 0$ but $U_t \neq 0$; indeed, crudely neglecting viscous terms lowers the order of the highest derivative from 2 to 1, and not all physical boundary conditions can be satisfied simultaneously). While it is known that satisfactory lift predictions can be obtained from the ideal fluid, classical boundary layer theory is required to correct the singularity at the wall by introducing a thin viscous layer (of thickness scaling like $1/\sqrt{Re}$), which fulfils the no-slip condition ($\mathbf{U} = \mathbf{0}$). In this approach, due to Prandtl (Prandtl, 1928), the BL is coupled to the ideal fluid in a "one-way" *weak* manner (simply matching the ideal fluid velocity at the wall and the BL velocity at infinity; see figure 4.13(a)). This treatment allows us for instance to predict the BL flow over a flat plate under zero pressure gradient and to obtain the corresponding drag force D, for example $D \propto W\sqrt{\rho\mu LU_\infty^3}$ for a flat plate of width W and length L, where ρ is the fluid density and μ its dynamic viscosity. Second-order effects can be added with a further improvement, which consists in taking into account the BL thickness as an apparent wall displacement, recomputing the ideal fluid and BL, and iterating until convergence (figure 4.13(b)). However, all these methods fail if wall shear stress becomes zero and the flow separates (Goldstein (1948) singularity). One of the first successes in going beyond the point of separation was obtained Catherall & Mangler (1966), who solved an *inverse* BL, prescribing its thickness and computing the velocity (instead of prescribing velocity from the ideal fluid and computing the BL thickness). IBL relies on a *strong* coupling of the ideal fluid and this *inverse* BL resolution (see figure 4.13(c) and Lagrée (2010)).
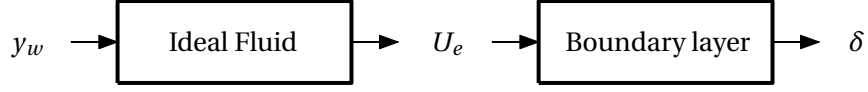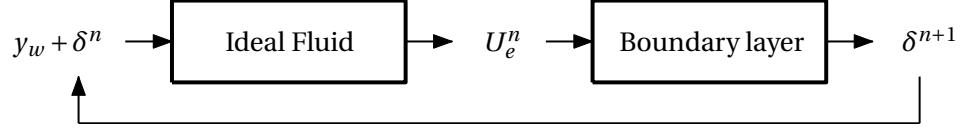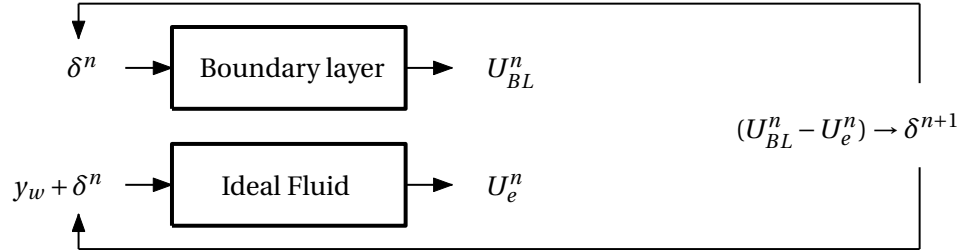
(*a*) Classical BL: one-way, *weak* coupling.

$y_w \longrightarrow$ | Ideal Fluid | $\longrightarrow U_e \longrightarrow$ | Boundary layer | $\longrightarrow \delta$

(*b*) Second-order BL with *strong* coupling.

$y_w + \delta^n \longrightarrow$ | Ideal Fluid | $\longrightarrow U_e^n \longrightarrow$ | Boundary layer | $\longrightarrow \delta^{n+1}$

(*c*) Interactive BL: *strong* coupling, *inverse* BL.

$\delta^n \longrightarrow$ | Boundary layer | $\longrightarrow U_{BL}^n$

$y_w + \delta^n \longrightarrow$ | Ideal Fluid | $\longrightarrow U_e^n$

$(U_{BL}^n - U_e^n) \rightarrow \delta^{n+1}$

Figure 4.13 – Several methods to solve the boundary layer. Given a wall geometry y_w, the ideal fluid yields the outer velocity U_e. (*a*) In the classical BL method, the BL is solved to get the displacement thickness δ from the outer velocity (*weak* coupling). (*b*) Second-order effects can be obtained by adding the BL displacement to the wall geometry, the ideal fluid then seeing the apparent wall $y_w + \delta$ (*strong* coupling). (*c*) IBL solves the *inverse* BL (the outer velocity is obtained from the thickness), coupling is *strong*. Only IBL handles separated flows. From Lagrée (2010).

More theoretical details can be found in Cebeci & Cousteix (1999); Sychev, Ruban, Sychev & Korolev (1998); Veldman (2001); Dechaume, Cousteix & Mauss (2005); Cousteix & Mauss (2004) and numerical aspects in Le Balleur (1978). Examples of applications include aerodynamics (Drela & Giles, 1987; Lock & Williams, 1987; Aftosmis, Berger & Alonso, 2006), arterial flows (Lorthois, Lagrée, Marc-Vergnes & Cassot, 2000; Lagrée, Van Hirtum & Pelorson, 2007), and geophysical flows (Lagrée, 2000).

In the present study, the same bump geometry as in chapter 2 is used, but its height is varied between $h/\delta^* = 0$ and 2 (figure 4.14). Recall that the bump summit is located at $x = x_b$, and δ^* is the displacement thickness of the incoming boundary layer measured at $x = x_b - 25\delta^*$. The IBL flow is solved using boundary layer equations expressed with different reference lengths in the streamwise and cross-stream directions, leading to non-dimensional cordinates $\overline{x} = x/L$ and $\widetilde{y} = y\sqrt{Re_L}/L$, with Reynolds number $Re_L = U_\infty L/\nu$. Here the length $L = x_b/2$ is chosen, i.e. the bump position $\overline{x}_b = 2$ is kept fixed for all configurations. The numerical inlet is located at $\overline{x} = 1$, where the displacement thickness is $\widetilde{\delta} = 1.72$ (since the
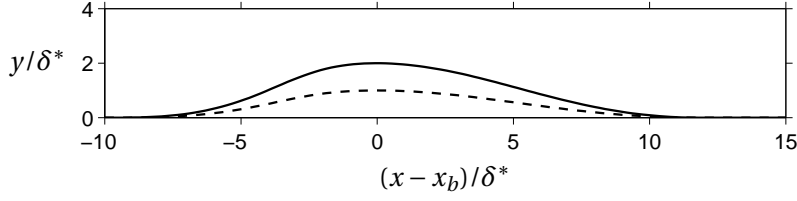
Figure 4.14 – Bump geometry for $h/\delta^* = 1$ and 2.

BL develops according to $\delta = 1.72\sqrt{\nu x/U_\infty}$). The following relations for bump height and Reynolds number can be derived:

$$Re_L = \frac{Re_{\delta^*}}{2}\left(25 + \frac{Re_{\delta^*}}{1.72^2}\right), \qquad \widetilde{h} = \frac{h}{\delta^*}\sqrt{\frac{2Re_{\delta^*}}{25 + Re_{\delta^*}/1.72^2}}. \tag{4.55}$$

This scaling is illustrated in figure 4.15. According to (4.55), the bump height in BL units tends to $\widetilde{h} = 1.72\sqrt{2}\,h/\delta^*$ as $Re_{\delta^*} \to \infty$. As shown in figure 4.16), Re_L is of order 10^4 for the values $Re_{\delta^*} \leq 700$ considered here. For comparison with Navier–Stokes simulations (method detailed in chapters 2, 3 and 4), all results are expressed in terms of Re_{δ^*} and units of δ^*.

Figure 4.17 shows the conditions $(Re_{\delta^*}, h/\delta^*)$ for incipient separation, i.e. when the smallest wall shear stress is exactly zero and the flow is on the verge of separating. The aqreement between IBL and NS is excellent. Figure 4.18 shows wall shear stress distributions for several conditions. The overall shape is well captured, with a slight decrease before the bump due to flow deflection, a large increase to a maximum before the bump summit (vertical dashed line) due to acceleration and BL thinning, followed by a large decrease and possibly separation. For $h/\delta^* = 0.5$ the flow is attached everywhere at all Re_{δ^*}, for $h/\delta^* = 1.0$ there is separation in a short region at $Re_{\delta^*} = 200$, and for $h/\delta^* = 1.5$ the recirculation region extends far downstream. Figure 4.19 shows the pressure gradient at the wall for the same conditions. The overall shape is well captured too, although the strong decrease upstream of the bump summit is slightly underestimated. Figure 4.20 shows the minimum shear stress along the wall, the largest backflow velocity and the location of stagnation points. The overall agreement is good, although differences can be observed for the largest values of h. This is not surprising since IBL, like other BL methods, is designed primarily not only for large Re but also for small wall variations $h \ll L$. Although the minimal wall shear stress is consistently underestimated (in absolute value), conditions for separation (thick dashed line) and locations of both stagnation points are very well predicted (as visible in figures 4.17-4.18 too).

The success of the IBL method is the first step towards a one-dimensional description of detached flows. Integral methods, like the von Kármán-Polhausen method (Schlichting, 1979; Lagrée, 2010), contain indeed a similar strong coupling between the boundary layer and the free-stream region, while the normal variable has been integrated out: they bear the promise for the design of even more efficient control strategies.
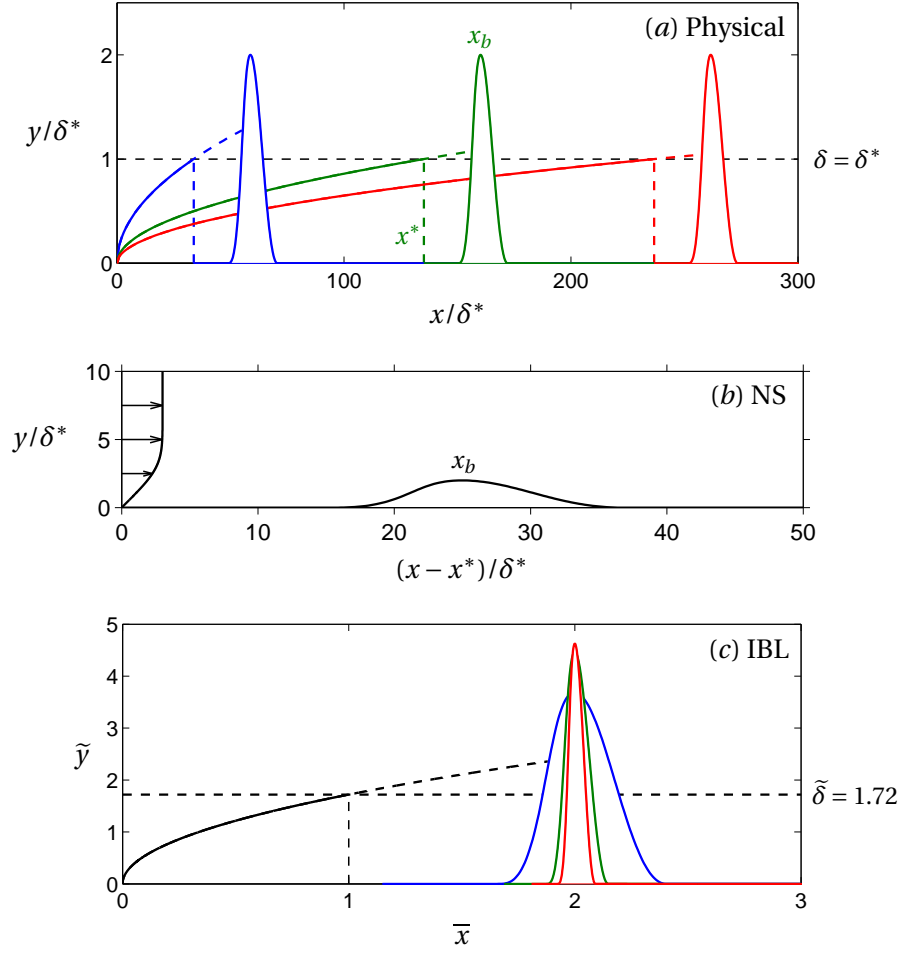
Figure 4.15 – Comparison of (*a*) physical flow set-up, (*b*) configuration used in Navier–Stokes simulations, and (*b*) configuration used in IBL calculations, for $h/\delta^* = 2$ and $Re_{\delta^*} = U_\infty\delta^*/\nu = 100, 400, 700$. The boundary layer starts at $x = 0$ and develops according to $\delta(x) = 1.72\sqrt{\nu x/U_\infty}$. The reference displacement thickness $\delta^* = \delta(x^*)$ is measured at the reference location $x^* = x_b - 25\delta^*$ (vertical dashed lines), where x_b is the location of the bump summit. In Navier–Stokes simulations, all configurations are identical: the bump summit is located $25\delta^*$ after the inlet x^*, where the BL displacement thickness is δ^*. In IBL calculations, the bump has a fixed position $\overline{x}_b = x_b/L = 2$ while its height increases towards $\widetilde{h} = 1.72\sqrt{2}\,h/\delta^*$ as the Reynolds number increases. The numerical inlet is at $\overline{x} = 1$.
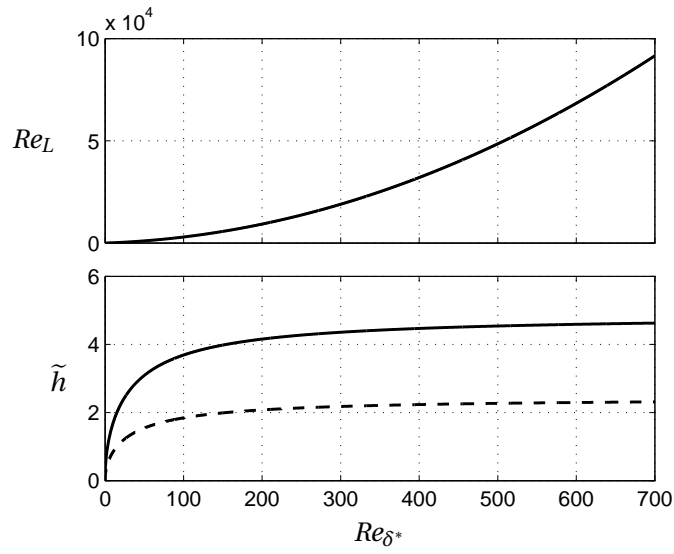
Figure 4.16 – Variation of IBL Reynolds number Re_L and IBL bump height $\widetilde{h}$ with Re_{δ^*}, for $h/\delta^* = 1$ (dashed line) and $h/\delta^* = 2$ (solid line).
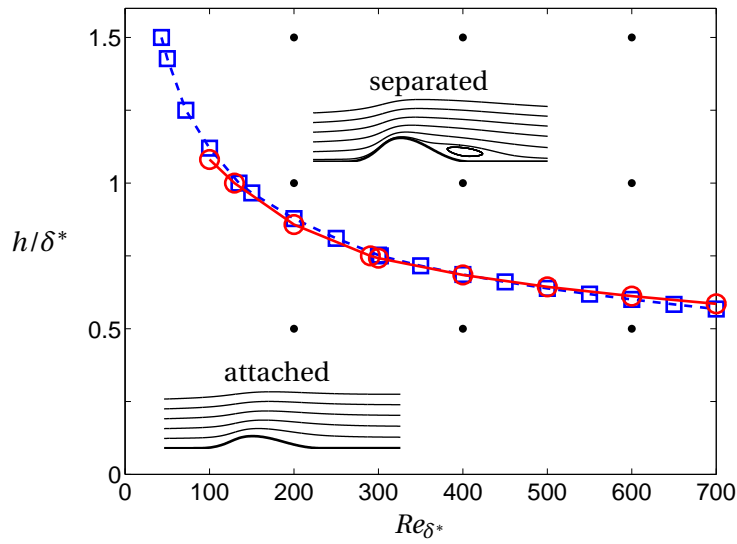
Figure 4.17 – Conditions of incipient separation ($\min_x \tau = 0$). Red solid line: IBL; blue dashed line: NS. Black dots correspond to conditions in figures 4.18-4.19.
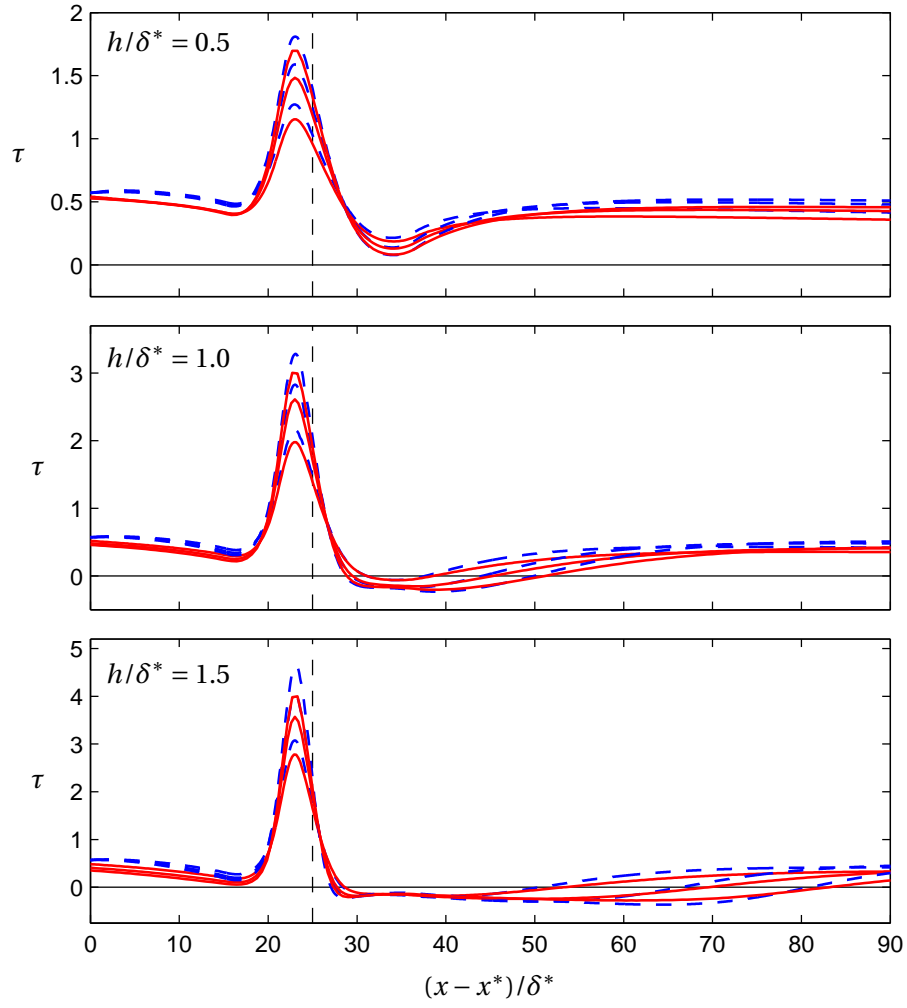
Figure 4.18 – Profiles of wall shear stress for $h/\delta^* = 0.5$, 1 and 1.5. In each panel $Re_{\delta^*} = 200$, 400, 600. Red solid line: IBL; blue dashed line: NS.
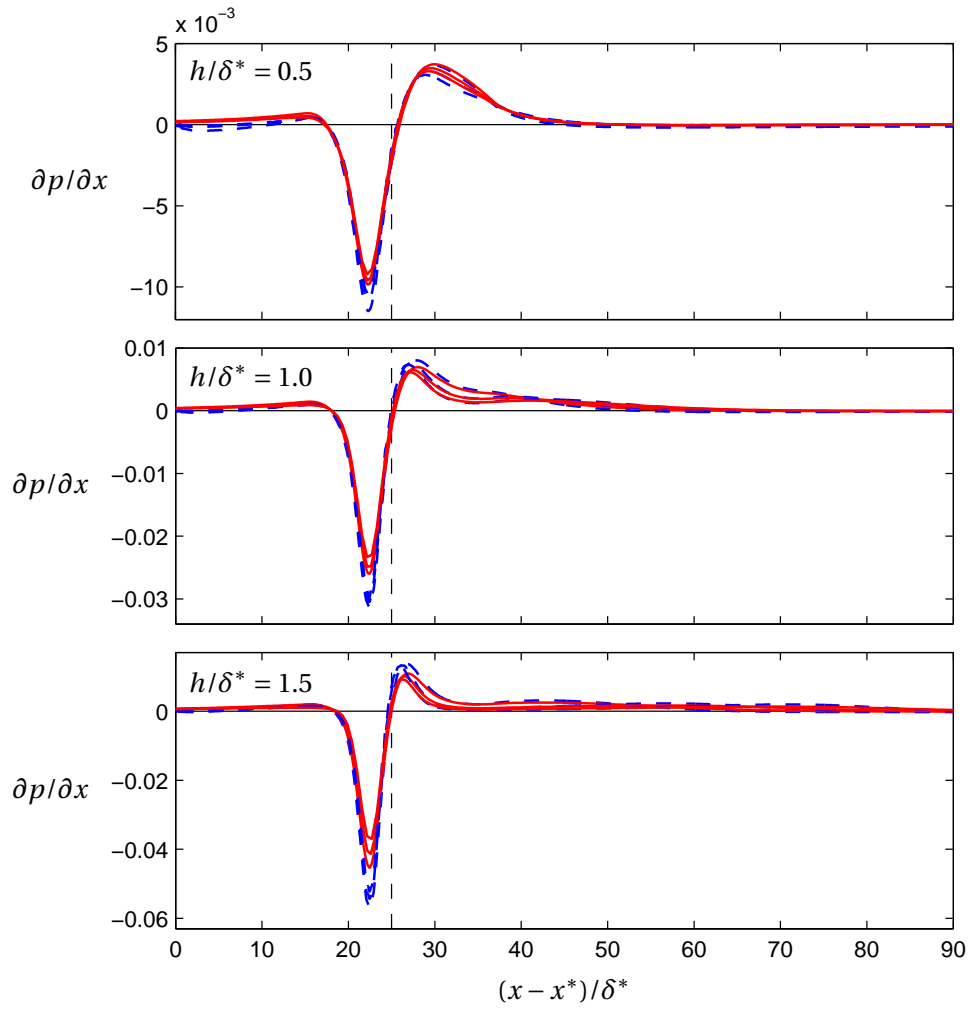
Figure 4.19 – Profiles of pressure gradient at the wall for $h/\delta^* = 0.5$, 1 and 1.5. In each panel $Re_{\delta^*} = 200, 400, 600$. Red solid line: IBL; blue dashed line: NS.
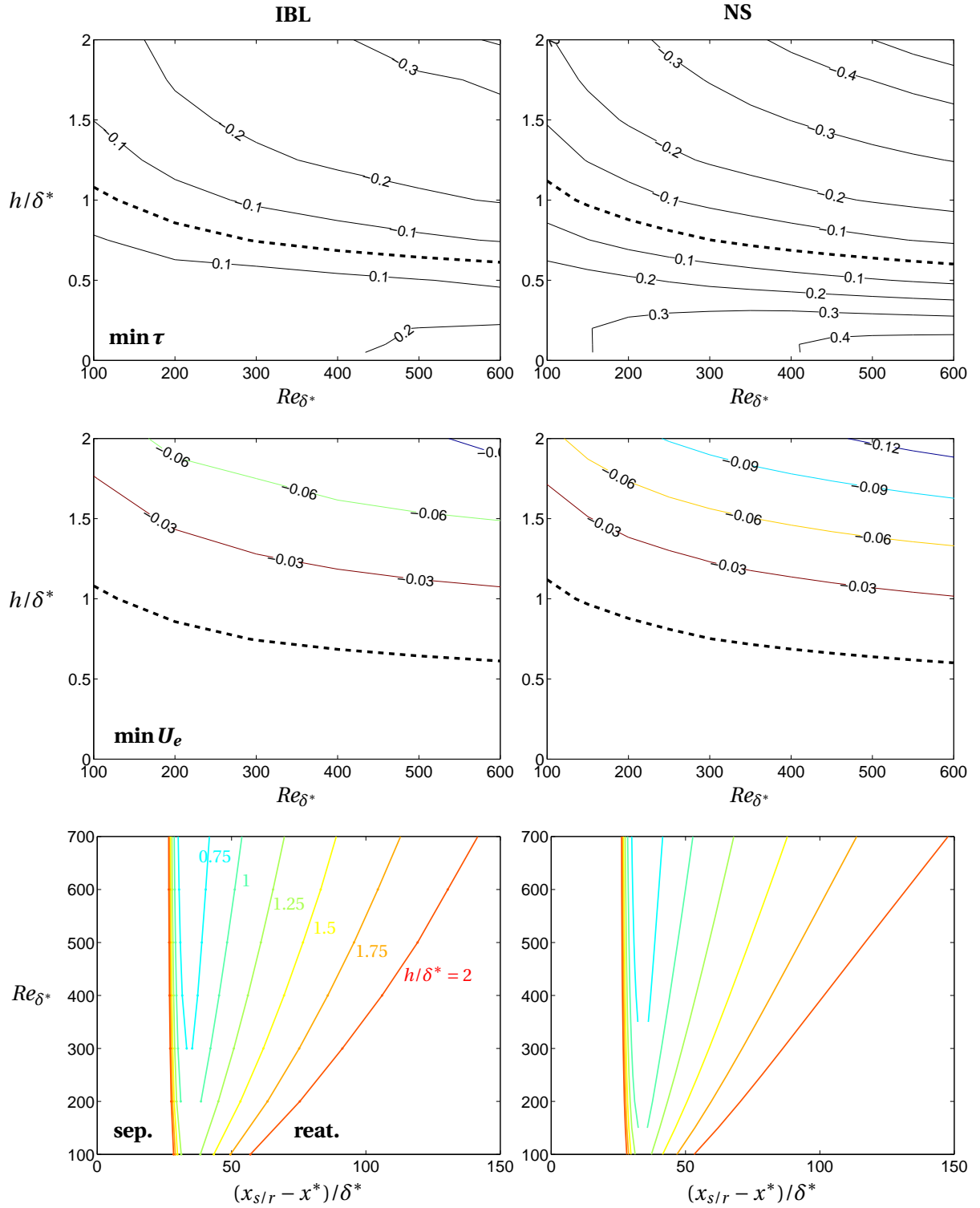
Figure 4.20 – Comparison of results from IBL (left) and NS (right): minimum wall shear stress (top), largest backflow velocity (middle), location of separation/reattachment points (bottom, where same colours code for the same bump height $0.75 \leq h/\delta^* \leq 2$).

4.3 Paper: *Controlled reattachment in separated flows: a variational approach to recirculation length reduction*

Controlled reattachment in separated flows:
a variational approach to recirculation length reduction

E. Boujo and F. Gallaire

LFMI, École Polytechnique Fédérale de Lausanne, CH-1015 Lausanne, Switzerland

A variational technique is used to derive analytical expressions for the sensitivity of recirculation length to steady forcing in separated flows. Linear sensitivity analysis is applied to the two-dimensional steady flow past a circular cylinder for Reynolds numbers $40 \leq Re \leq 120$, both in the subcritical and supercritical regimes. Regions which are the most sensitive to volume forcing and wall blowing/suction are identified. Control configurations which reduce the recirculation length are designed based on the sensitivity information, in particular small cylinders used as control devices in the wake of the main cylinder, and fluid suction at the cylinder wall. Validation against full non-linear Navier-Stokes calculations shows excellent agreement for small-amplitude control. The linear stability properties of the controlled flow are systematically investigated. At moderate Reynolds numbers, we observe that regions where control reduces the recirculation length correspond to regions where it has a stabilising effect on the most unstable global mode associated to vortex shedding, while this property does not hold any more at larger Reynolds numbers.

1   Introduction

Separation occurs in flow configurations with abrupt geometry changes or strong adverse pressure gradients. In practical engineering applications, separation is generally associated with low-frequency fluctuations which can have undesirable effects, e.g. deterioration of vehicle performance, fatigue of mechanical structures, etc. The control of separated flows is therefore an active research area. Part of the ongoing research work focuses on the laminar regime, where separated flows are steady at low Reynolds number and become unsteady above a threshold value. In this regime, stability theory can help design control strategies by providing insight into the physical phenomena involved in the transition to unsteadiness through, for example, the transient growth of particular initial perturbations, or the bifurcation of unsteady eigenmodes. Examples of separated flows commonly studied as archetypical configurations because of their fundamental interest include bluff bodies (e.g. square and circular cylinders), backward-facing steps, bumps, stenotic geometries, and pressure-induced separations over flat plates.

Sensitivity analysis uses a variational approach to calculate efficiently the linear sensitivity of some quantity to a modification of the flow or to a given actuation, thus suppressing the need to resort to exhaustive parametric studies. Hill (1992) applied sensitivity analysis to the

131

flow past a cylinder and computed the sensitivity of the most unstable growth rate to passive control by means of a second smaller cylinder, and successfully reproduced most sensitive regions previously identified experimentally by Strykowski & Sreenivasan (1990). Since then, sensitivity analysis gained popularity and was applied to evaluate sensitivity to flow modification or to passive control in various flows, both in local and global frameworks.

For example, Corbett & Bottaro (2001) designed a control strategy based on such a variational technique in order to reduce optimal transient growth in boundary layers. This was achieved by computing the sensitivity of an objective function involving energy, which was then iteratively minimized. Such quadratic cost functionals are very often employed in control theory, but sensitivity analysis can be applied to non-quadratic quantities as well. Bewley *et al.* (2001) minimized several kinds of cost functionals and successfully relaminarized the turbulent flow in a plane channel using wall transpiration. Bottaro *et al.* (2003) used a variational approach to compute the sensitivity of eigenvalues to base flow modification in the parallel plane Couette flow, as well as the most destabilising modification. Marquet *et al.* (2008) studied the sensitivity of the cylinder flow leading eigenvalue to base flow modification and to steady forcing in the bulk and, again, reproduced the regions of Strykowski & Sreenivasan (1990). Meliga *et al.* (2010) managed to control the first oscillating eigenmode in the compressible flow past a slender axisymmetric body by considering its sensitivity to steady forcing, both in the bulk (with mass, momentum or energy sources) and at the wall (with blowing/suction or heating). Recently, Brandt *et al.* (2011) also applied sensitivity analysis to evaluate the effect of steady control on noise amplification (maximal energy amplification under harmonic forcing in steady-state regime) in a globally stable flat-plate boundary layer.

In the present study, sensitivity analysis is applied to another quantity of interest in separated flows: the length of the recirculation region l_c. Many authors observed that in separated flows the recirculation length increases with *Re* (below the onset of instability): circular cylinder (experimental study by Taneda (1956), numerical study by Giannetti & Luchini (2007)), backward-facing step (experimental study by Acrivos *et al.* (1968), numerical study by Barkley *et al.* (2002)), wall-mounted bump (numerical study by Marquillie & Ehrenstein (2003), experimental study by Passaggia *et al.* (2012)), etc. As the recirculation region gets longer, both maximal backward flow and maximal shear increase. From a local stability viewpoint, this tends to destabilise the flow. In addition, since the shear layer elongates, incoming or developing perturbations are amplified over a longer distance while advected downstream, and any region of absolute instability is increased in length too. When the flow becomes unstable and unsteady, as is the case for the cylinder flow above threshold ($Re > Re_c$), the mean recirculation length decreases (Nishioka & Sato, 1978). This is interpreted as the result of a mean flow correction, and the decrease in the mean value of l_c naturally appears as a characteristic global order parameter of the bifurcation (Zielinska *et al.*, 1997).

The recirculation length therefore appears as a relevant macroscopic scalar parameter to characterize separated flows. This motivates the design of control strategies which directly target l_c, rather than eigenmode growth rates, transient growth, or noise amplification. In
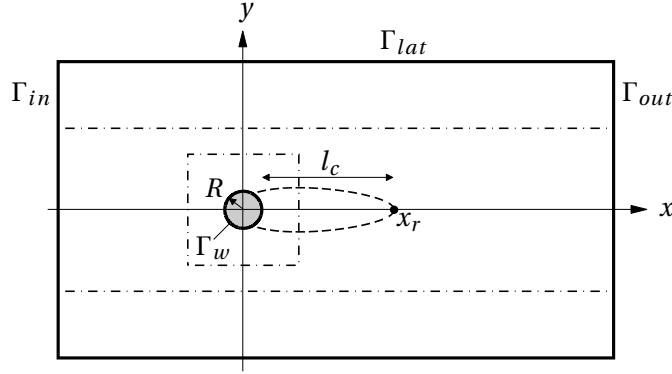
Figure 4.21 – Schematic of the problem geometry and computational domain.

other words, we propose control strategies which do not focus on the fate of perturbations but act upon a feature of the base flow itself.

We choose to design control configurations based on the steady-state base flow, and consider both subcritical and supercritical Reynolds numbers, $40 \leq Re \leq 120$. In the supercritical regime $Re > Re_c$, the uncontrolled steady-state base flow is linearly unstable and the actual flow observed in experiments or numerical simulations is unsteady; but the sensitivity of the steady-state recirculation length is of interest since reducing l_c might restabilise the flow. The stability of the controlled flow will be assessed systematically to determine when this approach is relevant.

This paper is organized as follows. Section 2 details the problem formulation and numerical methods. In particular, analytical expressions are derived for sensitivity of recirculation length to base flow modifications and to steady control, both volume forcing and wall blowing/suction. Results are presented in section 3: regions sensitive to forcing are identified, and several control configurations which allow to reduce l_c are selected to illustrate the method and to validate the sensitivity analysis against fully non-linear simulations. The linear stability properties of these controlled flows are investigated and discussed in section 4. Conclusions are drawn in section 5.

2   Problem formulation and numerical methods

The sensitivity of the recirculation length in a two-dimensional incompressible cylinder flow is investigated. A cylinder of radius R is located in a uniform flow. The fluid motion is described by the velocity field $\mathbf{U} = (U, V)^T$ of components U and V in the streamwise and cross-stream directions x and y, and the pressure field P. The state vector $\mathbf{Q} = (\mathbf{U}, P)^T$ is solution of the two-dimensional incompressible Navier–Stokes equations

$$\nabla \cdot \mathbf{U} = 0, \quad \partial_t \mathbf{U} + \mathbf{U} \cdot \nabla \mathbf{U} + \nabla P - Re^{-1} \nabla^2 \mathbf{U} = \mathbf{C} \tag{4.56}$$

133

where $Re = U_\infty D / \nu$ is the Reynolds number based on the cylinder diameter $D = 2R$, the freestream velocity U_∞ and the fluid kinematic viscosity ν, and $\mathbf{C}$ is a steady volume forcing in the bulk. The following boundary conditions are prescribed: uniform velocity profile $\mathbf{U}_b = (U_\infty, 0)^T$ at the inlet Γ_{in}, symmetry condition $\partial_y U_b = 0, V_b = 0$ on lateral boundaries Γ_{lat}, outflow condition $-P_b \mathbf{n} + Re^{-1} \nabla \mathbf{U}_b \mathbf{n} = \mathbf{0}$ on Γ_{out}, where $\mathbf{n}$ is the normal unit vector oriented outward the domain, blowing/suction $\mathbf{U}_b = \mathbf{U}_w$ on the wall control region Γ_c, and no-slip condition $\mathbf{U}_b = \mathbf{0}$ on the remaining cylinder wall region $\Gamma_w \backslash \Gamma_c$. In this paper attention is restricted to steady flows $\mathbf{Q}_b(x, y)$ which satisfy:

$$\nabla \cdot \mathbf{U}_b = 0, \quad \mathbf{U}_b \cdot \nabla \mathbf{U}_b + \nabla P_b - Re^{-1} \nabla^2 \mathbf{U}_b = \mathbf{C}. \tag{4.57}$$

2.1 Sensitivity of recirculation length

Assuming the flow is symmetric with respect to the symmetry axis $y = 0$, the recirculation length is defined as the distance from the cylinder wall rearmost point $(R, 0)$ to the reattachment point $\mathbf{x}_r = (x_r, 0)$ as shown in figure 4.21:

$$l_c = x_r - R. \tag{4.58}$$

The reattachment point is characterized by zero streamwise velocity, $U(x_r, 0) = 0$, and can therefore be computed with a bisection method on $U_c(x) = U(x, 0)$ along the symmetry axis.

Throughout this study, only flow modifications and forcings which are symmetric with respect to the symmetry axis will be considered; they result in symmetric flows, thus ensuring that the recirculation length (4.58) is well defined.

2.1.1 Sensitivity to base flow modification

Considering a small modification of the base flow $\boldsymbol{\delta Q}$, the variation of the recirculation length is expressed at first order as

$$\delta l_c = (\nabla_\mathbf{Q} l_c | \boldsymbol{\delta Q}) \tag{4.59}$$

where $\nabla_\mathbf{Q} l_c = (\nabla_\mathbf{U} l_c, \nabla_P l_c)^T$ is the sensitivity to base flow modification, $(\mathbf{a}|\mathbf{b}) = \int_\Omega \bar{\mathbf{a}} \cdot \mathbf{b} \, d\Omega$ denotes the two-dimensional inner product for real or complex fields, and the overbar stands for complex conjugate.

To allow for the calculation of this sensitivity, the recirculation length is rewritten as

$$l_c = \int_R^\infty H(-U_c(x)) \, dx = \int_R^\infty G(x) \, dx, \tag{4.60}$$

where $U_c(x) = U(x, 0)$ is the streamwise velocity on the symmetry axis and H is the Heaviside step function defined as $H(\alpha) = 0$ for $\alpha < 0$ and $H(\alpha) = 1$ for $\alpha > 0$. As illustrated in figure 4.22,
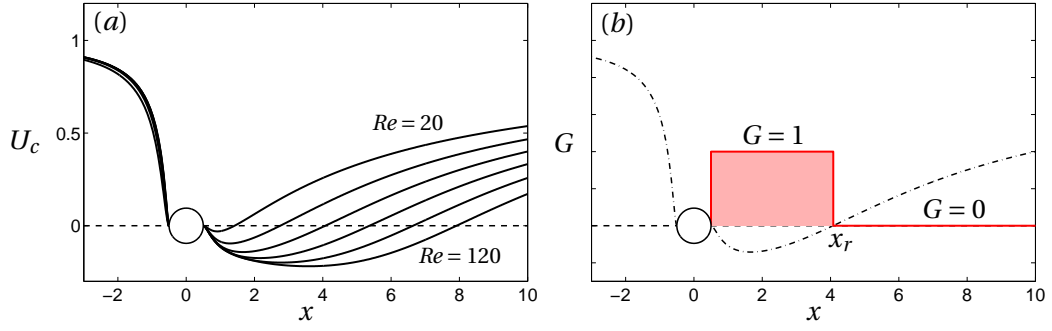
Figure 4.22 – (*a*) Streamwise velocity along the symmetry axis at $Re = 20, 40 \ldots 120$. (*b*) Integrand in the definition of the recirculation length (4.60), illustrated at $Re = 60$.

the integrand is equal to 1 in the recirculation region where $U_c(x) < 0$, and is equal to 0 downstream, therefore integrating along x from the rear stagnation point gives the recirculation length.

Using the same Lagrangian formalism as Hill (1992), the recirculation length variation due to a base flow modification $\boldsymbol{\delta Q} = (\boldsymbol{\delta U}, \delta P)^T$ is obtained as:

$$\delta l_c = \lim_{\epsilon \to 0} \frac{1}{\epsilon} \left[l_c(\mathbf{Q} + \epsilon \boldsymbol{\delta Q}) - l_c(\mathbf{Q}) \right] \tag{4.61}$$

$$= \lim_{\epsilon \to 0} \frac{1}{\epsilon} \int_R^\infty \left[H\left(-U_c(x) - \epsilon \delta U_c(x)\right) - H\left(-U_c(x)\right) \right] \mathrm{d}x \tag{4.62}$$

$$= \int_R^\infty - \left. \frac{\mathrm{d}H}{\mathrm{d}U} \right|_{U=-U_c(x)} \delta U_c(x) \, \mathrm{d}x \tag{4.63}$$

$$= \int_R^\infty \left(\frac{\mathrm{d}U_c}{\mathrm{d}x}(x) \right)^{-1} \frac{\mathrm{d}G}{\mathrm{d}x}(x) \, \delta U_c(x) \, \mathrm{d}x \tag{4.64}$$

$$= \int_R^\infty - \left(\frac{\mathrm{d}U_c}{\mathrm{d}x}(x) \right)^{-1} \delta(x - x_r) \, \delta U_c(x) \, \mathrm{d}x \tag{4.65}$$

$$= - \frac{\delta U_c(x_r)}{\mathrm{d}_x U_c|_{x=x_r}}, \tag{4.66}$$

where (4.64) comes from the differentiation of $G(x) = H(-U_c(x))$ using the chain rule, $\frac{\mathrm{d}G}{\mathrm{d}x}(x)$ $= - \left. \frac{\mathrm{d}H}{\mathrm{d}U} \right|_{U=-U_c(x)} \frac{\mathrm{d}U_c}{\mathrm{d}x}(x)$, and (4.65) is the result of $\frac{\mathrm{d}G}{\mathrm{d}x}(x) = -\delta(x - x_r)$ with $\delta(x)$ the Dirac delta function, since G jumps from 1 to 0 at $x = x_r$. If, for example, the streamwise velocity at the original reattachment point increases, then the recirculation region is shortened: this is understood physically as $U_c(x_r)$ becoming positive and the reattachment point moving upstream, while mathematically $\delta U_c(x_r) > 0$ and (4.61)-(4.66) yield $\delta l_c < 0$ (because $\mathrm{d}_x U_c|_{x=x_r} > 0$, see figure 4.22).

The sensitivity to base flow modification is identified as:

$$\nabla_{\mathbf{U}} l_c = -\frac{1}{\mathrm{d}_x U_c|_{x=x_r}} \begin{pmatrix} \delta(x_r, 0) \\ 0 \end{pmatrix}, \quad \nabla_P l_c = 0, \tag{4.67}$$

where $\delta(x, y)$ is the two-dimensional Dirac delta function, such that the inner product (4.59) between the two fields $\nabla_{\mathbf{Q}} l_c$ and $\boldsymbol{\delta}\mathbf{Q}$ is indeed δl_c as expressed by (4.66).

In wall-bounded flows, where reattachment occurs at the wall (e.g. behind a backward-facing step or a bump, or on a flat plate with adverse pressure gradient), the reattachment point is not characterized by zero streamwise velocity $U(x_r, 0) = 0$, but instead by zero wall shear stress, i.e. $\partial_y U|_{x=x_r, y=0} = 0$ with the wall assumed horizontal and located at $y = 0$ for the sake of simplicity. In this case the sensitivity reads:

$$\nabla_{\mathbf{U}} l_c = -\frac{1}{\partial_{xy} U|_{x=x_r, y=0}} \begin{pmatrix} \delta(x_r, 0)\partial_y \\ 0 \end{pmatrix}, \quad \nabla_P l_c = 0. \tag{4.68}$$

The sensitivity field $\nabla_{\mathbf{Q}} l_c$ in (4.67)-(4.68) is valid for any arbitrary base flow modification $\boldsymbol{\delta}\mathbf{U}$. As noted by Brandt *et al.* (2011), it is possible to derive a restricted sensitivity field for divergence-free base flow modifications. In the case of the cylinder flow, where (4.67) results in a localized Dirac delta function at the reattachment point in the x direction only, this restricted sensitivity field appears to present a dipolar structure.

2.1.2 Sensitivity to forcing

Now the sensitivity of the recirculation length to steady forcing is investigated. One considers a small-amplitude forcing: volume force in the bulk $\boldsymbol{\delta}\mathbf{C}(x, y)$, or blowing/suction $\boldsymbol{\delta}\mathbf{U}_w$ on part of the cylinder wall. The recirculation length variation at first order is

$$\delta l_c = (\nabla_{\mathbf{C}} l_c | \boldsymbol{\delta}\mathbf{C}) + \langle \nabla_{\mathbf{U}_w} l_c | \boldsymbol{\delta}\mathbf{U}_w \rangle \tag{4.69}$$

where $\langle \mathbf{a} | \mathbf{b} \rangle = \int_{\Gamma_c} \bar{\mathbf{a}} \cdot \mathbf{b} \, \mathrm{d}\Gamma$ denotes the one-dimensional inner product on the control boundary. The same Lagrangian formalism as in the previous section yields the sensitivities

$$\nabla_{\mathbf{C}} l_c = \mathbf{U}^\dagger, \quad \nabla_{\mathbf{U}_w} l_c = \mathbf{U}_w^\dagger = -P^\dagger \mathbf{n} - Re^{-1} \nabla \mathbf{U}^\dagger \mathbf{n}, \tag{4.70}$$

where the so-called adjoint base flow $\mathbf{Q}^\dagger = (\mathbf{U}^\dagger, P^\dagger)^T$ is a solution of the non-homogeneous linear system of equations

$$\nabla \cdot \mathbf{U}^\dagger = 0, \quad -\mathbf{U}_b \cdot \nabla \mathbf{U}^\dagger + \mathbf{U}^\dagger \cdot \nabla \mathbf{U}_b^T - \nabla P^\dagger - Re^{-1} \nabla^2 \mathbf{U}^\dagger = \nabla_{\mathbf{U}} l_c, \tag{4.71}$$

with the boundary conditions $\mathbf{U}^\dagger = \mathbf{0}$ on $\Gamma_{in} \cup \Gamma_w \cup \Gamma_c$, symmetry condition $\partial_y U^\dagger = 0, V^\dagger = 0$ on Γ_{lat}, and $P^\dagger \mathbf{n} + Re^{-1} \nabla \mathbf{U}^\dagger \mathbf{n} + \mathbf{U}^\dagger (\mathbf{U}_b \cdot \mathbf{n}) = \mathbf{0}$ on Γ_{out}.

2.1.3 Effect of a small control cylinder

It is of practical interest to study the effect of a particular kind of passive control on recirculation length and eigenvalues, namely a small control cylinder of diameter $d \ll D$ similar to the one used by Strykowski & Sreenivasan (1990) to suppress vortex shedding in a limited range of Reynolds number above instability threshold. The effect on the base flow of a small control cylinder located at $\mathbf{x}_c = (x_c, y_c)$ is modelled as a steady volume force of same amplitude as the drag force acting on this control cylinder, and of opposite direction:

$$\boldsymbol{\delta}\mathbf{C}(x,y) = -\frac{1}{2} dC_d(x,y) \|\mathbf{U}_b(x,y)\| \mathbf{U}_b(x,y) \delta(x-x_c, y-y_c) \tag{4.72}$$

where C_d is the drag coefficient of the control cylinder and depends on the local Reynolds number $Re_d(x,y) = \|\mathbf{U}_b(x,y)\| d/\nu$. Finally, variations of the recirculation length and eigenvalue (see section 4) are calculated from $\delta l_c = (\nabla_{\mathbf{C}} l_c | \boldsymbol{\delta}\mathbf{C})$ and $\delta\sigma = (\nabla_{\mathbf{C}}\sigma | \boldsymbol{\delta}\mathbf{C})$:

$$\delta l_c(x_c, y_c) = -\frac{1}{2} dC_d(x_c, y_c) \|\mathbf{U}_b(x_c, y_c)\| \nabla_{\mathbf{C}} l_c(x_c, y_c) \cdot \mathbf{U}_b(x_c, y_c), \tag{4.73}$$

$$\delta\sigma(x_c, y_c) = -\frac{1}{2} dC_d(x_c, y_c) \|\mathbf{U}_b(x_c, y_c)\| \nabla_{\mathbf{C}}\sigma(x_c, y_c) \cdot \mathbf{U}_b(x_c, y_c). \tag{4.74}$$

For a diameter $d = D/10$ and for the set of Reynolds numbers Re and locations (x_c, y_c) chosen hereafter, the Reynolds number of the control cylinder falls in the range $1 \leq Re_d \leq 15$. The expression of Hill (1992) has been generalized in this range according to $C_d(Re_d) = a + bRe_d^c$, based on a set of experimental data from Finn (1953) and Tritton (1959) and from numerical results obtained by the authors, yielding $a = 0.8558, b = 10.05, c = -0.7004$.

2.2 Linear stability

Writing the flow as the superposition of a steady base flow and time-dependent small perturbations, $\mathbf{Q}(x,y,t) = \mathbf{Q}_b(x,y) + \mathbf{q}'(x,y,t)$, linearising the Navier–Stokes equations (4.56) and using the normal mode expansion $\mathbf{q}'(x,y,t) = \mathbf{q}(x,y)e^{\sigma t}$, with $\sigma = \sigma_r + i\sigma_i$, the following system of equations is obtained:

$$\nabla \cdot \mathbf{u} = 0, \quad \sigma\mathbf{u} + \mathbf{U}_b \cdot \nabla\mathbf{u} + \mathbf{u} \cdot \nabla\mathbf{U}_b + \nabla p - Re^{-1}\nabla^2\mathbf{u} = \mathbf{0}, \tag{4.75}$$

together with the following boundary conditions: $\mathbf{u} = \mathbf{0}$ on $\Gamma_{in} \cup \Gamma_w \cup \Gamma_c$, symmetry condition $\partial_y u = 0, v = 0$ on Γ_{lat}, and outflow condition $-p\mathbf{n} + Re^{-1}\nabla\mathbf{un} = \mathbf{0}$ on Γ_{out}. Solving this generalized eigenvalue problem yields global modes $\mathbf{q}$ and associated growth rate σ_r and pulsation σ_i.

The sensitivity of an eigenvalue to base flow modification, defined by $\delta\sigma = (\nabla_{\mathbf{U}}\sigma | \boldsymbol{\delta}\mathbf{U})$, can be

computed as

$$\nabla_{\mathbf{U}}\sigma = -\mathbf{u}^{\dagger}\cdot\nabla\bar{\mathbf{u}}^{T} + \bar{\mathbf{u}}\cdot\nabla\mathbf{u}^{\dagger}, \tag{4.76}$$

where $\mathbf{q}^{\dagger} = (\mathbf{u}^{\dagger}, p^{\dagger})^{T}$ is the adjoint mode associated with σ. The sensitivity to steady forcing, defined by $\delta\sigma = (\nabla_{\mathbf{C}}\sigma \,|\, \boldsymbol{\delta}\mathbf{C}) + \langle\nabla_{\mathbf{U}_w}\sigma \,|\, \boldsymbol{\delta}\mathbf{U}_w\rangle$, can be computed as

$$\nabla_{\mathbf{C}}\sigma = \mathbf{U}^{\dagger}, \quad \nabla_{\mathbf{U}_w}\sigma = \mathbf{U}_w^{\dagger} = -P^{\dagger}\mathbf{n} - Re^{-1}\nabla\mathbf{U}^{\dagger}\mathbf{n} \tag{4.77}$$

where this time the adjoint base flow $(\mathbf{U}^{\dagger}, P^{\dagger})^{T}$ is a solution of the linear system

$$\nabla\cdot\mathbf{U}^{\dagger} = 0, \quad -\mathbf{U}_b\cdot\nabla\mathbf{U}^{\dagger} + \mathbf{U}^{\dagger}\cdot\nabla\mathbf{U}_b^{T} - \nabla P^{\dagger} - Re^{-1}\nabla^2\mathbf{U}^{\dagger} = \nabla_{\mathbf{U}}\sigma, \tag{4.78}$$

with boundary conditions $\mathbf{U}^{\dagger} = \mathbf{0}$ on $\Gamma_{in}\cup\Gamma_w\cup\Gamma_c$, $\partial_y U^{\dagger} = 0, V^{\dagger} = 0$ on Γ_{lat}, and $P^{\dagger}\mathbf{n} + Re^{-1}\nabla\mathbf{U}^{\dagger}\mathbf{n} + \mathbf{U}^{\dagger}(\mathbf{U}_b\cdot\mathbf{n}) + \mathbf{u}^{\dagger}(\bar{\mathbf{u}}\cdot\mathbf{n}) = \mathbf{0}$ on Γ_{out}. It is possible to relate the sensitivity of a given eigenvalue and the individual sensitivities of its growth rate and pulsation, $\delta\sigma_{r,i} = (\nabla_{\mathbf{U}}\sigma_{r,i} \,|\, \boldsymbol{\delta}\mathbf{U})$ according to $\nabla_{\mathbf{U}}\sigma_r = \mathrm{Re}\{\nabla_{\mathbf{U}}\sigma\}$ and $\nabla_{\mathbf{U}}\sigma_i = -\mathrm{Im}\{\nabla_{\mathbf{U}}\sigma\}$. The same relations hold for sensitivity to forcing.

2.3 Numerical method

All calculations are performed using the finite element software *FreeFem++* to generate a two-dimensional triangulation in the computation domain Ω shown in figure 4.21, of dimensions $-50 \le x \le 175$, $-30 \le y \le 30$, with the center of cylinder located at $x = 0, y = 0$. Bold lines indicate boundaries. The mesh density is successively increased from outer boundaries, thin dash-dotted lines, bold dash-dotted line, and cylinder wall. The resulting mesh has 246083 triangular elements. Variational formulations associated to the equations to be solved are spatially discretized using P2 and P1 Taylor-Hood elements for velocity and pressure respectively.

Base flows are computed using an iterative Newton method to solve equations (4.57), convergence being reached when the residual is smaller than 10^{-12} in L^2 norm. The eigenvalue problem (4.75) is solved using an implicitly restarted Arnoldi method. Adjoint base flows involved in the calculation of recirculation length sensitivity and eigenvalue sensitivity are obtained by inverting the simple linear systems (4.71) and (4.78).

Convergence was checked by calculating steady-state base flows with different meshes. Reducing the number of elements by 21%, the recirculation length varied by 0.2% or less over the range of Reynolds numbers $30 \le Re \le 120$. Values of drag coefficient and recirculation length over this same Re range are given in table 4.1 together with results from the literature. Compared to Giannetti & Luchini (2007), the maximum relative difference on l_c was 2%, of the same order as the values they report, while C_D differed by less than 1.7% from values computed by Henderson (1995). From linear stability calculations, the onset of instability characterized by $\sigma_r = 0$ was found to be $Re_c = 46.6$, in good agreement with the values re-

	C_D					l_c					Re_c
	20	40	60	100	120	20	40	60	100	120	
H95	2.06	1.54	1.31	1.08	1.01						
ZGDW97						0.94	2.28	3.62	6.30		
GL07	2.05	1.54				0.92	2.24	(3.6)	(6.2)	(7.5)	46.7
SL07											46.6
MSJ08											46.8
Present study	2.04	1.52	1.30	1.07	1.00	0.92	2.25	3.57	6.14	7.42	46.6

Table 4.1 – Drag coefficient C_D and recirculation length l_c for different values of Re, and critical Reynolds number Re_c. (Bracketed numbers are estimated from a figure.) H95: Henderson (1995); ZGDW97: Zielinska *et al.* (1997); GL07: Giannetti & Luchini (2007); SL07: Sipp & Lebedev (2007); MSJ08: Marquet *et al.* (2008).

ported in the literature. Also, the frequency σ_i of the most unstable global mode differed by less than 1.2% from results of Giannetti & Luchini (2007).

3 Results

In this section we consider subcritical and supercritical Reynolds numbers, $40 \leq Re \leq 120$, and focus on the steady-state recirculation length. Its sensitivity to flow modification and to control is presented in section 3.1, and examples of control configurations which reduce l_c are detailed in section 3.2. Stability properties are discussed later in section 4.

3.1 Sensitivity of recirculation length

Figure 4.23(*a*) shows the sensitivity of recirculation length to bulk forcing in the streamwise direction, $\nabla_{C_x} l_c = \nabla_{\mathbf{C}} l_c \cdot \mathbf{e}_x$. By construction, sensitivity analysis predicts that forcing has a large effect on l_c in regions where sensitivity is large. To be more specific, l_c can be reduced by forcing along $\mathbf{e}_x$ in regions of negative sensitivity $\nabla_{C_x} l_c < 0$: in the recirculation region (in particular close to the reattachment point), and near the sides of the cylinder just upstream of the separation points; l_c can also be reduced by forcing along $-\mathbf{e}_x$ in regions of positive sensitivity $\nabla_{C_x} l_c > 0$: at the outer sides of the recirculation region (in particular close to the reattachment point).

As mentioned in section 2.1.3, it is convenient in an experiment to use a small, secondary cylinder as a simple passive control device which produces a force which aligned with the local flow direction and depending non-linearly on the local velocity, as given by (4.72). The effect δl_c of such a control cylinder was computed from $\nabla_{\mathbf{C}} l_c$ according to (4.73). Results for a control cylinder of diameter $d = 0.10D$ are shown in figure 4.23(*b*). The recirculation length increases ($\delta l_c > 0$) when a control cylinder is located on the sides of the main cylinder upstream of the separation point , or in the shear layers; it decreases ($\delta l_c < 0$) when a control cylinder is located farther away on the sides of the shear layers. The minimal value of $\delta l_c / l_c$
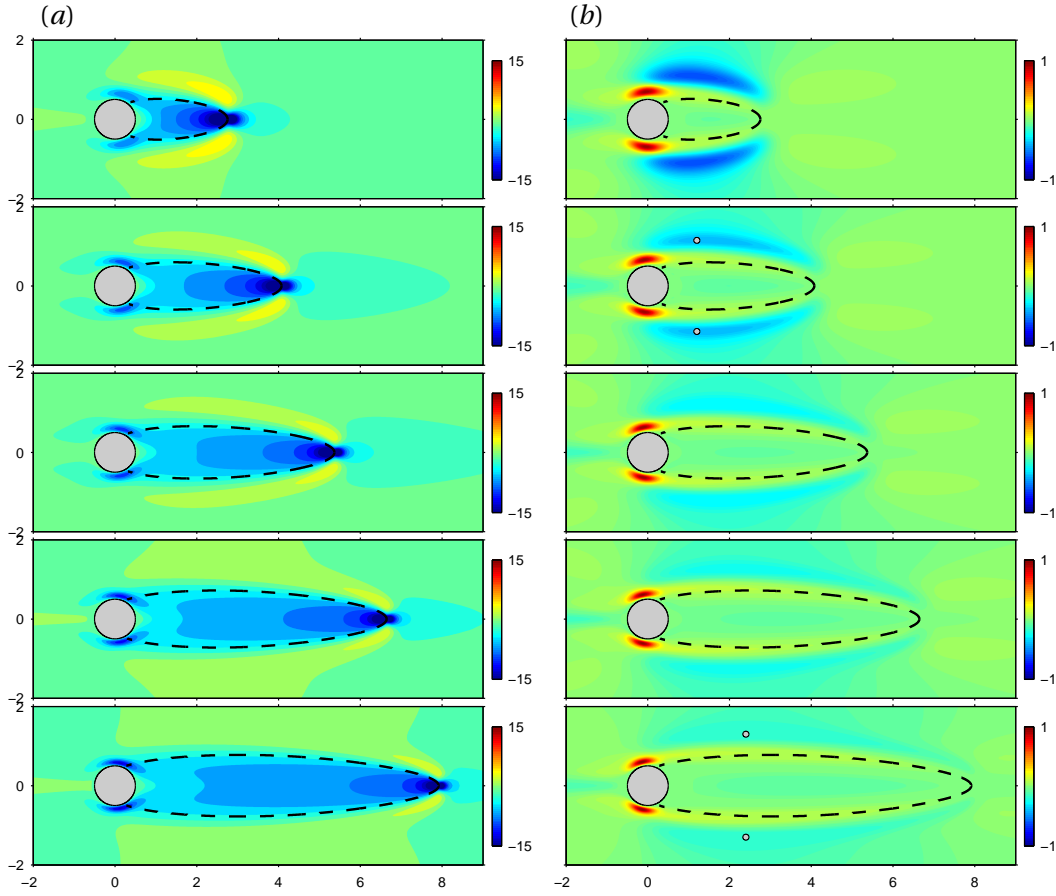
Figure 4.23 – (a) Normalized sensitivity of recirculation length to bulk forcing in the streamwise direction, $\nabla_{C_x} l_c / l_c$. (b) Normalized effect of a small control cylinder of diameter $d = 0.10D$ on recirculation length, $\delta l_c / l_c$. From top to bottom: $Re = 40, 60, 80, 100, 120$. The dashed line is the steady-state base flow separatrix. Black circles show the locations of control cylinders for configuration B discussed in section 4.3.

Figure 4.24 – Sensitivity of recirculation length to wall actuation $\nabla_{\mathbf{U}_w} l_c$. Flow is from left to right. Numbers correspond to the L^∞ norm of $\nabla_{\mathbf{U}_w} l_c / l_c$.

Figure 4.25 – Sketch of control configuration W.

becomes less negative as *Re* increases, meaning that a control cylinder of constant diameter becomes gradually less effective at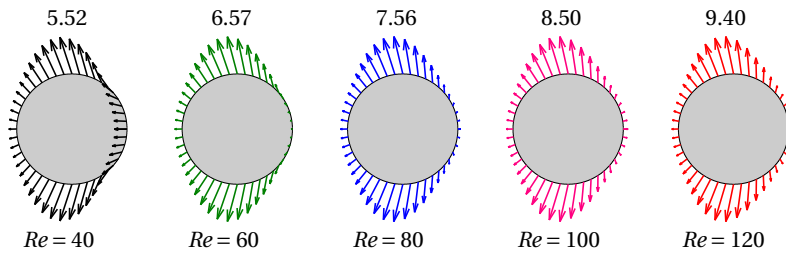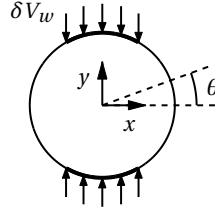 reducing l_c. Interestingly, regions associated with l_c reduction correspond qualitatively well to regions where vortex shedding was suppressed in the experiments of Strykowski & Sreenivasan (1990) (figure 20 therein) for the same diameter ratio. This point is further discussed in section 4.

Figure 4.24 shows the sensitivity of recirculation length to steady wall actuation, $\nabla_{\mathbf{U}_w} l_c$. Since the variation of l_c is given by the inner product $\delta\sigma = \langle \nabla_{\mathbf{U}_w}\sigma \,|\, \boldsymbol{\delta U}_w \rangle$, wall control oriented along the arrows increases l_c. In particular, the recirculation length is increased by wall blowing where arrows point towards the fluid domain, and by wall suction where arrows point inside the cylinder. The numbers above each plot correspond to the L^∞ norm of the rescaled sensitivity field $\nabla_{\mathbf{U}_w} l_c / l_c$. This norm increases (roughly linearly) with *Re*, indicating that the relative control authority is increasing. The shape of the sensitivity field does not vary much with *Re*, and reveals that the most efficient way to reduce l_c is to use wall suction at the top and bottom sides of the cylinder, in a direction close to wall normal.

3.2   Control of the recirculation length

The sensitivity fields obtained in the previous section can be used to control recirculation length. To illustrate this process, two control configurations predicted to reduce l_c are tested at two representative Reynolds numbers *Re* = 60 and 120, and for different control amplitudes:

- configuration B ("bulk"; sketched in figure 4.23): volume forcing with two control cylinders located symmetrically close to the point where l_c reduction is predicted to be maximal, at $\mathbf{x}^* = (x^*, \pm y^*) = (1.2, \pm 1.15)$ at *Re* = 60 and $\mathbf{x}^* = (2.4, \pm 1.3)$ at *Re* = 120;

- configuration W ("wall"; sketched in figure 4.25): vertical wall suction at the top and bottom sides, $\pi/3 \le |\theta| \le 2\pi/3$, with velocity δV_w.

Figure 4.26 shows the recirculation length variation δl_c for these configurations. In addition to predictions from sensitivity analysis (dashed lines), this figure shows non-linear results (solid lines) obtained by computing the actual controlled flow and its recirculation length for each configuration and each amplitude. In configuration B, the effect of control cylinders is
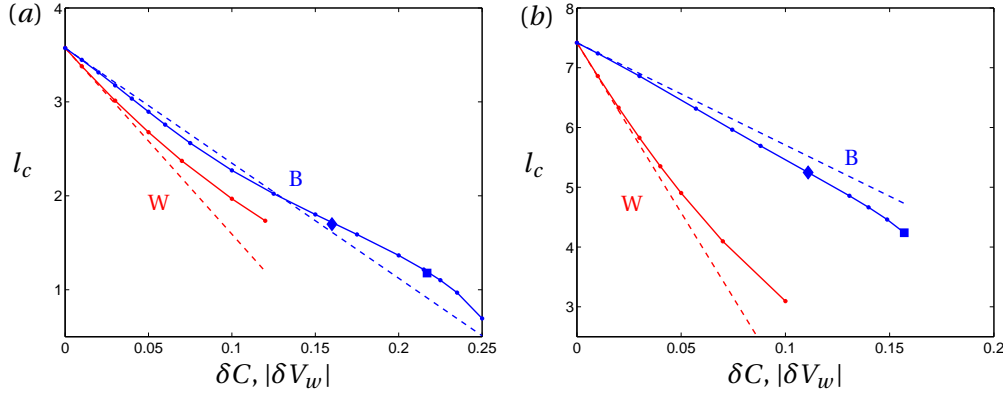
Figure 4.26 – Variation of recirculation length with control amplitude (δC in configuration B, $|\delta V_w|$ in configuration W). (*a*) $Re = 60$, (*b*) $Re = 120$. Dashed lines show predictions from sensitivity analysis, solid lines are non-linear results. Symbols correspond to control cylinders of diameter $d = 0.05D$ (♦) and $d = 0.10D$ (■).

modelled by the volume force (4.72); in configuration W, wall actuation is implemented as a velocity boundary condition with uniform profile. As expected, l_c is reduced, and the agreement between sensitivity analysis and non-linear results is excellent, with slopes matching at zero-amplitude, whereas non-linear effects appear for larger amplitudes. Non-linear simulations indicate that at $Re = 60$, controlling with two cylinders of diameter $d = 0.10D$ reduces l_c by more than 65%; a reduction of about 50% is achieved with control cylinders of diameter $0.05D$, and with wall suction of intensity $\delta V_w = 0.12$. At $Re = 120$, control cylinders of diameter $d = 0.10D$ reduce l_c by more than 40%; a reduction of about 30% is achieved with control cylinders of diameter $0.05D$, and with wall suction of intensity $\delta V_w = 0.04$.

Figure 4.27 shows examples of controlled flows, illustrating how the recirculation region is shortened. In configuration B, control cylinders of diameter $d = 0.10D$ located at $(x^*, \pm y^*)$ make the flow deviate and accelerate. As a result, the streamwise velocity increases between the two control cylinders in a long region extending far downstream, and the reattachment point moves upstream. In configuration W, fluid is sucked at the cylinder sides, which brings fluid with high streamwise velocity closer to the wall region, which in turn makes the recirculation region shorter.

4 Effect on linear stability

In the previous section, sensitivity analysis was performed on the steady-state base flow. It provided information on the sensitivity of the recirculation length and allowed to design efficient control strategies. These results are relevant only if the controlled flow is stable. Indeed, when increasing the Reynolds number above its critical value Re_c, the cylinder flow becomes linearly unstable, with a Hopf bifurcation leading to unsteady vortex shedding; one should therefore investigate whether the flow is stabilised by the control. In the subcritical regime $Re < Re_c$, one should also check that the flow is not destabilised by the control.
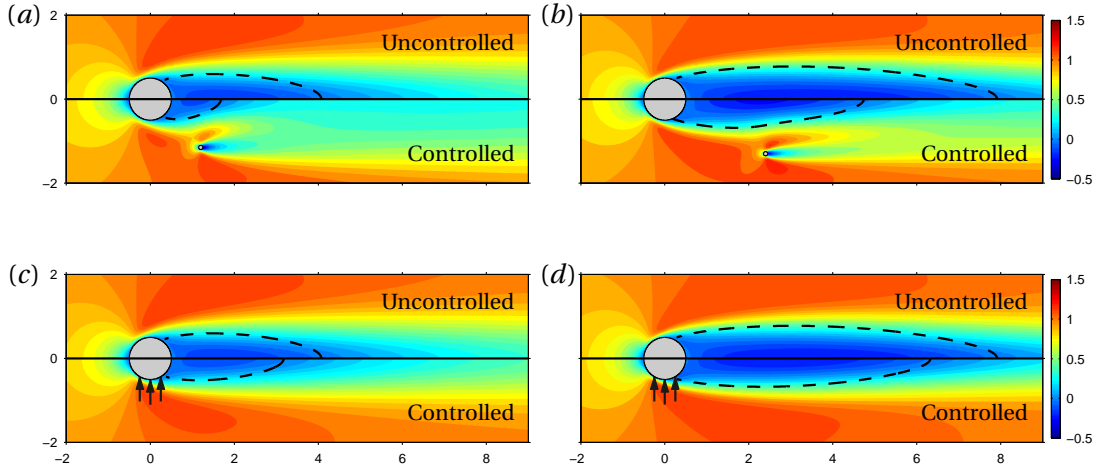
Figure 4.27 – Streamwise velocity of uncontrolled and controlled steady-state base flow. Left: $Re = 60$; right: $Re = 120$. (*a*)-(*b*) configuration B: two control cylinders of diameter $d = 0.10D$ located at $(x^*, \pm y^*)$; (*c*)-(*d*) configuration W: suction of amplitude $\delta V_w = 0.05$ and 0.03 respectively.

At $Re = 60$, one pair of complex conjugate eigenvalues ("mode 1") associated with the von Kármán street is unstable. Figure 4.28(*a*) shows the variation of the leading growth rate $\sigma_{1,r}$ with control amplitude. Both configurations B and W have a stabilising effect on the leading global mode. Full restabilisation is achieved with two control cylinders of diameter $d \simeq 0.04D$, or with wall suction of intensity $\delta V_w \simeq 0.08$. These control configurations do not destabilise other eigenmodes for any of the amplitudes tested.

A second pair of eigenvalues becomes unstable ("mode 2") at $Re \simeq 110$ (Verma & Mittal, 2011). Figure 4.28(*b*) shows the variation of $\sigma_{1,r}$ and $\sigma_{2,r}$ with control amplitude at $Re = 120$. Bulk
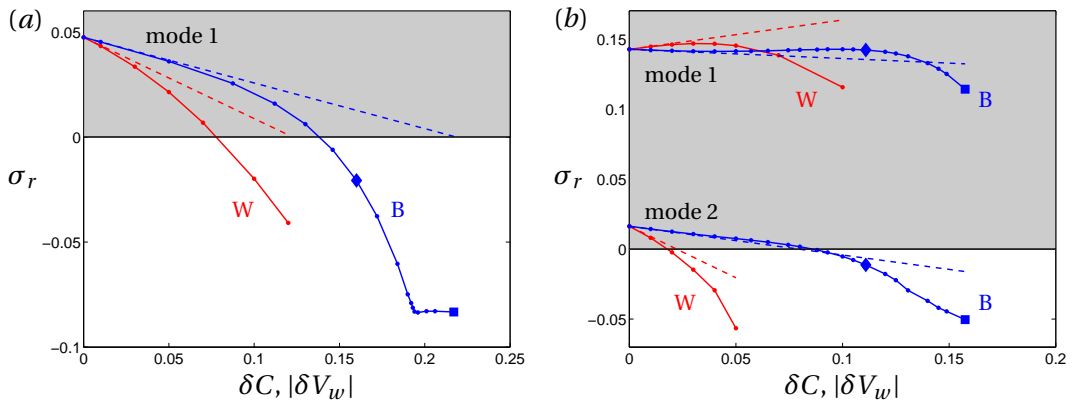

Figure 4.28 – Variation of leading growth rates with control amplitude. (*a*) $Re = 60$, (*b*) $Re = 120$. Same notations as in figure 4.26.

143

forcing has a stabilising effect on both unstable modes, but does not achieve full restabilisation. The straightforward strategy which allowed to stabilise the flow at $Re = 60$, namely placing control cylinders where the sensitivity analysis predicts they have the largest reducing effect on l_c, is therefore not successful at $Re = 120$. Wall forcing has a stabilising effect on mode 2 but a destabilising effect on mode 1 for reasonable control amplitude, and again the flow is not restabilised.

To investigate why control configurations which shorten the recirculation region also have a stabilising effect at $Re = 60$, but not at $Re = 120$, it is interesting to consider the sensitivity of the leading eigenvalue. Figure 4.29 compares the effect of a small control cylinder ($d = 0.10D$) on l_c, calculated from (4.73) and already shown in figure 4.23(b), and its effect on $\sigma_{1,r}$, calculated from (4.74). At $Re = 40$ and 60, δl_c and $\delta\sigma_{1,r}$ have very similar spatial structures. This means that a small control cylinder, when located where it reduces the recirculation length, almost always has a stabilising effect on the most unstable global mode. However, this similarity gradually disappears as Re increases. Regions where δl_c and $\delta\sigma_{1,r}$ have opposite signs grow in size, and at $Re = 120$ they extend along the whole shear layers, both inside and outside the recirculation region. To ease comparison, the contour where two symmetric control cylinders ($d = 0.10D$) render mode 1 just neutrally stable (i.e. where $\delta\sigma_{1,r} = -\sigma_{1,r}/2$) is reported on the map of δl_c. At $Re = 60$ this stabilising region overlaps with the region of recirculation length reduction, but as Re increases it moves upstream towards the region of recirculation length increase. In other words, control cylinders located where they reduce l_c are efficient in stabilising mode 1 at low Re, but gradually lose this ability at higher Re. In the latter regime, one may wonder if increasing the recirculation length is not a better way to stabilise the flow. It must be pointed out that the stabilising region shrinks as Re increases anyway, consistent with observations from Strykowski & Sreenivasan (1990) and Marquet *et al.* (2008).

All stabilising contours for $Re \geq 50$ are gathered in figure 4.30(a). The characteristic shrinking of the stabilising region is confirmed. Also shown for $Re \geq 40$ are the locus of two particular points: $\mathbf{x}_l$, where a control cylinder yields the largest l_c reduction, and $\mathbf{x}_\sigma$, where a control cylinder has the maximal stabilising effect on mode 1. It can clearly be observed that $\mathbf{x}_l$ and $\mathbf{x}_\sigma$ move in opposite directions, with $\mathbf{x}_l$ eventually going outside the stabilising region. Quantitative values of δl_c and $\delta\sigma_{1,r}$ are given in figures 4.30(b)-(c). With control cylinders located at $\mathbf{x}_l$, a recirculation length reduction of more than 35% can be achieved for any $Re \leq 120$. (With $\mathbf{x}_c = \mathbf{x}_\sigma$, the reduction is of course not as large, and the recirculation length actually increases when $Re \gtrsim 65$.) As stressed previously, however, the corresponding controlled steady-state base flow will be observed only if stable, i.e. if $\delta\sigma_{1,r}/\sigma_{1,r} \leq 1/2$ (region labelled S). This is the case if $\mathbf{x}_c = \mathbf{x}_\sigma$ (at least for $Re \leq 120$). But when control cylinders are located at $\mathbf{x}_l$, although they do have a stabilising effect ($\delta\sigma_{1,r} \leq 0$), the latter is too small to restabilise the flow when $Re \gtrsim 70$.

The same phenomenon is observed with sensitivity to wall forcing. Figure 4.31(a) shows the sensitivity of the most unstable growth rate to wall forcing. It compares very well with the results of Marquet & Sipp (2010a, figure 3 therein at $Re = 60$). Unlike the sensitivity of recircu-
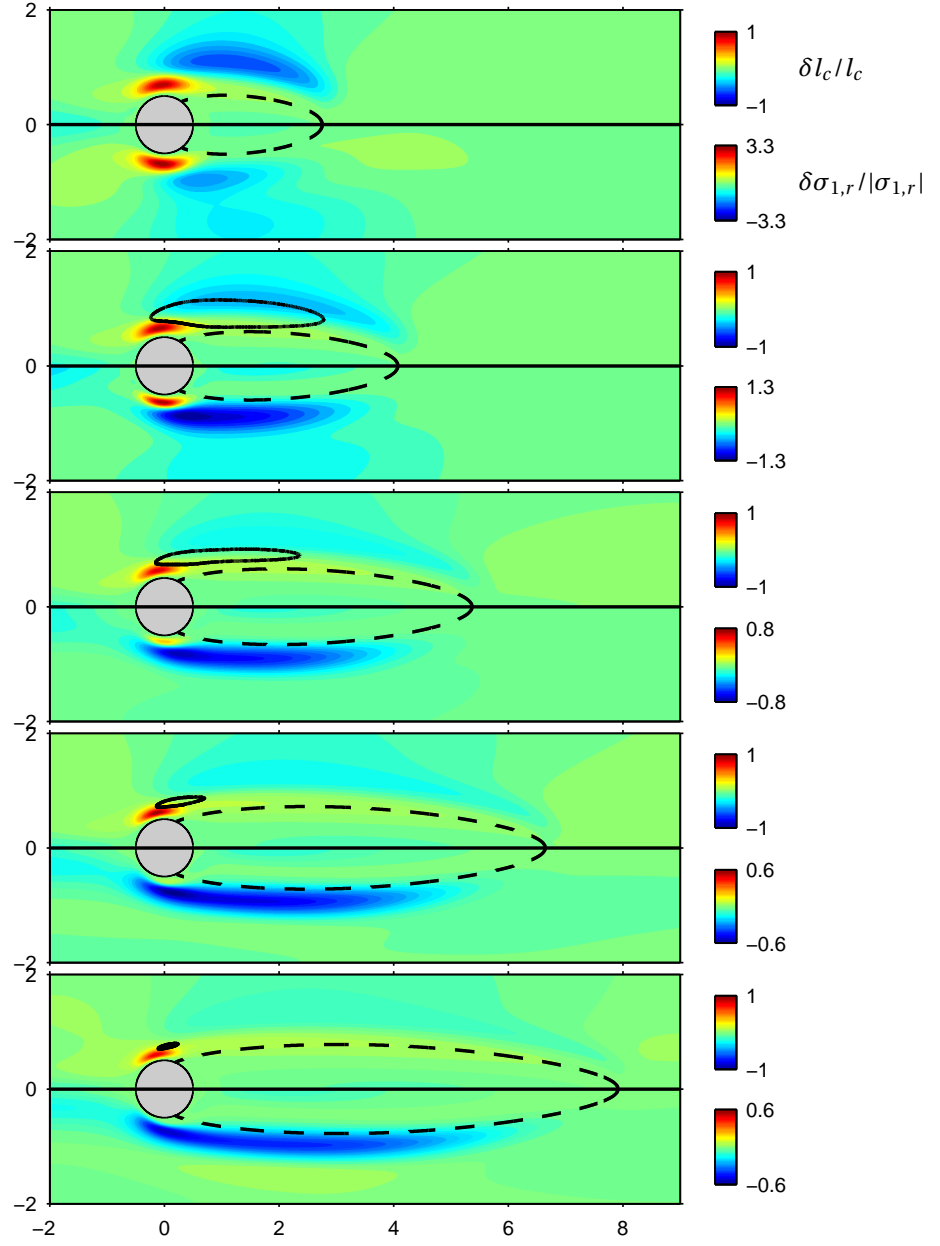
Figure 4.29 – Normalized effect of a small control cylinder ($d = 0.10D$) on the recirculation length, $\delta l_c/l_c$ (upper half of each panel), and on the most unstable growth rate, $\delta \sigma_{1,r}/|\sigma_{1,r}|$ (lower half). From top to bottom: $Re = 40, 60, 80, 100, 120$. The stabilizing contour $\delta \sigma_{1,r}/\sigma_{1,r} = -1/2$ for two symmetric control cylinders is reported on upper half plots for $Re > Re_c$.
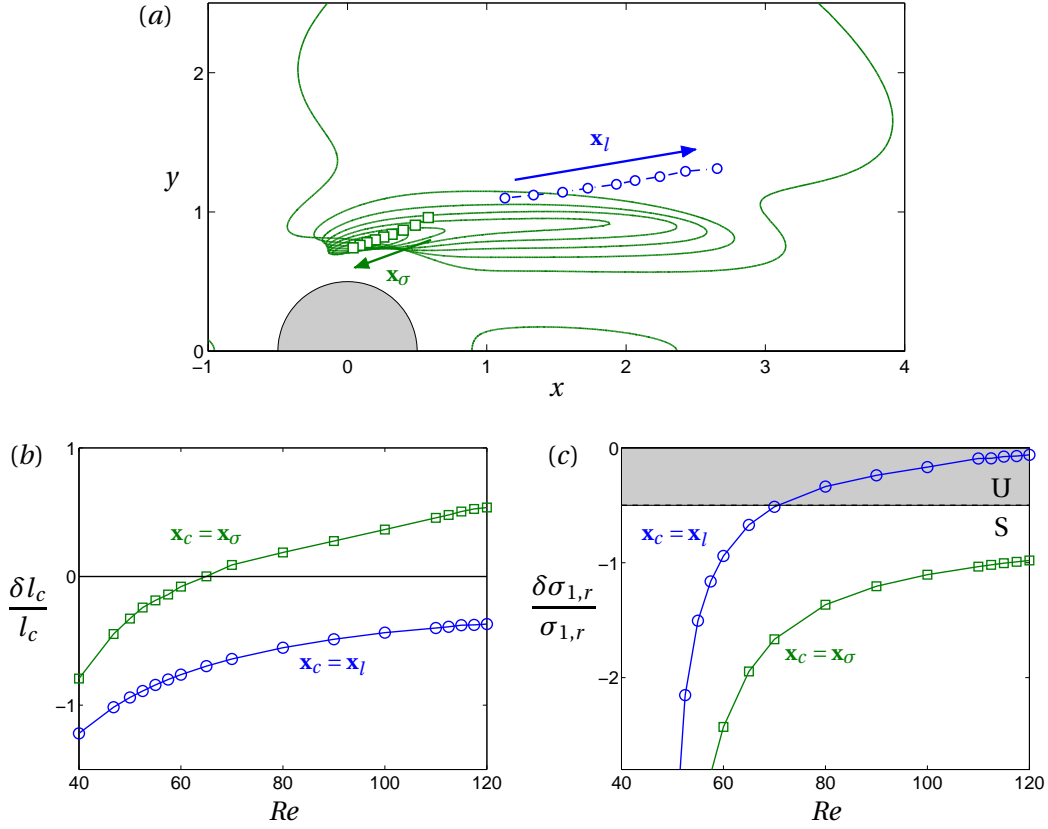
Figure 4.30 – (*a*) Locus of $\mathbf{x}_l$ (where $-\delta l_c/l_c$ is maximal) and $\mathbf{x}_\sigma$ (where $-\delta\sigma_{1,r}/|\sigma_{1,r}|$ is maximal) for a small control cylinder ($d = 0.10D$) at $Re = 40, 50 \ldots 120$. Solid lines show stabilizing regions $\delta\sigma_{1,r}/\sigma_{1,r} \leq -1/2$ for two symmetric control cylinders at $Re = 50, 60 \ldots 120$. (*b*)-(*c*) Effect of two symmetric control cylinders ($d = 0.10D$) located at $\mathbf{x}_l$ or at $\mathbf{x}_\sigma$: sensitivity analysis prediction for the normalized variation of (*b*) recirculation length, (*c*) growth rate of mode 1. The unshaded area corresponds to restabilization of mode 1.

Figure 4.31 – (*a*) Sensitivity of the leading growth rate to wall actuation $\nabla_{\mathbf{U}_w}\sigma_{1,r}$. Flow is from left to right. Numbers correspond to the L^∞ norm of $\nabla_{\mathbf{U}_w}\sigma_{1,r}/\sigma_{1,r}$. (*b*) Pointwise inner product of $\nabla_{\mathbf{U}_w}l_c$ (figure 4.24) and $\nabla_{\mathbf{U}_w}\sigma_{1,r}$ along the cylinder wall.

lation length (figure 4.24) which keeps more or less the same structure at all Reynolds numbers, $\nabla_{\mathbf{U}_w}\sigma_{1,r}$ varies substantially. In particular, at the 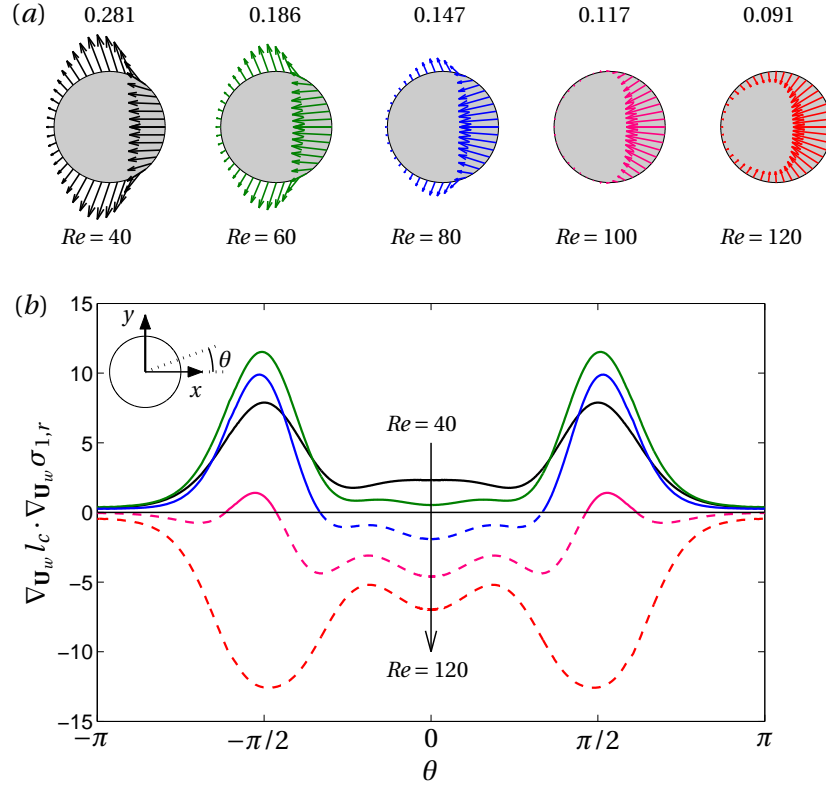top and bottom sides of the cylinder, wall-normal suction changes from largely stabilising to slightly destabilising. This translates into $\nabla_{\mathbf{U}_w}l_c$ and $\nabla_{\mathbf{U}_w}\sigma_{1,r}$ being very similar at $Re = 40$ but very different at $Re = 120$. Accordingly, the pointwise inner product of these two fields shown in figure 4.31(*b*) is positive everywhere on the cylinder wall at $Re = 40$ but negative everywhere at $Re = 120$. As a result, control configurations which shorten the recirculation length necessarily have a stabilising effect on mode 1 at low Reynolds numbers and a destabilising effect at higher Reynolds numbers. It should be noted that at $Re = 100$, it is still possible to reduce l_c and at the same time have a stabilising effect on mode 1 by using wall suction in a narrow region near $\theta = \pm\pi/2$.

5   Conclusions

In this study, the sensitivity of recirculation length to steady forcing was derived analytically using a variational technique. Linear sensitivity analysis was applied to the two-dimensional steady flow past a circular cylinder for both subcritical and supercritical Reynolds numbers $40 \leq Re \leq 120$. Regions of largest sensitivity were identified: l_c increases the most when small

control cylinders are located close to the top and bottom sides of the main cylinder, and decreases the most when control cylinders are located farther downstream, outside the shear layers; regarding wall forcing, l_c is most sensitive to normal blowing/suction at the sides of the cylinder. Validation against full non-linear Navier-Stokes calculations showed excellent agreement for small-amplitude control.

Using linear stability analysis, it was observed that control configurations which reduce l_c also have a stabilising effect on the most unstable eigenmode close to Re_c, both for bulk forcing and wall forcing. This property gradually disappears as Re is increased. This is explained by the spatial structures of the sensitivities of l_c and $\sigma_{1,r}$, which are very similar at low Re, but increasingly decorrelated at larger Re. Therefore, reducing the base flow recirculation length is an appropriate control strategy to restabilise the flow at moderate Reynolds numbers. At larger Re, aiming for an increase of l_c is actually more efficient. In any case, one should keep in mind that results concerning l_c reduction and obtained from a sensitivity analysis performed on the steady-state base flow are relevant only when the controlled flow is stable.

To better control the flow in the supercritical regime, the sensitivity of the mean flow recirculation length should be considered. Not only would a method allowing the control of the mean l_c be interesting in itself, but targeting this important parameter of the mean state (Zielinska *et al.*, 1997; Thiria & Wesfreid, 2007) could also help stabilise the flow. This work is in progress, but the difficulty of such an approach lies in that the mean flow and the fluctuations are non-linearly coupled, which prevents the derivation of a simple expression for the sensitivity of the mean recirculation length. It would help, though, to determine whether the mean flow recirculation length in separated flows should be reduced or increased in order to mitigate the instability. This extension of the sensitivity analysis to the mean recirculation length could also include the effect of periodic excitation, a control strategy often used in turbulent flows (Greenblatt & Wygnanski, 2000; Glezer & Amitay, 2002) and which can be interpreted as a mean-flow correction (Sipp, 2012).

This study confirms the high versatility of Lagrangian-based variational techniques, which allow us to compute the sensitivity of a great variety of quantities of interest in fluid flows. The recirculation length appears as a simple and relevant macroscopic parameter in separated flows, and can be targeted to design original control strategies. In the case of the cylinder flow, the fact that l_c is a good proxy for flow stabilisation only up to a certain Reynolds number might be specific to the absolute nature of the instability in bluff body wakes (Monkewitz, 1988). These flows are typical examples of "oscillators", and are appropriately described by global linear stability analysis (Chomaz, 2005). On the other hand, convectively unstable flows (or "noise amplifiers"), such as separated boundary layers, usually exhibit large optimal transient growth (maximal energy amplification of an initial perturbation) and large optimal gain (maximal energy amplification from harmonic forcing to asymptotic response for a globally stable flow) as a result of the non-normality of the linearized Navier-Stokes operator (Chomaz, 2005). One may wonder whether the recirculation length is more directly and strongly related to instability in such convectively unstable flows, and whether sensitivity

analysis applied to l_c would be efficient over a broader range of Reynolds numbers. The next step of this work is the application of a similar control strategy in wall-bounded separated boundary layer flows.

Acknowledgements

Chapter 5

Drag and lift

5.1 Introduction

The experimental study of Strykowski & Sreenivasan (1990) provides evidence that a small circular cylinder positioned in the wake of a main cylinder can alter vortex shedding at Reynolds numbers $Re \simeq 50 - 100$, above the first instability threshold. For specific locations of this control cylinder, the wake was stabilized, the shedding frequency was modified, and vortex shedding could even be completely suppressed. The effect on aerodynamic forces has been studied experimentally and numerically by Dalton *et al.* (2001) and others, who report reduction of the mean drag and of the fluctuating lift, as well as enhancement of the mean lift, at larger but still moderate Reynolds numbers ranging from 100 to 3000. Experimentally, the control cylinder technique has proven successful up to turbulent Reynolds numbers of order $10^4 - 10^5$ (Sakamoto *et al.*, 1991; Igarashi, 1997; Parezanović & Cadot, 2009, 2012). Drag reduction of 20-30% is achieved (depending on the geometry and the Reynolds number). Cadot *et al.* (2009) also assessed the ability of a second control cylinder to further increase the base pressure of a D-shaped cylinder and to reduce its drag.

Strykowski & Sreenivasan (1990) present their results in terms of sensitivity maps showing regions where shedding is most affected by the control cylinder. Similarly, Sakamoto *et al.* (1991) and Parezanović & Cadot (2012) report maps of global quantities (Strouhal number, mean or root mean square values of drag and lift). Although very valuable, these maps are highly time-consuming to produce since systematic experimental measurements (or numerical simulations) must be performed over a large parameter space, changing e.g. the position and diameter of the control cylinder. The experiment of Strykowski & Sreenivasan (1990) has been revisited by Hill (1992) and subsequently by Marquet *et al.* (2008), who used a linear analysis to assess the effect of an infinitely small control cylinder on the stability of the main cylinder flow, and obtained theoretical maps matching the experimental ones. Similar to previous chapters, the approach consists of: (i) computing the quantity of interest for the uncontrolled flow (here, a global stability analysis yields the growth rate and frequency of the

eigenmode responsible for the onset of vortex shedding), (ii) solving adjoint equations to obtain a sensitivity field, whose inner product with a localized force modelling the presence of the control cylinder yields the linear eigenvalue variation, and (iii) identifying regions where the control cylinder would stabilize the shedding eigenmode or modify its frequency. This approach is an attractive alternative to trial-and-error design since it allows us to evaluate quickly all possible positions of the control cylinder without calculating any controlled state.

The present chapter aims at predicting similarly the optimal placement of the control cylinder in an attempt to modify aerodynamic forces. The focus is on the drag of a square cylinder. Calculations are performed at $Re = 40$, in the stable regime.

5.2 Problem formulation

The two-dimensional steady-state flow past a square cylinder at zero angle of attack is considered. In the domain Ω, the velocity and pressure fields $(\mathbf{U}, P)^T = (U, V, P)^T$ are solutions of the stationary incompressible Navier–Stokes equations, which read in non-dimensional form

$$\nabla \cdot \mathbf{U} = 0, \quad \mathbf{U} \cdot \nabla \mathbf{U} + \nabla P - Re^{-1}\nabla^2 \mathbf{U} = \mathbf{0} \quad \text{in } \Omega, \tag{5.1}$$

$$\mathbf{U} = \mathbf{0} \quad \text{on } \Gamma_w \tag{5.2}$$

where Γ_w is the cylinder wall, and the Reynolds number $Re = U_\infty s/\nu$ is based on the magnitude of the free-stream velocity $(U_\infty, 0)^T$, the length s of the cylinder sides, and the fluid kinematic viscosity ν. The aerodynamic force acting on the cylinder is the integral of pressure and viscous stresses on the surface:

$$\mathbf{F} = \oint_{\Gamma_w} -\boldsymbol{\sigma}\,\mathbf{n}\,\mathrm{d}\Gamma = \oint_{\Gamma_w} P\mathbf{n} - Re^{-1}(\nabla\mathbf{U} + \nabla\mathbf{U}^T)\mathbf{n}\,\mathrm{d}\Gamma, \tag{5.3}$$

where $\boldsymbol{\sigma} = -P\mathbf{I} + Re^{-1}(\nabla\mathbf{U} + \nabla\mathbf{U}^T)$ is the stress tensor and $\mathbf{n}$ the unit normal pointing outward the domain. This force is classically decomposed into drag and lift forces, respectively in the streamwise and cross-stream directions (i.e. parallel and normal to the free-stream velocity): $D = \mathbf{F} \cdot \mathbf{e}_x$, $L = \mathbf{F} \cdot \mathbf{e}_y$. Accordingly, drag and lift coefficients are:

$$C_D = -2\mathbf{e}_x \cdot \oint_{\Gamma_w} \boldsymbol{\sigma}\,\mathbf{n}\,\mathrm{d}\Gamma, \quad C_L = -2\mathbf{e}_y \cdot \oint_{\Gamma_w} \boldsymbol{\sigma}\,\mathbf{n}\,\mathrm{d}\Gamma. \tag{5.4}$$

5.2.1 Drag sensitivity

Similar to previous chapters, a variational method is used to derive equations which allows to compute the sensitivity of drag and lift coefficients to a steady, small-amplitude control. Consider for instance a control force (source of momentum) $\mathbf{C}$ in the domain, and blowing or suction $\mathbf{U_c}$ in some region of the cylinder wall $\Gamma_c \subseteq \Gamma_w$. The flow field is now a solution of

the forced Navier–Stokes equations

$$\nabla \cdot \mathbf{U} = 0, \quad \mathbf{U} \cdot \nabla \mathbf{U} + \nabla P - Re^{-1} \nabla^2 \mathbf{U} = \mathbf{C} \quad \text{in } \Omega, \tag{5.5}$$

$$\mathbf{U} = \mathbf{U_C} \quad \text{on } \Gamma_c, \tag{5.6}$$

$$\mathbf{U} = \mathbf{0} \quad \text{on } \Gamma_w \setminus \Gamma_c. \tag{5.7}$$

The effect of control on the drag coefficient is at first order:

$$\delta C_D = (\nabla_{\mathbf{C}} C_D \,|\, \boldsymbol{\delta}\mathbf{C}) + \langle \nabla_{\mathbf{U_c}} C_D \,|\, \boldsymbol{\delta}\mathbf{U_c} \rangle, \tag{5.8}$$

where $\nabla_{\mathbf{C}} C_D = \partial C_D / \partial \mathbf{C}$ and $\nabla_{\mathbf{U_c}} C_D = \partial C_D / \partial \mathbf{U_c}$ are the sensitivities of C_D with respect to volume and wall control, respectively. The same expression holds for the lift coefficient. Hereafter the usual one- and two-dimensional L^2 inner products are used: $\langle \mathbf{a} \,|\, \mathbf{b} \rangle = \oint_{\Gamma_w} \mathbf{a} \cdot \mathbf{b} \, d\Gamma_w$, $(\mathbf{a} \,|\, \mathbf{b}) = \iint_\Omega \mathbf{a} \cdot \mathbf{b} \, d\Omega$.

In order to derive the sensitivities of drag and lift while satisfying the constraint (5.5)-(5.7), the following Lagrangian is introduced:

$$\mathscr{L}_D(\mathbf{Q}, \mathbf{C}, \mathbf{U_c}, \mathbf{Q}^\dagger, \mathbf{U_c}^\dagger) = C_D(\mathbf{Q}) - \left(\mathbf{Q}^\dagger \,\Big|\, \mathbf{N}(\mathbf{Q}) - (\mathbf{C}, 0)^T \right) - \left\langle \mathbf{U_c}^\dagger \,\Big|\, \mathbf{U} - \mathbf{U_c} \right\rangle. \tag{5.9}$$

As mentioned in chapter 1, if partial derivatives of $\mathscr{L}_D$ with respect to $\mathbf{Q}$, $\mathbf{Q}^\dagger$ and $\mathbf{U_c}^\dagger$ are zero, then (i) the total derivative of $\mathscr{L}_D$ with respect to control is

$$\frac{d\mathscr{L}_D}{d(\mathbf{C}, \mathbf{U_c})} = \frac{\partial \mathscr{L}_D}{\partial (\mathbf{C}, \mathbf{U_c})}, \tag{5.10}$$

and (ii) $\mathscr{L}_D = C_D$ since the constraints in (5.9) are identically satisfied. Finally, the sensitivities to control are:

$$\nabla_{\mathbf{C}} C_D = \frac{\partial \mathscr{L}_D}{\partial \mathbf{C}} = \mathbf{U}^\dagger, \quad \nabla_{\mathbf{U_c}} C_D = \frac{\partial \mathscr{L}_D}{\partial \mathbf{U_c}} = \mathbf{U_c}^\dagger, \tag{5.11}$$

where the first Lagrange multiplier $\mathbf{U}^\dagger$ is a solution of the adjoint equation $(\partial \mathbf{N}/\partial \mathbf{Q})^\dagger \mathbf{Q}^\dagger = \mathbf{0}$, obtained by setting $\partial \mathscr{L}_D / \partial \mathbf{Q} = \mathbf{0}$ and using integration by parts:

$$\nabla \cdot \mathbf{U}^\dagger = 0, \quad -\mathbf{U} \cdot \nabla \mathbf{U}^\dagger + \mathbf{U}^\dagger \cdot \nabla \mathbf{U}^T - \nabla P^\dagger - Re^{-1} \nabla^2 \mathbf{U}^\dagger = \mathbf{0} \quad \text{in } \Omega, \tag{5.12}$$

$$\mathbf{U}^\dagger = 2\mathbf{e}_x \quad \text{on } \Gamma_w, \tag{5.13}$$

while the second Lagrange multiplier $\mathbf{U_c}^\dagger$ is the adjoint stress

$$\mathbf{U}_c^\dagger = -P^\dagger \mathbf{n} - Re^{-1} (\nabla \mathbf{U}^\dagger + \nabla \mathbf{U}^{\dagger T}) \mathbf{n}. \tag{5.14}$$

Equations (5.12)-(5.13) are homogeneous in the domain but have non-homogeneous boundary conditions on the cylinder wall. This is unlike chapters 2, 3 and 4, where the adjoint

equations derived for sensitivities to control had homogeneous boundary conditions, like the base flow, and non-homogeneous equations of motion, with a forcing term equal to the sensitivity to flow modification. This comes from the very nature of drag, defined on the cylinder wall and contributing to $\partial \mathscr{L}_D / \partial \mathbf{Q}$ with boundary terms

$$2 \oint_{\Gamma_w} \mathbf{e}_x \cdot \left(\delta P \mathbf{I} - Re^{-1} (\nabla \delta \mathbf{U} + \nabla \delta \mathbf{U}^T) \right) \mathbf{n} \, \mathrm{d}\Gamma, \tag{5.15}$$

which must balance boundary terms arising from the integration by parts of $\left(\mathbf{Q}^\dagger \,\middle|\, (\partial \mathbf{N}/\partial \mathbf{Q}) \, \delta \mathbf{Q} \right)$:

$$- \oint_{\Gamma_w} \mathbf{U}^\dagger \cdot \left(\delta P \mathbf{I} - Re^{-1} (\nabla \delta \mathbf{U} + \nabla \delta \mathbf{U}^T) \right) \mathbf{n} \, \mathrm{d}\Gamma. \tag{5.16}$$

Note also that the viscous component of the adjoint stress in (5.14) is a *total* viscous stress containing both the velocity gradient and its transpose. In previous chapters, it contained only the velocity gradient, coming from the integration by parts of the viscous term $\nabla^2 \mathbf{U} = \nabla \cdot \nabla \mathbf{U}$ in the Navier–Stokes equations. However, for consistency with the definition of aerodynamic forces (5.3) in terms of total stress, it is convenient to write $\nabla^2 \mathbf{U} = \nabla \cdot (\nabla \mathbf{U} + \nabla \mathbf{U}^T)$, where the second term $\nabla \cdot \nabla \mathbf{U}^T = \nabla(\nabla \cdot \mathbf{U})$ is identically zero by incompressibility. This does not modify the end result.

5.2.2 Lift sensitivity

The same analysis as for drag holds, with the Lagrangian replaced by

$$\mathscr{L}_L(\mathbf{Q}, \mathbf{C}, \mathbf{U_c}, \mathbf{Q}^\dagger, \mathbf{U_c^\dagger}) = C_L(\mathbf{Q}) - \left(\mathbf{Q}^\dagger \,\middle|\, \mathbf{N}(\mathbf{Q}) - (\mathbf{C}, 0)^T \right) - \left\langle \mathbf{U_c^\dagger} \,\middle|\, \mathbf{U} - \mathbf{U_c} \right\rangle. \tag{5.17}$$

It results in the sensitivities

$$\nabla_\mathbf{C} C_L = \frac{\partial \mathscr{L}_L}{\partial \mathbf{C}} = \mathbf{U}^\dagger, \quad \nabla_{\mathbf{U_c}} C_L = \frac{\partial \mathscr{L}_L}{\partial \mathbf{U_c}} = \mathbf{U_c^\dagger}, \tag{5.18}$$

where the adjoint velocity $\mathbf{U}^\dagger$ is solution of the same equations (5.12)-(5.13) but with boundary condition $\mathbf{U}^\dagger = 2\mathbf{e}_y$ on Γ_w.

5.2.3 Sensitivity of combined functions

The same method can actually be applied to any function of lift and drag. For instance, consider the lift-to-drag ratio $\mathscr{J} = C_L/C_D$. Introducing the associated Lagrangian and differenti-

ating with respect to $\mathbf{Q}$, one finds the following contribution to boundary terms:

$$\frac{\partial \mathscr{J}}{\partial \mathbf{Q}} \delta \mathbf{Q} = \left(\frac{1}{C_D} \frac{\partial C_L}{\partial \mathbf{Q}} - \frac{C_L}{C_D^2} \frac{\partial C_D}{\partial \mathbf{Q}} \right) \delta \mathbf{Q} \tag{5.19}$$

$$= 2 \oint_{\Gamma_w} \left(\frac{1}{C_D} \mathbf{e}_y - \frac{C_L}{C_D^2} \mathbf{e}_x \right) \cdot \left(\delta P \mathbf{I} - Re^{-1} (\nabla \boldsymbol{\delta} \mathbf{U} + \nabla \boldsymbol{\delta} \mathbf{U}^T) \right) \mathbf{n} \, \mathrm{d}\Gamma, \tag{5.20}$$

which still has to be balanced by the term (5.16). Therefore the adjoint variable is solution of equations (5.12)-(5.13) but with boundary condition $\mathbf{U}^\dagger = (-2C_L/C_D^2, 2/C_D)^T$ on Γ_w, and the sensitivities of the lift-to-drag ratio to volume and wall control are the adjoint velocity and adjoint stress, respectively.

More generally, the contribution of an arbitrary function $\mathscr{J}(C_D, C_L)$ is

$$\frac{\partial \mathscr{J}}{\partial \mathbf{Q}} \delta \mathbf{Q} = \left(\frac{\partial \mathscr{J}}{\partial C_D} \frac{\partial C_D}{\partial \mathbf{Q}} + \frac{\partial \mathscr{J}}{\partial C_L} \frac{\partial C_L}{\partial \mathbf{Q}} \right) \delta \mathbf{Q} \tag{5.21}$$

$$= 2 \oint_{\Gamma_w} \left(\frac{\partial \mathscr{J}}{\partial C_D} \mathbf{e}_x + \frac{\partial \mathscr{J}}{\partial C_L} \mathbf{e}_y \right) \cdot \left(\delta P \mathbf{I} - Re^{-1} (\nabla \boldsymbol{\delta} \mathbf{U} + \nabla \boldsymbol{\delta} \mathbf{U}^T) \right) \mathbf{n} \, \mathrm{d}\Gamma, \tag{5.22}$$

so the adjoint velocity is solution of equations (5.12)-(5.13) but with boundary condition $\mathbf{U}^\dagger = (2\partial \mathscr{J}/\partial C_D, 2\partial \mathscr{J}/\partial C_L)^T$ on Γ_w. Interestingly, since adjoint equations are linear, one does not need to actually solve a new problem if sensitivities of C_D and C_L are already available: the sensitivity of any function $\mathscr{J}$ is readily obtained as

$$\nabla_* \mathscr{J} = \frac{\partial \mathscr{J}}{\partial C_D} \nabla_* C_D + \frac{\partial \mathscr{J}}{\partial C_L} \nabla_* C_L, \tag{5.23}$$

where $*$ stands for volume or wall control.

5.2.4 Sensitivity of pressure and viscous drag

It might be of interest to compute the individual sensitivities of pressure drag and viscous drag

$$C_{D,p} = 2\mathbf{e}_x \cdot \oint_{\Gamma_w} P \mathbf{n} \, \mathrm{d}\Gamma, \quad C_{D,v} = -2\mathbf{e}_x \cdot \oint_{\Gamma_w} Re^{-1} (\nabla \mathbf{U} + \nabla \mathbf{U}^T) \mathbf{n} \, \mathrm{d}\Gamma, \tag{5.24}$$

either to analyse the effect of control on each component separately, or to compare sensitivity maps with experimental results where only one of these components was available to measurement (e.g. Parezanović & Cadot (2012)). For separated flows, drag is almost entirely due to pressure at large Reynolds number but contributions from pressure and viscosity are of the same order at smaller Reynolds number, as shown in figure 5.1. However, trying to repeat the analysis with $\mathscr{J} = C_{D,p}$, for instance, the boundary term arising from the differentiation
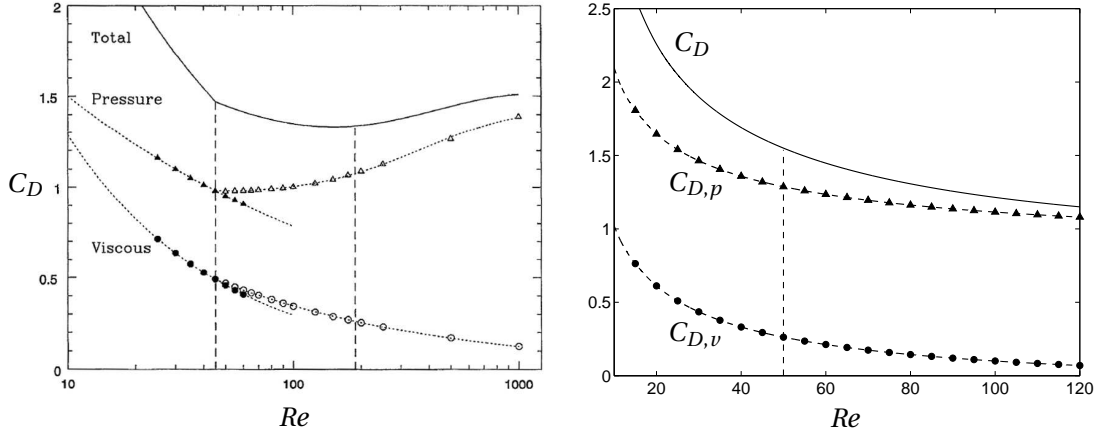
Figure 5.1 – Pressure and viscous drag coefficient. (*a*) Circular cylinder (filled symbols: steady base flow, unstable above $Re_c \simeq 47$; open symbols: mean values for the unsteady flow), from Henderson (1995). (*b*) Square cylinder (steady base flow, unstable above $Re_c \simeq 50$).

with respect to **Q** is

$$2 \oint_{\Gamma_w} \mathbf{e}_x \cdot \delta P \mathbf{n} \, \mathrm{d}\Gamma, \tag{5.25}$$

which seems impossible to balance with (5.16). This difficulty is not solved by integrating by parts the pressure stress only (instead of the total stress), since this would make the boundary term possible to cancel but, this time, volume terms would not allow us to identify the adjoint equation properly.

In the very particular case of the square cylinder at zero angle of attack, and when no wall control is applied, one can take advantage of the geometry: explicit calculation with $\mathbf{n} = (\pm 1, 0)^T$ and $\mathbf{n} = (0, \pm 1)^T$ shows that the front and rear faces only contribute to pressure drag (and viscous lift), while the top and bottom faces only contribute to viscous drag (and pressure lift). To compute the sensitivity of pressure drag, one can therefore solve equations (5.12)-(5.13) with boundary conditions $\mathbf{U}^\dagger = 2\mathbf{e}_x$ on the front and rear faces and $\mathbf{U}^\dagger = \mathbf{0}$ on the top and bottom faces.

Fortunately, the analysis is actually possible for arbitrary geometries. The point is to notice that viscous stresses at the wall are only tangential (Castro, Lozano, Palacios & Zuazua, 2007): $\mathbf{n} \cdot (\nabla \mathbf{U} + \nabla \mathbf{U}^T) \mathbf{n} = 0$. This can be used to recast the pressure drag coefficient (5.24) as

$$C_{D,p} = 2\mathbf{e}_x \cdot \oint_{\Gamma_w} P \mathbf{n} \, \mathrm{d}\Gamma = -2 \oint_{\Gamma_w} (\mathbf{n} \cdot \boldsymbol{\sigma} \, \mathbf{n})(\mathbf{n} \cdot \mathbf{e}_x) \, \mathrm{d}\Gamma. \tag{5.26}$$

Now the integration by part yields the boundary term

$$2 \oint_{\Gamma_w} \left[\mathbf{n} \cdot \left(\delta P \mathbf{I} - Re^{-1}(\nabla \boldsymbol{\delta U} + \nabla \boldsymbol{\delta U}^T) \right) \mathbf{n} \right] (\mathbf{n} \cdot \mathbf{e}_x) \, \mathrm{d}\Gamma, \tag{5.27}$$
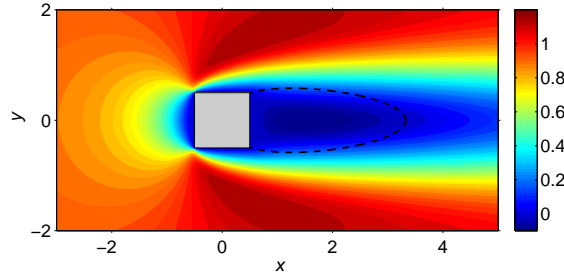
Figure 5.2 – Separatrix and streamwise velocity of the steady flow at $Re = 40$.

which can be balanced by (5.16) if the following condition is chosen: $\mathbf{U}^\dagger = 2\mathbf{n}(\mathbf{n} \cdot \mathbf{e}_x)$. Solving (5.12)-(5.13) with this boundary condition on Γ_w yields the adjoint velocity, and thus the sensitivities of the pressure drag coefficient. The sensitivities of the viscous drag coefficient can be simply recovered as $\nabla_* C_{D,v} = \nabla_* C_D - \nabla_* C_{D,p}$, where $*$ stands for volume or wall control.

5.3 Numerical method

All calculations are performed with a finite element method, similar in all aspects to that presented in section 2.1 and chapters 3-4. The mesh is highly refined close to the cylinder wall (336048 triangular elements) in order to obtain good accuracy for drag and lift results. Recall that the base flow equations (5.1)-(5.2) are solved with an iterative Newton method, and the linear adjoint equations (5.12)-(5.13) with a direct inversion. Figure 5.2 shows the streamwise velocity of the steady flow at $Re = 40$. The length of the recirculation region is about 2.8, and the drag coefficient $C_D = 1.67$.

5.4 Results

All results are obtained at $Re = 40$. In this regime the steady flow is stable, since vortex shedding appears via a Hopf bifurcation at the critical Reynolds number $Re_c \simeq 50$, similar to the circular cylinder.

5.4.1 Sensitivity to volume control

Figure 5.3 shows the sensitivity of drag and lift coefficients to volume control in the x and y directions. Red (resp. blue) regions indicate where a force along $\mathbf{e}_x$ or $\mathbf{e}_y$ would increase (resp. decrease) $C_{D/L}$. With respect to the $y = 0$ axis, drag has a symmetric sensitivity to streamwise control and an antisymmetric sensitivity to cross-stream control; conversely, lift has an antisymmetric sensitivity to streamwise control and a symmetric sensitivity to cross-stream control. This agrees with intuition. Drag is most sensitive to streamwise control in a large region upstream of the cylinder along the $y = 0$ axis, and to cross-stream control near the separation points. Lift is most sensitive to streamwise control near the cylinder corners,
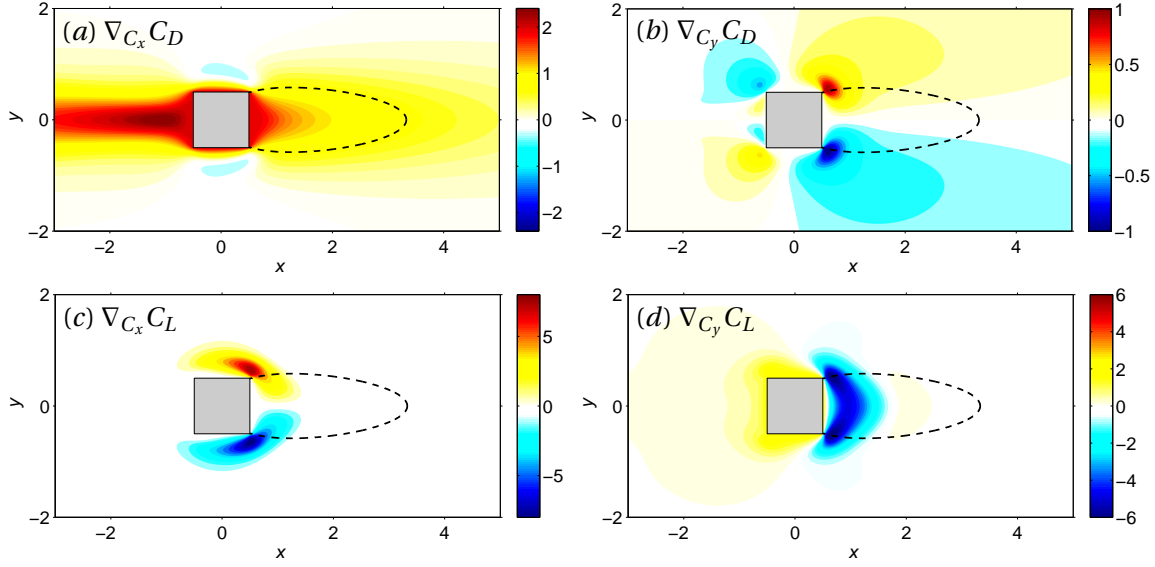
Figure 5.3 – Sensitivity to volume control: sensitivity of (*a*)-(*b*) drag coefficient and (*c*)-(*d*) lift coefficient, with respect to (*a*)-(*c*) a force in the streamwise direction $\mathbf{e}_x$, (*b*)-(*d*) a force in the cross-stream direction $\mathbf{e}_y$.

and to cross-stream control near the separations points and in the upstream part of the recirculation region.

5.4.2 Sensitivity to a control cylinder

The method already presented in previous chapters is used to predict the effect of a small circular control cylinder of diameter d inserted in the flow at $\mathbf{x}_c = (x_c, y_c)$: assuming the control cylinder feels the same drag force as in a uniform flow of velocity $\mathbf{U}(\mathbf{x}_c)$, the force $\boldsymbol{\delta}\mathbf{C}$ exerted by the control cylinder on the fluid is modelled as a steady force of same direction and amplitude, but opposite orientation:

$$\boldsymbol{\delta}\mathbf{C}(x, y) = -\frac{1}{2}d\,C_d(x, y)\,||\mathbf{U}(x, y)||\,\mathbf{U}(x, y)\,\delta(x - x_c, y - y_c) \tag{5.28}$$

where C_d is the drag coefficient of the control cylinder and depends on the local Reynolds number $Re_d(x, y) = ||\mathbf{U}(x, y)||\,d/v$. The drag coefficient of the main (square) cylinder therefore varies due to the presence of the control cylinder according to:

$$\delta C_D(\mathbf{x}_c) = (\nabla_{\mathbf{C}}C_D\,|\,\boldsymbol{\delta}\mathbf{C}) = -\frac{1}{2}d\,C_d(\mathbf{x}_c)\,||\mathbf{U}(\mathbf{x}_c)||\,\nabla_{\mathbf{C}}C_D(\mathbf{x}_c)\cdot\mathbf{U}(\mathbf{x}_c). \tag{5.29}$$

Figure 5.4(*a*) shows the expected variation δC_D as a function of $\mathbf{x}_c$ for a control cylinder of diameter $d = 0.1$. Two regions allow us to reduce the square drag: a large region in front of the cylinder, extending far upstream on the symmetry axis, and a second region on both sides of the recirculation region. In the first one, a maximum reduction of about 20% ($\delta C_D \simeq -0.3$)
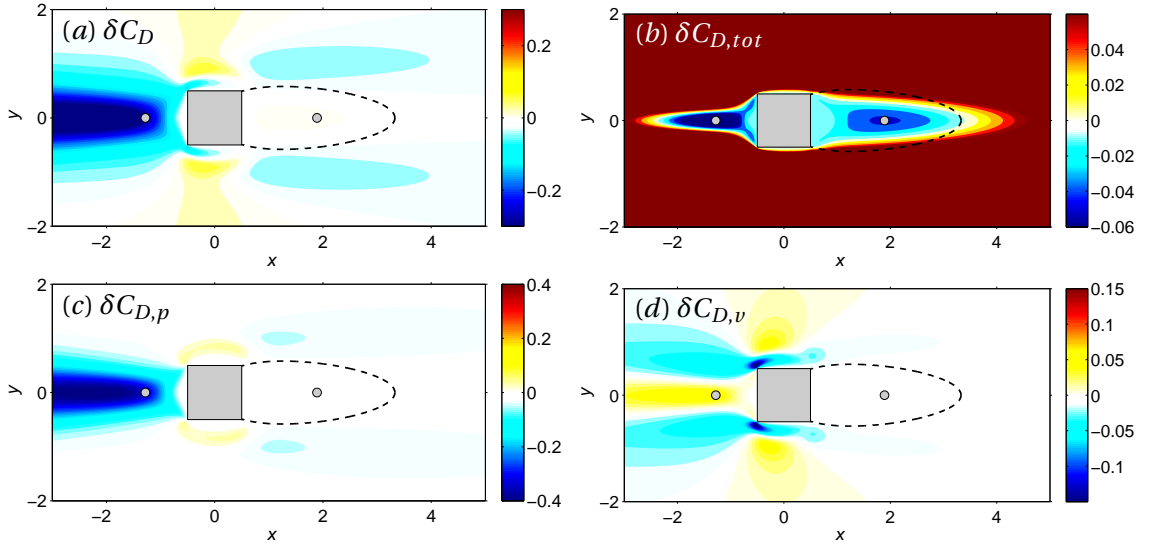
Figure 5.4 – Effect of a control circular cylinder of diameter $d = 0.1$ on (a) drag coefficient of the main square cylinder, (b) total two-cylinder drag coefficient, (c)-(d) pressure and viscous components of (a). Circles show control cylinder locations used for validation (figure 5.5).

can be achieved by inserting the control cylinder on the symmetry axis at $\mathbf{x}_c \simeq -1$ or -2, while the effect is much smaller downstream. Conversely, drag is increased by inserting the control cylinder on the upper or lower side of the main cylinder. The recirculation region has a smaller sensitivity because low velocities in this area result in weak control forces (5.28).

If the control objective is drag reduction, it is important to assess the net effect by taking into account the contribution of the control cylinder itself to the drag force, $-\boldsymbol{\delta}\mathbf{C}\cdot\mathbf{e}_x$. The total drag coefficient variation reads in this case:

$$\delta C_{D,tot} = (\nabla_{\mathbf{C}} C_D \,|\, \boldsymbol{\delta}\mathbf{C}) = -\frac{1}{2} d\, C_d(\mathbf{x}_c)\, ||\mathbf{U}(\mathbf{x}_c)||\, (\nabla_{\mathbf{C}} C_D(\mathbf{x}_c) - 2\mathbf{e}_x)\cdot\mathbf{U}(\mathbf{x}_c). \tag{5.30}$$

Figure 5.4(b) shows this total "two-cylinder" variation for the same control cylinder diameter $d = 0.1$. Upstream, the region where the main drag reduction is larger than the drag induced by the control cylinder is now limited to a thin and short strip of the symmetry axis, for $x_c \gtrsim -2$. Downstream, it appears that reduction of the total drag is not achieved outside the recirculation region, as the control cylinder drag spoils the main cylinder reduction. On the other hand, a small region of total drag reduction is observed inside the recirculation region: interestingly, the main drag is not much affected there, but the backward flow turns the control cylinder into a source of thrust. Nevertheless, this effect is weak (note the different scales in (a) and (b)).

Next, individual contributions from pressure and viscous effects to the main cylinder drag are analysed as described in section 5.2.4. Solving the adjoint problem with modified boundary conditions, and evaluating the effect of a small control cylinder yields maps 5.4(c)-(d) for
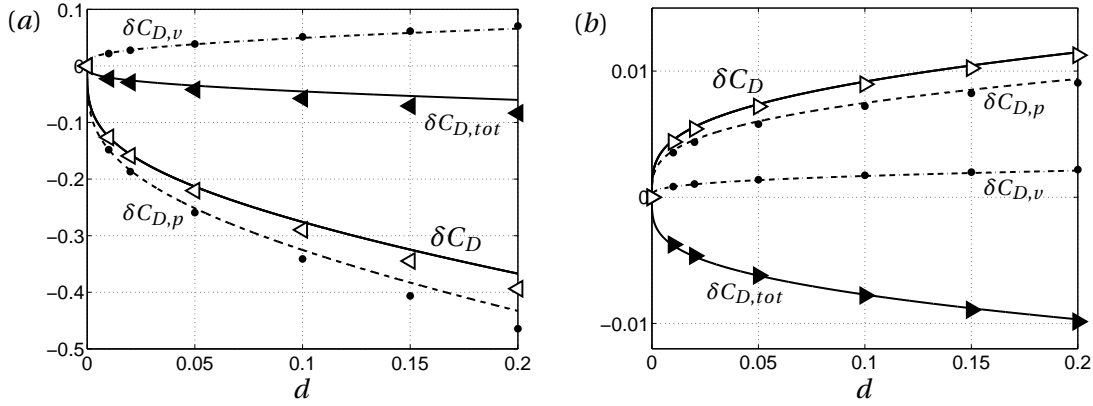
Figure 5.5 – Drag variation due to a small control cylinder of diameter d located at (a) $\mathbf{x}_c = (-1.3, 0)$ and (b) $\mathbf{x}_c = (1.9, 0)$. Lines show predictions from sensitivity analysis, symbols are results from non-linear simulations including the control cylinder as a volume force (5.28). Main (square) cylinder drag: open symbols and solid lines, two-cylinder total drag: filled symbols and solid lines, pressure and viscous contributions to the main cylinder drag: dots and respectively dashed and dash-dotted lines.

the variation of pressure drag coefficient $\delta C_{D,p}$, and the variation of viscous drag coefficient $\delta C_{D,v}$, respectively. The similarity of figures 5.4(a) and (c) indicates that in most regions the effect of the control cylinder is due to pressure effects. On the sides of the recirculation region, both pressure and viscous effects contribute to drag reduction. Conversely, on the symmetry axis upstream of the cylinder, and on the top and bottom sides close to the walls, these effects are competing: upstream, pressure effects dominate and yield an overall drag reduction (because the flow is slowed down downstream of the control cylinder, pressure on the square front wall is decreased and the pressure difference with the rear wall is reduced); close to the sides, viscous effects dominate and yield an overall drag reduction (because the control cylinder deflects the flow outwards, decreasing wall shear stress). Still on the top and bottom sides but farther away from the walls, viscous effects are dominant (the flow is accelerated between the two cylinders, thus wall shear stress and drag increase).

Figure 5.5 illustrates and validates the method for two positions of the control cylinder: $\mathbf{x}_c = (-1.3, 0)$ and $\mathbf{x}_c = (1.9, 0)$. Lines are predictions from sensitivity analysis while symbols correspond to actual non-linear simulations with the control cylinder modelled as (5.28), where the two-dimensional Dirac delta is approximated by a Gaussian function of appropriate size with respect to the mesh size (standard deviation 0.006). The main cylinder drag is shown with solid lines and open symbols, pressure drag with dashed lines and dots, viscous drag with dash-dotted lines and dots. The agreement between sensitivity and nonlinear results is good, despite slight nonlinear effects noticeable when $d \gtrsim 0.1$. Sensitivity predictions are not straight lines because the drag first-order variation (5.29) is linear with respect to the force $\boldsymbol{\delta}\mathbf{C}$, not the diameter d. As expected from figure 5.4(a), the first position (upstream) is associated with a large drag reduction, while the second one (downstream) yields a slight increase. The total two-cylinder drag is also shown (solid lines and filled symbols). In agreement with

figure 5.4(b), the control cylinder produces drag on its own when located upstream, and drag reduction drops from $\simeq -17\%$ for the main cylinder alone to $\simeq -3\%$ when both cylinders are taken into account. Conversely, the control cylinder is a source of thrust in the recirculation region and, although the effect is small, turns the slight drag increase of the main cylinder into a slight total drag decrease.

5.4.3   Sensitivity to wall control

Figures 5.6(a)-(b) show sensitivity maps of drag and lift coefficients with respect to wall actuation. As in previous chapters, arrows pointing from the cylinder towards the fluid domain indicate that wall blowing (resp. suction) in the same direction increases (resp. decreases) $C_{D/L}$. The sensitivity of C_D is symmetric in U_c and antisymmetric in V_c with respect to the $y = 0$ axis (like the uncontrolled flow field $(U, V)^T$ and the sensitivity to volume control $\nabla_{\mathbf{C}} C_D$); conversely, the sensitivity of C_L is antisymmetric in U_c and symmetric in V_c. Regarding drag, the largest variation is obtained with actuation normal to the wall on front and rear faces, and with actuation tilted by about $45°$ on top and bottom faces. Regarding lift, the largest variation is obtained with actuation normal to the wall except near downstream corners, i.e. close to separation points.

Scale bars show that, globally, lift is more sensitive than drag to wall control. More interestingly, drag and lift can be modified independently, choosing actuation locations and directions carefully so as to take advantage of symmetry properties or relative sensitivity magnitudes. For instance: (i) a combination of wall-normal suction on both top and bottom sides reduces drag without affecting lift; (ii) a combination of suction on the top side and blowing on the lower side increases lift without affecting drag; (iii) actuation at the front or rear wall modifies drag while lift shows little or no variation. As these examples suggest, configurations can be tailored to control objectives.

Figures 5.6(c)-(f) show individual contributions from pressure and viscous effects. Lift sensitivity is almost completely dominated by pressure effects. Drag variations come from pressure only on the rear face, but from a combination of both pressure and viscous effects on other faces: they add up on the front face and compete on top and bottom faces.

Two examples of localized wall-normal blowing/suction are shown in figure 5.7: actuation (i) on the front face at $y_c = 0$, and (ii) on the top face at $x_c = 0.2$. Actuation is applied as a velocity boundary condition, with the following properties: total flow rate W ($W > 0$ for blowing, $W < 0$ for suction), Gaussian profile centred around x_c or y_c, and width (standard deviation) 0.05. As predicted by figures 5.6(a)-(b), blowing reduces C_D in case (i) (fig.5.7(a)) and reduces C_L in case (ii) (fig.5.7(b)). The agreement between sensitivity predictions (solid lines) and actual nonlinear results (open symbols) is good, but nonlinear effects are observed, which are particularly strong in case (i). Theses nonlinear effects are more pronounced for the pressure component (dashed lines) than for its viscous counterpart (dash-dotted lines).
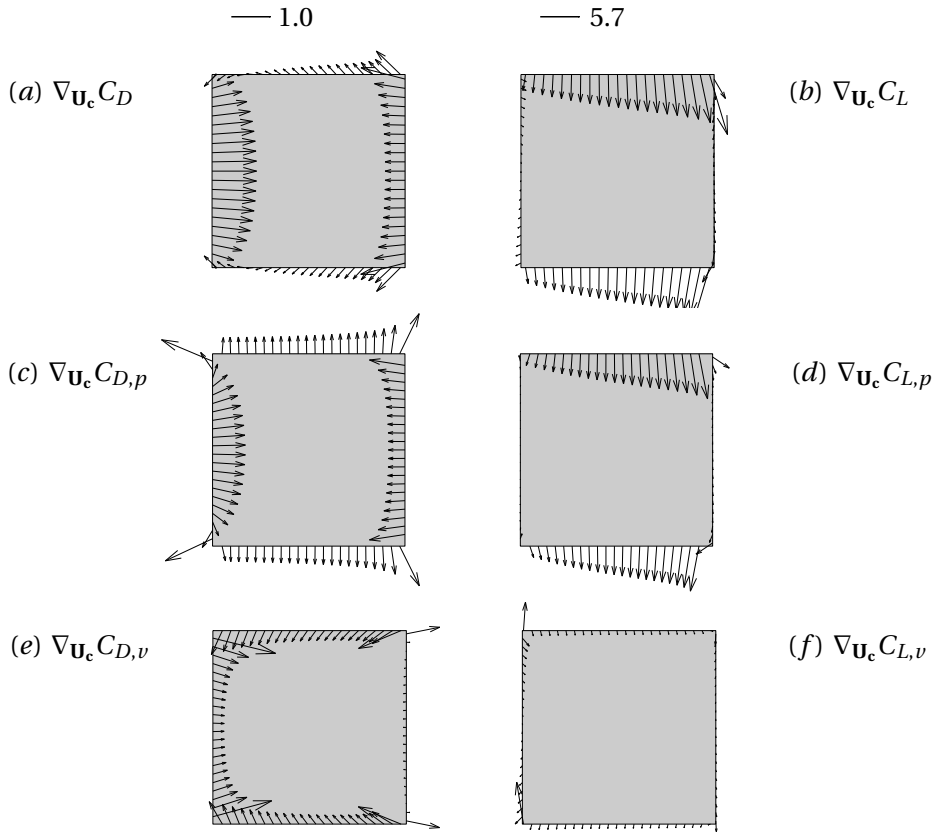
—— 1.0 —— 5.7

(a) $\nabla_{\mathbf{U_c}} C_D$

(b) $\nabla_{\mathbf{U_c}} C_L$

(c) $\nabla_{\mathbf{U_c}} C_{D,p}$

(d) $\nabla_{\mathbf{U_c}} C_{L,p}$

(e) $\nabla_{\mathbf{U_c}} C_{D,v}$

(f) $\nabla_{\mathbf{U_c}} C_{L,v}$

Figure 5.6 – Sensitivity to wall control. (a): drag coefficient, (b): lift coefficient, (c)-(d): pressure contribution, (e)-(f): viscous contribution. Arrows point in the direction of positive sensitivity.
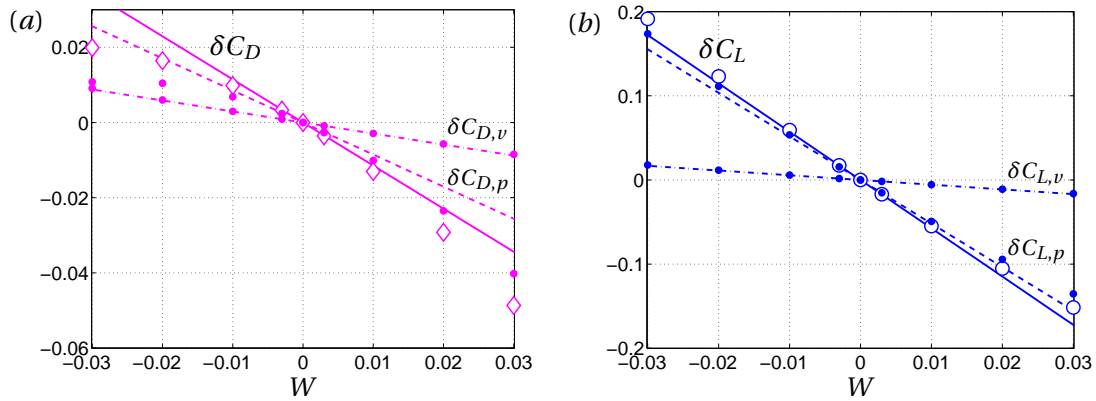

Figure 5.7 – Variation of aerodynamic coefficients when localized wall-normal control is applied with flow rate W ($W > 0$ for blowing, $W < 0$ for suction): (a) drag coefficient for control on the front face at $x_c = -0.5$, $y_c = 0$, (b) lift coefficient for control on the top face at $x_c = 0.2$, $y_c = 0.5$. As in figure 5.5, solid lines show $C_{D/L}$, dashed lines pressure contribution, dash-dotted lines viscous contribution.
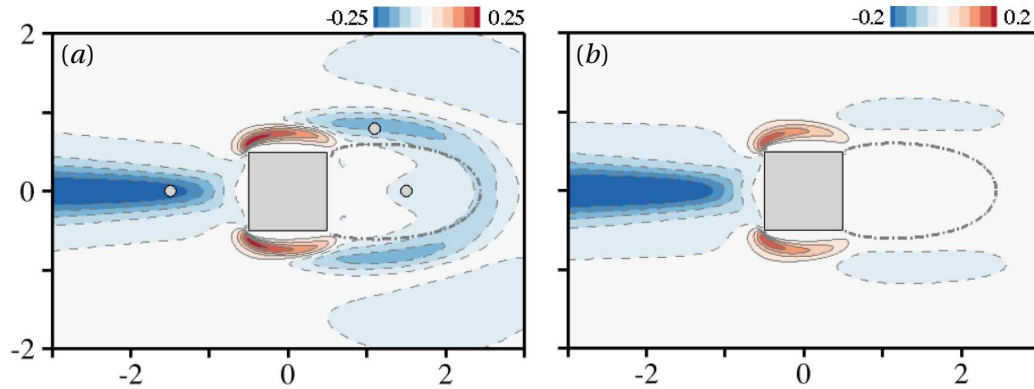
Figure 5.8 – Effect of a control circular cylinder of diameter $d = 0.1$ on the mean drag coefficient at $Re = 100$. Sensitivity analysis conducted (*a*) from adjoint-looping or (*b*) from the mean flow without coupling of the Reynolds stresses. From Meliga *et al.* (2014).

5.5 Conclusion

Recently, the sensitivity of the mean drag (as well as drag and lift fluctuations) was computed in the supercritical regime $Re > Re_c$ (Meliga, Boujo, Pujals & Gallaire, 2014). The method consisted in using "adjoint looping", i.e. integrating the Navier–Stokes equations forward in time and the adjoint equations backward (see chapter 1 for applications to optimal growth and optimal control). An example is given in figure 5.8(*a*) at $Re = 100$. The sensitivity thus obtained is useful as it allows us to predict the effect of any control without computing the controlled flow. Still, this approach comes with large memory requirements to store the direct solution needed for the adjoint problem. In order to reduce the computational burden, an alternative simplified method was proposed where the sensitivity of the "frozen" mean flow is calculated neglecting the modification of the unsteady vortex shedding by the control and therefore its nonlinear contribution to the mean drag. As shown in figure 5.8(*b*), these assumptions result in some error but allow a successful identification of the main regions of large sensitivity, which suggests that the method can be extended to turbulent flows if enough care is taken (Meliga *et al.*, 2012).

Conclusion

Summary

In an effort to develop new flow control methodologies, sensitivity analysis was applied to several quantities of interest in steady laminar separated flows. Maps of sensitivity to small-amplitude steady control were computed by solving appropriate adjoint equations. Both control in the fluid (volume force or control cylinder) and control at a wall (blowing and suction) were considered. Taking advantage of the power of adjoint methods, these sensitivity maps were obtained at low computational cost, i.e. without ever solving actual controlled flows. The predictive character of these maps allowed the identification of regions where control would be the most effective in altering flow characteristics. Quantities of interest considered in this work include the amplification of external harmonic and stochastic forcing in convectively unstable flows, geometric properties (such as the position of stagnation points, the separatrix angles, the area of backflow/recirculation regions), and aerodynamic forces. For most of these quantities, adjoint equations were newly derived.

Chapter 2: The amplification of external perturbations (harmonic optimal gain) in the stable flow past a wall-mounted bump was found to reach very large values. A subcritical bifurcation induced by small-amplitude perturbations was indeed observed, illustrating the strong amplifier nature of this flow. Sensitivity analysis revealed that harmonic gain could be drastically reduced at all frequencies, using wall suction in the most sensitive region, i.e. the bump summit (figure 1). Direct numerical simulations confirmed the effectiveness of this control configuration in reducing amplification in the stable regime and in delaying transition. Sensitivity analysis applied to leading eigenvalues in the unstable regime led to the same conclusion, namely that wall suction at the bump summit has a stabilising effect. Experiments in a water channel supported the above results: at large enough flow rates, wall control at the bump summit reduced the amplitude of temporal fluctuations in the recirculation region and in the shear layer. At smaller flow rates, however, a strong Kelvin-Helmholtz shear layer instability was triggered by the control; the clarification of this phenomenon requires further investigation.

Chapter 3: With the aim of simplifying control design, complex in the case of harmonic perturbations because several frequencies have to be taken into account simultaneously, the
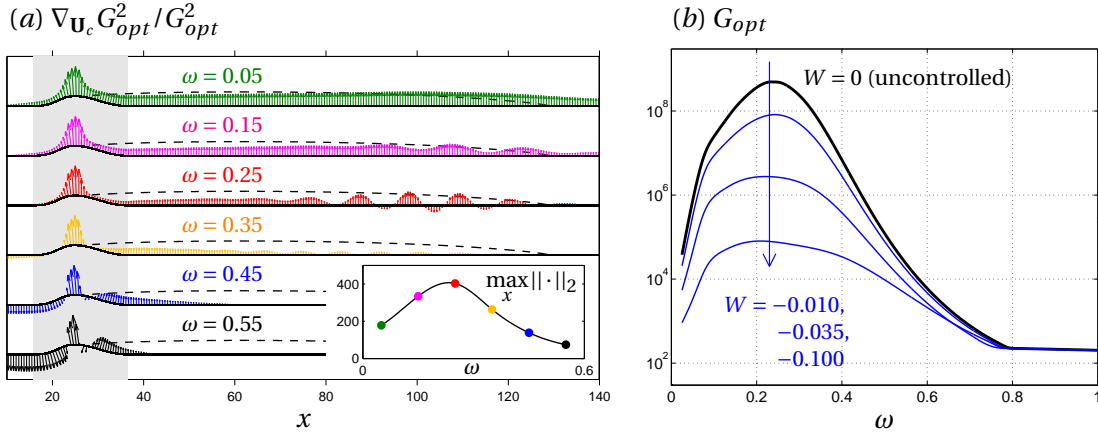
Conclusion

Figure 1 – Sensitivity and control of optimal harmonic gain in the flow past a wall-mounted bump at $Re = 580$. (a) Sensitivity of optimal gain at frequencies $\omega = 0.05, 0.15, \ldots 0.55$ to steady wall control (rescaled for each frequency by the largest point-wise L^2 norm; this maximal value is shown in the inset). From figure 2.11. (b) Reduction of the optimal gain when applying vertical wall suction at the bump summit. From figure 2.13.
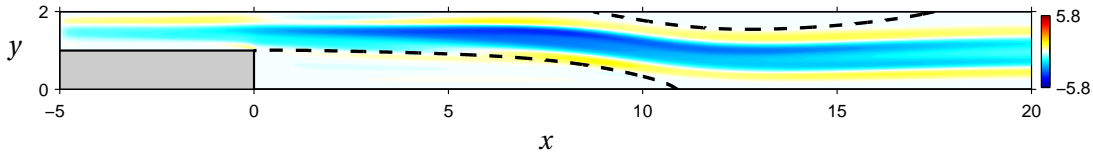

Figure 2 – Sensitivity and control of noise amplification in the flow past a backward-facing step at $Re = 500$ (expansion ratio $\Gamma = 0.5$): effect of a small control cylinder of diameter $d = 0.05$ on the stochastic gain. From figure 3.11.

amplification of stochastic perturbations was considered as a convenient alternative. Computing the sensitivity of this single quantity involves a weighted sum of the sensitivities of optimal and sub-optimal harmonic gains. In the flow past a backward-facing step, it was found that the sensitivity of the stochastic gain was well captured by that of the optimal harmonic gain at the optimal frequency, both for volume control and for wall control (figure 2). This result might be general in strongly non-normal flows if amplification is large in a particular range of frequencies and if the optimal harmonic gain is well separated from sub-optimal gains in this frequency range. When these conditions are satisfied, sensitivity computation becomes much cheaper.

Chapter 4: Original methods made possible the derivation of sensitivity of geometric quantities in separated flows (figure 3). The link with stability properties was also investigated. The position of the reattachment point in the bump flow was found to be very sensitive to control, and its sensitivity map was largely similar to that of backflow area and recirculation area. The sensitivity maps of these three quantities closely reproduce that of the optimal harmonic gain, indicating that this flow becomes a weaker amplifier when the extent of its recirculation region is reduced. In contrast, the separatrix angles and the position of the separation point appeared fairly insensitive and robust to control. In the flow past a circular cylinder, the sen-
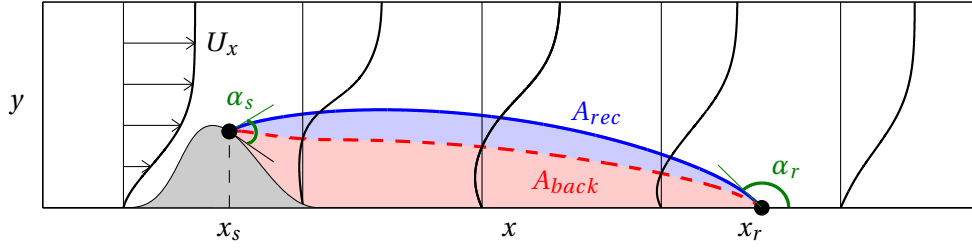
Figure 3 – Geometric quantities of interest in separated flows: location of separation and reattachment points x_s, x_r, angles of the separatrix at the wall α_s, α_r, recirculation area A_{rec} and backflow area A_{back}. From figure 4.1.
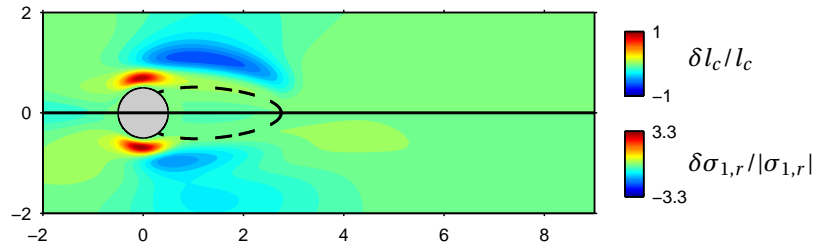

Figure 4 – Link between geometric quantities and stability properties in the flow past a circular cylinder at $Re = 40$: effect of a small control cylinder ($d = 0.10D$) on the recirculation length (upper half) and on the most unstable mode's growth rate (lower half). From figure 4.29

sitivity of the recirculation length was strongly correlated to that of the leading eigenmode's growth rate close to the linear instability threshold (figure 4). Therefore, shortening the recirculation region in this flow makes it more stable and can suppress vortex shedding. Farther away from the onset of instability, no link appears between linear stability and base flow recirculation length. Considering instead the mean flow recirculation length could yield valuable results.

In order to predict separation while reducing computational time, the Interactive Boundary Layer method was successfully applied to the bump flow and showed very good agreement with Navier–Stokes simulations (figure 5). This is a first step towards a one-dimensional streamwise description of separated flows, through its lumped version where the strong coupling between the boundary layer and the free-stream region are integrated out in the cross-stream direction. In view of the relative effectiveness of geometric indicators to serve as surrogate for stability properties, these strongly coupled integral methods hold the promise for even more efficient control schemes.

Chapter 5: As an interesting complementary approach to aerodynamic shape optimization, the sensitivity of aerodynamic forces to control was presented for the flow past a square cylinder (figure 6). A careful analysis showed that lift and drag could be modified independently using appropriate wall control configurations, allowing for example drag reduction at con-
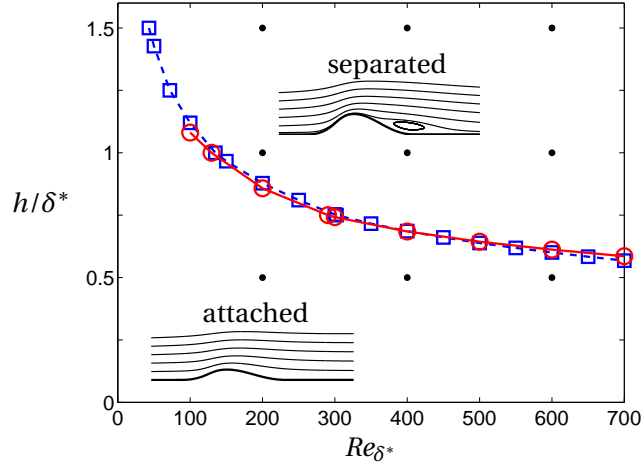
167

Figure 5 – Interactive Boundary Layer theory for the efficient calculation of separation properties: incipient separation (zero wall shear stress) in the flow past a wall-mounted bump, for different Reynolds numbers and bump height ratios. Red: IBL; blue: Navier–Stokes. From figure 4.17.

stant lift or lift enhancement at constant drag. The sensitivity of drag and lift combinations (like the lift-to-drag ratio) can be obtained at no additional cost. The sensitivity of pressure and viscous forces could be analysed separately from a modified adjoint problem, providing insight into physical mechanisms and facilitating comparison with pressure-only or shear stress-only experimental measurements.

Perspectives

The present thesis suggests that a wide variety of flow properties, if not all, can be analysed in terms of sensitivity to steady actuation, opening interesting perspectives for the control of separated flows. In this work, focus was on steady two-dimensional configurations. Therefore it seems natural in the future to investigate unsteady and/or three-dimensional aspects. Possible directions to pursue this line of research further include the following.

(i) **Unsteady laminar flows**, e.g. with adjoint looping, where the full unsteady equations are solved forward and the associated unsteady adjoint equations are then solved backward to obtain the sensitivity of interest. This approach is rigorously exact but computationally expensive (long CPU time, large memory requirement). In some cases, an attractive alternative is to use a suitable modelling of relevant physical phenomena: time-averaging, amplitude equations, or self-consistent models describing non-linear limit cycles with a reduced number of flow structures. For instance Meliga *et al.* (2014) computed drag sensitivity for a square cylinder at $Re = 100$ from the frozen mean flow and obtained a good agreement with exact results from adjoint looping (figure 7); questions then arise as to whether this method is still satisfactorily predictive in other flows, and whether regions of poorer agreement can be identified beforehand (possibly as regions
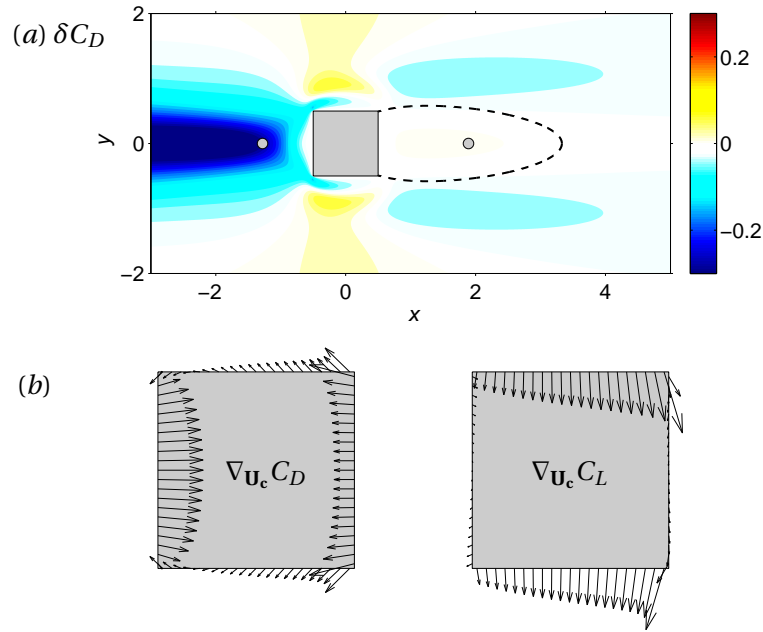
Figure 6 – Aerodynamic sensitivity of a square cylinder at $Re = 40$. (a) Effect on drag of a control circular cylinder of diameter $d = 0.1$. (b) Sensitivity of drag and lift to wall control. From figures 5.4-5.6.
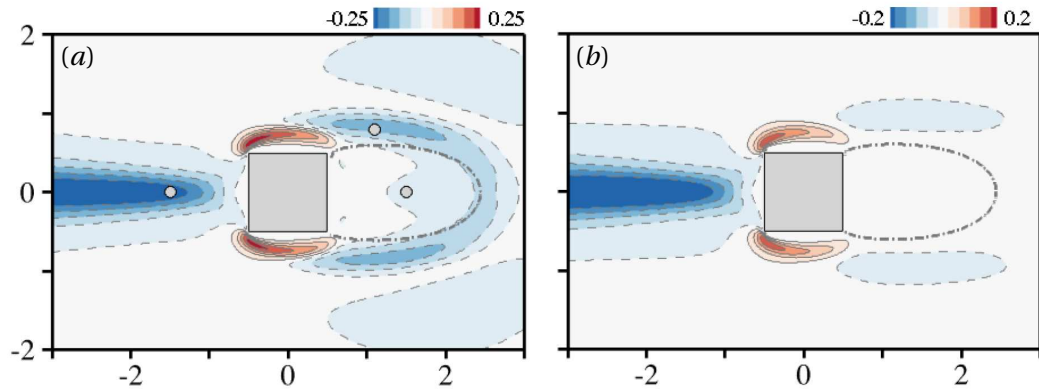

Figure 7 – Effect of a control circular cylinder of diameter $d = 0.1$ on the mean drag coefficient at $Re = 100$. Sensitivity analysis conducted (a) from unsteady adjoint-looping or (b) from the mean flow without coupling of the Reynolds stresses. From Meliga *et al.* (2014). Reproduced from figure 5.8.
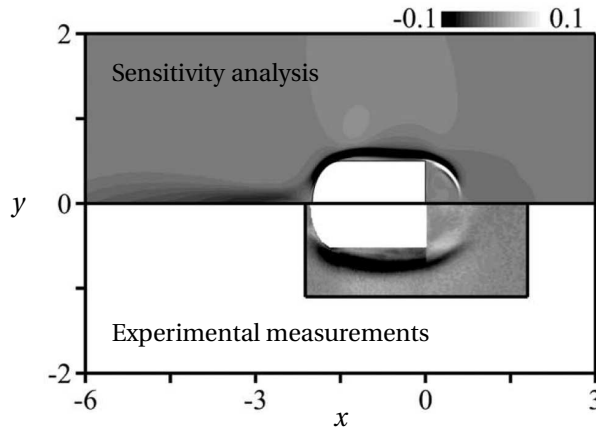
Figure 8 – Effect of a small control cylinder (diameter $d = 0.04$) on vortex shedding frequency (eigenfrequency) in the flow past a D-shaped cylinder at $Re = 13000$. Upper half: turbulent adjoint-based sensitivity analysis (Meliga *et al.*, 2012); lower half: measurements (Parezanović & Cadot, 2012). Reproduced from figure 1.12.

of large Reynolds stresses, which are neglected in the frozen mean flow assumption) without calculating the exact sensitivity for comparison purposes.

Recently, Mantić Lugo, Arratia & Gallaire (2014) proposed a self-consistent model yielding with good accuracy the saturation dynamics of the non-linear limit cycle in the wake of a circular cylinder; this model too could serve as the basis for a simplified and computationally inexpensive sensitivity analysis.

(ii) **Turbulent flows**, similar to (i) in spirit but requiring in addition the derivation of adjoint equations for turbulent variables. Meliga *et al.* (2012) followed this approach and obtained the sensitivity of vortex-shedding frequency in the wake of a D-shaped cylinder at $Re = 13000$, in very good agreement with experimental measurements from Parezanović & Cadot (2012) (figure 8). Mettot, Sipp & Bézard (2014) recently obtained similar results *without* taking turbulence into account, but further investigation is required to determine whether this simplification applies to other flows. In any case, it would be interesting to investigate the relationship between recirculation length and drag coefficient in turbulent separated flows, like the one reported by Parezanović & Cadot (2012) for a bluff body (figure 9).

(iii) **Unsteady control**, in particular **periodic** wall actuation. It is known indeed that, from an experimental perspective, alternative blowing and suction is both easier to implement and more effective than unidirectional blowing or suction. Parametric studies often reveal the existence of an optimal range of frequencies, where control is the most effective. For instance, Garnier *et al.* (2012) observed an optimal frequency for the control of the recirculation area in the lee of a two-dimensional rounded backward-facing step using periodic blowing and suction close to the separation point in LES and unsteady RANS simulations (figure 10). Sensitivity analysis might be well-suited to predict in a simple
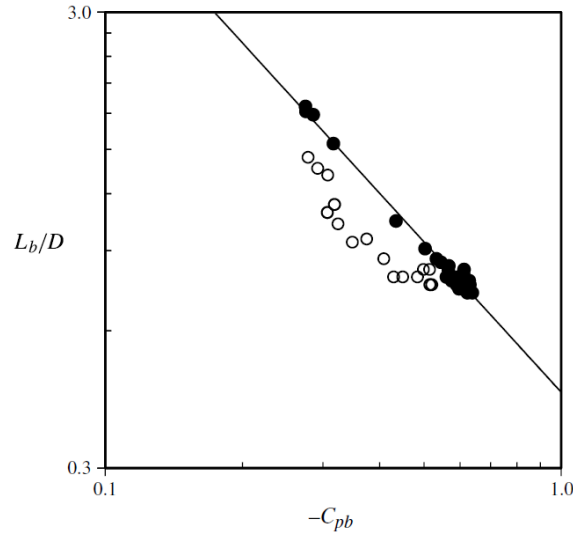
Figure 9 – Increasing the recirculation length reduces the drag coefficient (base pressure coefficient) of a D-shaped cylinder in a turbulent flow at $Re = 13000$. Here a small control cylinder ($d = 0.12D$) is inserted $0.4D$ downstream the cylinder base, at different heights inside (filled circles) and outside (open circles) the recirculation region (Parezanović & Cadot, 2012).

way this optimal control frequency range. One could think of an appropriate combination of Reynolds stresses originating from the response to periodic wall control, and the already available sensitivity of recirculation area (or any other quantity of interest).

(iv) **Spanwise-periodic control of nominally two-dimensional flows**, such as streamwise streaks in two-dimensional wakes or boundary layers. Fransson, Talamelli, Brandt & Cossu (2006) showed experimentally that transition to turbulence could be delayed in a boundary layer by imposing a steady spanwise-periodic flow modification using roughness elements designed to enforce optimal perturbations (streamwise vortices amplified into streamwise streaks). Figure 11 shows how Tollmien–Schlichting waves lead to transition in the uncontrolled boundary layer while the streaky boundary layer remains laminar. Hwang & Cossu (2010) computed in a parallel Couette flow the optimal response to initial conditions, harmonic forcing and stochastic forcing (in this case, the small number of degrees of freedom allowed for the direct resolution of a Lyapunov equation to obtain the stochastic response, without resorting to integration over frequencies as in chapter 3); the sensitivity of these optimal responses could easily be computed with the addition of a transverse wavenumber.

Another interesting feature of the spanwise-periodic control of two-dimensional flows is the fact that the first-order sensitivity of eigenvalues is zero in such configurations (Hwang, Kim & Choi, 2013; Del Guercio, Cossu & Pujals, 2014): small-amplitude flow modification and control that are periodic in the transverse direction are predicted to have no effect on linear stability properties; at larger amplitude, however, they are observed to be more efficient than two-dimensional flow modifications in stabilizing par-
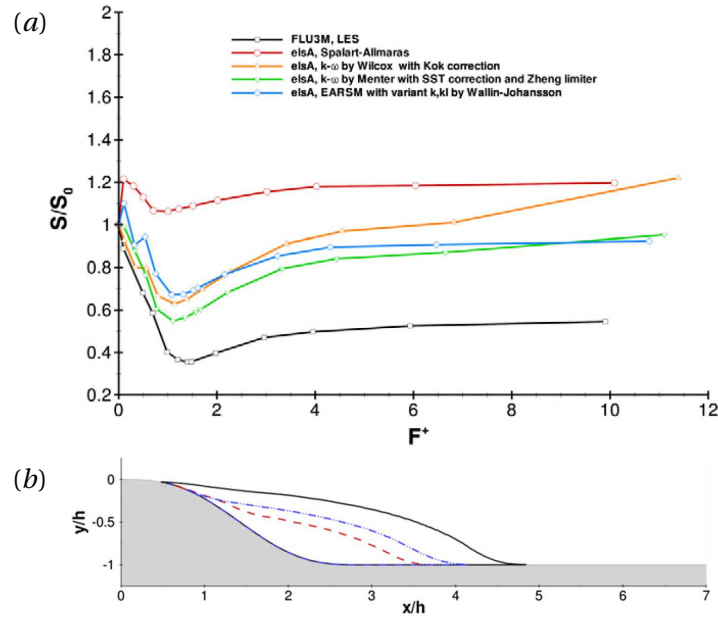
Figure 10 – Unsteady control of the recirculation area in the separated flow past a rounded backward-facing step at $Re = 30000$. (*a*) Variation in recirculation area vs. frequency of periodic wall blowing/suction; (*b*) separating streamline in the uncontrolled flow (solid line) and several controlled flows (dashed lines). From Garnier *et al.* (2012).
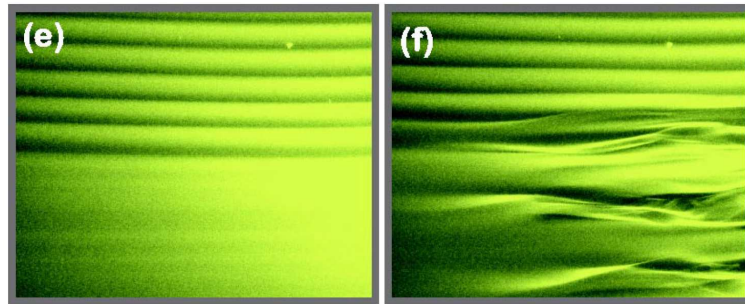
Figure 11 – Three-dimensional control of a two-dimensional boundary layer. Left: roughness elements create streamwise vortices which are amplified downstream and form streamwise streaks (upper half), whereas the uncontrolled boundary layer is two-dimensional (lower half). Right: when perturbing the whole flow with Tollmien–Schlichting waves, the uncontrolled boundary layer undergoes transition while the controlled one remains laminar (Fransson *et al.*, 2006).

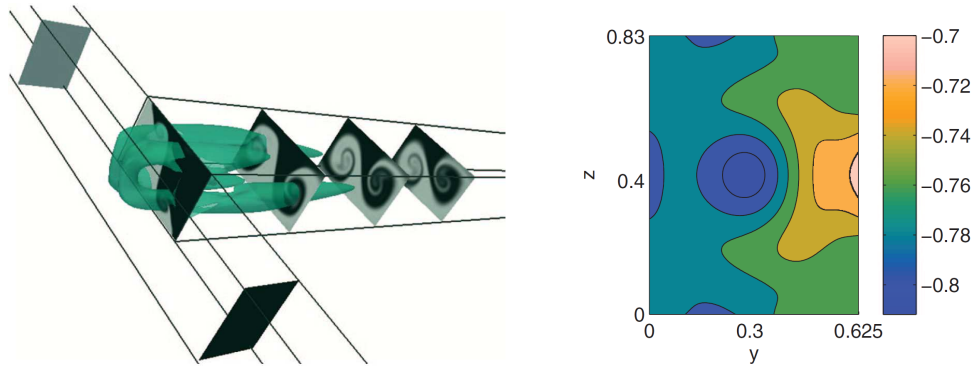Figure 12 – Three-dimensional sensitivity analysis (Fani *et al.*, 2013). (*a*) T-junction flow (two inlets on the left, outlet on the right) computed by DNS above the instability threshold: vortices (iso-surface of λ_2 criterion) and cross-sections of passive tracer illustrating mixing. (*b*) Sensitivity to modification of the inlet velocity profile: an incompletely developed profile with larger velocity at the center of the inlet has a stabilizing effect.

allel wakes (Del Guercio *et al.*, 2014), therefore an appropriate sensitivity analysis taking second-order effects into account is required to reconcile theoretical predictions with observed non-zero variations.

(v) Three-dimensional flows, either **spanwise-periodic flows**, where transverse variations are conveniently described with a limited number of Fourier modes, or on a more computationally intensive level, **fully three-dimensional flows**, such as non-axisymmetric bodies of finite width (e.g. Ahmed body, wall roughness elements), flows confined in channels of finite extent, or even more complex arbitrary geometries. For instance, Fani, Camarri & Salvetti (2013) computed in a three-dimensional T-junction flow the sensitivity of the leading eigenmode to flow modification (in the volume or at the inlet) and to wall control (figure 12).

In addition to the above-mentioned extensions to unsteady and three-dimensional cases, looking for original descriptions of quantities of interest will broaden the range of control opportunities. For instance, Monokrousos *et al.* (2011) considered viscous dissipation as a measure of turbulence. They used adjoint methods to find the initial condition of minimum energy leading to transition to turbulence in a plane Couette flow; similar methods could guide the design of efficient control strategies to delay or promote transition. Foures *et al.* (2014) recently optimized the mixing of a passive scalar in a plane Poiseuille flow, using as objective functions (i) the variance of the scalar field or (ii) a "mix-norm" targeting large-scale structures, and found these mixing measures more efficient than energy amplification (figure 13). Mixing can also be improved by controlling separation. Wang *et al.* (2003) developed such an approach to create unsteady separation points at prescribed locations using tangential blowing and suction on the wall of a bluff body, in order to create attracting material lines which "collect fluid particles from the [...] wall regions and inject the particles into the
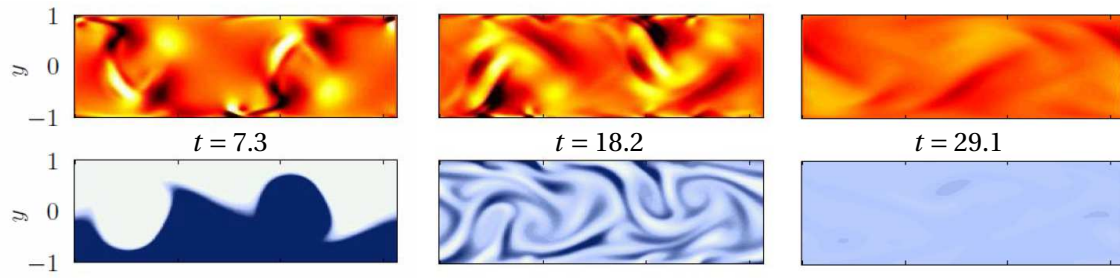
173

Figure 13 – Optimal mixing in a plane Poiseuille flow using actuation at the walls ($y = \pm1$): perturbation vorticity field (top) and passive scalar field to be mixed (bottom), at three successive times (left to right). Mixing is more effective when optimizing the variance of the scalar or its "mix-norm" rather than energy amplification. From Foures *et al.* (2014).
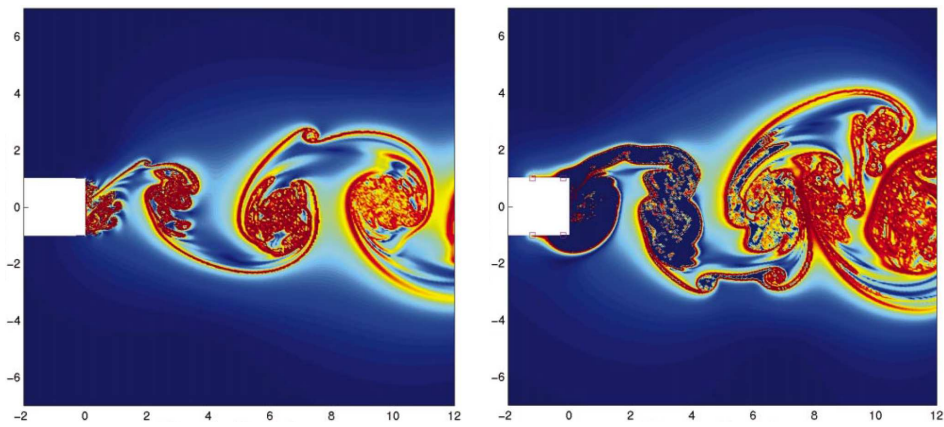
Figure 14 – Prescribing the location of separation points to improve mixing (Wang *et al.*, 2003): snapshots of the uncontrolled (left) and controlled (right) flow. Hot colors correspond to large values of the Direct Lyapunov Exponent field and show Lagrangian coherent structures (attracting material lines).

wake" (figure 14). A related method allowed Alam *et al.* (2006) to enforce reattachment at a prescribed location and reduce the recirculation length in the flow past a backward-facing step. Reducing the extent of flow separation is desirable not only in mixing applications aiming at a good level of homogeneity, but also when long residence times must be avoided, for example in arterial flow where red blood cells are to deliver oxygen quickly (in fact, residence time itself could be chosen as objective function for sensitivity analysis or optimization). The manipulation of other geometric quantities, as illustrated in chapter 4, might prove very interesting for accurate flow control not only at macro scales but also at smaller scales (Chen & Brenner, 2004), including a number of microfluidic applications (see e.g. Schneider, Mandre & Brenner, 2011).

Bibliography

ACRIVOS, A., LEAL, L.G., SNOWDEN, D.D. & PAN, F. 1968 Further experiments on steady separated flows past bluff objects. *Journal of Fluid Mechanics* **34**, 25–48.

AFTOSMIS, M., BERGER, M. & ALONSO, J. 2006 Applications of a cartesian mesh boundary-layer approach for complex configurations. In *44th AIAA Aerospace Sciences Meeting and Exhibit*.

ÅKERVIK, E., EHRENSTEIN, U., GALLAIRE, F. & HENNINGSON, D.S. 2008 Global two-dimensional stability measures of the flat plate boundary-layer flow. *European Journal of Mechanics - B/Fluids* **27** (5), 501–513.

ALAM, M.-R., LIU, W. & HALLER, G. 2006 Closed-loop separation control: An analytic approach. *Physics of Fluids (1994-present)* **18** (4).

ALIZARD, F., CHERUBINI, S. & ROBINET, J.-C. 2009 Sensitivity and optimal forcing response in separated boundary layer flows. *Physics of Fluids* **21** (6), 064108.

ALIZARD, F. & ROBINET, J.-C. 2007 Spatially convective global modes in a boundary layer. *Physics of Fluids (1994-present)* **19** (11).

BAGHERI, S., HENNINGSON, D.S., HOEPFFNER, J. & SCHMID, P.J. 2009 Input-output analysis and control design applied to a linear model of spatially developing flows. *Applied Mechanics Reviews* **62**.

BARBAGALLO, A., SIPP, D. & SCHMID, P.J. 2009 Closed-loop control of an open cavity flow using reduced-order models. *Journal of Fluid Mechanics* **641**, 1–50.

BARKLEY, D., GOMES, M.G.M. & HENDERSON, R. D. 2002 Three-dimensional instability in flow over a backward-facing step. *Journal of Fluid Mechanics* **473**, 167–190.

BEAUDOIN, J.-F., CADOT, O., AIDER, J.-L. & WESFREID, J.-E. 2006 Drag reduction of a bluff body using adaptive control methods. *Physics of Fluids (1994-present)* **18** (8).

BECKER, R., KING, R., PETZ, R. & NITSCHE, W. 2007 Adaptive closed-loop separation control on a high-lift configuration using extremum seeking. *AIAA Journal* **45** (6), 1382–1392.

Bibliography

BERNARD, A., FOUCAUT, J.M., DUPONT, P. & STANISLAS, M. 2003 Decelerating boundary layer: A new scaling and mixing length model. *AIAA Journal* **41** (2), 248–255.

BEWLEY, T.R., MOIN, P. & TEMAM, R. 2001 DNS-based predictive control of turbulence: an optimal benchmark for feedback algorithms. *Journal of Fluid Mechanics* **447**, 179–225.

BLACKBURN, H.M., BARKLEY, D. & SHERWIN, S.J. 2008 Convective instability and transient growth in flow over a backward-facing step. *Journal of Fluid Mechanics* **603**, 271–304.

BOTTARO, A., CORBETT, P. & LUCHINI, P. 2003 The effect of base flow variation on flow stability. *Journal of Fluid Mechanics* **476**, 293–302.

BOUJO, E., EHRENSTEIN, U. & GALLAIRE, F. 2013 Open-loop control of noise amplification in a separated boundary layer flow. *Physics of Fluids* **25** (12).

BOUJO, E. & GALLAIRE, F. 2014 Controlled reattachment in separated flows: a variational approach to recirculation length reduction. *Journal of Fluid Mechanics* **742**, 618–635.

BRANDT, L., SIPP, D., PRALITS, J.O. & MARQUET, O. 2011 Effect of base-flow variation in noise amplifiers: the flat-plate boundary layer. *Journal of Fluid Mechanics* **687**, 503–528.

BUTLER, K.M. & FARRELL, B.F. 1992 Three-dimensional optimal perturbations in viscous shear flow. *Physics of Fluids A: Fluid Dynamics* **4** (8), 1637–1650.

CADOT, O., THIRIA, B. & BEAUDOIN, J.-F. 2009 Passive drag control of a turbulent wake by local disturbances. In *IUTAM Symposium on Unsteady Separated Flows and their Control* (ed. Marianna Braza & Kerry Hourigan), *IUTAM Bookseries*, vol. 14, pp. 529–537. Springer Netherlands.

CASTRO, C., LOZANO, C., PALACIOS, F. & ZUAZUA, E. 2007 Systematic continuous adjoint approach to viscous aerodynamic design on unstructured grids. *AIAA Journal* **45** (9), 2125–2139.

CATHERALL, D. & MANGLER, K. W. 1966 The integration of the two-dimensional laminar boundary-layer equations past the point of vanishing skin friction. *Journal of Fluid Mechanics* **26**, 163–182.

CEBECI, T. & COUSTEIX, J. 1999 *Modeling and Computation of Boundary Layer Flows.* Springer-Verlag.

CHEN, H.H. & BRENNER, M.P. 2004 The optimal faucet. *Physical Review Letters* **92**, 166106.

CHERUBINI, S., DE PALMA, P., ROBINET, J.-C. & BOTTARO, A. 2011 The minimal seed of turbulent transition in the boundary layer. *Journal of Fluid Mechanics* **689**, 221–253.

CHOI, H., HINZE, M. & KUNISCH, K. 1999 Instantaneous control of backward-facing step flows. *Applied Numerical Mathematics* **31** (2), 133–158.

176

CHOI, H., JEON, W.-P. & KIM, J.K. 2008 Control of flow over a bluff body. *Annual Review of Fluid Mechanics* **40**, 113–139.

CHOMAZ, J.M. 2005 Global instabilities in spatially developing flows: Non-normality and nonlinearity. *Annual Review of Fluid Mechanics* **37**, 357–392.

CORBETT, P. & BOTTARO, A. 2000 Optimal perturbations for boundary layers subject to stream-wise pressure gradient. *Physics of Fluids* **12** (1), 120–130.

CORBETT, P. & BOTTARO, A. 2001 Optimal control of nonmodal disturbances in boundary layers. *Theoretical and Computational Fluid Dynamics* **15** (2), 65–81.

CORDIER, L. 2009 Workshop on flow control methods and applications (lecture notes). Université de Poitiers.

COSSU, C. 2014 An introduction to optimal control, lecture notes from the FLOW-NORDITA summer school on advanced instability methods for complex flows, Stockholm, Sweden, 2013. *Applied Mechanics Reviews* **66** (2).

COSSU, C. & CHOMAZ, J. M. 1997 Global measures of local convective instabilities. *Phys. Rev. Lett.* **78**, 4387–4390.

COUSTEIX, J. & MAUSS, J. 2004 Approximations of the Navier–Stokes equations for high Reynolds number flows past a solid wall. *Journal of Computational and Applied Mathematics* **166** (1), 101–122, proceedings of the International Conference on Boundary and Interior Layers - Computational and Asymptotic Methods.

DALTON, C., XU, Y. & OWEN, J.C. 2001 The suppression of lift on a circular cylinder due to vortex shedding at moderate Reynolds numbers. *Journal of Fluids and Structures* **15** (3–4), 617–628.

DECHAUME, A., COUSTEIX, J. & MAUSS, J. 2005 An interactive boundary layer model compared to the triple deck theory. *European Journal of Mechanics - B/Fluids* **24** (4), 439–447.

DEL GUERCIO, G., COSSU, C. & PUJALS, G. 2014 Stabilizing effect of optimally amplified streaks in parallel wakes. *Journal of Fluid Mechanics* **739**, 37–56.

DERGHAM, G., SIPP, D. & ROBINET, J.-CH. 2013 Stochastic dynamics and model reduction of amplifier flows: the backward facing step flow. *Journal of Fluid Mechanics* **719**, 406–430.

DRELA, M. & GILES, M. B. 1987 Viscous-inviscid analysis of transonic and low Reynolds number ows. *AIAA Journal* **25**, 1347–1355.

EHRENSTEIN, U. & GALLAIRE, F. 2005 On two-dimensional temporal modes in spatially evolving open flows: The flat-plate boundary layer. *Journal of Fluid Mechanics* .

EHRENSTEIN, U. & GALLAIRE, F. 2008 Two-dimensional global low-frequency oscillations in a separating boundary-layer flow. *Journal of Fluid Mechanics* **614**, 315–327.

Bibliography

EHRENSTEIN, U., PASSAGGIA, P.Y. & GALLAIRE, F. 2011 Control of a separated boundary layer: reduced-order modeling using global modes revisited. *Theoretical and Computational Fluid Dynamics* **25** (1-4), 195–207.

FANI, A., CAMARRI, S. & SALVETTI, M.V. 2012 Stability analysis and control of the flow in a symmetric channel with a sudden expansion. *Physics of Fluids (1994-present)* **24** (8).

FANI, A., CAMARRI, S. & SALVETTI, M. V. 2013 Investigation of the steady engulfment regime in a three-dimensional T-mixer. *Physics of Fluids (1994-present)* **25** (6).

FARRELL, B. F. & IOANNOU, P. J. 1996 Generalized stability theory. Part I: Autonomous operators. *Journal of the Atmospheric Sciences* **53**, 2025–2040.

FERNHOLZ, H.H., JANKE, G., SCHOBER, M., WAGNER, P.M. & WARNACK, D. 1996 New developments and applications of skin-friction measuring techniques. *Measurement Science and Technology* **7** (10), 1396.

FIEDLER, H.E. & FERNHOLZ, H.-H. 1990 On management and control of turbulent shear flows. *Progress in Aerospace Sciences* **27** (4), 305–387.

FINN, R. K. 1953 Determination of the drag on a cylinder at low Reynolds numbers. *Journal of Applied Physics* **24** (6), 771–773.

FOURES, D.P.G., CAULFIELD, C.P. & SCHMID, P.J. 2013 Localization of flow structures using ∞-norm optimization. *Journal of Fluid Mechanics* **729**, 672–701.

FOURES, D.P.G., CAULFIELD, C.P. & SCHMID, P.J. 2014 Optimal mixing in two-dimensional plane Poiseuille flow at finite Péclet number. *Journal of Fluid Mechanics* **748**, 241–277.

FRANSSON, J.H.M., BRANDT, L., TALAMELLI, A. & COSSU, C. 2004 Experimental and theoretical investigation of the nonmodal growth of steady streaks in a flat plate boundary layer. *Physics of Fluids (1994-present)* **16** (10), 3627–3638.

FRANSSON, J.H.M., TALAMELLI, A., BRANDT, L. & COSSU, C. 2006 Delaying transition to turbulence by a passive mechanism. *Phys. Rev. Lett.* **96**, 064501.

GALLAIRE, F. 2002 Instabilités d'un jet tournant et contrôle de l'éclatement tourbillonnaire. PhD thesis, École Polytechnique.

GALLAIRE, F., CHOMAZ, J.-M. & HUERRE, P. 2004 Closed-loop control of vortex breakdown: a model study. *Journal of Fluid Mechanics* **511**, 67–93.

GALLAIRE, F., MARQUILLIE, M. & EHRENSTEIN, U. 2007 Three dimensional transverse instabilities in detached boundary layers. *Journal of Fluid Mechanics* .

GARNAUD, X., LESSHAFFT, L., SCHMID, P. J. & HUERRE, P. 2013 The preferred mode of incompressible jets: linear frequency response analysis. *Journal of Fluid Mechanics* **716**, 189–202.

GARNIER, E., PAMART, P.Y., DANDOIS, J. & SAGAUT, P. 2012 Evaluation of the unsteady RANS capabilities for separated flows control. *Computers & Fluids* **61**, 39–45.

GASTER, M. 1962 A note on the relation between temporally-increasing and spatially-increasing disturbances in hydrodynamic stability. *Journal of Fluid Mechanics* **14**, 222–224.

GAUTIER, N. & AIDER, J.-L. 2013 Control of the separated flow downstream of a backward-facing step using visual feedback. *Proceedings of the Royal Society A* **469** (2160).

GIANNETTI, F., CAMARRI, S. & LUCHINI, P. 2010 Structural sensitivity of the secondary instability in the wake of a circular cylinder. *Journal of Fluid Mechanics* **651**, 319–337.

GIANNETTI, F. & LUCHINI, P. 2007 Structural sensitivity of the first instability of the cylinder wake. *Journal of Fluid Mechanics* **581**, 167–197.

GLEZER, A. & AMITAY, M. 2002 Synthetic jets. *Annual Review of Fluid Mechanics* **34** (1), 503–529.

GOLDSTEIN, S. 1948 On laminar boundary-layer flow near a position of separation. *The Quarterly Journal of Mechanics and Applied Mathematics* **1** (1), 43–69.

GREENBLATT, D. & WYGNANSKI, I.J. 2000 The control of flow separation by periodic excitation. *Progress in Aerospace Sciences* **36** (7), 487–545.

GAD-EL HAK, M. 1996 Modern developments in flow control. *Applied Mechanics Reviews* **49** (7), 365–379.

HALLER, G. 2004 Exact theory of unsteady separation for two-dimensional flows. *Journal of Fluid Mechanics* **512**, 257–311.

HENDERSON, R.D. 1995 Details of the drag curve near the onset of vortex shedding. *Physics of Fluids* **7** (9), 2102–2104.

HENNING, L. & KING, R. 2007 Robust multivariable closed-loop control of a turbulent backward-facing step flow. *Journal of Aircraft* **44** (1), 201–208.

HERVÉ, A., SIPP, D., SCHMID, P. J. & SAMUELIDES, M. 2012 A physics-based approach to flow control using system identification. *Journal of Fluid Mechanics* **702**, 26–58.

HILL, D. C. 1992 A theoretical approach for analyzing the restabilization of wakes. *AIAA 92-0067* .

HOFFMAN, J. 2005 Computation of mean drag for bluff body problems using adaptive DNS/LES. *SIAM Journal on Scientific Computing* **27** (1), 184–207.

HWANG, Y. & COSSU, C. 2010 Amplification of coherent streaks in the turbulent Couette flow: an input–output analysis at low Reynolds number. *Journal of Fluid Mechanics* **643**, 333–348.

Bibliography

HWANG, Y., KIM, J. & CHOI, H. 2013 Stabilization of absolute instability in spanwise wavy two-dimensional wakes. *Journal of Fluid Mechanics* **727**, 346–378.

IGARASHI, T. 1997 Drag reduction of a square prism by flow control using a small rod. *Journal of Wind Engineering and Industrial Aerodynamics* **69–71**, 141–153.

JAMESON, A., MARTINELLI, L. & PIERCE, N.A. 1998 Optimum aerodynamic design using the Navier–Stokes equations. *Theoretical and Computational Fluid Dynamics* **10** (1-4), 213–237.

JUILLET, F., SCHMID, P.J. & HUERRE, P. 2013 Control of amplifier flows using subspace identification techniques. *Journal of Fluid Mechanics* **725**, 522–565.

KAIKTSIS, L., EM KARNIADAKIS, G. & ORSZAG, S.A. 1996 Unsteadiness and convective instabilities in two-dimensional flow over a backward-facing step. *Journal of Fluid Mechanics* **321**, 157–187.

KIM, J. & BEWLEY, T.R. 2007 A linear systems approach to flow control. *Annual Review of Fluid Mechanics* **39**, 383–417.

LAGRÉE, P.-Y. 2000 Erosion and sedimentation of a bump in fluvial flow. *Comptes Rendus de l'Académie des Sciences - Series {IIB} - Mechanics* **328** (12), 869–874.

LAGRÉE, P.-Y. 2010 Interactive boundary layers. In *Asymptotic Methods in Fluid Mechanics: Survey and Recent Advances, CISM Courses and Lectures, vol. 523* (ed. H. Steinrück), pp. 247–286. Springer-Verlag, Wien New York.

LAGRÉE, P.-Y., VAN HIRTUM, A. & PELORSON, X. 2007 Asymmetrical effects in a 2D stenosis. *European Journal of Mechanics - B/Fluids* **26** (1), 83–92.

LANZERSTORFER, D. & KUHLMANN, H.C. 2012 Global stability of the two-dimensional flow over a backward-facing step. *Journal of Fluid Mechanics* **693**, 1–27.

LAUGA, E. & BEWLEY, T.R. 2004 Performance of a linear robust control strategy on a nonlinear model of spatially developing flows. *Journal of Fluid Mechanics* **512**, 343–374.

LE BALLEUR, J.C 1978 Couplage visqueux non-visqueux: Méthode numérique et applications aux écoulements bidimensionnels transsoniques et supersoniques. *La Recherche Aérospatiale* **2**, 65–76.

LIGHTHILL, M.J. 1963 Introduction. Boundary layer theory. In *Laminar Boundary Layers* (ed. L. Rosenhead), pp. 46–113. Oxford University Press.

LIONS, J.L. 1971 *Optimal control of systems governed by partial differential equations*. New York: Springer-Verlag.

LOCK, R.C. & WILLIAMS, B.R. 1987 Viscous-inviscid interactions in external aerodynamics. *Progress in Aerospace Sciences* **24** (2), 51–171.

LÖFDAHL, L. & GAD-EL HAK, M. 1999 MEMS-based pressure and shear stress sensors for turbulent flows. *Measurement Science and Technology* **10** (8), 665.

LORTHOIS, S., LAGRÉE, P.-Y., MARC-VERGNES, J.-P. & CASSOT, F. 2000 Maximal wall shear stress in arterial stenoses: Application to the internal carotid arteries. *Journal of Biomechanical Engineering* .

LU, F.K. 2010 Surface oil flow visualization. *The European Physical Journal Special Topics* **182** (1), 51–63.

LUCHINI, P. & BOTTARO, A. 2014 Adjoint equations in stability analysis. *Annual Review of Fluid Mechanics* **46** (1), 493–517.

MANTIĆ LUGO, V., ARRATIA, C. & GALLAIRE, F. 2014 A self-consistent model for the saturation dynamics of the vortex shedding around the mean flow in the unstable cylinder wake. *Under revision* .

MARQUET, O. & SIPP, D. 2010*a* Active steady control of vortex shedding: an adjoint-based sensitivity approach. In *Seventh IUTAM Symposium on Laminar-Turbulent Transition* (ed. Philipp Schlatter & Dan S. Henningson), *IUTAM Bookseries*, vol. 18, pp. 259–264. Springer Netherlands.

MARQUET, O. & SIPP, D. 2010*b* Global sustained perturbations in a backward-facing step flow. In *Seventh IUTAM Symposium on Laminar-Turbulent Transition* (ed. Philipp Schlatter & Dan S. Henningson), *IUTAM Bookseries*, vol. 18, pp. 525–528. Springer Netherlands.

MARQUET, O., SIPP, D. & JACQUIN, L. 2008 Sensitivity analysis and passive control of cylinder flow. *Journal of Fluid Mechanics* **615**, 221–252.

MARQUILLIE, M. & EHRENSTEIN, U. 2002 Numerical simulation of separating boundary-layer flow. *Computers & Fluids* .

MARQUILLIE, M. & EHRENSTEIN, U. 2003 On the onset of nonlinear oscillations in a separating boundary-layer flow. *Journal of Fluid Mechanics* **490**, 169–188.

MCLACHLAN, B.G. 1989 Study of a circulation control airfoil with leading/trailing-edge blowing. *Journal of Aircraft* **26** (2), 817–821.

MELIGA, P., BOUJO, E., PUJALS, E. & GALLAIRE, F. 2014 Sensitivity of aerodynamic forces in laminar and turbulent flow past a square cylinder. *Submitted to Physics of Fluids* .

MELIGA, P. & GALLAIRE, F. 2011 Control of axisymmetric vortex breakdown in a constricted pipe: Nonlinear steady states and weakly nonlinear asymptotic expansions. *Physics of Fluids (1994-present)* **23** (8).

MELIGA, P., PUJALS, G. & SERRE, E. 2012 Sensitivity of 2-D turbulent flow past a D-shaped cylinder using global stability. *Physics of Fluids (1994-present)* **24** (6).

Bibliography

MELIGA, P., SIPP, D. & CHOMAZ, J.-M. 2010 Open-loop control of compressible afterbody flows using adjoint methods. *Physics of Fluids* **22** (5), 054109.

METTOT, C., SIPP, D. & BÉZARD, H. 2014 Quasi-laminar stability and sensitivity analyses for turbulent flows: Prediction of low-frequency unsteadiness and passive control. *Physics of Fluids (1994-present)* **26** (4), –.

MEUNIER, P. & LEWEKE, T. 2003 Analysis and treatment of errors due to high velocity gradients in particle image velocimetry. *Experiments in Fluids* **35** (5), 408–421.

MITTAL, S. & RAGHUVANSHI, A. 2001 Control of vortex shedding behind circular cylinder for flows at low reynolds numbers. *International Journal for Numerical Methods in Fluids* **35** (4), 421–447.

MOHAMMADI, B. & PIRONNEAU, O. 2001 *Applied shape optimization for fluids*. Oxford: Clarendon Press.

MONKEWITZ, P.A. 1988 A note on vortex shedding from axisymmetric bluff bodies. *Journal of Fluid Mechanics* **192**, 561–575.

MONOKROUSOS, A., BOTTARO, A., BRANDT, L., DI VITA, A. & HENNINGSON, D.S. 2011 Nonequilibrium thermodynamics and the optimal path to turbulence in shear flows. *Phys. Rev. Lett.* **106**, 134502.

NAUGHTON, J.W. & SHEPLAK, M. 2002 Modern developments in shear-stress measurement. *Progress in Aerospace Sciences* **38** (6–7), 515 – 570.

NISHIOKA, M. & SATO, H. 1978 Mechanism of determination of the shedding frequency of vortices behind a cylinder at low Reynolds numbers. *Journal of Fluid Mechanics* **89**, 49–60.

OSEEN, C. W. 1910 Über die Stokes'sche Formel, und über eine verwandte Aufgabe in der Hydrodynamik. *Arkiv för matematik, astronomi och fysik* **vi** (29).

PAREZANOVIĆ, V. & CADOT, O. 2009 The impact of a local perturbation on global properties of a turbulent wake. *Physics of Fluids* **21** (7).

PAREZANOVIĆ, V. & CADOT, O. 2012 Experimental sensitivity analysis of the global properties of a two-dimensional turbulent wake. *Journal of Fluid Mechanics* **693**, 115–149.

PASSAGGIA, P.-Y. & EHRENSTEIN, U. 2013 Adjoint based optimization and control of a separated boundary-layer flow. *European Journal of Mechanics - B/Fluids* **41** (0), 169–177.

PASSAGGIA, P.-Y., LEWEKE, T. & EHRENSTEIN, U. 2012 Transverse instability and low-frequency flapping in incompressible separated boundary layer flows: an experimental study. *Journal of Fluid Mechanics* **703**, 363–373.

PASTOOR, M., KING, R., NOACK, B.R. & TADMOR, G. 2005 Observers and feedback control for shear layer vortices. In *Decision and Control, 2005 and 2005 European Control Conference. CDC-ECC '05. 44th IEEE Conference on*, pp. 506–511.

PRALITS, J.O., BRANDT, L. & GIANNETTI, F. 2010 Instability and sensitivity of the flow around a rotating circular cylinder. *Journal of Fluid Mechanics* **650**, 513–536.

PRANDTL, L. 1928 Über Flüssigkeitbewegung bei sehr kleiner Reibung / On the motion of fluids with very little viscosity. Technical Memorandum NACA-TM-452. NACA, translation of a 1904 lecture at the Third International Congress of Mathematicians in Heidelberg.

PRASAD, A. & WILLIAMSON, C.H.K. 1997 A method for the reduction of bluff body drag. *Journal of Wind Engineering and Industrial Aerodynamics* **69–71**, 155–167.

PRESS, W.H., TEUKOLSKY, S.A., VETTERLING, W.T. & FLANNERY, B.P. 1994 *Numerical recipes in FORTRAN: the art of scientific computing*, 2nd edn. Cambridge University Press.

PRINGLE, C.C.T. & KERSWELL, R.R. 2010 Using nonlinear transient growth to construct the minimal seed for shear flow turbulence. *Physical Review Letters* **105**, 154502.

PROUDMAN, I. & PEARSON, J. R. A. 1957 Expansions at small Reynolds numbers for the flow past a sphere and a circular cylinder. *Journal of Fluid Mechanics* **2**, 237–262.

PUJALS, G., DEPARDON, S. & COSSU, C. 2010 Drag reduction of a 3D bluff body using coherent streamwise streaks. *Experiments in Fluids* **49** (5), 1085–1094.

RABIN, S. M. E., CAULFIELD, C. P. & KERSWELL, R. R. 2012 Triggering turbulence efficiently in plane Couette flow. *Journal of Fluid Mechanics* **712**, 244–272.

REYNOLDS, O. 1883 An experimental investigation of the circumstances which determine whether the motion of water shall be direct or sinuous, and of the law of resistance in parallel channels. *Philosophical Transactions of the Royal Society of London* **174**, pp. 935–982.

ROUSSOPOULOS, K. & MONKEWITZ, P.A. 1996 Nonlinear modelling of vortex shedding control in cylinder wakes. *Physica D: Nonlinear Phenomena* **97** (1–3), 264–273.

ROWLEY, C.W. 2005 Model reduction for fluids, using balanced proper orthogonal decomposition. *International Journal of Bifurcation and Chaos* **15** (03), 997–1013.

RÜEDI, J.-D. 2002 Instabilities of artificial streaks in a laminar boundary layer. PhD thesis, EPFL.

SAKAMOTO, H., TAN, K. & HANIU, H. 1991 An optimum suppression of fluid forces by controlling a shear layer separated from a square prism. *Journal of Fluids Engineering* **113** (2), 183–189.

SCHLICHTING, H. 1979 *Boundary Layer Theory*. New York: McGraw-Hill.

SCHMID, P.J. & HENNINGSON, D.S. 2001 *Stability and transition in shear flows*. Springer.

SCHNEIDER, T.M., MANDRE, S. & BRENNER, M.P. 2011 Algorithm for a microfluidic assembly line. *Physical Review Letters* **106**, 094503.

Bibliography

SCHUMM, M., BERGER, E. & MONKEWITZ, P.A. 1994 Self-excited oscillations in the wake of two-dimensional bluff bodies and their control. *Journal of Fluid Mechanics* .

SEIFERT, A., DARABI, A. & WYGNANSKI, I. 1996 Delay of airfoil stall by periodic excitation. *Journal of Aircraft* **33** (4), 691–698.

SEIFERT, A. & PACK MELTON, L. 2006 Identification and control of turbulent boundary layer separation. In *IUTAM Symposium on One Hundred Years of Boundary Layer Research* (ed. G.E.A. Meier, K.R. Sreenivasan & H.J. Heinemann), pp. 199–208. Springer.

SINHA, S.N., GUPTA, A. K. & OBERAI, M. 1981 Laminar separating flow over backsteps and cavities. I - Backsteps. *AIAA Journal* **19**, 1527–1530.

SIPP, D. 2012 Open-loop control of cavity oscillations with harmonic forcings. *Journal of Fluid Mechanics* **708**, 439–468.

SIPP, D. & LEBEDEV, A. 2007 Global stability of base and mean flows: a general approach and its applications to cylinder and open cavity flows. *Journal of Fluid Mechanics* **593**, 333–358.

SIPP, D. & MARQUET, O. 2013 Characterization of noise amplifiers with global singular modes: the case of the leading-edge flat-plate boundary layer. *Theoretical and Computational Fluid Dynamics* **27** (5), 617–635.

STRYKOWSKI, P. J. & SREENIVASAN, K. R. 1990 On the formation and suppression of vortex 'shedding' at low Reynolds numbers. *Journal of Fluid Mechanics* .

SYCHEV, V.V., RUBAN, A.I., SYCHEV, VIC.V. & KOROLEV, G.L. 1998 *Asymptotic Theory of Separated Flows*. Cambridge University Press.

TANEDA, S. 1956 Experimental investigation of the wakes behind cylinders and plates at low Reynolds numbers. *Journal of the Physical Society of Japan* **11** (3), 302–307.

TCHOUFAG, J., MAGNAUDET, J. & FABRE, D. 2013 Linear stability and sensitivity of the flow past a fixed oblate spheroidal bubble. *Physics of Fluids (1994-present)* **25** (5).

THIRIA, B. & WESFREID, J. E. 2007 Stability properties of forced wakes. *Journal of Fluid Mechanics* **579**, 137–161.

TIAN, Y., SONG, Q. & CATTAFESTA, L. 2006 Adaptive feedback control of flow separation. In *3rd AIAA Flow Control Conference*. AIAA-2006-3016.

TOMOTIKA, S. & AOI, T. 1951 An expansion formula for the drag on a circular cylinder moving through a viscous fluid at small Reynolds numbers. *The Quarterly Journal of Mechanics and Applied Mathematics* **4** (4), 401–406.

TREFETHEN, L.N., TREFETHEN, A.E., REDDY, S.C. & DRISCOLL, T.A. 1993 Hydrodynamic stability without eigenvalues. *Science* **261** (5121), pp. 578–584.

TRITTON, D.J. 1959 Experiments on the flow past a circular cylinder at low Reynolds numbers. *Journal of Fluid Mechanics* **6**, 547–567.

URSENBACHER, T. 2000 Traitement de vélocimétrie par images digitales de particules par une technique robuste de distorsion d'images. PhD thesis, EPFL.

VAN DYKE, M. 1982 *An album of fluid motion*. The Parabolic Press.

VELDMAN, A.E.P. 2001 Matched asymptotic expansions and the numerical treatment of viscous-inviscid interaction. In *Practical Asymptotics* (ed. H.K. Kuiken), pp. 189–206. Springer Netherlands.

VERMA, A. & MITTAL, S. 2011 A new unstable mode in the wake of a circular cylinder. *Physics of Fluids* **23** (12), 121701.

VONLANTHEN, R. & MONKEWITZ, P.A. 2013 Grid turbulence in dilute polymer solutions: PEO in water. *Journal of Fluid Mechanics* **730**, 76–98.

WANG, Y., HALLER, G., BANASZUK, A. & TADMOR, G. 2003 Closed-loop Lagrangian separation control in a bluff body shear flow model. *Physics of Fluids (1994-present)* **15** (8), 2251–2266.

WEICKGENANNT, A. & MONKEWITZ, P.A. 2000 Control of vortex shedding in an axisymmetric bluff body wake. *European Journal of Mechanics - B/Fluids* **19** (5), 789–812.

WELDON, M., PEACOCK, T., JACOBS, G. B., HELU, M. & HALLER, G. 2008 Experimental and numerical investigation of the kinematic theory of unsteady separation. *Journal of Fluid Mechanics* **611**, 1–11.

WERLÉ, H. 1974 Le tunnel hydrodynamique au service de la recherche aérospatiale. *ONERA Publ. 156* .

WERLÉ, H. 1980 *La Recherche Aérospatiale* **5**, 35–49.

WILSON, J., SCHATZMAN, D., ARAD, E., SEIFERT, A. & SHTENDE, T 2013 Suction and pulsed-blowing flow control applied to an axisymmetric body. *AIAA Journal* **51** (10), 2432–2446.

ZHOU, K., DOYLE, J. C. & GLOVER, K. 1996 *Robust and optimal control*. New Jersey: Prentice Hall.

ZIELINSKA, B. J. A., GOUJON-DURAND, S., DUŠEK, J. & WESFREID, J. E. 1997 Strongly nonlinear effect in unstable wakes. *Phys. Rev. Lett.* **79**, 3893–3896.

Curriculum Vitae

Edouard Boujo

Ch. du Devin 55, Lausanne 1012, Switzerland
Phone: (+41)(0)77 451 07 28
Email: edouard.boujo@epfl.ch

Born: February 12, 1982
Nationality: French
Married

Education

2014: Ph.D. in mechanical engineering, under the supervision of Prof. F. Gallaire, EPFL, Lausanne (Swizerland).

2006: M.Sc. in aeronautical & vehicle engineering, KTH, Stockholm (Sweden).
Research work under the supervision of Prof. T. Kajishima, Osaka Univ., Osaka (Japan).

2004: M.Sc. in engineering sciences, École Polytechnique, Palaiseau (France).
Research work under the supervision of Prof. T. Yamaguchi, Tohoku Univ., Sendai (Japan).

Work experience

2006-2009: Engineer in aerodynamics & thermal management, Nissan, Atsugi (Japan)

Language skills

French: mother tongue
English: good (TOEIC 965)
Japanese: good (JLPT 1)
Spanish, Swedish: basic

Teaching

Teaching assistant at EPFL in *Fluid Flows* (2011-2013) and *Hydrodynamics* (2010-2013).

Publications

Peer-reviewed journal articles

1. Boujo, E., Ehrenstein, U. & Gallaire, F. 2013 Open-loop control of noise amplification in a separated boundary layer flow. *Physics of Fluids* **25** (12).

2. Boujo, E. & Gallaire, F. 2014 Controlled reattachment in separated flows: a variational approach to recirculation length reduction. *Journal of Fluid Mechanics* **742**, 618-635.

3. Boujo, E., Gallaire, F. & Ehrenstein, U. 2014 Open-loop control of a separated boundary layer, *Comptes Rendus Mécanique*, **342** (6-7), 403-409.

4. Meliga, P., Boujo, E., Pujals, G. & Gallaire, F. 2014 Sensitivity of aerodynamic forces in laminar and turbulent flow past a square cylinder. Submitted to *Physics of Fluids.*

5. Boujo, E. & Gallaire, F. 2014 Manipulating flow separation: sensitivity of stagnation points, separatrix angles and recirculation area to steady actuation. Submitted to *Proceedings of the Royal Society A.*

6. Boujo, E. & Gallaire, F. 2014 Sensitivity and open-loop control of stochastic response in a noise amplifier flow: the backward-facing step. Submitted to *Journal of Fluid Mechanics.*

Conference papers

1. Boujo, E. & Gallaire, F. Etude expérimentale de l'écoulement derrière une bosse, *20ème Congrès Français de Mécanique*, Besançon, France, 2011.

2. Boujo, E., Gallaire, F. & Ehrenstein, U. Open-loop control of a separated boundary layer, *3rd GDR "Separation Flow Control" Symposium*, Lille, France, 2013.

Conference proceedings

1. Boujo, E. & Gallaire, F. Sensitivity of optimal gains in a detached boundary layer, *9th Euromech European Fluid Mechanics Conference*, Rome, Italy, 2012.

2. Boujo, E. & Gallaire, F. Optimal open-loop control of the recirculation length in the wake of a cylinder, *65th Annual Meeting of the American Physical Society's Division of Fluid Dynamics*, San Diego, USA, 2012.

3. Boujo, E. & Gallaire, F. Forced reattachment in separated flows: a variational approach to recirculation length reduction, *Colloquium Euromech 547 "Trends in Open Shear Flow Instability"*, Palaiseau, France, 2013.